Frequency domain functional near infrared spectroscopic imaging for the assessment of human brain health

By

Guy Antony Perkins

A thesis submitted to
the University of Birmingham
for the degree of
DOCTOR OF PHILOSOPHY

Physical Sciences for Health
School of Chemistry
College of Engineering and Physical Sciences
University of Birmingham
November 2024

ABSTRACT

This thesis explores the use and development of frequency domain (FD) functional near infrared spectroscopy (fNIRS) and diffuse optical tomography (DOT) for use in the assessment of human brain health, with a focus on traumatic brain injury (TBI). The focus on TBI was chosen because TBI has the highest incident of all neurological disorders. TBI is caused when an external force impacts the head, causing an acceleration on the brain and depending on the magnitude and duration of this force, can have several minor and serious consequences on the brain. Currently TBI is graded, mild (mTBI), moderate (M-TBI) or severe (S-TBI) using a subjective assessment, the Glasgow coma scale, with supplementary imaging performed on S-TBI in the form of x-ray CT or MRI scans. These forms of imaging can not be done at the bedside, or outside of clinical environments, and in the case of MRI scans, can be resource expensive. In addition, the subjective assessments may be influenced by factors outside of the TBI itself, which means there exists an opportunity for portable, more resource efficient, objective assessment for TBI. The use of diffuse optics may present as a tool to supplement the aforementioned tools for the assessment of TBI and this thesis investigates the use of frequency domain diffuse optics of brain imaging, for the application of traumatic brain injury assessment.

This thesis develops the use of FD fNIRS and DOT for functional brain imaging, which plays a role in assessing brain health. In the FD, light is emitted sinusoidally on the surface of the scalp, this light is then absorbed and scattered throughout tissue and some of that light is then detected. The measurements made are changes in the intensity (amplitude)

and phase of the modulated light and it is these changes in intensity and more significantly phase that are crucial to unlocking the advantages of FD versus the much used continuous wave (CW) paradigm in diffuse optics. In CW measurements, only changes in intensity are measured, and it has been demonstrated that phase measurements actually sample deeper than intensity measurements. As well as sampling deeper and thus sampling the cortical tissue more than intensity, phase data is also less sensitive to superficial tissue changes. This thesis investigates and explores the use of phase and intensity data with FD measurements, showing that the inclusion of phase data when applied to functional brain imaging increases the contrast of measured brain activation for both fNIRS and DOT. This is performed with a specially designed workflow, to combine recent advancements of data analysis in fNIRS literature, such as short signal regression to minimise superficial tissue influence, optical subject specific registration for accurate placement of source-detector probes on the 3D subject model and a bespoke 3D printed probe holder for the subject neoprene helmet to perform standard and dual slope measurements. Through these design considerations, this workflow enables and enhances the demonstration of FD fNIRS and DOT for functional brain imaging.

The final working chapter in this thesis demonstrates an experimental protocol for imaging S-TBI patients in the intensive care unit, using a lab based FD device and an injected contrast dye. It also provides insight into the challenges of imaging in this type of clinical environment. In addition, this thesis explores another unique aspect of phase data, that the distribution of sensitivity changes as a function of modulation frequency. Through simulations and then measurements on a phantom mimicking functional activation, it is shown that combining measurements of phase at different modulation frequencies increases the accuracy and resolution of DOT, unlocking the best performance of FD diffuse optics. These findings give the platform to FD fNIRS and DOT, in that when assessing human brain health, they provide a more accurate imaging of functional brain activation than the equivalent CW measurements, which could be vital for when assessing human brain health.

DEDICATION

Dedicated to my Mum and Dad

Paw Paw and Gung Gung

Grandma and Grandad

Vincent and Uncle Guy

Thank you.

ACKNOWLEDGMENTS

Throughout my PhD I met many wonderful people and was afforded many opportunities to do things I had never even imagined of. I would like to say thank you to my colleagues around me in the room of LG34, Ben, Alex, and George who guided me during the first few months of my PhD and even shared some time together in Warsaw right before the pandemic. Then I would like to thank Robin, whom I spent many hours with in the CHBH, trying to solve many problems and our amazing experiences with in Fort Lauderdale, Boston and San Francisco. I would also like to thank Andrew and particularly Mario, for giving me the opportunity to conduct research in an intensive care unit and for being great people to work with. There have been many academics that have helped me along the way, Felipe, Sam, Adam, David, thank you to them all. I will always be grateful for the support and guidance of my supervisor and friend, Hamid. Throughout my PhD, I had heard many stories of other PhD students having negative experiences with their supervisors, but I can't fault Hamid, throughout my PhD he gave me support, encouragement and guidance that I will always be grateful for. I will remember our times together in Birmingham, Warsaw, Fort Lauderdale, the White mountains, Boston and San Francisco. Finally a thank you to my family and my friends, who were with me everyday from the start until the end of my PhD, my Mum, Dad, Paw Paw, Richard, my Uncle Yui, Sid, Mark, Dan, Kieran, Sam, Matt and at the very end of my PhD journey, Elena.

PUBLICATIONS RESULTING FROM THIS THESIS

Peer Reviewed Journal Papers:

1. Perkins GA, Eggebrecht AT, Dehghani H. Multi-modulated frequency domain high density diffuse optical tomography. Biomedical Optics Express. 2022;13(10):5275. doi:10.1364/boe.467614

2. Perkins GA, Eggebrecht AT, Dehghani H. Quantitative evaluation of frequency domain measurements in high density diffuse optical tomography. Journal of Biomedical Optics. 2021;26(05). doi:10.1117/1.jbo.26.5.056001

Peer Reviewed Conference Proceedings:

1. Perkins GA, Dehghani H. Multi paradigm frequency domain workflow for human brain imaging. Optical Tomography and Spectroscopy of Tissue XV. 2023; doi:10.1117/12.2649776

2. Perkins GA, Dehghani H. Utilization of Frequency Domain fNIRS to improve contrast. Hardware session. fNIRS Conference 2022.

3. Perkins GA, Forcione M, Dehghani H. Inclusion of scattering in frequency domain functional near infrared spectroscopy increases contrast of parameter recovery. Biophotonics Congress: Biomedical Optics 2022 (Translational, Microscopy, OCT, OTS, BRAIN). 2022; doi:10.1364/ots.2022.os2d.6

4. Perkins GA, Dehghani H. Frequency domain near infrared spectroscopy and high

density diffuse optical tomography improves quantitative accuracy. Hardware session. fNIRS Virtual Conference 2021.

5. Perkins GA, Lucas SJ, Dehghani H. Subject specific atlas based frequency domain diffuse optical tomography. XXII Polish Conference on Biocybernetics and Biomedical Engineering. 2021.

6. Perkins GA, Lucas SJ, Dehghani H. Subject specific atlas-based frequency domain diffuse optical tomography. Diffuse Optical Spectroscopy and Imaging VIII. 2021; doi:10.1117/12.2615230

7. Perkins GA, Dehghani H. Multi Frequency domain measurements improves localisation in high density diffuse optical tomography: A phantom study. Biophotonics Congress: Biomedical Optics 2022 (Translational, Microscopy, OCT, OTS, BRAIN). 2022; doi:10.1364/translational.2022.jm3a.34

8. Perkins GA, Dehghani H. Frequency domain functional near infrared spectroscopy and diffuse tomography improves quantitative accuracy. Diffuse Optical Spectroscopy and Imaging VIII. 2021; doi:10.1117/12.2615214

Awards:

1. SPIE Photonics West BiOS: Three Minute Poster Presentation 1st Place 2021. San Francisco, United States.

2. Centre for Human Brain Health PhD paper of the year nomination 2021. Birmingham, United Kingdom.

3. Three Minute Thesis Challenge University of Birmingham finalist 2021. Birmingham, United Kingdom.

Just like moons and like suns,

With the certainty of tides,

Just like hopes springing high,

Still I'll rise.

Maya Angelou, Still I Rise

Contents

List of Figures

List of Tables

Acronyms

AC Alternating Current. 13

BBB Blood Brain Barrier. 43

BTE Boltzmann Transport Equation. 8

CL Co-Lateral. 143

*CMR*02 Cerebral metabolic rate for oxygen. 44

CSF Cerebral Spinal Fluid. 56

CT Computed Tomography. 40

CW Continuous Wave. 11

CW Differential pathlength factor. 7

DC Direct Current. 13

DOT Diffuse Optical Tomography. 11

DS Dual Slopes. 23

DTOF Distribution time of flight. 15

DWT Discrete Wavelet Transform. 140

ECT Extracranial tissue. 184

ERES Effective Resolution. 61

EROS Event Related Optical Signals. 22

FD Frequency Domain. 13

FEM Finite Element Model. 19

FOV Field of View. 58

FWHM Full Width Half Maxima. 61

HD High Density. 21

HFO High frequency oscillations. 26

HRF Haemodynamic Response Function. 129

Hb Deoxygenated Haemoglobin. 2

HbO Oxygenated Haemoglobin. 2

ICG Indocyanine Green. 43

ICP Cerebral Blood Flow. 44

ICP Inter-cranial Pressure. 43

ICT Intracranial tissue. 184

ICU Intensive care uni. 44

LFO Low frequency oscillations. 26

LHS Left Hand Side. 150

$LOCA$ Localisation Error. 61

$M-TBI$ Moderate Traumatic Brain Injury. 40

MA motion artifacts. 30

MRI Magnetic Resonance Imaging. 40

$NIRFAST$ Near Infrared Fluorescence and Spectral Tomography. 51

$NIRS$ Near Infrared Spectroscopy. 51

NN Nearest Neighbour. 58

PLA Polylactic Acid. 125

PSF Point Spread Functions. 83

RHS Right Hand Side. 150

ROI Region of Interest. 137

$S-D$ Source-Detector. 23

$S-TBI$ Severe Traumatic Brain Injury. 40

SDS Source Detector Separation. 144

SNR Signal to Noise Ratio. 89

$SPA-fNIRS$ Systemic physiology augmented functional near infrared spectroscopy. 28

SSR Short signal regression. 31

TBI Traumatic Brain Injury. 39

UL Uni-Lateral. 143

WHO World Health Organisation. 38

$fMRI$ Functional Magnetic Resonance Imaging. 88

$fNIRS$ functional near infrared spectroscopy. 2

mFD Multi-Frequency Domain. 90

$mTBI$ Mild Traumatic Brain Injury. 40

pvc polyvinyl chloride. 97

$vLFO$ Very low frequency oscillations. 26

Chapter One

Diffuse Optics

The research in this thesis concerns the development of a medical imaging technique called functional near infrared spectroscopy (fNIRS), which is a method for detecting functional brain activity using light. This technique uses fibers incident on the surface of the head of a subject or patient whereby light is emitted on the scalp of a person and is detected a few centimeters away on a different position on the scalp. The light travels in a curved banana shaped path and some of that light travels through the surface of the cortex and by measuring changes in the light detected, functional brain activity can be inferred. This is done by calculating changes in oxygenated hemoglobin (HbO) and deoxygenated hemoglobin (Hb), which from functional brain activation are called the hemodynamic response function (HRF) from the changes in the measured data, which is represented in figure 1.1.

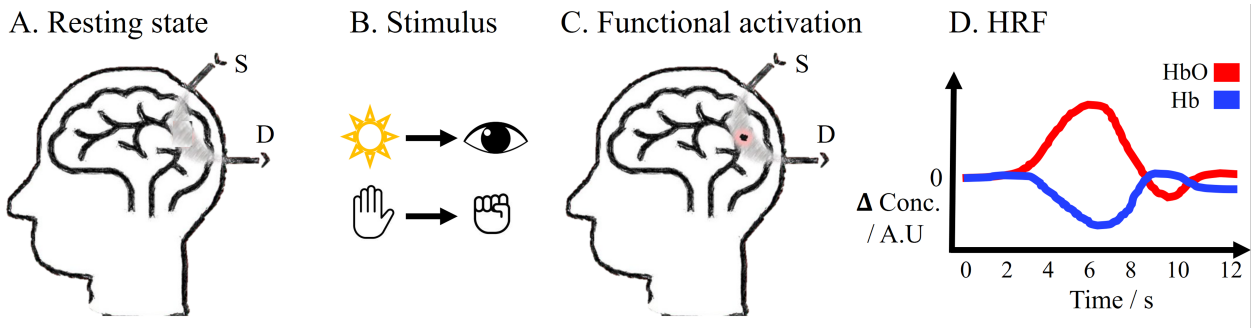

Figure 1.1: The fundamental basis of fNIRS. A. A brain in a resting state with light being measured by a detector D, from a source S. The light samples the surface of the cortex. B. A stimulus occurs for some activation, for example light stimulation to the eyes or movement stimulation via hand movement. C. The stimulus causes a functional activation localised in the cortex. D. Neuronal activity requires energy. This means there is an increase in the demand for oxygen and as a result, local cerebral blood flow increases to deliver this oxygen, in the form of HbO. This means there is a local increase in HbO. The rate of increase of cerebral blood flow is more than the rate of oxygen consumption, i.e there is an over compensation of cerebral blood flow, which is why the local concentration of HbO increases and the relative local concentration of Hb decreases. This is the canonical HRF.

There are three main paradigms within fNIRS, which concern the way in which light is emitted and detected and this thesis aims to develop the use of a paradigm of fNIRS called 'Frequency domain', for more accurate imaging of functional brain activation. In the frequency domain, light emitted is modulated sinusoidally and there are two types of data which are measured, the intensity (amplitude) and phase of the modulated photons, of which the latter has a dependence on the modulation frequency of the emission of light. The development of more accurate imaging from fNIRS is important because fNIRS is underpinned by the diffuse propagation of photons in matter, which in the context of medical imaging is an ill-posed problem. This means research in the development of hardware or the processing of data to improve the accuracy of image reconstruction is vital, particularly for clinical application using fNIRS.

fNIRS has the potential to be useful for clinical applications, because the imaging modality is portable, relatively low cost, non ionising, non invasive and can be supplementary

with other currently used clinical medical imaging techniques such as MRI and X-ray. In particular, information about human brain health can in part be evaluated by functional brain imaging, because for some pathologies, abnormal or reduced brain function is related to worse brain health. This thesis is titled 'Frequency domain functional near infrared spectroscopic imaging for the assessment of human brain health' and investigates two main questions. Firstly, how can frequency domain fNIRS best be used for functional brain imaging and what is the best use of frequency domain data for functional brain imaging.

To address the aforementioned questions, this thesis explains the fundamental physics underpinning fNIRS and explores the relevance and use case of fNIRS for human brain health assessment. Then, starting from simulation, to phantom acquisition and then human subjects, the use and benefits of frequency domain fNIRS are evaluated and discussed. It is shown that maximum performance from frequency domain data can be extracted by taking advantage of multiple modulation frequencies and the combination of the intensity and phase data in frequency domain. In order to navigate the complexities of fNIRS, the physics behind the technique must be understood and these are explored in this chapter.

1.1 Photon propagation in matter

There are two optical properties that underpin the transport of light in biological tissue. These are absorption and scattering. Absorption is where light is absorbed by a chromophore in a medium, with a chromophore being any molecule that can absorb light. Examples of chromophores in biological tissue are water, lipids, and proteins such as haemoglobin (Oxygenated and deoxygenated), DNA, RNA and melanin. Scattering occurs due to gradients and discontinuities in the refractive index of various structures in biological tissue. Elastic scattering changes the direction of the propagation of light (inelastic scattering also changes

the energy of light). These events are represented in figure 1.2.

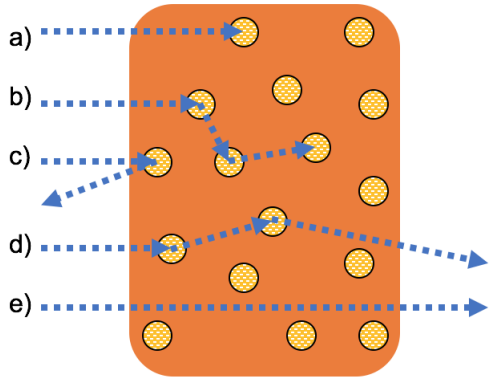

Figure 1.2: The different events that can take place for a photon entering a medium. a. The photon is absorbed. b. The photon undergoes multiple scattering events and is then absorbed. c. The photon is scattered at an angle which causes it to exit the medium and into free space. d. The photon undergoes multiple scattering event and leaves the medium. e. The photon doesn't interact with the medium and passes straight through.

fNIRS was born from the fact that there exists a range of wavelengths in which light can easily travel through human tissue, which is between approximately 650 to 1350 nm (Lane, Xue, and Nie, 2018). Between these wavelengths, light is absorbed less by the prominent chromophore in tissue, particularly water and lipids, which means that it is possible to emit light incident on human skin and measure the transmitted light up to a few centimeters away. This is demonstrated by the absorption spectra for HbO, Hb and water in figure 1.3, where between approximately 650 to 1350 nm, the absorption of HbO, Hb and water are lower than the surrounding wavelengths.

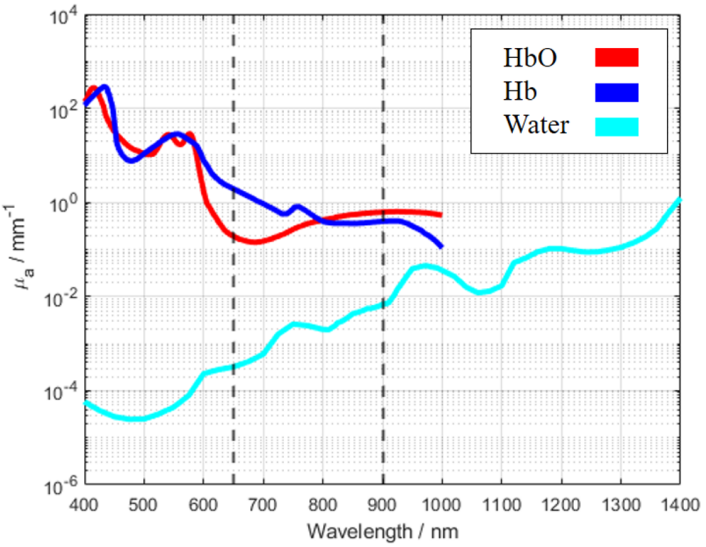

Figure 1.3: The absorption coefficient shown for HbO, Hb and water between 400 nm to 1400 nm. Values were tabulated by Hale and Querry, 1973 and Wray et al., 1988, with dashed lines indicating the range of wavelengths that NIRS studies use, which are from 650 nm to 900 nm, Quaresima and Ferrari, 2019.

The absorption and scattering properties of a medium are quantified by the absorption and scattering coefficient, μ_a and μ_s (SI units of m^{-1}) respectively and are related to the mean free path length before an absorption event takes place, l_a (equation 1.1) and a scattering event occurs, l_s (equation 1.2).

$$\mu_a = \frac{1}{l_a} \tag{1.1}$$

$$\mu_s = \frac{1}{l_s} \tag{1.2}$$

To take into account multiple scattering events, we can consider the reduced scattering coefficient, μ_s' and is shown in equation 1.3,

$$\mu_s' = \mu_s(1-g) \tag{1.3}$$

where g is the anisotropy factor. g ranges from 0 to 1. For completely isotropic scattering, g=0, whereas for completely forward scattering, g=1. g for biological tissue is typically around 0.9 (Bigio and Fantini, 2016). Typically when speaking about the scattering coefficient, it is μ_s' which is being considered. An optical medium can be considered as scattering medium due to the presence of particles that scatter photons, either isotropically or anisotropically. A diffuse medium is where scattering events occur a lot more than absorption events, i.e $\mu_s' >> \mu_a$ which means that photons 'forget' their original propagation direction and the light field is considered diffuse. Later this will be referred to as the diffusion approximation.

For photons travelling in a medium, the differential change in intensity dI is related to the differential optical pathlength dx, by equation 1.4,

$$dI = -\mu_a I dx \tag{1.4}$$

which can be integrated over a distance L, and for incident light I_i and transmitted light I_t. For non scattering media, this gives equation 1.5,

$$I_t = I_i e^{-\mu_a L} \tag{1.5}$$

Equation 1.5 can be turned into the Beer-Lambert law by introducing the fact that the absorption is related to chromophore concentration, C by equation 1.6, where ϵ is the molar extinction coefficient,

$$\mu_a = \epsilon C \tag{1.6}$$

and both μ_a and ϵ are a function of wavelength. The Beer-Lambert law is then given by equation 1.7,

$$A = -log_{10}\frac{I_t}{I_i} = \epsilon C L \tag{1.7}$$

where A is the optical absorbance (In $\log_{10}$ and 'optical density' the natural log.). For an infinitesimal change in absorption dμ_a, the Beer Lambert law becomes equation 1.8

$$d\mu_a = \frac{dA}{L} = -\frac{1}{L}\frac{dI_t}{I_t} \tag{1.8}$$

In order to accommodate for attenuation due to scattering, the Beer-lambert law can be introduced to the diffusion approximation, whereby scattering events dominate over absorption. Equation 1.8 becomes the modified Beet-Lambert law (Delpy et al., 1988), equation 1.9,

$$d\mu_a = -\frac{1}{rDPF}\frac{dI_t}{I_t} \tag{1.9}$$

where r is the direct distance between a light source and observation point, DPF is the differential pathlength factor (equation 1.10). The DPF is the ratio of the mean optical pathlength <L> and the direct distance and for the diffusion approximation is given by equation 1.10,

$$DPF = \frac{\sqrt{3\mu_s'}}{2\sqrt{\mu_a}} \tag{1.10}$$

The propagation of photons in biological tissue can be thought of in the particle view of photons, rather than the wave idea of photons. Photons enter a medium and can be scattered and absorbed by molecules in that medium. We can start with the Boltzmann Transport Equation (Bigio and Fantini, 2016) (BTE, or radiative transfer equation), which considers the balance of energy density, or photon number in light. The BTE considers photons flowing at a constant speed in a medium, where absorption, scattering and light emission can happen. Without reproducing the mathematics, the instantaneous change in angular energy density per unit volume and per unit solid angle of direction of propagation is based on contributions from diffusion, collisions and sources of light (fluorescence). The conditions of the diffusion approximation are that $\mu_s' \gg \mu_a$, light source emission is isotropic and the change in optical signal from the light source is slower than the transit time of photons in a medium.
The diffusion contribution represents the net gain or loss of photons as a result of the flow of photons in a volume. The collision contribution represents the loss of photons due to absorption of photons, or scattering of photons from the volume element. Photons can also be gained from scattering, by scattered photons entering the volume element. The diffusion approximation can be applied to the BTE using a pixel basis to give equation 1.11 (Dehghani, Eames, et al., 2009),

$$-\nabla \cdot \kappa(r)\nabla\phi(r,\omega) + (\mu_a(r) + \frac{i\omega}{c_m(r)}\phi(r,\omega) = q_0(r,\omega) \tag{1.11}$$

where, κ is given by equation 1.12, ϕ(r,ω) is the photon fluence rate at position r and modulation frequency ω, c_m is the speed of light in a medium at a point r (equation 1.13, where c_0 is the speed of light in a vacuum and n(r) the refractive index at r.) and q_0(r,ω) is

an isotropic source.

$$\kappa = \frac{1}{3(\mu_a + \mu_s')} \tag{1.12}$$

$$c_m(r) = \frac{c_0}{n(r)} \tag{1.13}$$

Following from equation 1.11 and the principles discussed in section 1.1, photon propagation from a given source to a detector is represented in figure 1.4 where the jacobian (also known as the sensitivity or the 'A matrix') is shown for a single source and detector on the surface of a 2D rectangular finite element model. The jacobian is a mapping function that relates how changes in optical properties of a medium causes changes in measured data. Figure 1.4 demonstrates that NIR light diffusing through a medium where scattering dominates over absorption, and with optical properties similar to that of human tissue will follow a banana shaped curve from a given source to a detector. It is important to note that light will travel in other directions outside of the banana curve, however this light is not measured by the detector and thus the jacobian only represents light emitted from a source and measured at a detector. Figure 1.4 also shows that the sensitivity is not homogeneous. There is highest sensitivity closer to the source and detector and lowest non zero sensitivity in areas where a photon would have a large path length from the source to detector (the bottom perimeter of the banana curve), or where photons would have to undergo multiple scattering events at less likely angles (the upper perimeter of the banana curve).

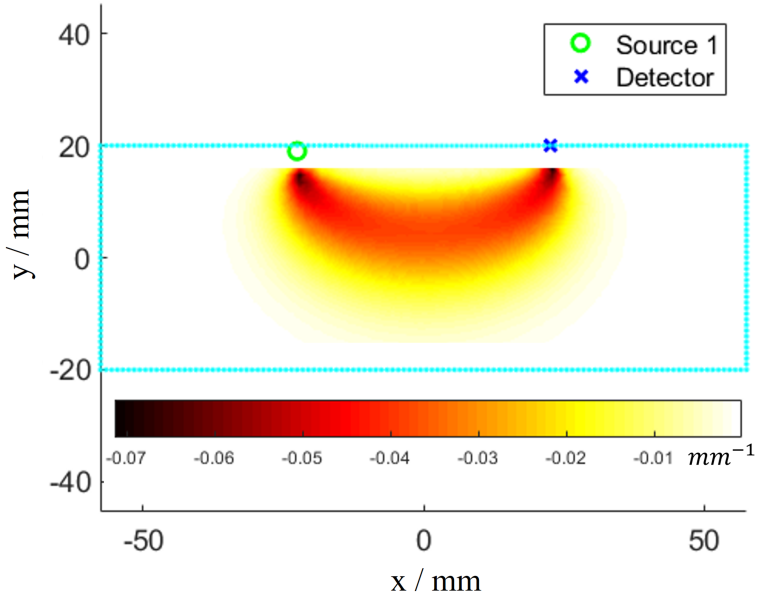

Figure 1.4: The jacobian (sensitivity matrix) is shown for a single source-detector measurement on a 2D rectangular finite element model. This was generated using NIRFAST (Dehghani, Eames, et al., 2009).

In addition, the jacobian demonstrates the depth sensitivity because it represents where light samples from a source-detector measurement, which creates important considerations for data analysis and experimental design in that the longer the source-detector separation, the deeper the sensitivity of the measurement. As source detector separation increases from 20 to 65 mm, it is expected that the depth sensitivity increases monotonically (Strangman, Z. Li, and Q. Zhang, 2013). It is from these fundamental principles that imaging with diffuse optics is built on. The specific data collection and data processing procedures will be explained in the following chapters in this thesis.

1.2 Paradigms of diffuse optics

In the context of human brain imaging using diffuse optics, there are several techniques which belong to the umbrella term functional Near Infrared Spectroscopy (fNIRS) and diffuse

optical tomography (DOT), which are continuous wave (CW), frequency domain (FD), time domain (TD), diffuse correlation spectroscopy (DCS) and broadband NIRS, with each of these having their own advantages and disadvantages. Outside of the classification of fNIRS exists other biomedical optics techniques, such as optical coherence tomography (Fujimoto et al., 2000), bioluminescence tomography (BLT) (Han, Cong, and G. Wang, 2006) and Spatial Frequency Domain Imaging (SFDI) (Gioux, Mazhar, and Cuccia, 2019). The latter three techniques are outside the scope of this thesis and will not be discussed, however a brief overview of the fNIRS techniques will be given in the following sections. This thesis will primarily focus on the use of FD fNIRS and FD DOT.

In the context of diffuse optics and fNIRS, the majority of studies are performed using difference imaging (Herold et al., 2018), in particular all CW and most FD studies are difference imaging. This is because with the types of data in CW (intensity of photons) and FD (intensity and phase of modulated photons) fNIRS, it is relatively simple to obtain baseline measurements and then use changes in the measured data from the baseline to calculate changes in optical properties and then changes in oxygenated and deoxygenated hemoglobin.

1.2.1 Continuous Wave

CW fNIRS is the most simple technique compared to FD and TD, because in CW light is emitted at a constant intensity from a source, and then measures how the intensity (number of photons) changes over time. From these changes in intensity, changes in the absorption coefficient are calculated and then by considering measurements at two or more wavelengths, changes in oxygenated and deoxygenated hemoglobin are calculated. CW devices are the most commonly used in the fNIRS community and this is due to their relative low cost compared to FD and TD systems, their potential to be portable, since the instrumentation

is simpler than FD or TD, and the data analysis from changes in intensity is relatively robust and simple to implement. Because of these reasons, CW systems are used across the entire spectrum of brain imaging needs from psychology (Kanazawa and Dan, 2018) to medicine (Forcione, Yakoub, et al., 2020), social (Sun et al., 2021) and sports science (Herold et al., 2018).

However, the CW paradigm has some disadvantages compared to FD and TD. Firstly, it is only possible to use CW for difference imaging, whereas absolute imaging is possible with FD and TD, which means CW would not be applicable in certain clinical applications where absolute parameters need to be measured. Secondly, as will be explored in this thesis, measurements from CW are more sensitive to superficial tissue and have a shallower sensitivity than phase data in FD measurements (Doulgerakis, Eggebrecht, and Dehghani, 2019).

In recent years, the biggest advancement in the hardware of CW fNIRS has been the use of portable devices. A device with emerging popularity is the Gowerlabs Lumo (Gowerlabs, United Kingdom (Vidal-Rosas et al., 2021)), which is a portable CW fNIRS device capable of high density diffuse optical tomography. The device consists of a cap, with several hexagonal tiles that can be placed across the surface of the head to sample different regions of the brain. The biggest strengths of the device are the portability, the ability to sample the entire cortical surface and the ease of use. It is these three factors that have encouraged researchers from across the fNIRS community to use the device, particular those from more 'applied' neuroimaging backgrounds.

1.2.2 Frequency Domain

This thesis focuses on using FD measurements and therefore the methodology in FD will be comprehensively covered. FD measurements are where the amplitude of light is sinusoidally modulated at a modulation frequency, f (MHz) and the light measured that has been transmitted through a medium at that same modulation frequency f is detected, but with a phase-shift as governed by the average photon path. Some photons will travel a shorter distance from the source to the detector, by sampling shallower and some photons will travel a longer distance from the source to the detector, by sampling deeper. When the average distance travelled by a group of photons increases, the time recorded for photons to go from the source to the detector increases.

The FD signal has three components, the DC intensity, which is analogous to CW measurement, the AC intensity (I) , which is the intensity of light oscillating at the given modulation frequency, and the phase (ϕ), which represents the phase difference in degrees of the emitted and detected modulated light. For this thesis, the the use of the word intensity doesn't include any phase component of the measurement, and therefore 'intensity' is analogous to the 'amplitude' of the signal. The phase of the detected light therefore provides information regarding how much it has been delayed (on average) as a result of photon interactions with a medium, i.e scattering. The phase is directly related to the time delay of light, τ, such that ϕ is in the order of $\omega\tau$, where $\omega = 2\pi f$ and ω is the angular modulation frequency. For a good signal to noise ratio, it is required that $\omega\tau \approx 1 \quad (radians)$ (Bigio and Fantini, 2016). If $\omega\tau$ was $\ll 1$, there would not be a measurable phase change. If $\omega\tau$ was $\gg 1$, then the AC amplitude decreases and could be below the level of noise.

In the context of imaging biological tissue, time delays are on the order of nanoseconds

(for source-detector separations of 2-3 centimetres), which yields modulation frequencies in the order of 100 MHz. For a source-detector separation of r, the measured signal is given by Eq. (1.14) (Fantini and Sassaroli, 2020,)

$$Signal = DC(r) + AC(r,\omega)e^{i\phi(r,\omega)}e^{-i\omega t} \quad , \tag{1.14}$$

where the DC(r), AC(r,ω) and $\phi(r,\omega)$ denote the distance and modulation frequency dependencies of three measurable components of the signal. For the case that $\omega = 0$ MHz, equation 1.14 yields the CW case, which is just the DC amplitude, as it is shown in equations 12.3-12.5 in the book by Bigio and Fantini, 2016 that AC(r,$\omega = 0$) = DC(r) and ϕ(r,$\omega = 0$) = 0.

From these measurements, changes in intensity and phase can be recorded, which are then used to obtain changes optical properties, namely absorption (μ_a) and reduced scattering (μ_s'). In biological tissue imaging, these are then used to recover changes in chromophore concentration, which are typically HbO and Hb, but can also include cytochrome c oxidase for sampling at 3 or more wavelengths. The measurement of these chromphores are important because HbO and Hb indicate brain activity, due to the demand of energy from neuron activation and the energy comes from respiration in the cells. Compared to CW, the advantages of FD comes from the use of phase data, as it samples deeper than intensity data and is less influenced by superficial tissue. Whilst cheaper than typical TD systems, FD systems are generally more expensive than their CW counterparts, and the hardware of FD systems requires more complex electronics than CW systems, which means it is harder to create portable FD devices.

1.2.3 Time Domain

TD fNIRS emits individual photons which are then measured by their time of flight from the source to the detector. A distribution of time of flight (DTOF) is created from millions of photons, and then features of the distribution allow optical properties to be recovered. Temporal filtering can be performed on the measurement of photons in order to achieve selective depth sensitivity. This is explored by Wabnitz et al., 2020, by selecting moments or time-windows in the measured data. Time windows are when the number of photons in a given time window are summed, which offers better SNR compared to the original time channels of the DTOF. Moments are derived from features of the DTOF, such that the zeroth moment is the total photon count, the first moment is the mean time of flight and the second moment is the variance of the DTOF. Then, changes in the moments of the DTOF are related to changes in the absorption coefficient of the medium that the DTOF was collected from (Ortega-Martinez et al., 2022).

The main advantage of TD measurements is that it allows absolute optical parameters to be recovered and the depth sensitivity can be tuned based upon time gating the DTOF. It follows that early arrival photons have traveled a smaller distance in tissue than late arrival photons, which on average would have sampled deeper in tissue. Historically, TD systems have been expensive, and large, therefore not portable. However, recent developments in TD hardware have yielded portable systems, such as the Kernal Flow (Kernal, United States) (Ban et al., 2022) and the PIONIRS TD device (PIONIRS, Italy) (Lacerenza et al., 2020), which allow users to take portable TD measurements. A summary of the differences between the CW, FD and TD paradigms can be seen in table 1.1 and an accompanying figure, figure 1.5, shows the differences between the measured data between the paradigms.

Table 1.1: A table summarising the key features and differences between CW, FD and TD.

Feature	**CW**	**FD**	**TD**
Cost	Low	Medium	High
Delta μ_a	Yes	Yes	Yes
Absolute μ_a	No	Yes	Yes
Delta μ_s'	No	Yes	Yes
Absolute μ_s'	No	Yes	Yes
Data measured	Intensity	Intensity, Phase	Time of flight
Depth sampling	Shallower	Deeper	Deepest
Portable systems	Yes	Yes	Yes

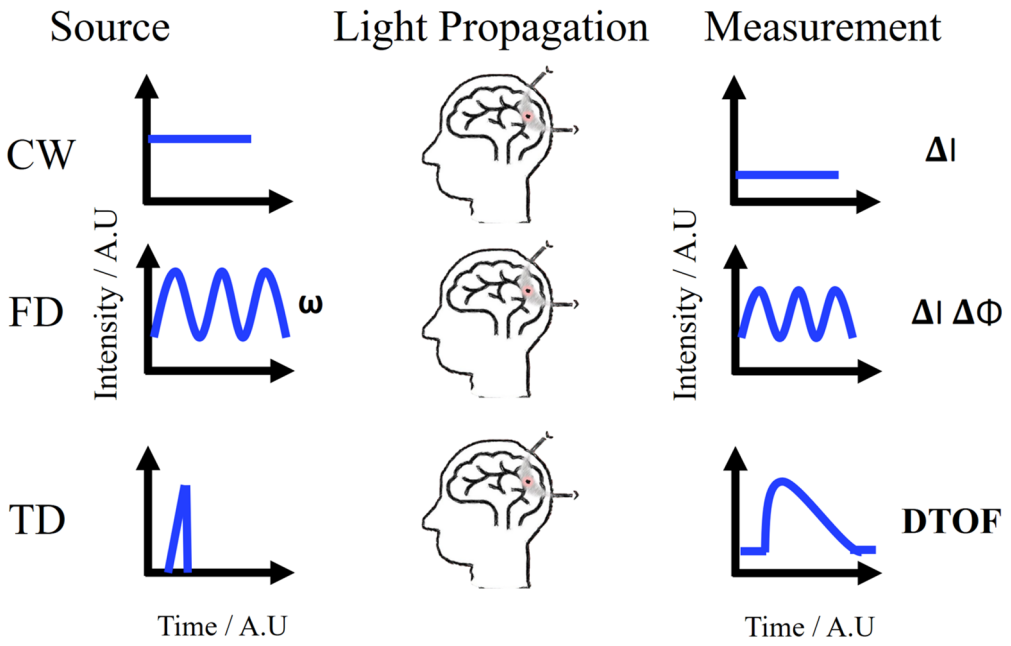

Figure 1.5: The differences between emission and detection of light in the CW, FD and TD paradigms. For CW changes in intensity, ΔI are measured, for the FD data in this thesis, intensity and phase $\Delta\phi$ are measured at a modulation frequency ω and for TD, the DTOF is measured.

1.3 Development of fNIRS and DOT

1.3.1 Spectroscopy

The use of the terms 'fNIRS' and 'DOT' describe different techniques of analysis stemming from the same underlying principles and their uses have different advantages, limitations and requirements. The first use of measuring cerebral hemodynamics using near infrared light came from Jöbsis, 1977, where they used a single light source, emitting a range of near infrared wavelengths and a single detector each side of the head and recorded changes in intracranial HbO and blood volume in response to hypoxic episodes of a subject. This study demonstrated the first use of NIRS, with the 'functional' prefix dropped since this study was not investigating functional brain activation. The changes in hemodynamics are spectroscopic, which means there is not spatial information within the parameter recovery. The only spatial information on the hemodynamic data is from prior knowledge of the location of the source and detector probes on the surface of the scalp.

It wasn't until the early 1990's when functional activation was investigated using NIRS, when four separate labs Chance et al., 1993, Kato et al., 1993, Hoshi and Tamura, 1993 and Villringer et al., 1993 used NIRS to detect cortical changes in hemodynamics due to functional activation and hence fNIRS was born. Chance et al., 1993 used NIRS and analysed the frequency power spectrum of subjects in a resting state and stimulus state to demonstrate that in the stimulus state, peak frequencies were observed that represented functional activation. More typical of the fNIRS studies seen in the present day, Kato et al., 1993, Hoshi and Tamura, 1993 and Villringer et al., 1993 demonstrated changes in HbO and Hb due to functional brain activation, with the canonical increase in HbO and decrease in Hb described, as seen in figure 1.1.

1.3.2 Topography

The next advancement within fNIRS is instead of using spectroscopy, is to use topography. Topography is where changes in hemodynamics from the fNIRS measurements are back projected onto a 2D surface, of which the surface represents the surface of the brain. The first use of topography to map human brain function using fNIRS was reported by Maki et al., 1995 when they performed measurements on the left fronto-central region of the brain from motor activation and observed significant increases in HbO and HbT and decreases in Hb during contralateral motor activation. Furthermore the history of NIRS and fNIRS leading to topography can be found by Koizumi et al., 1999. Topography is performed by reconstructing a linear interpolation of the fNIRS data, which uses a mesh model of the scalp and the surface of the brain, as described by Takeuchi et al., 2009. The halfway point between the source and detector on the surface of the scalp is described as the NIRS point, and the interpolated value from the measured data is derived from a weighted function, which scales the measured data based upon the inverse power (usually inverse square) of the distance between the NIRS point and the interpolated point on the surface of the brain. NIRS points within a specified radius (typically 24 mm) are included in the interpolation for a given point on the surface of the brain. This is calculated for each point on the surface of the brain to form the complete topographic image.

The advantage of topography compared to spectroscopy is that it offers spatial information of where changes in hemodynamics occur on the surface of the brain (Franceschini et al., 2003), however topography may be contaminated by changes in hemodynamics in the scalp because there is no consideration to the difference in sensitivity in the scalp and on the brain surface for given measurements in the back projection that tomopgraphy relies on. One of the solutions to minimise this is to consider tomography using fNIRS, which is known as diffuse optical tomography, 'DOT'.

1.3.3 Tomography

DOT aims to reconstruct changes in optical properties and therefore hemodynamics in 3D space, such as Gibson et al., 2006. This is performed by using a 3D model of the head, typically a finite element model (FEM) where the geometry of the different layers of tissue (skin and scalp, skull, cerebral spinal fluid, grey matter and white matter) are represented using their different optical properties and thicknesses. An FEM is a model of tissue or matter which is made up of vertices, which form a polygon, such as a tetrahedron and each tetrahedron is a node within the FEM. Then each node is assigned a different optical property corresponding to a tissue type. FEM's of the adult head can be created from averaged MRI acquisitions of the human head, such as Strangman, Q. Zhang, and Z. Li, 2014, where they averaged 27 anatomical MRI scans. The FEM of an adult head can contain on order of 50,000 nodes. DOT works by using an FEM of the adult head and the associated jacobian, which states the sensitivity at each node. Then from fNIRS measurements from multiple source-detector pairs, changes in optical properties at each node within the FEM are calculated.

The advantage of tomography compared to topography, is that in tomography because the differences in sensitivity are accounted for from brain tissue and non brain tissue, the changes in hemodynamics seen on the surface of the cortex will be more accurate than that of topography. As well as this, tomography takes into account depth sensitivity and if an accurate anatomical FEM is used, then the non homogeneous layers of tissue types can be accounted for. The disadvantage of tomography and topography compared to spectroscopy is that spectroscopy can work with any number of measurement channels, i.e spectroscopic results can be obtained with a single source-detector pair, whereas for effective and meaningful tomography and topography, multiple source-detector measurements must be used. Having multiple measurement channels across a region of interest means that there is more

prior information that can be used when performing the tomographic reconstruction, since channels will have overlapping sensitivity. It is also required that there are different source-detector distances, because the depth sensitivity and sensitivity profile changes as a function of source-detector separation. From Strangman, Z. Li, and Q. Zhang, 2013, increasing the source-detector separation, increases the depth sensitivity monotonically up to 65 mm separation and for sensitivity to the brain alone for every 10 mm increase in separation up to 45 mm, sensitivity to gray matter increases an additional 4%. It is also important to have shorter measurements channels in DOT, in order to account for changes in superficial tissue, however this is a data pre-processing technique within itself called 'Short channel regression' and will be discussed in section 1.4.

As established in the previous paragraph, having more overlapping channels and varying source-detector separations is required for DOT. The latest advancement from DOT is called high density DOT (HD-DOT) and HD-DOT is where there are a 'high density' of source-detector channels over a given region of interest on the scalp. For example in 2007, retinotopic mapping of adult human visual cortex was performed using a high density grid of 24 sources and 28 detectors on the visual cortex, which showed improved accuracy over previous studies (Zeff et al., 2007). Whilst the exact number and density of measurement channels is not clearly defined, a study by Tian, Alexandrakis, and Liu, 2009 used various numbers of source-detector densities and found that image reconstruction quality in DOT did not improve after increasing the number of overlapping measurements for a given surface area past three. In addition to this, a common source-detector array seen in the literature of HD-DOT has a regular repeating rows of sources and detectors such that there are up to four measurable nearest neighbour measurements. These are 13 mm (NN1), 29 mm (NN2), 39 mm (NN3) and 47 mm (NN4) (Eggebrecht et al., 2014). A representation of a typical array for fNIRS, DOT and HD-DOT can be seen in figure 1.6, where for the same region of interest, a varying number of sources and detectors are presented. As the number of sources

and detectors increases in the same area of space, the number of measurements increases and hence there are more overlapping channels. As well as this, more sources and detectors allows for measurements at varying source-detector separations, although for ease of viewing only channels are displayed by coloured lines for the shortest and second shortest measurements, which for the HD array is representative of NN1 and NN2. White and Culver, 2010 evaluated the performance of a typical sparse array and a HD array by performing simulations on a head model. They showed that the effective resolution of the HD array was approximately 13 mm whereas for sparse array was 30 mm for evaluating the reconstruction of point perturbations across an imaging array.

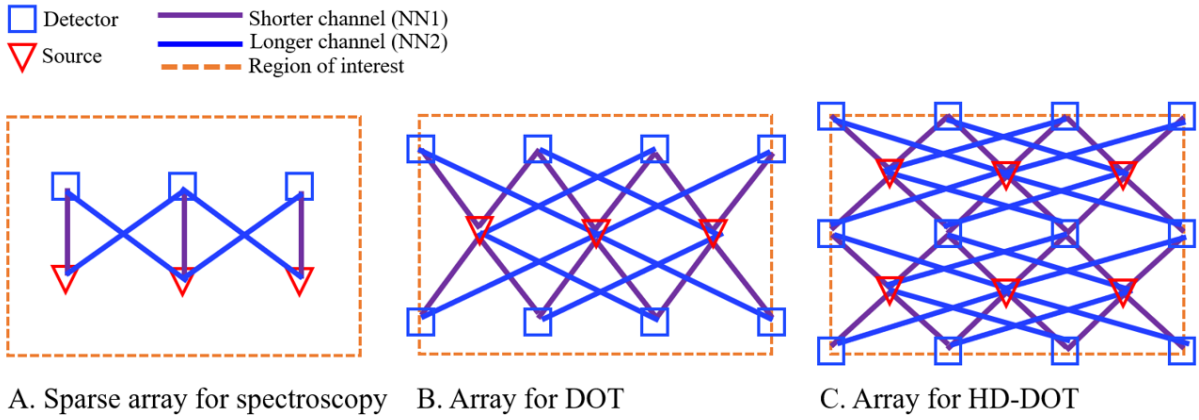

Figure 1.6: Three different source detector arrays showing typical arrangements for A. fNIRS measurements B. DOT measurements and C. HD-DOT measurements. Each array covers the same are region of interest and for illustrative purposes the shortest and second shortest measurement channels are shown.

This demonstrates that HD-DOT is currently the best method for functional brain imaging using diffuse optics in terms of image resolution, however HD-DOT has the drawback that it requires a high number of source and detectors, which can be costly and provide technical challenges. These challenges can range from having good source-detector contact on the scalp across the head or region of interest, as with a high number of probes requires engineering solutions such as helmets (Ban et al., 2022 and Vidal-Rosas et al., 2021) as well as minimising cross talk between sources and detector saturation. Currently studies within

the domain of fNIRS and DOT use various source-detector arrays and are not confined to those shown in figure 1.6 and there are examples of CW (Eggebrecht et al., 2014 and T. Huppert et al., 2006), FD (Perkins, Eggebrecht, and Dehghani, 2022) and TD (Ban et al., 2022) hardware that can perform fNIRS and DOT with various imaging arrays.

1.3.4 FD advancements

So far, this section has given an overview of the main developments in diffuse optics regarding the use of NIRS to fNIRS to topography, DOT and then HD-DOT, typically these have been performed using CW hardware. Alongside this, advancements in the FD and TD paradigms have been made. This thesis focuses on the development in the FD, which will be discussed in the last part of this section. Although FD data has been utilised previously for the recovery of scattering related changes, such as those of Event-related optical signal (EROS) (Gratton, Corballis, et al., 1995 and Gratton and Fabiani, 2010), the major advancements to date has been the utilisation of frequency domain measurements for recovery of the absorption related (vascular) signals. The use of FD-fNIRS has been previously demonstrated and review of the measurement technique has been extensively reported (Tuchin, 2015), however, there has been no quantification of the performance benefits of FD-fNIRS for recovery of vascular related focal activation signals until Doulgerakis, Eggebrecht, and Dehghani, 2019. They showed that FD measurements, through both amplitude and phase of the measured signal, offer an improved effective resolutions than CW measurements for second (29 mm) to fourth (47 mm) nearest neighbour source-detector separations, both with and without noise. The performance of FD has been shown to be better than CW as depth increases in human head model: recovery from cortical activity shows that FD can recover cortical activity whereas CW shows same recovery at superficial tissue.

A more recent advancement is through the concept of using dual slopes (DS) for

FD NIRS measurements(Blaney, Sassaroli, et al., 2020). A normal source-detector (S-D) measurement simply provides the signal at one detector from a given source. A single slope method, considers a single source and two detectors (such as those often utilised by the Hamamatsu NIRO systems), whereas the dual slope is defined as the average of two single slopes, such that the distance from a given source and detector are the same as those from another source and detector pair. One of the major advantages of the dual slope method is that it mathematically cancels the contributions of measurement error due to source-detector placement, detector drift or any other unwanted temporal fluctuations during an experiment. The dual slope method with two sources and two detectors has shown to offer maximal sensitivity at a depth of 5 mm and 11 mm for amplitude and phase measurements respectively, under typical conditions of fNIRS blood-perfused tissue, as compared to < 2 mm and < 5 mm for single distance S-D arrangements.

Blaney, Fernandez, et al., 2023 showed that using phase data with DS improved the hemodynamic response, by measuring visual cortex activation using a specifically made source-detector array to maximise the number of DS available. Their biggest advantage reported from DS imaging was the ability to suppress superficial tissue changes without the need for short separation channels, which could have implications for future source-detector designs in FD measurements. Alongside these hardware developments there have been advances made in software, data processing and analysis. These advancements will be discussed in the following section 1.4 alongside a description of the typical data processing pipeline for fNIRS and DOT.

1.4 Data collection and processing

Data processing in fNIRS and DOT follow a similar order of operation across all published studies, which have an input of measured data, and the output of spectroscopic or tomographic changes in HbO, Hb and HbT. A recent publication by Yücel et al., 2021 evaluated the different practices in fNIRS data analysis and set out to recommend guidelines for future fNIRS data processing. For each chapter in this thesis, the data processing steps are fully outlined and explained for the specific pipeline in that chapter. This section will explain an overview of data collection, processing and parameter recovery for fNIRS and DOT and an outline of this is represented in figure 1.7.

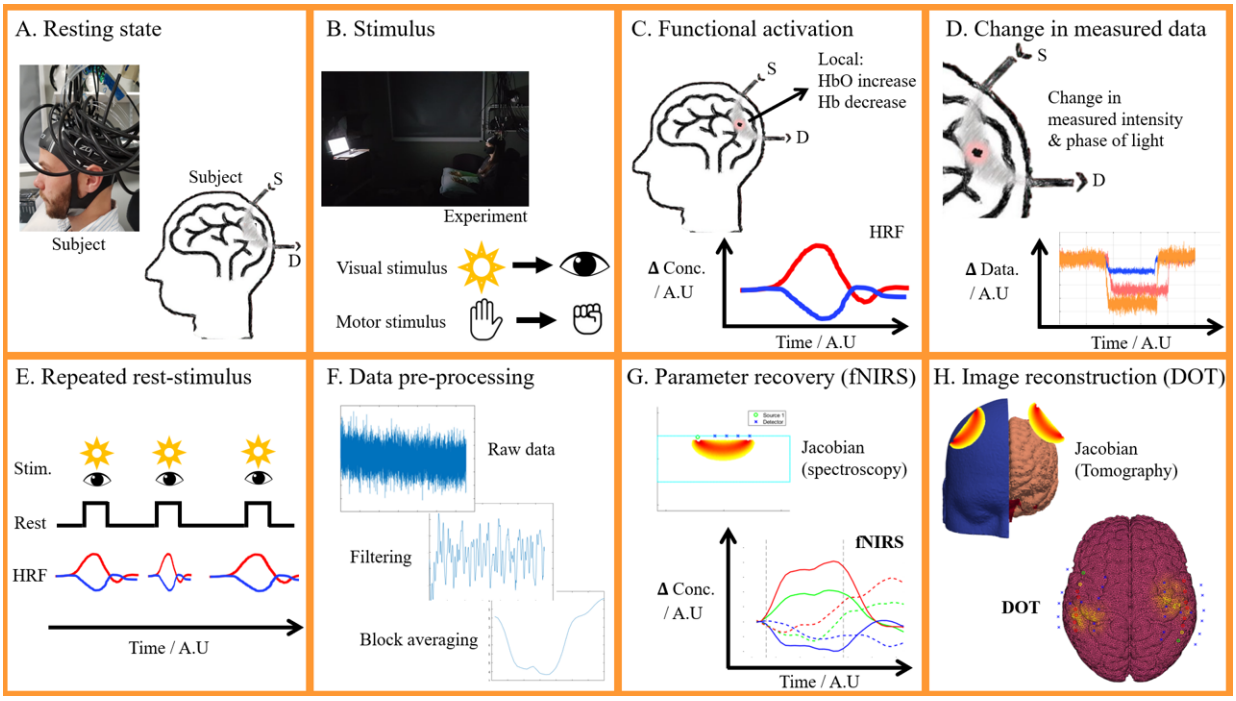

Figure 1.7: A representation of the entire data collection, pre-processing and processing workflow for typical fNIRS and DOT. A. A subject is at resting state with source-detector probes on their scalp. Light is sampling their superficial tissue and surface of the brain. B. A stimulus is presented to the subject. A visual and motor stimulus are given for examples. C. To respond to the stimulus, neurons are activated in the brain causing a localised change in HbO and Hb. D. Due to the hemodynamic changes, there are changes in the measured data. In FD measurements these are changes in the intensity and phase. E. The rest-stimulus period is repeated in order to have a series of hemodynamic responses to the stimulus. F. The raw data collected is then pre-processed through various filtering before the rest-stimulus periods are block averaged. G. Parameter recovery is performed to obtain channel by channel spectroscopic changes in HbO, Hb and HbT, which is fNIRS. H. Using an FEM of the subject's head and it's jacobian, tomographic reconstruction is performed to show changes in HbO, Hb and HbT on the surface of the cortex.

1.4.1 Data collection

Data collection (figure 1.7 A. to E.) within fNIRS and DOT can follow different experimental protocols. The work in this thesis uses a block design, which means that there are repeated periods of resting state followed by a stimulus condition. There is an initial baseline rest period typically lasting between 60 s to 120 s, then the stimulus events will be between 10 s

to 30 s, coupled with rest events lasting between 10 s to 30 s. It is good practice to randomise the length of the stimulus and rest periods within a certain threshold. This is because there are cyclical physiological noise in tissue that may coincide with the stimulus-rest periods. If they coincide with the stimulus-rest periods, then false positives may be found instead of true functional brain activation (Tachtsidis et al., 2009). The sources of physiological noise can be categorised into three bands (Kirilina et al., 2013), high frequency oscillations (HFO), low frequency oscillations (LFO) and vLFO (very low frequency osculations). In the HFO range there are changes in blood flow due to respiration and heart rate, which occurs at approximately 0.3 Hz, LFO are predominately from Mayer Wave oscillations. These are slow changes in blood pressure and occur at around 0.1 Hz and is debated how far Mayer waves propagate into the skin and cerebral regions (Tong and Frederick, 2010). Finally skin blood flow can operate in the LFO and vLFO range. The frequency of a stimulus rest period can be between 0.05 Hz (10 second stimulus and 10 second rest) to 0.016 Hz (30 second stimulus and 10 second rest), which occupies the territory of vLFO, therefore it is desirable to randomise the length of the stimulus and rest period.

The motivation of a block design experimental protocol is that each time the stimulus occurs, there will be a functional brain activation, which induces the hemodynamic response (figure 1.7 A. to C.) and then during the rest period the hemodynamics return to a baseline state. This causes changes in the measured data (figure 1.7 D.) and in order to increase the signal to noise ratio of measuring the HRF, the stimulus-rest period is repeated many times (figure 1.7 E.). This is done so that during the data pre-processing, these stimulus-rest periods can be averaged, which is a process called block averaging.

Other experimental design protocols are used in fNIRS and DOT, such as event related design and resting state design (Yücel et al., 2021). Event related design (Plichta et al., 2006) is used for when different stimulus conditions may be presented 'randomly' in different orders to the subject and these may last much shorter than the stimuli in block design (3 s to 5

s). Resting state design is used for the investigation of functional connectivity of the brain, which is looking at how different areas and networks of the brain operate together (Akila and Johnvictor, 2023). Other considerations in data collection concern the physical coupling of source-detector probes to the subjects head, or for phantom studies, source-detector probes to the surface of the phantom. Typically non portable systems are constricted to use in a dedicated laboratory, since the device requires housing in a rack or on a shelf, and will be large and heavy. Fibers will go from the device and then be placed onto the subject's head. The placement of these fibers onto the head will vary for system to system, but mostly a form of cap will hold source-detector probes in place. Portable systems will also need to couple fibers to the subjects head, but instead of the system being large and heavy, the system will either be contained in a small, lightweight module and the source-detector probes will be self contained in a cap on the subject's head. A review of cap design in fNIRS were conducted by Kassab et al., 2015, The primary objective of any fNIRS cap should be to couple source-detector probes to the surface of the scalp with consistent good contact throughout the duration of an experiment, such that if the subject moves, the change in coupling or contact is minimal. In addition good contact requires the fibers to be able to pass through some hair on the scalp to maximise the transmission of light from the fiber end into the scalp, and light exiting the scalp into a detection fiber. The cap needs to be comfortable for the subject, such that the subject can perform the tasks in the experiment and wear the cap for the duration of the experiment. An example of what data collection looks like in practice can be seen in figure 1.8, where the ISS Imagent (ISS, Champaign, IL, USA) is used. This is the same device used for the data collection throughout this thesis. It features source modules, which have sources at 690 nm and 830 nm and two detector modules. The ISS Imagent is a FD device so that the light is emission is modulated at a modulation frequency, for the ISS Imagent this ranges from 0 MHz to 312 MHz. There are two detector modules. There are up to 32 sources across the two modules (two wavelengths of light create one 'source') and up to 30 detectors across the two modules. The fibers are

then coupled to the subject's scalp via a cap and then the subject performs the tasks as indicated by the screen during the experiment.

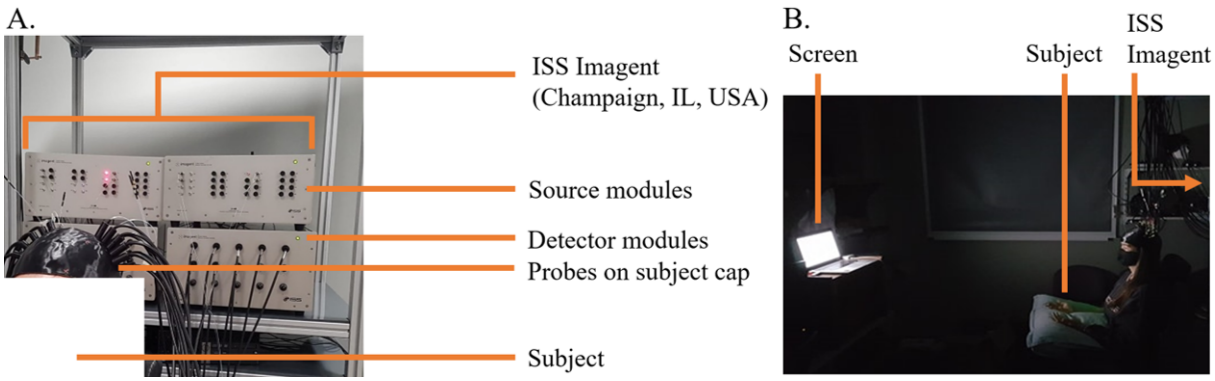

Figure 1.8: A. The source and detector modules for the ISS Imagent. B. A typical experimental set up.

1.4.2 Data pre processing

Once that data has been collected from an experiment, there are a series of pre-processing steps (figure 1.7 F.) that are performed. The purpose of data pre-processing is to make sure that changes in the data are only influenced by changes due to the hemodynamic response from functional brain activation. In reality this is hard to achieve, because there will be various physiological and instrumental noises causes changes in measured data as mentioned in the previous subsection. Alongside data pre-processing is the use of systemic physiology augmented - fNIRS (SPA-fNIRS), which has been developed by various groups (Diamond et al., 2006 and Felix Scholkmann, Tachtsidis, et al., 2022). These methods aim to use measurements of systemic physiology to regress these signals and influences out of the NIRS data so that the NIRS data is only influenced by functional brain hemodynamics. The majority of labs are not privy to systemic physiology measurements, so this subsection will focus on typical pre-processing steps.

Usually data is recorded from all channels, meaning there will be measurements from

all sources to all detectors. The placement and design of probes mean that not all measurement channels will be useable, either due to the source-detector separation being too high for a measurable signal (for adults more than 45 mm) or there may be poor probe coupling to the scalp. This means that the first step in any data pre-processing pipeline is to asses the quality of the signal and only use 'good' channels for the rest of the analysis. In CW and FD measurements, a good channel for intensity will be above a certain threshold for intensity, i.e a certain number of photons are being measured by a detector from a given source and be below a standard deviation threshold, i.e the variation in the intensity of photons over time is below the level of noise in the system. Different pieces of hardware will have different scales for measuring intensity so there is no threshold that can be applied universally, but for the standard deviation, typically this figure is below 10% (or 20 dB Yücel et al., 2021). Another method of selection good channels is to analyse the power spectrum of a channel and detect the cardiac response at approximately 1 Hz. If the cardiac response is small or not present, then it is likely the channel has poor scalp coupling since the light being measured has not sampled tissue (Hernandez and Pollonini, 2020). It is also important to note that for the same measurement channel, two (or more) measurements are made corresponding to the number of wavelengths used, so for that channel to be considered 'good', all measurements at all wavelengths will need to pass quality control thresholds.

Once data has passed a quality control check, it is converted to 'optical density' (A when using the natural log), as per equation 1.7 in section 1.1, which means that the time series becomes difference data with respect to a baseline (the mean of each channel). Measurements in fNIRS are sensitive to movement of the subject and probes because any movement can change the coupling of the source-detector probe on the scalp. This can cause 'motion artifacts' (MA) in the data and these MA's can either cause a spike in the data or a baseline shift and since fNIRS is performing difference data imaging, changes in baseline or intensity spikes can mask functional activation in the data. Therefore it is

important to detect and correct the MA's. MA's can be detected by finding sudden changes in the intensity of data within a small time window or by a method called global variance of temporal derivatives (GVDT) by Sherafati et al., 2020 where the variance of intensity across all channels are taken into account as a metric to detect MA's.

Both Huang et al., 2022 and Brigadoi, Ceccherini, et al., 2014 offer evaluations of different MA correction methods and the main techniques are spline interpolation, wavelet filtering and principal component analysis. Spline interpolation acts on each MA such that the period of motion is modeled via a cubic spline interpolation and then this is subtracted from the original signal, effectively removing the motion artifact from the signal. The data is then reconstructed since the spline correction causes a shift in the baseline. The spline interpolation is parameterised by the degree of the spline function, ranging from a linear interpolation to a cubic interpolation (F. Scholkmann et al., 2010). Typically spline is good at removing baseline shifts however it will only act on detected MA's, so it is only effective if the MA's are correctly classified.

Wavelet filtering (Molavi and Dumont, 2012) is where the signal is decomposed into wavelet coefficients and then removing coefficients which are more likely to be caused by motion, which is effective at removing spike artifacts. This is done by applying a discrete wavelet transform on the time series and abrupt changes in the intensity of the signal will appear as large isolated coefficients in the discrete wavelet domain. Finally principal component analysis decomposes the time series signal into principal components, which represent where the largest causes of variation are in the time series data. Since MA's can cause large changes in the data, it is expected that the largest N principal component represents the variance from the MA, therefore reconstructing the time series without the largest N principal component removes the MA (Y. Zhang et al., 2005). The choice of which MA correction techniques to use will depend on the use case and individual experiment, but generally one of spline or wavelet filtering yields good performance and Brigadoi, Ceccherini, et al., 2014

found that using wavelet performed better than other techniques.

Once MA's have been detected and corrected for, the next filtering step is to apply a bandpass filter. This is done in order to remove changes in the time series which come from physiology such as the cardiac signal (1 Hz) or Mayer waves (0.1 Hz). Typical high and low pass values are 0.01 Hz and 0.09 Hz respectively (Yücel et al., 2021), so that low frequency system drift and $\approx$ 0.1 Hz Mayer waves can be suppressed. The last form of filtering that is common practice to apply is short signal regression (SSR). Short channel measurements (below 15 mm source-detector separation) mostly sample superficial tissue, whilst longer channels (above 25 mm source-detector separation) sample both superficial tissue and the surface of the cortex. The premise of SSR is to use the short channels to regress changes in the data from hemodynamic changes in superficial tissue from the longer channels, so that the longer channels only contain influence from changes in hemodynamics from brain tissue. Brigadoi and Cooper, 2015 found that the optimal separation for a SSR channel was 8.4 mm in adults and 2.15 mm in the term-age infant and D. G. Wyser et al., 2022 found that applying SSR is key in order to have reproducible HRF results, due to the influence of the superficial tissue on measurements. Phase data in FD measurements may offer an advantage over intensity data, due to the fact it has been shown that phase data is less influenced by superficial tissue (Doulgerakis, Eggebrecht, and Dehghani, 2019). The use and implementation of SSR can be followed in chapter 5.2.4.

As eluded to before, the final step in data pre-processing is to block average the data such that there is a short (2 s to 5 s) baseline period before each stimulus, the length of the stimulus (10 s to 30 s) and length of the corresponding rest (10 s to 30 s). This is done by summing the changes in optical density across the baseline-stimulus-rest period and then obtaining the average of this from all of the stimulus events. The block averaged data can then be used for parameter recovery and image reconstruction which will be described in the following sub sections.

1.4.3 Parameter recovery

The purpose of parameter recovery is to use the changes in optical density to obtain changes in the absorption coefficient and then recover changes in HbO and Hb respectively. There are two general methods in order to obtain changes in the absorption coefficient. The first is to use the modified Beer-Lambert law (given by equation 1.9) and an adapted version of the modified Beer-Lambert law is shown below in equation 1.15,

$$\Delta\mu_a = -\frac{\Delta A}{rDPF} \tag{1.15}$$

where $\Delta\mu_a$ is the change in the absorption coefficient, ΔA is the change in optical density, r is the source-detector separation, DPF is the differential pathlength factor. The DPF is a scaling factor that takes into account that there is a difference between the source-detector separation as measured on the surface of the scalp and the average path length that a photon will take from the source to the detector in tissue. A general equation for the DPF has been formulated by Felix Scholkmann and Wolf, 2013 for a given wavelength and age of subject and can be used with equation 1.15 above to obtain changes in the absorption coefficient. Changes in chromophore concentration are related to changes in the absorption coefficient by equation 1.16,

$$\Delta\mu_a = \Delta C\epsilon \tag{1.16}$$

where ϵ is the extinction coefficient of the chromophore, which describes how strongly a chromophore absorbs light and then changes in chromophore concentration can be calculated using equation 1.17,

$$\begin{bmatrix} \Delta HbO \\ \Delta Hb \end{bmatrix} = \begin{bmatrix} \epsilon_{\lambda_1 HbO} & \epsilon_{\lambda_1 Hb} \\ \epsilon_{\lambda_2 HbO} & \epsilon_{\lambda_2 Hb} \end{bmatrix}^{-1} \begin{bmatrix} \Delta\mu_{a\lambda_1} \\ \Delta\mu_{a\lambda_2} \end{bmatrix}. \tag{1.17}$$

The subscripts for the extinction coefficient and the change in absorption coefficient denote the chromophore (HbO or Hb) and the wavelength number (λ_1 or λ_2), assuming two wavelengths are used. For spectroscopy, each measurement channel will yield it's own change in HbO and Hb and this will be for each point in time, across the block averaged time period.

The second method for parameter recovery is to use a semi-infinite FEM with its associated Jacobian to generate changes in the absorption coefficient. As described by figure 1.4, the Jacobian represents how much influence changes in optical properties in a given voxel have on measured data and can be generated using NIRFAST (Dehghani, Eames, et al., 2009). A Jacobian from a 2D semi infinite model has a single value of sensitivity as a function of source-detector separation. For each discrete source-detector separation, a different single valued Jacobian can generated, J, then changes in the absorption coefficient are given by equation 1.18

$$\Delta\mu_a = \Delta A J^{-1} \tag{1.18}$$

Following from equation 1.18 if the Jacobian is not formed as a square matrix, then a moore-penrose pseudoinverse (Penrose, 1955) with Tikhonov regularization is used to approximate the inverse of the Jacobian, $J^{-1} \approx J^{\#}$. $J^{\#}$ is given by equation 1.19,

$$J^{\#} = J^T(JJ^T + \alpha I)^{-1} \tag{1.19}$$

where I is an identity matrix and α is the regularisation term, given by equation 1.20,

$$\alpha = \lambda * max[diag(JJ^T)] \tag{1.20}$$

where λ is the regularisation parameter chosen to be 0.01, usually this is chosen empirically. A study of comparing source (sources of optical property changes) localization techniques with discussion about choosing the regularisation parameter was conducted by Tremblay et al., 2018. Once changes in the absorption coefficient are obtained, changes in HbO and Hb can be calculated using the same equation 1.17.

1.4.4 Image reconstruction

Whilst chapter 1.4.3 discussed parameter recovery which is the basis of fNIRS, this section will discuss image reconstruction which is the basis of DOT. Image reconstruction is performed through the use of a 3D jacobian, which like the 2D jacobian mapped changes in data to changes in absorption coefficient over time (equation 1.18), maps changes in data to changes in absorption coefficient in both time and 3D space. Jacobians can be generated using NIRFAST (Dehghani, Eames, et al., 2009) in the domain of diffuse optics, or with TOAST (Schweiger and Arridge, 2014) or MCX (Fang and Boas, 2009) using Monte-Carlo simulations of photon propagation. Instead of using the diffusion approximation to calculate analytical solutions to photon propagation in matter (equation 1.11), Monte-Carlo models use numerical solutions to model individual photon propagation in matter. This thesis only uses the diffusion approximation with NIRFAST for jacobian generation.

Typically the colin-27 segmentation (Strangman, Q. Zhang, and Z. Li, 2014) FEM is used for the head model, then once the Jacobian is generated, the same processing as stated with equation 1.17 and equations 1.18 to 1.20 can be used, with the jacobian having

a number of columns defined by the number of the nodes in the head FEM and the number of rows defined by the number of measurement channels. A matrix will be generated of the change in the absorption coefficient, with the number of rows being the number of nodes in the head FEM and the number of columns being the number of points in time in the block averaged period meaning for each point in time, every voxel in the head model will have a change in absorption coefficient. Finally by applying equation 1.17, changes in HbO and Hb will be given for each voxel in the head FEM for each point in time and then these changes in chromophore can be displayed for the surface of the cortex to see the results of the DOT. An example of this is represented in figure 1.7 H.

The difference between fNIRS using the methods described in parameter recovery (section 1.4.3) and DOT using the methods described in image reconstruction (section 1.4.4) can be seen in figure 1.9. Figure 1.9 A. shows spectroscopic changes in HbO, Hb and HbT on the left hemisphere of the cortex in response to motor activation, whereas figure 1.9 B. shows the same response but for the right hemisphere with changes in HbO on the surface of the cortex itself using DOT.

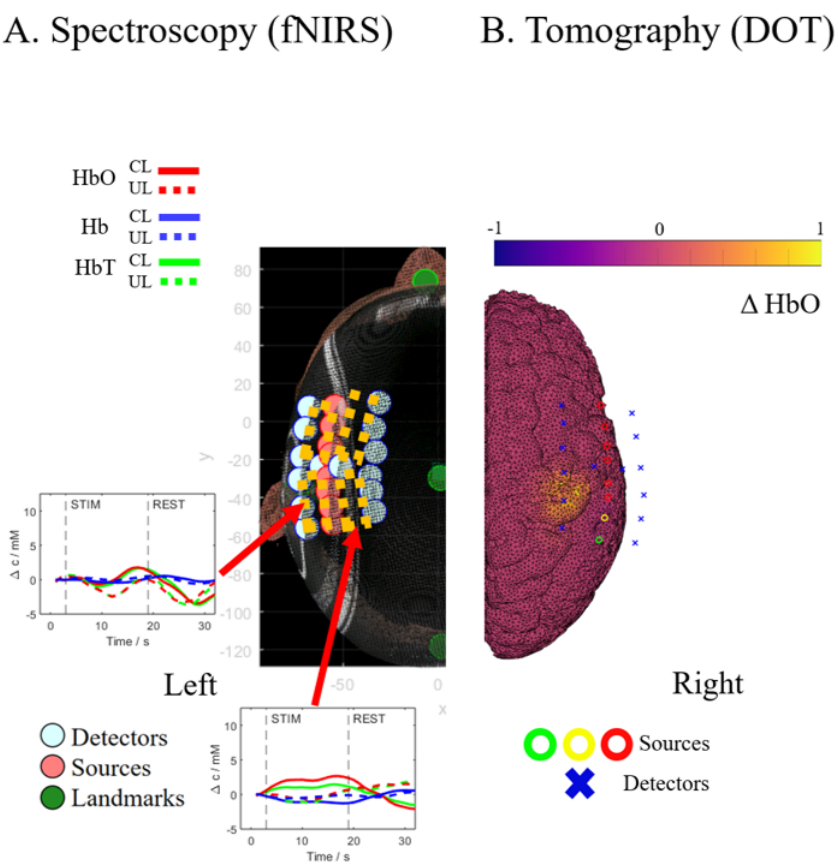

Figure 1.9: A. A representation of fNIRS shown on the left hemisphere of a subject, displaying changes in HbO, Hb and HbT. B. A representation of DOT shown on the right hemisphere of the same subject. A single frame in time is shown displaying changes in HbO. The activation seen is from functional activity in the motor cortex for both fNIRS and DOT.

In this chapter, the fundamental theory behind diffuse optics and the development and implementation of fNIRS and DOT have been discussed. Each hardware and software advancement has aimed to improve the accuracy of the imaging, primarily in being able to show the true reality of functional brain activation on the surface of the cortex.

The advancements can be summarised into three facets. Firstly, for the hardware advancements adding more sources and detectors has allowed tomographic images instead of spectroscopic ones, which aims to show hemodynamic changes from the cortex with less influence from superficial tissue. Secondly, the development of high density systems, the

image resolution from DOT has improved. Finally advancements in data processing such as SSR aim to minimise the influence of superficial tissue changes in both fNIRS and DOT. This thesis will be building upon these three facets using FD data, with the aim to show that there is less superficial tissue influence using phase FD data compared to intensity CW data and that exploring the modulation frequency of FD data can lead to better image resolution in DOT. These advancements will all be useful in the domain of using diffuse optics for investigating human brain health, as will be explored in the next chapter. Chapter 2 will evaluate the current use of diffuse optics for human brain health and reveal the opportunities of development in this field.

Chapter Two

Diffuse Optics For Brain Health

Brain health is important, the World Health Organisation (WHO) states that poor brain health or problems relating to brain health make up one-third of the global disease burden and these include disorders relating to neurodevelopemental disorders (such as autism spectrum disorders), neurodegenerative disorders (such as Alzheimer's disease), mental health disorders and diseases (depression and anxiety) and neurological disorders effecting the central nervous system (Y. Chen et al., 2022). The WHO states that "Brain health is the state of brain functioning across cognitive, sensory, social-emotional, behavioural and motor domains" (WHO, 2023), the US Centers for Disease Control and Prevention defined brain health as "ability to perform all the mental processes of cognition, including the ability to learn and judge, use language, and remember" (Y. Wang, Pan, and H. Li, 2020).

Y. Chen et al., 2022 reviewed literature of definitions of brain health and found that there were four common themes that contributed to defining brain health. These were, 'Exists along a continuum' i.e brain health is not binary of being 'good' or 'bad', 'A multidimensional construct', which means there are many facets which contribute to brain health, it is 'A dynamic state occurring along the life course' and it 'Includes both subjective (i.e., self-perception) and objective (i.e., measurable) components:'. Furthermore,

Y. Wang, Pan, and H. Li, 2020 highlighted that there are opportunities for research within the challenges of human brain health, such that there are little metrics or objective measures to quantify brain health and that there is little knowledge about the mechanisms of brain dysfunction.

It is from the challenges of brain health that attracts the use of diffuse optics to this field of brain health. As explained in chapter 1, diffuse optics can be used to image functional brain activity in the form of fNIRS and DOT, which means that based upon the premise that brain function is linked to brain health, then fNIRS and DOT can be used to investigate brain health. As already mentioned, there are different pathology's and types of brain health problems and the highest incident of all neurological disorder in the world is traumatic brain injury (TBI) (Maas et al., 2022), therefore the main focus of this chapter will revolve around traumatic brain injury and what opportunities exist with the development of fNIRS and DOT.

2.1 Traumatic Brain Injury

2.1.1 Pathology of TBI

TBI is caused when an external force impacts on someone's head, which causes an acceleration on the brain within the skulls and this can have various bio-physical and bio-chemical consequences leading to a cascade of events occurring in the brain. Several effects from TBI can occur as a result of a varying grade of brain dysfunction, which include but are not limited to, loosing consciousness, cognitive impairment through sight, motor control, memory, dizziness, headaches and even death. Currently, TBI is clinically assessed using

the Glasgow Coma Scale, (Jain and Iverson, 2023), which scores the visual (4 to 1), verbal (5 to 1) and motor (6 to 1) response of a patient. The three grades are then summed and this is used to classify the severity of the TBI, with mild (mTBI) being 13 to 15, moderate (M-TBI) being 9 to 12 and severe (S-TBI) being 3 to 8, which can be seen in table 2.1.

Table 2.1: The assessment of the Glasgow coma scale, which uses the sum of the best eye response (4 to 1), the best verbal response (5 to 1) and the best motor response (6 to 1) to grade a TBI into mild (13 to 15), moderate (9 to 12) and severe (3 to 8).

Grade (Best to worst)	**Best Eye Response**	**Best Verbal Response**	**Best Motor Response**
6	n/a	n/a	Obeys commands
5	n/a	Orientated	Localizing pain
4	Eyes open spontaneously	Confused	Withdrawel from pain
3	Eye opening to sound	Inappropriate words	Abnormal flexion to pain
2	Eye opening to pain	Incomprehensible sounds	Abnormal extension to pain
1	No eye opening	No verbal response	No motor response

Currently these responses are assessed subjectively, with different tests and standards used for assessment across the world. In the UK, 1.4 million patients attend hospital following a head injury, of which 200,000 are then admitted to hospital (Lawrence et al., 2016). It is the biggest cause of death and disability for under 40's in the UK (*Overview | Head injury* 2023), so there is a real need to be able to accurately diagnose and monitor patients, so that they can receive the appropriate treatment. Currently x-ray CT is the most common method for monitoring patients, whilst magnetic resonance imaging (MRI), positron emission tomography and electroencephalogram are also used. These all offer different advantages and disadvantages.

For example, the use of x-ray CT can tell the clinician structural information about the skull, such as if there are any fractures or haemorrhages present. Whilst an x-ray is relatively quick and simple to perform in a clinical setting, the patient is exposed to ionising radiation and the information obtained is purely structural and not functional. The use of MRI's are typically reserved for severe TBI cases when there is a persistent neurological defect not explainable or detectable from x-ray CT (Lee et al., 2021) and although MRI's are capable of giving greater anatomical detail than X-ray CT's, they are resource expensive in a hospital and some patients may be unable to undergo an MRI scan, such as those with metal implants in their bodies. Therefore there exists an opportunity and potential for other imaging modalities to be used across the spectrum of TBI in both a clinical and non clinical environment. One such suitable imaging modality is the use of diffuse optics in the form of functional near infrared spectroscopy (fNIRS) and diffuse optical tomography (DOT) for three key reasons. Firstly, diffuse optics are non invasive, which means they don't require any surgical intervention to use, secondly many systems are portable, which means they can be used at the bedside or on the patient in non clinical environments and finally they are compatible with other devices or implants that patients may have. The following section will discuss the different areas where diffuse optics could be used within TBI, and will provide the motivations and reasoning's for the other sections presented in this thesis.

2.1.2 The use of diffuse optics in TBI

There should be careful consideration over how to use diffuse optics for assessing traumatic brain injury. The first consideration should be the severity of TBI to target, because this changes the profile of clinical questions that should be aimed to be answered, in order to provide useful clinical information. For example, S-TBI patients will not be able to perform any functional tasks, which means functional brain imaging using fNIRS would be redundant.

The imaging would also be required to be carried out at the bedside, due to the potential critical, but stable condition of the patient. Therefore any system used would need to be portable, or transportable within the practical limitations of a hospital. As mentioned in chapter 1.4.1 for fNIRS in a laboratory environment, another consideration is the type of cap and probe tips that can be used, in particular the cap should not apply excessive pressure to the patients skull, due to the sensitivity and delicate balance of the inter-cranial pressure (ICP) of the patient. In S-TBI, it is likely the patient will have external wounds on the head, covered by bandages and dry blood, as well as having an invasive ICP monitor in the skull. This means a cap or probe system would need to be flexible with it's head coverage as to avoid contacting these sensitive areas and to avoid disturbing the ICP monitor.

From these considerations, it follows that diffuse optics should be used to gain physiological information about the subject for S-TBI, and severe cases of M-TBI. An example would be in the form of assessing the blood brain barrier (BBB) damage, which could be interpreted by assessing perfusion across the BBB. This concept was investigated by Forcione in 2020 (Forcione, Antonio M Chiarelli, et al., 2020), where they conducted a review over the use of the contrast dye indocyanine green (ICG), for contrast enhanced NIRS on M-TBI and S-TBI. Their hypothesis was that an M-TBI or S-TBI patient would have BBB damage, so by injecting ICG into their veins, the ICG would circulate in the bloodstream and the ICG that reached the brain would perfuse out through the BBB. This perfusion in theory could be measurable using DOT, since the passage and therefore change of ICG concentration across the BBB would cause local changes in optical absorption. Then performing spectroscopic and/or tomographic analysis would show changes in perfusion of ICG across the BBB depending on where the BBB was, and the extent of the BBB damage, and that performing this analysis on non TBI patients would reveal different ICG kinetic. So that patients could be classified between TBI and non TBI.

The review lead to a preliminary study (Forcione, Yakoub, et al., 2020) being con-

ducted in 2020, where they enrolled 5 M-TBI/S-TBI patients and 5 non TBI trauma patients (Patients admitted to hospital due to other physical trauma, without TBI). They performed NIRS measurements by placing optical probes on the patients forehead and then acquired data 2 minutes before the injection of ICG and 10 minutes after the injection. They analysed the changes in effective attenuation coefficient over time and parameterised the width, rate of exponential increase, rate of exponential decrease and rate of linear decay of the signal. They found differences in these parameters between the TBI and non-TBI patients however they were not statistically significant. They suggested that future studies should come up with different methods to quantify the ICG kinetic, in order to distinguish between TBI and non-TBI patients.

Roldán in 2021 conducted a review of NIRS in TBI (Roldán and Kyriacou, 2021) where they evaluated two main areas of study: oxygenation and autoregulation. Oxygenation refers to the absolute and relative concentrations of oxygen in the blood, namely through oxyhaemoglobin, deoxyhemoglobin, total haemoglobin and in the context of TBI, regional cerebral tissue oxygen saturation (rSO_2). When a TBI occurs, the brain may suffer from a lower supply of oxygen due to ischemia and the duration of ischemia can have severely negative effects. For example, 10 s of ischemia can lead to lack of consciousness (*Nolte's The Human Brain* 2023). It is essential blood reaches the brain, because this is how oxygen and nutrients are delivered to the brain, which then allows molecule exchange to happen, i.e taking carbon dioxide and other waste products out of the brain. Therefore measuring oxygenation saturation in the brain can give an indication of how the brain is using oxygen. rSO_2 can be linked to cerebral venous oxygenation and this has been shown to correlate with jugular bulb venous saturation($Sj0_2$). This is a cerebral parameter that reflects the balance between the cerebral blood flow (CBF) and the cerebral metabolic rate for oxygen ($CMR0_2$) (Nakamura, 2011). When the brain requires more oxygen, $Sj0_2$ decreases, because the brain extracts more oxygen, and when the brain's demand for oxygen is lower than the supply of

oxygen from the CBF, $Sj0_2$ increases.

After a TBI, the balance and coupling between the CBF and the $CMR0_2$ is lost, meaning that if there is an increase in intercranial blood pressure, there will be an associated decrease in the perfusion of blood in the brain, i.e brain hypoperfusion. This occurs without a proportional decrease in the metabolic requirements in the brain, i.e the $CMR0_2$ doesn't proportionally decrease. This means the brain is using more oxygen than the amount of oxygen that is being delivered, therefore $Sj0_2$ can decrease below normal values of 65-75% to below 55%, which increases the chance of a less favourable outcome (Stocker, 2019). rSO_2 could be measured using diffuse optics, which would give an indication of $Sj0_2$ and thus could give clinically relevant information about brain health of the patient. An example study of NIRS measurements being used to obtain rSO_2 in TBI patients is by Vilke in 2014 (Vilkė et al., 2014). They measured patients rSO_2 in an intensive care unit (ICU), on the left and right hemisphere of the brain respectively, and then established a relationship of the values measured to the outcome (mortality) of the patient. They found that when rSO_2 values after 1 hour since the patients admission to ICU, did not exceed 68.0% in the left hemisphere and 68.3% in the right hemisphere, the hazard ratio for death increased by 17.7 times and 5.1 times respectively.

Another review (Weigl et al., 2016) into the use of NIRS in monitoring TBI, was conducted and they found that from 1980 to June 2015, the main topics of the use of NIRS were on hematoma detection, brain oxygenation, cerebral perfusion, cerebral autoregulation, cerebral metabolism and neurorehabilitation. Hematoma detection is done by seeing the difference in optical density between the left and right hemispheres. Brain oxygenation can be derived from looking at the change in concentration of HbR, HbO and HbT. For the other parameters listed, non CW or FD NIRS techniques were used. The review reports that NIRS can be used as a precursor to x-ray CT scans or to compliment other imaging modalities, but not to replace any of them. This is the same conclusion found by Davies,

2017. There are conflicting studies about if ICP can be detected with NIRS parameters such as rSO_2. The premise being a threshold of rSO_2 could indicate a critically elevated ICP, but no studies so far have shown this.

At the moment, NIRS devices are not used in the mainstream clinical practice. According to a review of monitoring of the adult traumatic brain injury, this is mainly due to concerns of signal contamination by superficial artefacts (Davies, Su, et al., 2015). However the review highlights that NIRS would be a useful technique to monitor if adequate brain tissue oxygenation and vascular homeostasis was maintained following TBI and resuscitation periods. The report also suggests that the most promising use of NIRS in a TBI context is for the detection of intracranial hematomas, which is the collection of blood within the skull due to rupture of the blood vessel or trauma. A study by Davies, Clancy, et al., 2019 tested if FD-NIRS was as good at detecting changes in brain tissue oxygen tension as well as a currently used invasive device. Out of the 16 patients monitored, the FD-NIRS device detected severe hypoxic episodes in 9 people and moderate hypoxic episodes in 7 people. The subjective score of the FD device was 'good' to 'relatively poor', therefore is not in a state to replace the invasive monitor.

So far, this chapter has discussed the use of diffuse optics looking at non functional imaging, i.e the brain at resting state and the examples have been with M-TBI and S-TBI. There is an application of functional imaging using diffuse optics with mTBI, particular in the case of patients suffering from concussion, which is a symptom of mTBI. There have been several studies that have investigated concussion patients using fNIRS/DOT, with many of them looking at functional activation of the brain.

Forcione, Antonio Maria Chiarelli, et al., 2020 used DOT to asses brain activation in the prefrontal cortex on two concussion patients. This was a proof of concept study used to demonstrate the design of an experimental protocol, suitable for clinical environment,

in this case a sports concussion clinic. The subjects performed a word generation task, in a stimulus-rest block design experiment, and then a FD device was used to record the fNIRS data. The data collection also featured the design of a custom made cap suitable for concussion clinic patients, i.e a cup which could comfortably hold probes on the forehead and frontal areas of the patients. Then tomographic reconstruction were performed and the expected hemodynamic response was observed in the prefrontal cortex. The next step from this experiment would be to compare the functional activity between a cohort of concussion clinic patients and non concussion, but similar profiled healthy subjects, to assess if there are any differences between these two groups. Any differences could be explainable by the mTBI.

In addition to prefrontal activation, motor cortex activation can be investigated for mTBI in the motor cortex. Urban et al., 2015 used CW fNIRS to compare motor cortex activation between 12 mTBI and 8 non TBI patients performing a finger tapping task. They found that there was a reduction in the functional coherence between the motor cortex activation in the left and right hemispheres in the mTBI patients compared to the healthy controls. This suggests that there is less interhemispheric functional connectivity in the concussion patients, however the study could not say what was responsible for this. Three ideas proposed were that these results were due to dysfunction in the white matter tracts, or due to metabolic dysfunction or due to damage to brain cells as a result of the mTBI.

From all of the aforementioned studies, there are several key areas of diffuse optics that could be developed in order to better assessing TBI, which this thesis will aim to investigate. The first is the desire for more available channels of measurement in space, in order to facilitate tomographic reconstruction, as well as the already achieved spectroscopic reconstruction. This could have improved the studies of Forcione, Yakoub, et al., 2020, where they looked at spectroscopic curves of the passage of ICG across the BBB in M-TBI and S-TBI. If they had more channels available, it would have been possible to perform

tomographic reconstruction of the passage of ICG, which may have led to more clinically relevant results.

With the study of Forcione, Antonio Maria Chiarelli, et al., 2020, where they looked at the functional activation of the prefrontal cortex, they used a frequency domain system, which recorded intensity and phase data, however they only used intensity data in their analysis. This means there is the potential that the results of the functional activation could be more accurate if phase data was used in the data analysis (Doulgerakis, Eggebrecht, and Dehghani, 2019). In addition to this, if there were more source-detector probes available, a source-detector array could be designed so that short signal regression could be used, which like the use of phase data, would reduce the influence of hemodynamic changes in superficial tissue.

Another area of development is imaging accuracy, in terms of localisation of changes of optical properties and in the image resolution. For example, Urban et al., 2015 investigated functional connectivity in mTBI patients, but were limited to a sparse array of sources and detectors, with a relatively low tomographic resolution. Increased resolution with tomography, particularly using HD-DOT, could allow for functional connectivity to be assessed with smaller regions of the cortex, and better localisation would mean a higher accuracy of the identification of the region of the brain being activated. Another aspect of development is in the fact that rarely are the MRI's of patients available to use, or acquired in the first place, particularly with non S-TBI patients. This means that when image reconstruction occurs, in the case of tomography, generic template models have to be used, which do not account for individual differences in anatomy. Finally, in both the functional activation studies and the non functional activation studies in assessing TBI, the surface of the cortex is of primary interest, either due to the desire to detect cortex activity, or to investigate the BBB, therefore it is advantageous to sample as close to the surface of the cortex as possible. This could be achieved by incorporating phase data into fNIRS/DOT, since it is known that phase samples

deeper than intensity (Doulgerakis, Eggebrecht, and Dehghani, 2019).

With these development goals in mind, this thesis aims to address these challenges and needs for diffuse optics to assess functional activation in the brain, which plays a role in assessing human brain health, as explored with traumatic brain injury. The current limitations with the literature are that the full suite of data analysis techniques which were covered in chapter 1.4 were not all used in each of the studies discussed in this chapter when looking at functional activation or that phase data wasn't used when it was available. For example, Forcione, Yakoub, et al., 2020 and Forcione, Antonio Maria Chiarelli, et al., 2020 had phase data available and chose not to use it in the data analysis, which limited the analysis to intensity only. Urban et al., 2015 and Forcione, Antonio Maria Chiarelli, et al., 2020 did not use short signal regression, due to the design and placement of the source-detector probes which means the influence of superficial tissue was not minimised or accounted for. Therefore, the main focus of this thesis will be in the advancement, evaluation and development of FD fNIRS and DOT, as applied to human brain imaging. This will be done by investigating and incorporating phase data and the range of current data analysis techniques into a workflow in order to perform the most accurate human brain imaging with FD fNIRS and DOT.

Chapter Three

Multi Frequency HD-DOT simulations

The first chapter in this thesis introduced and described fNIRS and DOT in the domain of diffuse optics for brain imaging and the second chapter examined the use and potential of fNIRS and DOT for investigating human brain health by functional brain imaging. This chapter explores the potential of the use of FD measurements, in particular the use of phase data and its dependence on modulation frequency in order to achieve deeper sampling in tissue and more accurate functional brain imaging. As outlined in chapter 1.3.4, FD measurements using phase data have been shown to offer better depth sensitivity and are less affected by superficial tissue, compared to analogous intensity, CW only measurements, highlighting the fact that it is advantageous to use FD measurements in fNIRS and HD-DOT. As many studies use CW, FD or TD measurements alone, or the combination of CW and FD, to date, no work has quantitatively compared the performance of CW vs FD vs CW & FD data and the use of combined multiple modulation frequencies. This chapter will present an objective and comprehensive evaluation of the performance between these data types as applied in HD-DOT.

As a note, for this chapter, the terms 'intensity' are used to describe the amplitude of the frequency domain signal, the 'phase' is the change in phase of the modulated light

and correspond to the acronyms, CW, FD and CW&FD as denoted in table 3.1. For the CW&FD case, it is stated if a single modulation frequency ($\omega_n = \omega_1$) or three modulation frequencies ($\omega_n = \omega_3$) were used.

Table 3.1: The definitions of the acronyms CW, FD and CW&FD used in this chapter. Here intensity is analogous to amplitude.

Chapter	**CW**	**FD**	**CW+FD**
3	Intensity	Phase	Intensity & Phase (ω_n)

FD measurements can be made at different modulation frequencies, typically on the order of 100 MHz, little work has been done on the evaluation of the difference in performance due to different modulation frequencies for HD-DOT. It is known that inclusion of FD data can increase sampling depth (Doulgerakis, Eggebrecht, and Dehghani, 2019), and that the magnitude of phase measurements has a modulation frequency dependency as seen in equation 1.14, therefore making the modulation frequency an interesting parameter to investigate.

There are three main objectives that will be addressed in this work for the application of FD-HD-DOT: The first is to quantify the performance of CW vs FD vs CW&FD. The second is to evaluate the effects of using different modulation frequencies and the third is to evaluate the effect of combining measurements at multiple modulation frequencies (mFD). Methods of the computational work will be explained in section 3.2 with the results presented in section 3.3. Firstly, the behaviour of intensity and phase data in FD will be discussed using simulations on a simple phantom.

3.1 Theory

It is a standard result (Bigio and Fantini, 2016) in NIRS that the data measured from a light source is a function of the absorption and scattering coefficients of the path taken by the photons being detected. In order to investigate the opportunities for development of FD data, the initial step is to lay out the relationship between measured data, in intensity and phase and optical properties. NIRFAST (Dehghani, Eames, et al., 2009), a modelling and simulation software was used, with a 2D circle mesh (figure 3.1). The mesh has 16 sources and detectors, equally spaced apart on the source of the 2D circle, which was chosen so that many source-detector measurement distances could be sampled over a comprehensive range and the use of a simple geometry allows for fast computation. The mesh had homogeneous optical properties and only measurements from source 1 (green circle) were being considered. The values of absorption coefficients used were 0.01^{-1} to 0.05 mm^{-1}, in increments of $0.01mm^{-1}$ and scattering coefficients used was $1mm^{-1}$ to $5mm^{-1}$ in increments of $1mm^{-1}$. The absorption coefficients were changed, whilst the scattering coefficient kept constant to produce five different readings, then the opposite was done keeping the absorption coefficient constant.

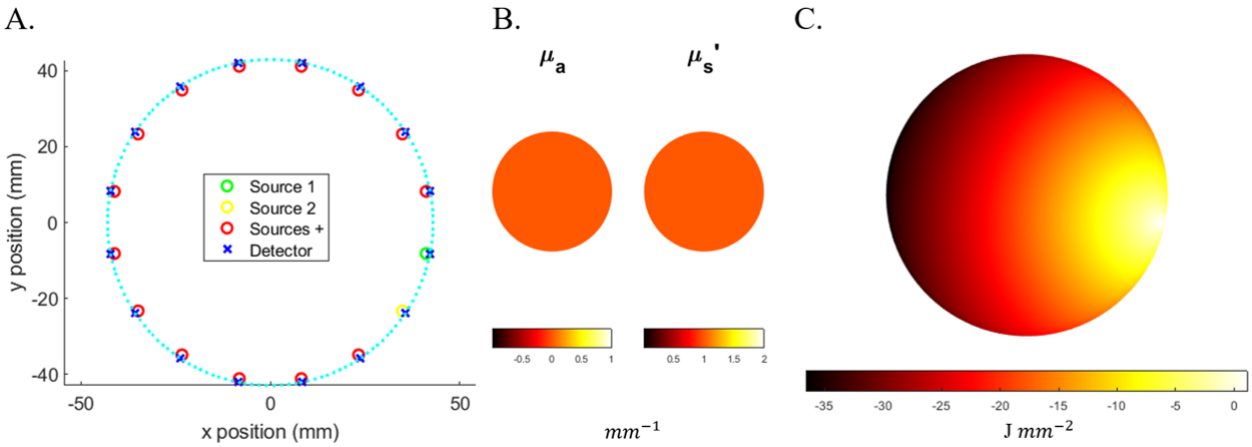

Figure 3.1: A. The 2D circle mesh used to investigate how measured data changes as a function of optical properties and modulation frequency. There are 1785 nodes in the FEM mesh, with a radius of 43 mm. The mesh has 16 sources and detectors equally spaced on the surface of the circle. The blue dots represent a node. The nodes are hidden in the middle of the circle. B. The absorption and reduced scattering coefficients of the mesh. C. The light fluence from source 1 in the mesh.

The behaviour of intensity and phase, as a function of absorption, scattering and source-detector distance are well known, however it is important to demonstrate and understand these fundamental results. It is convention to use the natural log of intensity, as in difference data imaging, when calculating the difference between two log values, they can be divided due to logarithmic rules. This eliminates calibration factors from the log values, as they cancel out. Figure 3.2A and B show that log intensity decreases as a function of distance. This is because a larger distance between source and detectors means photons are more likely to undergo more absorption's and scattering events. This reduced the number of photons detected. For increasing absorption at constant scattering (figure 3.2A), the log intensity decreases for the same reasons aforementioned. Increasing the scattering coefficient (figure 3.2B), means it is more likely for scattering to occur. This will increase the pathlength of photons travelling from the source to detector, in turn making it more likely absorption will happen.

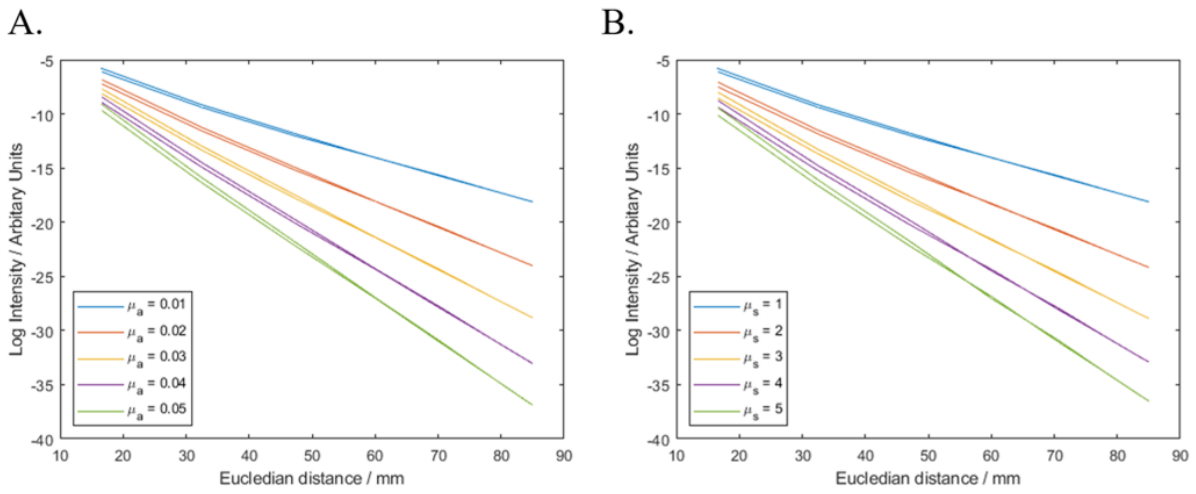

Figure 3.2: A. How the log Intensity changes as a function of the absorption coefficient, keeping scattering constant. From increasing the absorption coefficient from 0.01mm^{-1} to 0.05mm^{-1}, log Intensity decreases. B. The same relationship is true for increasing the scattering coefficient. It should also be noted that log Intensity decreases linearly as a function of source-detector distance. There are two curves for each optical property due to the asymmetry in the FEM.

For phase measurements, increasing the absorption coefficient causes the phase to decrease (figure 3.3A). This is because a higher absorption will suppress phase contributions from photons traveling a longer path. This effectively favours photons traveling shallower, shorter paths from the source to the detector, as a shorter path length will on average lead to less absorption events. The opposite is true for increasing the scattering parameter (figure 3.3B), keeping absorption constant. The phase increases because it is more likely that a higher number of scattering events take place. This will increase the time of flight of photons, due to the increase of path length.

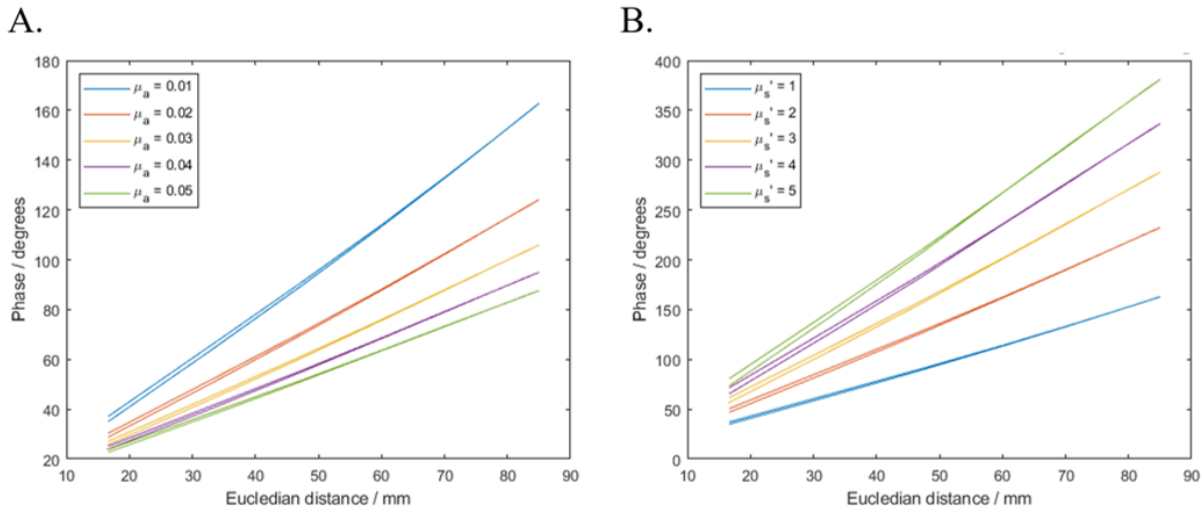

Figure 3.3: A. How the phase changes as a function of the absorption coefficient, keeping scattering constant. From increasing the absorption coefficient from 0.01mm^{-1} to 0.05mm^{-1}, phase decreases. B. For increasing the scattering coefficient, the measured phase increases. This is due to the path length of photons increasing from a higher number of scattering events. It should also be noted that phase increases linearly as a function of source-detector distance.

The modulation frequency of the ISS is the frequency at which the light source is sinusoidally modulated. So a modulation frequency of 100 MHz, means that the light source is sinusoidally modulated one hundred million times a second. Before investigating the effects of changing the modulation frequency on the ISS with phantom measurements, simulations can be performed. For a given source-detector separation, increasing the modulation frequency, increases the measured change in phase. This result agrees with previous studies (Fan, Dehghani, and Eggebrecht, 2021), where the phase was simulated across 0 MHz to 1000 MHz modulation frequency in a human brain. The larger the source-detector separation, the larger the increase of phase is with increasing modulation frequency. This is shown in figure 3.4A. For log Intensity (figure 3.4B), changing the modulation frequency has negligible effects. This is because the intensity part of the light signal is independent of modulation frequency. Whereas the phase contribution of the signal had modulation frequency dependence. The range of modulation frequencies chosen are between 50 MHz to 200 MHz. This

is because these represent a range of frequencies that can be used with the ISS, as well as for allowing sufficient contrast in log Intensity and phase data.

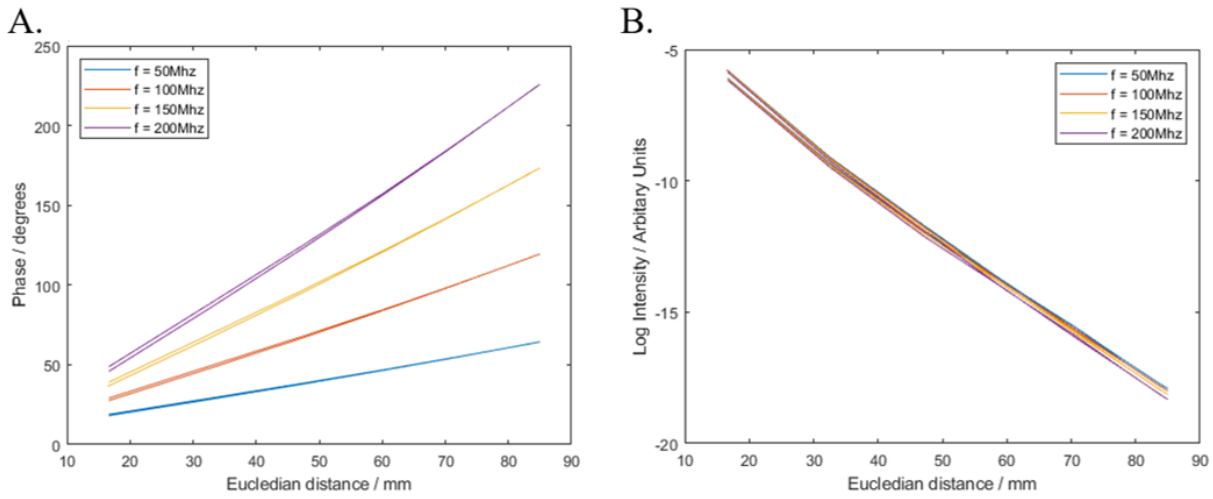

Figure 3.4: A. How phase changes as a function of modulation frequency. For a given source-detector separation, the phase increases with an increase in modulation frequency. There are two lines for each modulation frequency due to asymmetries in the mesh, since the mesh has a non zero resolution. B. How the log intensity changes with modulation frequency. Log intensity measurement is independent of modulation frequency, as there is no frequency dependency on the amplitude of a frequency domain signal.

From figures 3.2, 3.3 and 3.4, without considering system calibration on the ISS, measured data will be a function of optical properties of the medium and modulation frequency of the light sources. More importantly, this means that by varying the modulation frequency, different information can be obtained about a medium. This idea underpins the quantitative evaluation study. Next, data was collected on a phantom to understand the system response of the ISS.

3.2 Methods

To replicate the layers sampled in the human head, a simple three layer finite element model (FEM) was created using the NIRFAST (Near Infrared Fluorescence and Spectral

Tomography) software package (Dehghani, Eames, et al., 2009), figure 3.5a and b. This simplified model was used to allow a direct comparison to previous work outlining the benefits of HD-DOT, as well as providing a robust geometry for analysis of the results (White and Culver, 2010). The mesh has dimensions of 160 mm , 100 mm and 30 mm in x, y and z respectively. The nodal resolution of the FEM is 1 mm , giving a total of 504,091 nodes (blue dots), corresponding to 2,880,000 linear tetrahedral elements. The three layers in the mesh are separated in the z axis: Layer 1 (z = 0 mm to z = -14 mm) represents the skin, scalp and cerebral spinal fluid (CSF), layer 2 (z = -14 mm to z = -16 mm) represents gray matter (cortex) and layer 3 (z = -16 mm to z = -30 mm) represents white matter (deep brain tissue).

The thickness of each layer was chosen based on the average anatomy from previous studies. The skin and scalp thickness of 14 mm was derived from the sum of the average scalp and skin thickness (6.9 mm and 6.0 mm respectively) (Strangman, Q. Zhang, and Z. Li, 2014), where they segment the Colin27 head model. The thickness of the gray matter layer (cortex) was chosen as 2mm (Fischl and Dale, 2000), where they segmented cortex thicknesses from MRI images of 30 subjects and obtained an average gray matter thickness of 2.5 mm, which for this work is rounded down to 2 mm. Finally, the third layer, white matter thickness was chosen to be 14 mm, so overall the mesh had a depth of 30 mm (figure 3.5b).

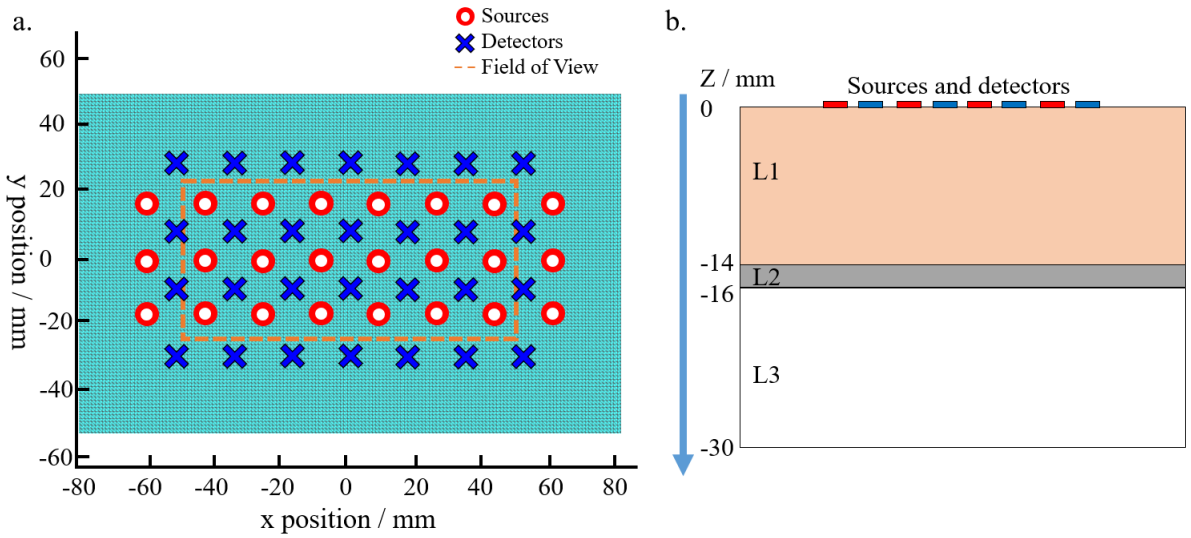

Figure 3.5: a. A top down view of the HD grid FEM. There are 24 sources (blue crosses) and 28 detectors (red circles). b. A schematic view in the Z plane of the FEM depicting three different layers. Layer 1 represents the skin, scalp and CSF. Layer 2 represents gray matter and layer 3 represents white matter. The absorption and reduced scattering coefficients of the three layers are shown in table 3.2.

The optical properties, table 3.2, were averaged from various studies at 690 nm, 750 nm , 780 nm and 830 nm (Bevilacqua et al., 1999 , Torricelli et al., 2001 and Okada et al., 1997) found in Strangman, Q. Zhang, and Z. Li, 2014, so they represent a realistic range of NIRS wavelengths. For layer 1, a weighted average of the optical properties for the skin, scalp and CSF were taken based upon their average thickness (Strangman, Q. Zhang, and Z. Li, 2014). Layers 2 and 3 are the optical properties of gray matter and white matter respectively.

Table 3.2: The absorption and reduced scattering coefficients for each layer in the FEM (Strangman, Q. Zhang, and Z. Li, 2014, Bevilacqua et al., 1999, Torricelli et al., 2001 and Okada et al., 1997).

	Absorption Coefficient mm^{-1}	Reduced scattering coefficient mm^{-1}
Layer 1	0.0139	0.755
Layer 2	0.0195	1.10
Layer 3	0.0169	1.35

On the surface of the model, 24 sources and 28 detectors are arranged in the conventional 'high density' arrangement (Eggebrecht et al., 2014 and Doulgerakis, Eggebrecht, and Dehghani, 2019), with nearest neighbour (NN) distances between a given source and multiple detectors of 13.04 mm (NN1), 29.10 mm (NN2), 39.04 mm (NN3) and 46.92 mm (NN4), giving rise to 348 measurement channels. Due to extensive artefacts observed at the edges of the high density grid, a reduced field of view (FOV) is used to present the results of the analysis. This field of view can be seen in figure 3.5a as an orange dotted line. The FOV has dimensions of 102 mm in the x axis, 50 mm in the y axis and is centered at x = y = 0 mm.

There are three types of simulated data used, CW (amplitude only), FD (phase only) and the combination of the two, CW&FD (amplitude and phase). Then for each of these data types, there are three modulation frequencies used, defined as 78.125 MHz, 140.625 MHz, 203.125 MHz (based on ISS Imagent) as well as a combination of the three. To introduce realistic noise into the simulated data, a noise model was taken from Doulgerakis, Eggebrecht, and Dehghani, 2019. Resting state data was from a subject at 140.625 MHz at 830 nm and 690 nm. Analysis of the data provided the percentage variation of the log mean intensity and raw phase noise in degrees by calculating the standard deviation of the two signals respectively, using the same NN1 to NN4 distances as used in this study. The amplitude and phase noise were then averaged from 830 nm and 690 nm and added to the simulated CW and FD data respectively. It is assumed for CW data, the noise is constant and that for FD data the noise scales linearly as a function of modulation frequency.

There are four main steps in the developed methodology: (1) Calculating the Jacobian (Sensitivity matrix), (2) Generating simulated measurements, (3) Image reconstruction, and finally (4) Calculation of performance metrics from the reconstructed images. The presented work will only consider the accuracy for recovering μ_a from boundary measurement, assuming a known scattering property, which can be considered valid for imaging functional vascular

related changes as in human brain fNIRS studies.

Photon propagation can be described using a forward model based on the diffusion approximation (Dehghani, Eames, et al., 2009). From the forward model, the inverse problem can be solved for which the Jacobian, J (sometimes called the Sensitivity or 'A' matrix) is used. The Jacobian is a matrix for a given modulation frequency that defines the influence of the spatially varying optical properties ∂X within the model on the change in the measured data as collected for a given source/detector pair, ∂Y. Then the Jacobian is given by equation 3.1,

$$\partial Y = J\partial X \quad . \tag{3.1}$$

The Jacobian as defined has separate components (kernels) for each data-type (amplitude and phase), resulting from changes in the absorption coefficient (μ_a). A different Jacobian is therefore calculated for each modulation frequency for each data-type (amplitude/phase). The dimension of the Jacobian is the defined as the number of measurements pairs by number of nodes within the model. From this sensitivity matrix, simulated data was calculated using equation 3.2.

Activations were made at three discrete depths of -14, -15 and -16 mm respectively. Specifically, target activations are defined by creating a matrix, X_{sim}, (dimensions of number of nodes in the entire model $\times$ number of required activation (at a given node)). Each element of X_{sim} is then set to zero apart from a point activation which is set to 10.5. An activation of magnitude 10.5 is used as it causes a maximum of a 5% change in measured CW data at 141 MHz, which is as observed from in vivo experiments of visual cortex activations (Zhan, 2013). Simulated functional measurements, Y_{sim}, are then generated by equation 3.2,

$$Y_{sim} = JX_{sim} \quad . \tag{3.2}$$

Using the generated data from single target activation, image reconstruction can be performed. Previous work has utilised a realistic measure of the noise to simulated data from a multi-layered head model and demonstrated that the inclusion of phase measurements does improve image recovery as compared to intensity measurements alone (Doulgerakis, Eggebrecht, and Dehghani, 2019). Following from equation 3.2, a moore-penrose pseudoinverse (Penrose, 1955) with Tikhonov regularization is used to approximate the inverse of the Jacobian, $J^{-1} \approx J^{\#}$. J$^{\#}$ is given by equation 3.3,

$$J^{\#} = J^T(JJ^T + \alpha I)^{-1} \tag{3.3}$$

where I is an identity matrix and α is the regularisation term, given by equation 3.4,

$$\alpha = \lambda * max[diag(JJ^T)] \tag{3.4}$$

where λ is the regularisation parameter chosen to be 0.01 for both CW and FD simulated data. Using the pseudo-inverse Jacobian, the reconstruction of changes in optical properties X_{recon} is given by equation 3.5,

$$X_{recon} = J^{\#}Y_{sim} \quad . \tag{3.5}$$

For each point activation at a single depth in the HD grid FOV, 3 dimensional spatially varying image reconstruction is performed (at 5253 nodes $\times$ 3 depths in z). To calculate the performance metrics for given activation point within the cortex, only nodes within the

cortex layer (layer 2 in figure 3.5b) were considered for analysis.

The choice of performance metrics are adapted from the work of White and Culver, 2010 to allow a direct comparison with established standards. Specifically, these are the localisation error (LOCA), the full width half maximum (FWHM) and the effective resolution (ERES), which are used to quantify how accurate image reconstructions are, particularly in the context of cortical activation. A description of how the three metrics are calculated is given in figure 3.6.

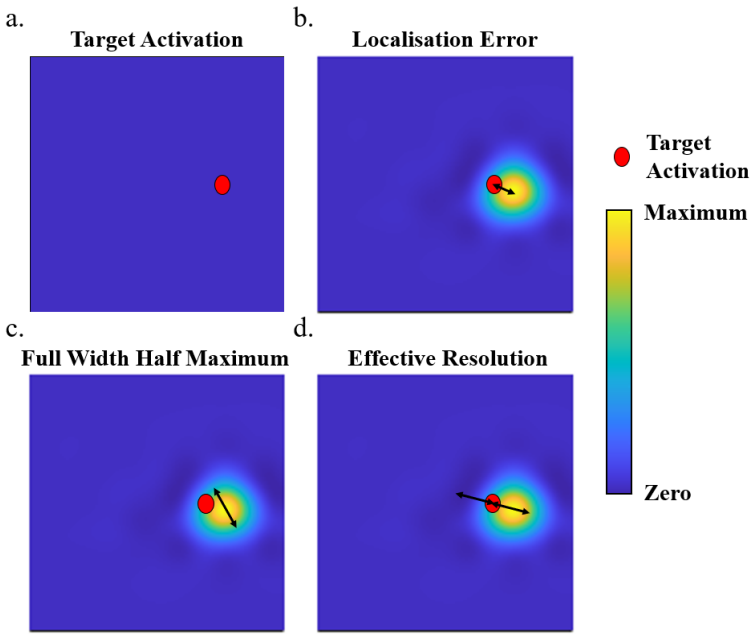

Figure 3.6: A diagram of how each performance metric is calculated. a. A single node is set to 10.5 (activated), whilst all other nodes are set to zero. Image reconstruction is then performed everywhere. Only nodes within the cortex are considered for the performance metrics. b. The LOCA is given by the distance between the target activation and the maximum recovery of the reconstruction. c. The FWHM is given by the maximum distance between any two nodes that are more than or equal to 50% of the maximum of the reconstruction. d. The ERES is twice the maximum distance between the target activation and any node that is more than or equal to 50% of the maximum of the reconstruction.

LOCA is given by the distance between the target activation and the location of

the recovered maximum of the reconstruction. This represents the minimum spatial error between where cortical activation occurs and where the tomographic reconstruction places the maximum of the recovery. FWHM is given by the maximum distance between any two nodes in the reconstruction that are more than or equal to 50% of the maximum of the reconstruction. ERES is twice the maximum distance between the target activation and any node in the reconstruction that is more than or equal to 50% of the maximum of the reconstruction. ERES combines the concept of mislocalisation, as well as recovering of to be bigger than it is. Therefore it represents a more realistic performance metric.

To calculate each performance metric, image reconstruction was performed which has been described above and summarised in figure 3.7 a to c.

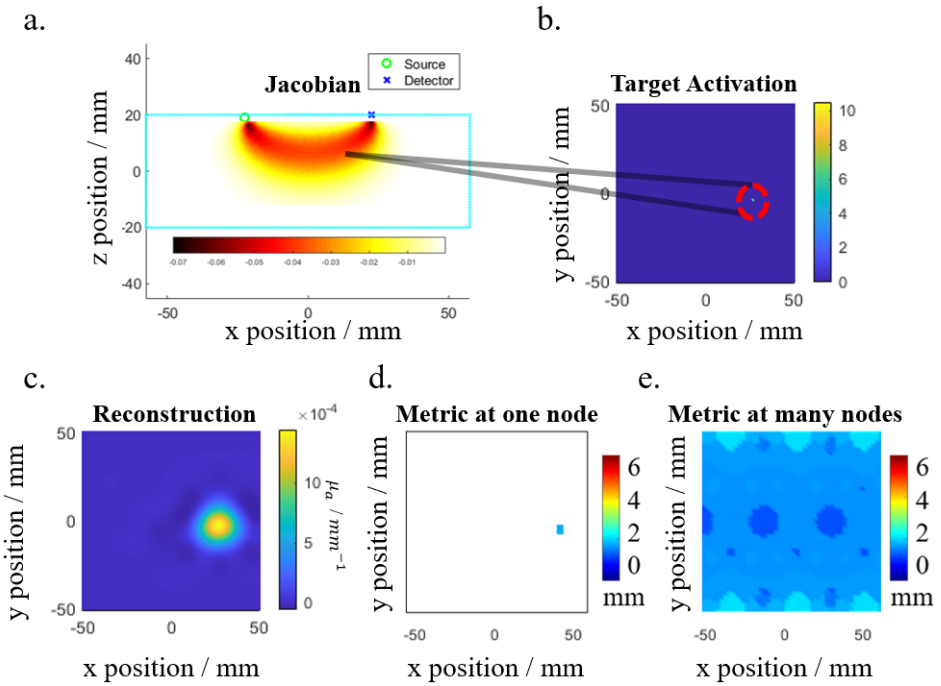

Figure 3.7: The processes involved in generating the performance metrics. a. A Jacobian (mm) is shown for a 2D FEM with 1 source and 1 detector. This shows the sensitivity of a measurement being made at detector 1 from source 1, due to a point activation at that node. b. Each node is then activated or perturbed by setting the node to 10.5, which would cause a maximum of a 5% change in CW data at 141 MHz (Zhan, 2013). c. From the point activation, image reconstruction is performed at every node within the mesh. d. Each performance metric is then calculated by considering nodes within the cortex. e. Steps b-d are then repeated for every node within the cortex layer. The average value and standard deviation of each performance metric can then be calculated.

After image reconstruction, the metrics are calculated for each node for a single depth within the cortex layer of the model. There are 5253 nodes for a given depth, and 15,759 nodes for the cortex layer. Then the average value of a given metric is calculated individually at 3 individual layers at -14 mm, -15 mm and - 16mm respectively, as well for the entire cortex layer (averaged across all depths). The entire model is used for image reconstruction. Then, only nodes within the cortex layer are used for metric calculations.

To evaluate the resolving power of the different data types and modulation frequencies, two point perturbations were simulated at a depth of -15 mm (middle of the cortex layer).

They were placed along y = 0 mm and at ± X mm in the x axis. Figure 3.8 shows two examples of point activation as separated by ± 13 mm (a and b) and and ± 11 mm (c and d). The recovered activations are normalised so that the maximum is unity. A metric to determine how close the two point activations can be before being unable to be identified as two separate points, is by considering the minimum of the recovery profile to be greater than 0.5 (i.e. at full width half maximum). Other metrics to determine separation is looking at a 3 dB, or 0.707 of the maximum value separation. If the minimum of the recovery profile is less than 0.707 then the two activations may be considered as separated. Any threshold used to determine separation can be argued as arbitrary and fundamentally is subjective. For example, figure 3.8c and d show a separation which is less than the FWHM separation, however it could be argued that the two activations can still be separated. A lower value at the minima means that the two points are easier to resolve. For this analysis FWHM (0.5) and 3 dB (0.707) separation are considered.

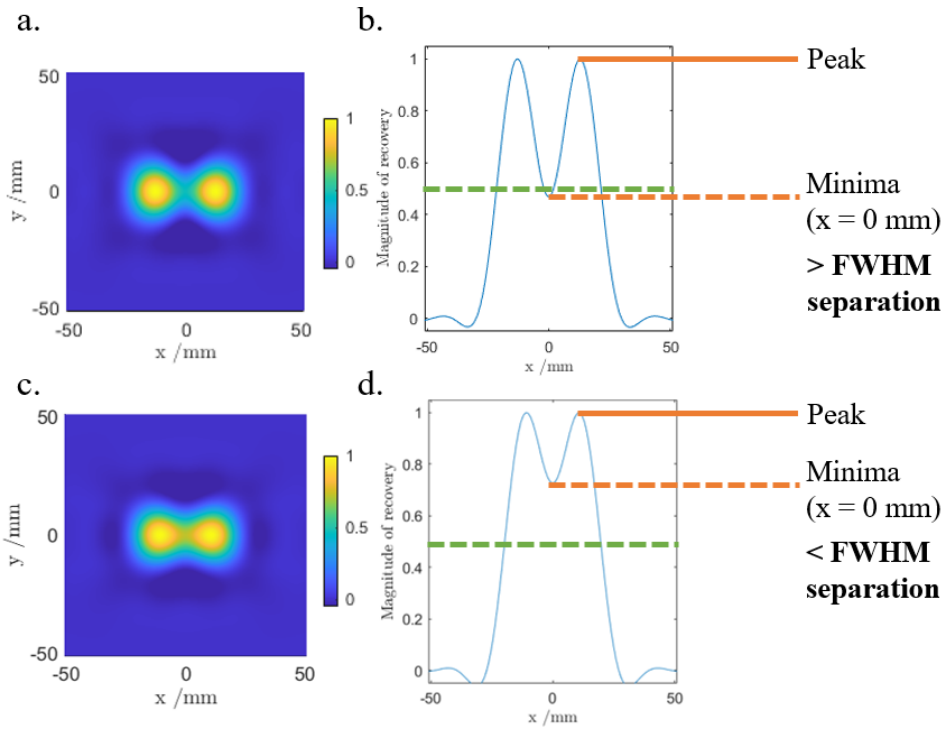

Figure 3.8: Diagrams showing the separation of two point activations. a. Image reconstruction of two point activations at ±13 mm respectively in the x axis. The reconstructions are summed from the two activations and normalized. b. A graph showing the magnitude of the reconstruction along the x axis at y = 0 mm. The graph shows that there is a FWHM separation, since the minima is below 50% of the maximum recovery. c. As described for a. , but the two activations are at ±11 mm respectively. d. As described for b. , but there is now less than FWHM separation. This is because the minima is above 50% of the maximum recovery.

3.3 Results

The results of the three performance metrics, LOCA, FWHM and ERES are shown and discussed in the following sections. In sections 3.3.1 to 3.3.3, the results shown are averaged from point activation's across the cortex layer (Z = -14 mm to Z = -16 mm) within the field of view as shown in figure 3.5a. Section 3.3.4 shows results in each layer of the cortex individually within the field of view as shown in figure 3.5. Finally, section 3.3.5 provides numerical results from the dual point spread function analysis at a depth of Z = - 15 mm.

3.3.1 CW vs FD vs CW&FD

Figure 3.9 shows the LOCA, FWHM and ERES respectively for CW, FD and the combined CW & FD simulated data. This was performed at a modulation frequency of 140.625 MHz. The average value of each metric is shown in table 3.3. For the LOCA, FD performs 12.78% better than CW alone, and the combined measurement of CW & FD is 47.05% better than CW alone. The combined CW&FD measurement for LOCA also results in a more uniform central region than either CW or FD, as well as less artifacts around the edge of the FOV. This is particularly seen on the left and right hand side of the FOV. It is only in the CW case that the LOCA dramatically increase to a maximum of 5.55 mm in the corners. For comparison, the FD and CW&FD measurements reach a maximum of 3.74 mm and 4.03 mm respectively.

For the FWHM, FD performs 6.73% better than CW and the combined measurement of CW & FD is 8.71% better than CW alone. Whilst the magnitude of performance increase by combining CW and FD is less than shown with LOCA, the standard deviation of the FWHM drastically reduces. The FD case has a 71.08% lower standard deviation than CW, and the CW&FD case has a 125.39% lower standard deviation than CW. This can be seen visually, with the FWHM - CW result in figure 3.9 showing artefacts on the top and bottom of the FOV.

The FD and combined measurement of CW & FD have greatly reduced artefacts in these areas. For the ERES, FD performs 5.92% better than CW and the combined measurements are 9.40% better than CW alone. For the ERES the FD and combined measurements have lower artefacts around the edges of the FOV and a more uniform center. In the particular the FD and combined measurements have standard deviations which are approximately 30% lower than that of the CW measurements.

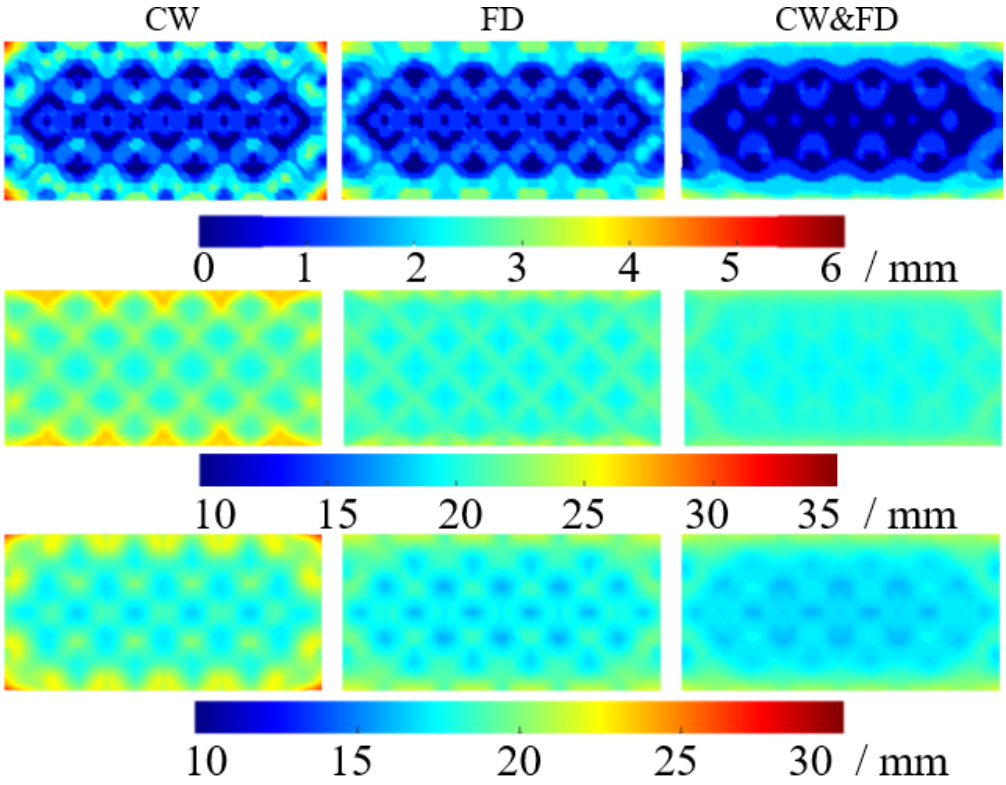

Figure 3.9: The LOCA (first row), FWHM (second row) and ERES (third row) are shown at 140.625 MHz for the CW, FD and CW & FD case respectively. The graphs are the average of point activations within the cortex layer from a depth of -14 mm to -16 mm and within the FOV shown in figure 3.5a.

Table 3.3: The average and standard deviation of the LOCA, FWHM and ERES for the CW, FD and CW & FD measurements. Row's one to three are without noise and row's four to six are with noise. These are at 140.625 MHz and are the average of point activations in the cortex layer from a depth of -14 mm to -16 mm within the FOV shown in figure 3.5a. These results can be seen in figure 3.9.

	Metric	CW	FD	CW&FD
Noise Free	LOCA / mm	1.50 ± 0.90	1.33 ± 0.83	1.02 ± 0.90
	FWHM / mm	19.96 ± 1.42	18.70 ± 0.83	18.36 ± 0.63
	ERES / mm	21.64 ± 1.97	20.43 ± 1.50	19.78 ± 1.52
Noise Added	LOCA / mm	1.50 ± 0.90	1.79 ± 0.94	1.46 ± 0.80
	FWHM / mm	19.97 ± 1.42	20.96 ± 5.80	19.30 ± 2.09
	ERES / mm	21.66 ± 1.97	24.94 ± 11.31	21.67 ± 4.10

The inclusion of noise can be seen in rows four to six of table 3.3. In the noise added model, FD measurements perform worse as compared to the CW measurements. However,

despite the decreased average performance of FD alone, the combined CW&FD perform better than either CW or FD alone for the LOCA and FWHM. For the ERES, CW&FD performs marginally worse than CW alone.

Distribution of metrics in table 3.3:

Table 3.3 shows the mean and standard deviation of the performance metrics, presented to four and three significant figures respectively, and to discuss the appropriateness of this and the implications this has on the results, violin plots are shown in figure 3.10. These plots show the distribution, and box plots (IQR ranges (q1 and q3) and median) of the performance metrics for each given data type, which allows for further comparison of how the data type influences the performance.

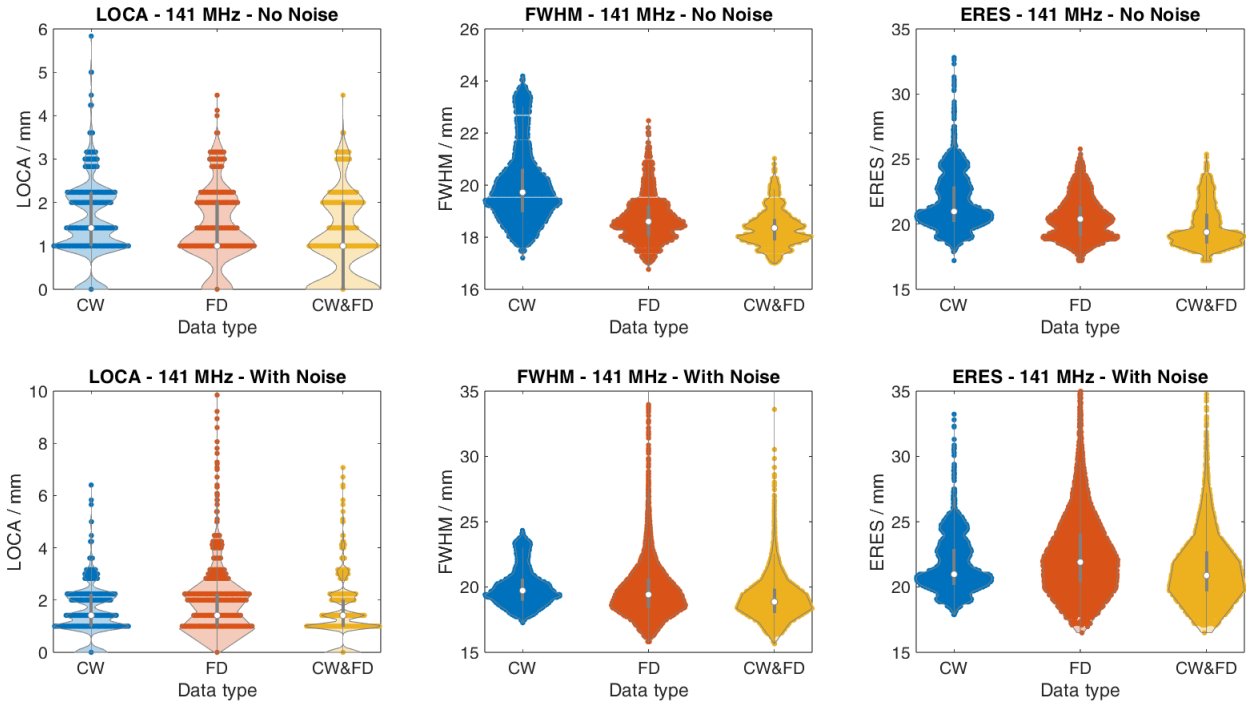

Figure 3.10: Violin plots of the LOCA, FWHM and ERES at 141 MHz without and with noise for the three data types, CW, FD and CW&FD respectively, as shown in figure 3.9, and table 3.3.

Figure 3.10 shows that for the LOCA without noise case, the main influence on the

lower mean value LOCA for CW&FD compared to FD and then CW is that q1 for CW&FD is 0 mm, compared to 1 mm for the separate FD and CW cases. For the noise added case for the LOCA, the mean values in table 3.3 are reflected well in the violin plots, where the FD case is worst performing, and the CW and CW&FD case performing similarly. For the FWHM comparison, without noise it can be seen that the FD and CW&FD cases outperform the CW case, with the q3 of CW&FD and median of FD lower than the Q1 of CW. However in the noise case, the performance of the three data types converge, with visible overlap between the three data type's iq ranges. The median and q1's of FD and CW&FD are lower than that of the CW case, which can be attributed to how there are more FWHM values below 19.7 mm (CW - Median), whilst it can be seen that the added noise causes a larger maximum (worse) FWHM with the addition of phase data compared to the CW case. The differences between data types for the ERES behaves similarly to the FWHM metric, in that without noise, the median of CW&FD is lower than the q1 of the CW case, but when noise is added the performances converge. The inclusion of phase data with noise has a lower floor than the intensity only CW case, however a compromise is that it comes with a higher ceiling, with respect to performance.

For each data type and metric apart from one case, there are statistically significant differences between all distributions, by virtue of non overlap between the 95% confidence intervals. The case where there is no statistically significant differences are in the noise added case considering the LOCA.

3.3.2 Effect of Modulation Frequency

The LOCA, FWHM and ERES were evaluated for three different modulation frequencies of 78.125 MHz, 140.625 MHz and 203.125 MHz. For convenience these will be referred to as 78 MHz, 141 MHz and 203 MHz respectively. Figure 3.11 shows the three metrics for CW and

the combined data types (CW&FD), with the FD results omitted as the trend is similar to those presented above. The average values of these results are shown in table 3.4.

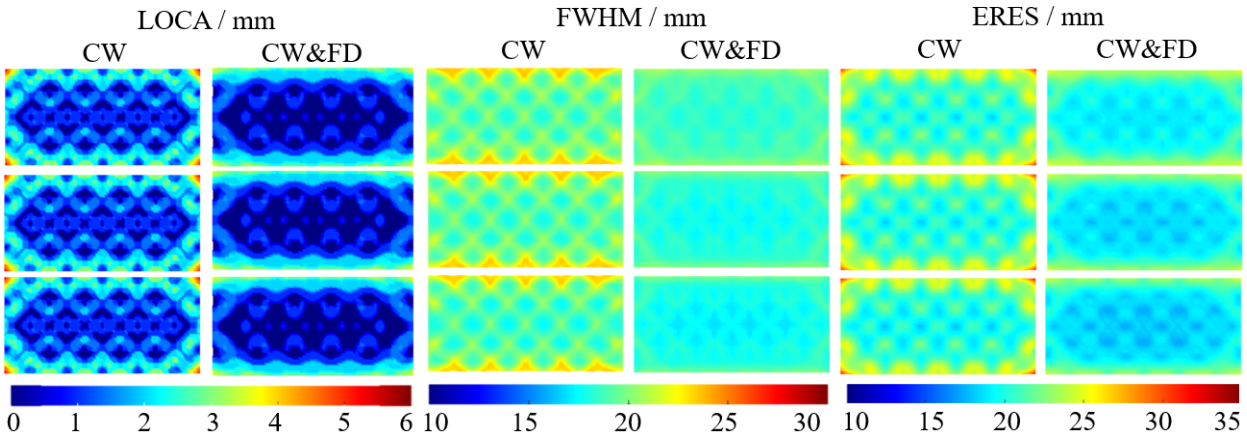

Figure 3.11: The LOCA, FWHM and ERES are shown at 78 MHz (first row), 141 MHz (second row) and 203 MHz (third row) respectively. For each modulation frequency, the CW and CW&FD measurements are shown. The graphs are the average of point activations within the cortex layer from a depth of -14 mm to -16 mm and within the FOV shown in figure 3.5a.

As expected from the single modulation frequency case in figure 3.9, the combined measurement performs better than the CW measurement across all three modulation frequencies. Increasing the modulation frequency increases the performance of both CW and CW&FD for each metric. In the case of the LOCA, this improvement is smaller, with a 0.67% (0.01 mm) change for CW and a 5.88% change for CW&FD case. For the FWHM, going from 78 MHz to 141 MHz causes an 1.82% and 5.15% increase in performance for CW and CW&FD respectively. A significant increase in performance of 11.47% is shown when considering the difference between CW at 78 MHz to CW&FD at 203 MHz. For all modulation frequencies, the CW&FD case show less artefacts around the top and bottom of the FOV than CW. The standard deviation of FWHM stays near constant across modulation frequencies, with the CW&FD measurements showing a 125.39% decrease in standard deviation compared to CW. For the ERES, there is a 1.82% increase for CW measurements

from 78 MHz to 203 MHz and an 4.83% increase for CW&FD measurements. Again, the most significant increase in performance occurs when considering both increasing modulation frequency and use of CW&FD combined measurements instead of just CW measurements of 12.02%.

Table 3.4: The average and standard deviation of the LOCA, FWHM and ERES for the CW and CW&FD measurements. These are evaluated at 78 MHz (first row), 141 MHz (second row) and 203 MHz (third row). They are the average of point activations in the cortex layer from a depth of -14 mm to -16 mm within the FOV shown in figure 3.5a. These results can be seen in figure 3.11.

LOCA / mm		FWHM / mm		ERES / mm	
CW	CW & FD	CW	CW & FD	CW	CW & FD
1.50±0.89	1.08±0.93	20.11±1.39	18.97±0.62	21.80±1.93	20.40±1.58
1.50±0.90	1.02±0.90	19.96±1.42	18.36±0.63	21.64±1.97	19.78±1.52
1.49±0.90	1.02±0.88	19.75±1.42	18.04±0.65	21.41±2.04	19.46±1.50

Distribution of metrics in table 3.4:

Violin plots of the data shown in table 3.4 are presented in figures 3.12 (LOCA), 3.13 (FWHM) and 3.14 (ERES). For the LOCA and considering the CW case, as shown in table 3.4, increasing modulation frequency has minimal changes in the distribution of the LOCA, as they have the same median, q1 and q3 for 78, 141 and 203 MHz. The difference between the mean values of 1.50 (CW 78 and 141 MHz) and 1.49 (203 MHz) could be explained by the addition of a few visible outlier data points for the LOCA above 4 mm for 78 and 141 MHz, compared to 203 MHz. For the CW&FD case, the lower mean LOCA of 1.02 mm from the 141 and 203 MHz cases compared to 1.08 mm of 78 MHz can be attributed to a small shift in the distribution of LOCA values above the median, since the median values for the three modulation frequencies are all 1 mm. Whereas, the q3 value for 78 MHz is 2.03 mm compared to 2.00 mm in the 141 and 203 MHz case respectively. For just considering the LOCA, these are minimal differences.

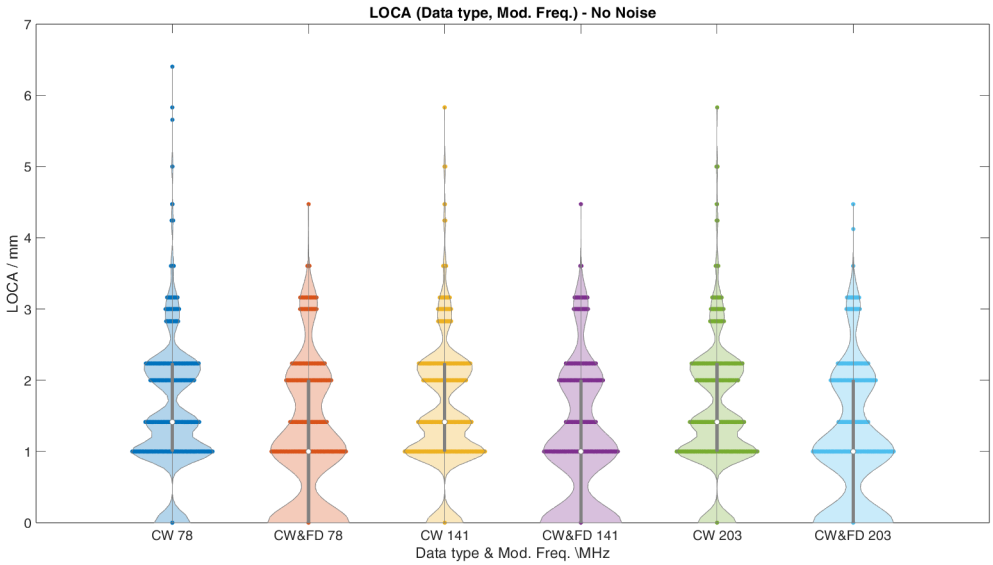

Figure 3.12: Violin plots of the LOCA at 78, 141 and 203 MHz for the CW and CW&FD data types respectively, as shown in figure 3.11 and table 3.4.

For considering the FWHM, as shown in figure 3.13, and the ERES in figure 3.14, it can be seen that there are many discrete bands of FWHM values for each data type and modulation frequency, i.e these performance metrics yield discrete values due to the calculation of them from the image reconstruction on a FEM. It can be seen that the range of the distribution of each modulation frequency is smaller for the combined CW&FD case, compared to the CW only case. As well as this, it can be seen that for 141 and 203 MHz, there is no overlap between the iqr of the CW and CW&FD cases respectively, which suggests a significant difference between the two data types for FWHM performance. It should be noted that the notches of the box plots are not shown in these figures, since size of the notches were too small to be appreciable in the figures due to the large range of the data.

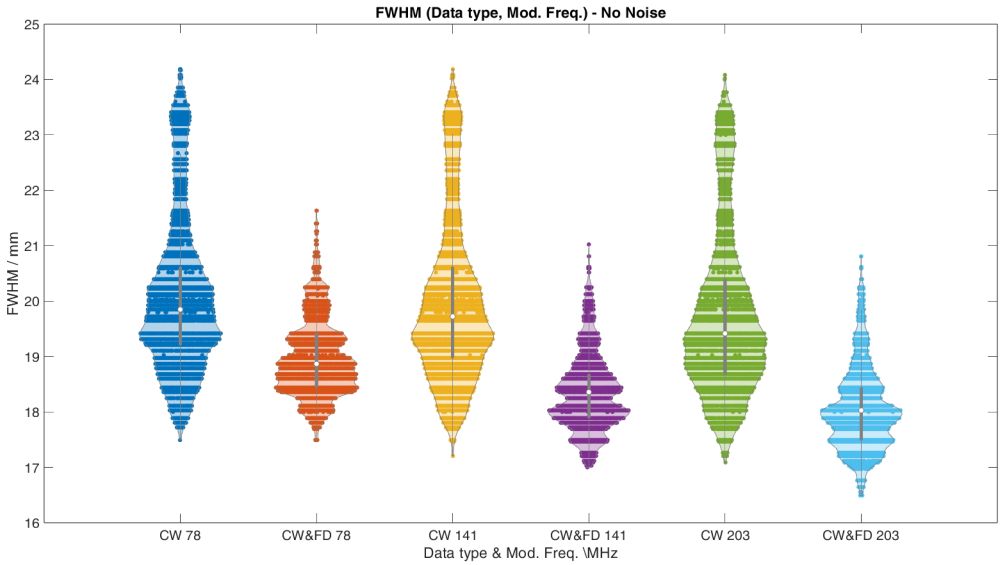

Figure 3.13: Violin plots of the FWHM at 78, 141 and 203 MHz for the CW and CW&FD data types respectively, as shown in figure 3.11 and table 3.4.

The violin plots for the ERES support the results in table 3.4 in that the biggest change in ERES comes from changing the data type, rather than the modulation frequency. It was stated that the most significant increase in performance of FWHM and ERES came from considering the decrease in FWHM and ERES from the 78 MHz CW case to the 203 MHz CW&FD case when discussing the results from table 3.4. The violin plots in figures 3.13, and 3.14 support this, since for the FWHM the q1 of 78 MHz CW is 19.2 mm and the q3 of the 203 MHz CW&FD case has a lower value of 18.4 mm, in addition for the ERES, the q1 of 78 MHz CW is 20.3 mm and the q3 of the 203 MHz CW&FD case has the same value of 20.3 mm. The relative differences between the FWHM and ERES comparisons can be attributed to the fact that the LOCA is influenced less by data type and modulation frequency and the ERES is linked to the LOCA in it's calculation, whereas the FWHM calculation is completely independent on the localisation performance.

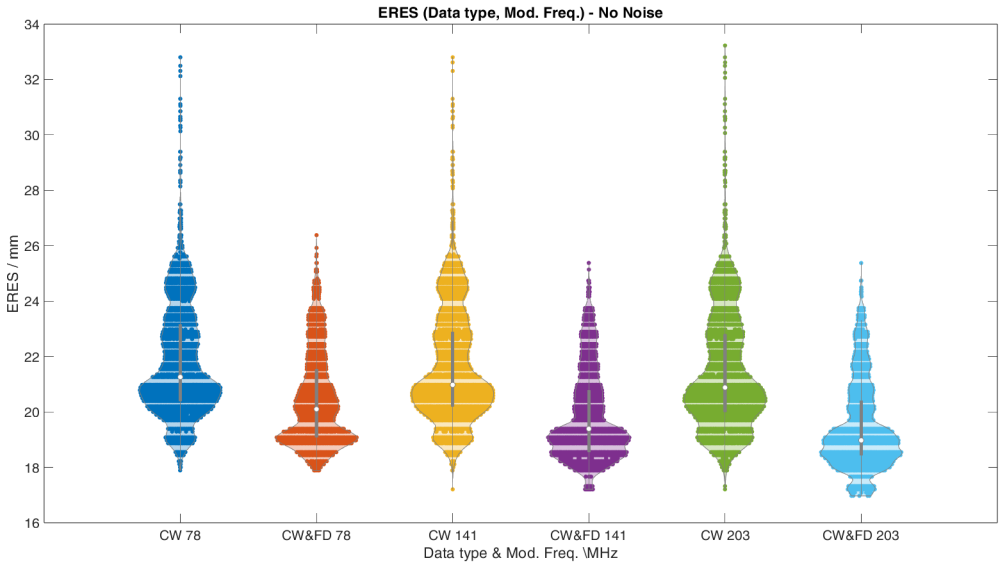

Figure 3.14: Violin plots of the ERES at 78, 141 and 203 MHz for the CW and CW&FD data types respectively, as shown in figure 3.11 and table 3.4.

3.3.3 Combining Modulation Frequencies

The LOCA, FWHM and ERES were evaluated using 140.625 MHz and then by combining measurements at all three frequencies. Figure 3.15 shows the three metrics evaluated using CW&FD measurements. CW measurements were omitted as the CW contribution to three combined modulation frequency measurements were calculated to be the same as reference modulation frequency of 141 MHz. The average of these results are shown in table 3.5.

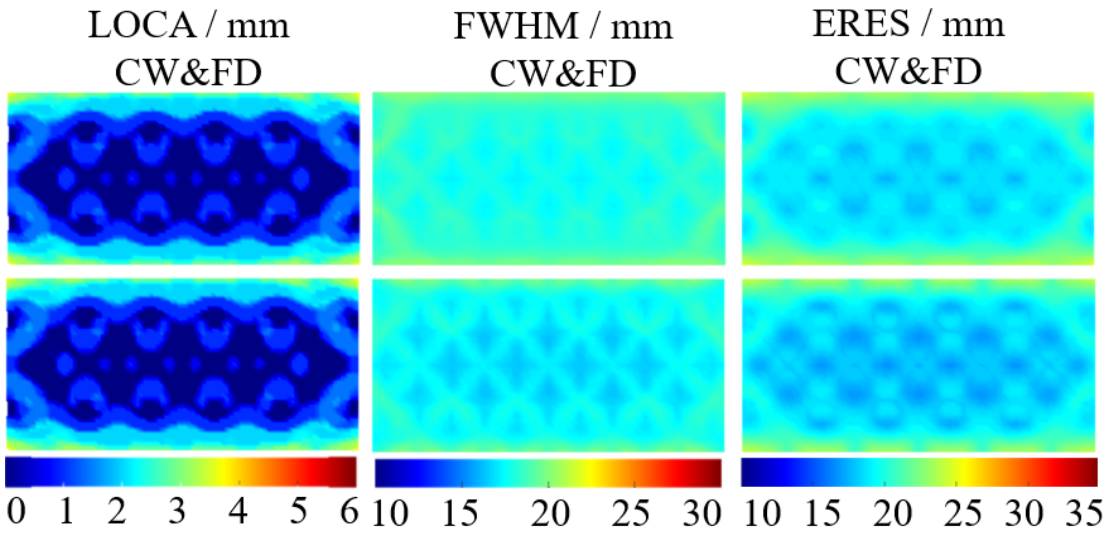

Figure 3.15: The LOCA, FWHM and ERES are shown using 140.625 MHz (first row) and the combined 78.125 MHz, 140.625 MHz and 203.125 MHz (second row) modulation frequencies. The CW&FD measurements are shown. The graphs are the average of point activations within the cortex layer from a depth of -14 mm to -16 mm and within the FOV shown in figure 3.5a.

For the LOCA, there is a 6.86% performance decrease combining three modulation frequencies as compared to the single frequency case. The FWHM and ERES show an increase in performance due to combining the modulation frequencies. For the FWHM, using three modulation frequencies is 4.68% (0.72 mm) better than the single frequency case. The minimum FWHM value of the three combined modulation frequencies is 16.56 mm compared to 17.31 mm for the ERES, the performance increase is 3.61% (0.69 mm). Although the FWHM decreases with combining modulation frequencies, the standard deviation increases by 14.28% (0.09 mm) and remains near constant for the ERES. Overall the lowest FWHM and ERES are found using the three combined modulation frequencies using the combined CW&FD data.

Table 3.5: The average and standard deviation of the LOCA, FWHM and ERES for CW&FD measurements. These are evaluated at a single frequency, 140,625 MHz and three combined frequencies 78.125 MHz, 140.625 MHz and 203.125 MHz. Row's one and two are without noise and row's three and four are with noise. They are the average of point activations in the cortex layer from a depth of -14 mm to -16 mm within the FOV shown in figure 3.5a. These results can be seen in figure 3.15.

	Modulation Frequency / MHz	LOCA / mm (CW&FD)	FWHM / mm (CW&FD)	ERES / mm (CW&FD)
Noise Free	141	1.02 ± 0.90	18.36 ± 0.63	19.78 ± 1.52
	78 & 141 & 203	1.09 ± 0.87	17.64 ± 0.72	19.09 ± 1.54
Noise Added	141	1.46 ± 0.80	19.30 ± 2.09	21.67 ± 4.10
	78 & 141 & 203	1.39 ± 0.79	18.27 ± 1.37	20.38 ± 2.68

The inclusion of noise can be seen in rows three and four of table 3.5. In the noise added model the combination of the three modulation frequencies increase imaging performance in each of the three metrics. This is 4.8% (0.07 mm) for the LOCA, 5.4% (1.03 mm) for the FWHM and 6.0% (1.29 mm) for the ERES. The combination of three modulation frequencies also decreases the standard deviation across the three metrics. This is most noticeable for the ERES, where the decrease is 34.6% of the three modulation frequencies compared to the single case.

Distribution of metrics in table 3.5:

The violin plots show the distribution of data from table 3.5 for the LOCA in figure 3.16, the FWHM in figure 3.17 and the ERES in figure 3.18. For the LOCA without noise, the 141 MHz and the combined 78,141 and 203 MHz case performs similarly as explained, with the same q1, median and q3 values, however with the inclusion of noise, the median of the single modulation frequency case is 1.41 mm, whereas the combined modulation frequency case has a median of 1 mm, which is also the same as it's q1 value, suggesting that the combined case does marginally better to alleviate noise for localisation accuracy.

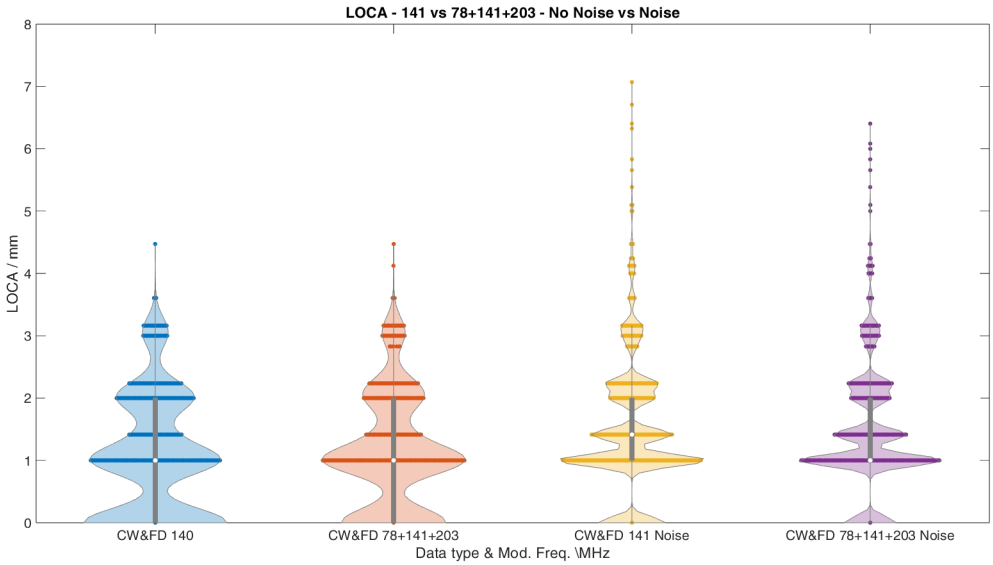

Figure 3.16: Violin plots of the LOCA at 141 MHz compared to the combined CW&FD at 78, 141 and 203 MHz respectively with and without added noise, as shown in figure 3.15 and table 3.5.

For the FWHM (figure 3.17) and ERES (figure 3.18), for both the no noise and noise added cases respectively, there are significant improvements from combining modulation frequencies, which supports the data and discussion from table 3.5, as denoted by non overlapping 95% confidence intervals. In particular for the noise added cases, for the FWHM the 95% confidence intervals are 18.84 mm to 18.89 mm for 141 MHz and 18.00 mm to 18.05 mm for the combined modulation frequency case. For the ERES the 95% confidence intervals for 141 MHz are 20.84 mm to 20.92 mm, and for the combined modulation frequencies these are 19.97 mm to 20.03 mm.

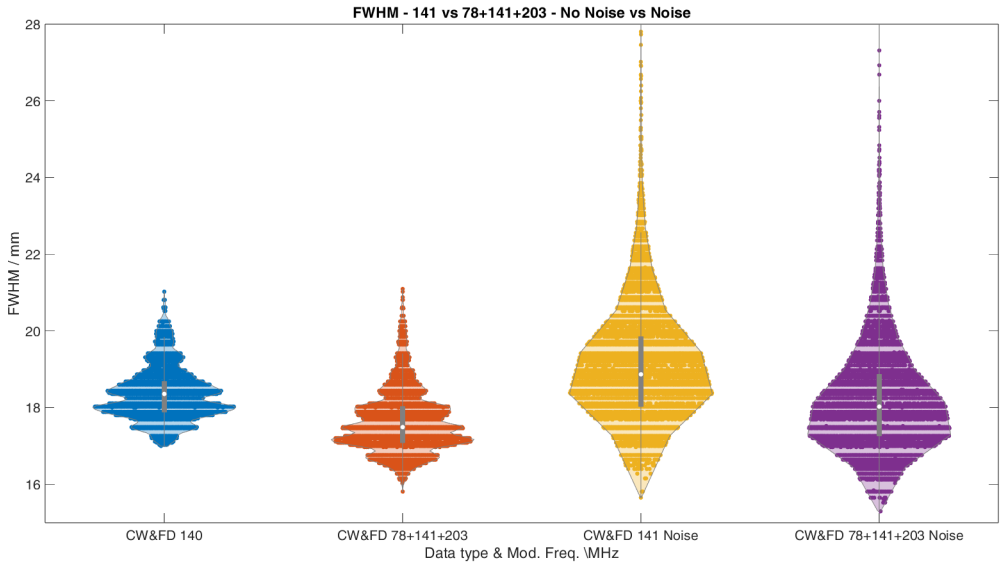

Figure 3.17: Violin plots of the FWHM at 141 MHz compared to the combined CW&FD at 78, 141 and 203 MHz respectively with and without added noise, as shown in figure 3.15 and table 3.5.

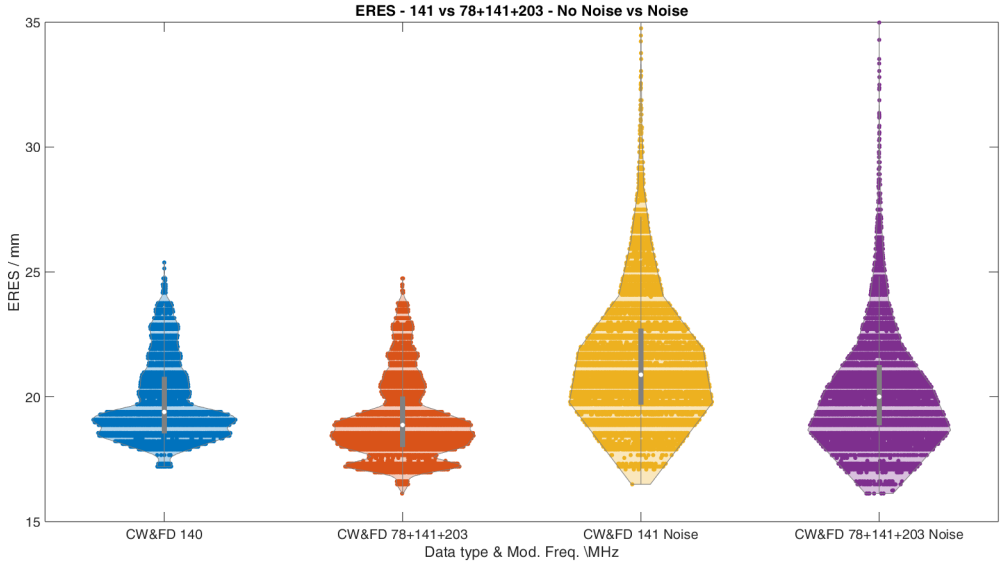

Figure 3.18: Violin plots of the ERES at 141 MHz compared to the combined CW&FD at 78, 141 and 203 MHz respectively with and without added noise, as shown in figure 3.15 and table 3.5.

3.3.4 Performance across depth of cortex

In sections 3.3.1, 3.3.2 and 3.3.3 the results of the LOCA, FWHM and ERES were shown as the average across the depth of the cortex (-14 mm to -16 mm), however in this section the metrics are evaluated at each discrete depth in the cortex, namely at -14 mm, -15 mm and -16 mm. CW, FD and CW&FD data types are evaluated at 141 MHz and the combined 78 & 141 & 203 MHz. The LOCA gets worse as a function of depth and is seen in all data types and modulation frequencies as shown in figure 3.19 and table 3.6. As expected, the combination of CW and FD data performs better than just FD and CW alone. This is across both the single 141 MHz and combined 78 & 141 & 203 MHz modulation frequencies respectively. For 141 MHz, the LOCA at -14 mm for CW is worse than that of FD at -16 mm. Similarly, the LOCA at -14 mm for FD is worse than that of CW&FD at -16 mm. This shows that FD has a better LOCA at higher depths than CW and the combined data type does even better than FD at higher depths within the cortex. The combined data type performs worse in the combined modulation frequency case than for the single modulation frequency. However, the decrease in performance is 6% of the standard deviation of both of these values. This may not be considered significant.

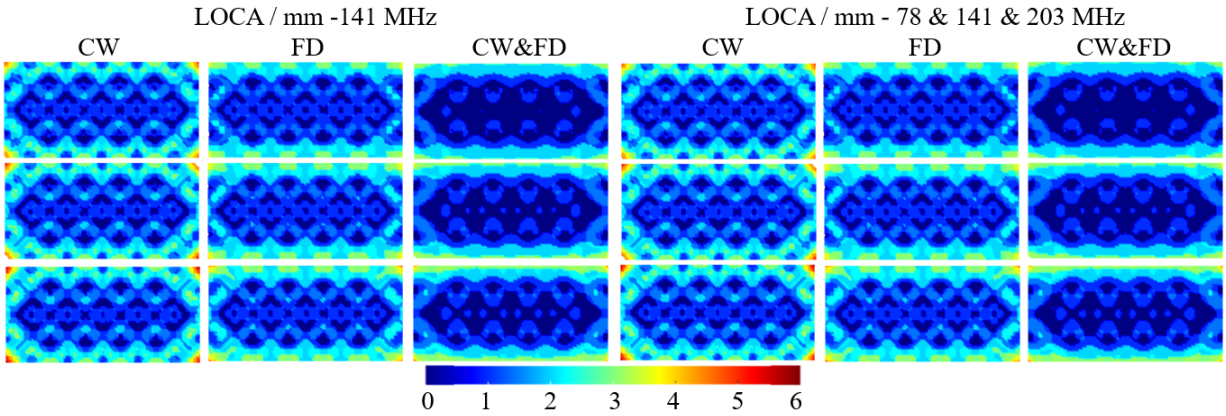

Figure 3.19: The LOCA for CW, FD and CW&FD at 141 MHz (left three columns) and the combined 78 & 141 & 203 MHz (right three columns). The first row is at a depth of 14 mm, the second row is at a depth of 15 mm and the bottom row is at a depth of 16 mm.

Table 3.6: The average and standard deviation of the LOCA for CW, FD and CW&FD at 141 MHz (left three columns) and the combined 78 & 141 & 203 MHz (right three columns). They are the average of point activations within a single layer of the FEM. These results can be seen in figure 3.19.

	LOCA / mm (141 MHz)			LOCA / mm (78 & 141 & 203 MHz)		
Activation Depth / mm	CW	FD	CW&FD	CW	FD	CW&FD
-14	1.46 ± 0.88	1.21 ± 0.83	0.87 ± 0.90	1.46 ± 0.88	1.10 ± 0.87	0.93 ± 0.87
-15	1.50 ± 0.91	1.35 ± 0.85	1.04 ± 0.94	1.50 ± 0.91	1.28 ± 0.92	1.11 ± 0.90
-16	1.53 ± 0.94	1.44 ± 0.89	1.16 ± 0.96	1.53 ± 0.94	1.38 ± 0.94	1.22 ± 0.92

The FWHM increases as a function of depth for all data types and modulation frequencies. This is shown in figure 3.20 and table 3.7. Again, the CW&FD data type performs better than FD or CW alone in all cases. For 141 MHz the FWHM at -16 mm of FD is less than that of CW at -14 mm. Similarly, the FWHM of CW&FD at -16 mm is better than FD at -14 mm. This is what is observed for the LOCA, however, for the combined modulation frequency whilst the FD follows this pattern compared to CW, CW&FD at -16 mm is not better than FD at -14 mm. CW data shows the largest standard deviation of FWHM for both the single and multiple modulation frequency by a factor of two compared to FD and CW&FD. This increase in standard deviation can be seen from artefacts on the top and bottom of the FOV in figure 3.20 at each depth in the cortex.

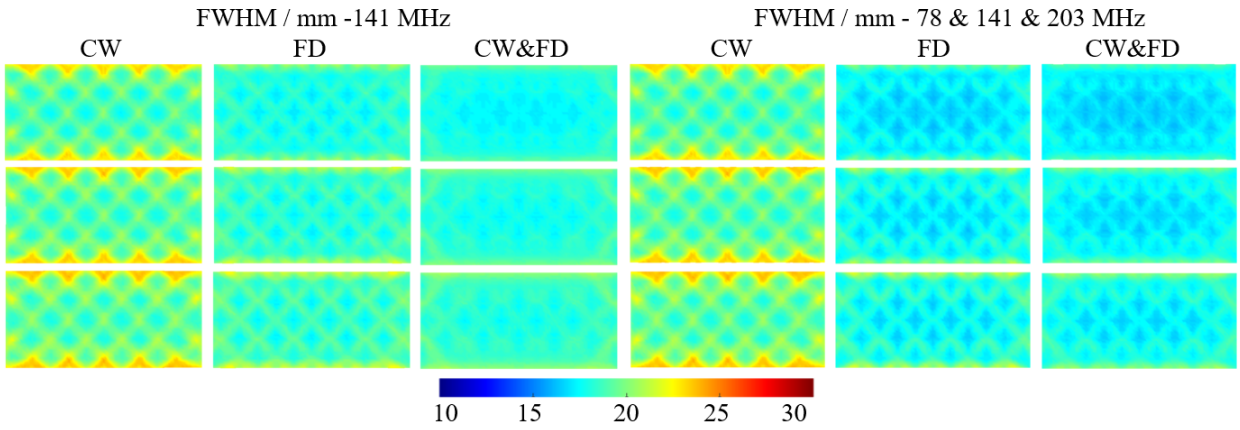

Figure 3.20: The FWHM for CW, FD and CW&FD at 141 MHz (left three columns) and the combined 78 & 141 & 203 MHz (right three columns). The first row is at a depth of 14 mm, the second row is at a depth of 15 mm and the bottom row is at a depth of 16 mm.

Table 3.7: The average and standard deviation of the FWHM for CW, FD and CW&FD at 141 MHz (left three columns) and the combined 78 & 141 & 203 MHz (right three columns). They are the average of point activations within a single layer of the FEM. These results can be seen in figure 3.20.

	FWHM / mm (141 MHz)			FWHM / mm (78 & 141 & 203 MHz)		
Activation Depth / mm	CW	FD	CW&FD	CW	FD	CW&FD
-14	19.73 ± 1.40	18.36 ± 0.74	18.00 ± 0.59	19.73 ± 1.40	17.47 ± 0.74	17.27 ± 0.63
-15	19.98 ± 1.43	18.72 ± 0.84	18.39 ± 0.64	19.98 ± 1.43	17.87 ± 0.88	17.65 ± 0.73
-16	20.18 ± 1.44	19.03 ± 0.92	18.39 ± 0.68	20.18 ± 1.44	18.20 ± 0.99	18.00 ± 0.84

Similar to the LOCA and FWHM, ERES gets worse as a function of depth. This can be seen in figure 3.21 and table 3.8. For 141 MHz, FD measurements offer a modest increase in performance compared to CW (6% to 7%). CW&FD performs slightly better (3%) than FD throughout the cortex. Using three modulation frequencies offers further performance increase. The ERES at -14 mm using three modulation frequencies is 0.72 mm or 3.88% better than using 141 MHz alone. At -16 mm, the benefit remains similar. Multi modulation frequency is 0.64 mm or 3.25% better than 141 MHz alone. The artefacts seen in the FWHM (figure 3.20) are also seen for the ERES (figure 3.21), however are less prominent on the top and bottom of the FOV. There are artifacts seen on the left and right edges of

the FOV not seen with the FWHM. These artifacts are seen the most in the CW case, which is reflected in the standard deviation of the FWHM and is approximately 25% lower for FD and CW&FD (1.5 mm) compared to CW (2.0 mm).

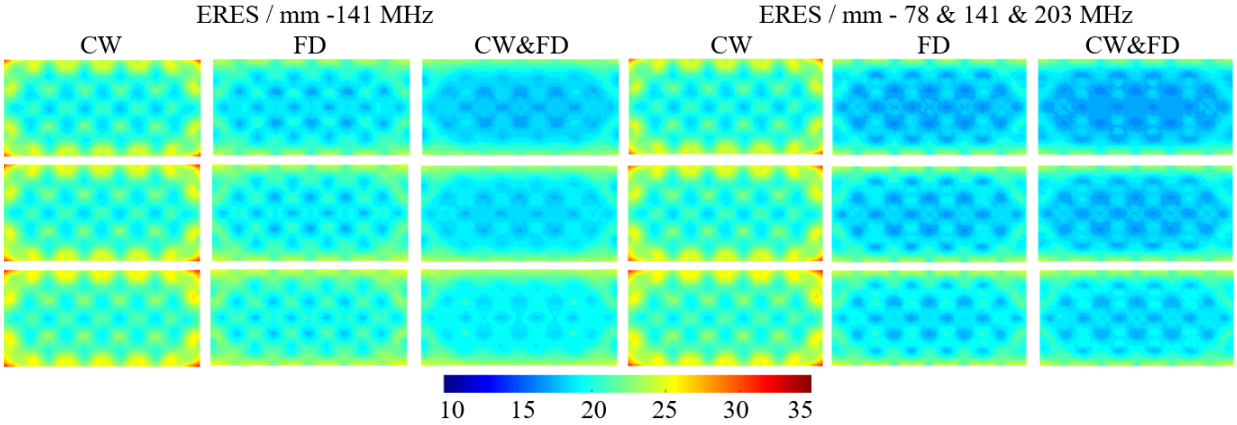

Figure 3.21: The ERES for CW, FD and CW&FD at 141 MHz (left three columns) and the combined 78 & 141 & 203 MHz (right three columns). The first row is at a depth of 14 mm, the second row is at a depth of 15 mm and the bottom row is at a depth of 16 mm.

Table 3.8: The average and standard deviation of the ERES for CW, FD and CW&FD at 141 MHz (left three columns) and the combined 78 & 141 & 203 MHz (right three columns). They are the average of point activations within a single layer of the FEM. These results can be seen in figure 3.21.

	ERES / mm (141 MHz)			ERES / mm (78 & 141 & 203 MHz)		
Activation Depth / mm	CW	FD	CW&FD	CW	FD	CW&FD
-14	21.23 ± 1.94	19.90 ± 1.47	19.26 ± 1.53	21.23 ± 1.94	18.91 ± 1.58	18.54 ± 1.54
-15	21.61 ± 1.99	20.38 ± 1.52	19.75 ± 1.53	21.61 ± 1.99	19.40 ± 1.61	19.04 ± 1.55
-16	22.10 ± 2.00	20.99 ± 1.55	20.33 ± 1.52	22.10 ± 2.00	20.03 ± 1.63	19.69 ± 1.55

3.3.5 Dual activation point spread function analysis

For this analysis, CW, FD and CW&FD data types were used, at 141 MHz, 203 MHz and the combined 78, 141 and 203 MHz. For all data types and modulation frequencies, decreasing the separation increases the minimum value of the center of the recovery. This can be seen in figure 3.8, which shows that a smaller separation (c.) leads to a higher minima (d.).

Decreasing the separation to zero causes the minimum value to tend to 1 (i.e Not separated at all). At 141 MHz, FD has lower minimum values of the central minima than CW by about 25% at a separation of ± 15 mm. The combined CW&FD is 36% lower than CW. Increasing the modulation frequency to 203 MHz increases the resolving power. For FD, 3 dB separation is lost after a separation of ± 12 mm at 141 MHz, whereas at 203 MHz 3 dB separation is lost at ± 11 mm. This is a net 2 mm difference. The difference between FD and FD&CW is smaller than the difference between changing modulation frequencies. Therefore, increasing modulation frequency or even combining them yields the greatest increase in resolving power. For example, using CW&FD data at a separation of ± 12 mm, yields a separation of 0.59 at 141 MHz, 0.55 at 203 MHz and 0.49 at the three combined modulation frequencies. At ± 11 mm with CW&FD data, 3dB separation is not achieved at 141 MHz (0.72), but is with 203 MHz (0.69) and the combined frequencies (0.62).

At ± 10 mm, the minimum separation at 141 MHz and 203 MHz converges for CW, FD and CW&FD. There is only a 4.5% difference between CW (0.89) and CW&FD (0.85). However, at the three combined modulation frequencies, there is still a 14.6% difference between CW (0.89) and CW&FD (0.76). At ± 9 mm , this difference is a 6.25%. Only at a separation of ± 8 mm do the minimum values converge to 0.99. The full results can be seen in table 3.9 (141 MHz), table 3.10 (203 MHz) and table 3.11 (78 & 141 & 203 MHz).

Table 3.9: The minima values between the two PSF (Point Spread Functions) separations at 141 MHz. The two PSF's are at y = 0 mm, z = -15 mm and the x co-ordinates are given in row one. The recoveries are normalized so that the maximum is unity across a given modulation frequency.

x co-ordinates / ± mm	15	14	13	12	11	10
CW	0.4116	0.5010	0.5967	0.6966	0.7968	0.8907
FD	0.3013	0.3945	0.4986	0.6116	0.7303	0.8463
CW&FD	0.2649	0.3591	0.4681	0.5914	0.7255	0.8593

Table 3.10: As table 3.9 but at 203 MHz.

x co-ordinates / ± mm	15	14	13	12	11	10
CW	0.3864	0.4760	0.5729	0.6752	0.7791	0.8778
FD	0.2620	0.3538	0.4581	0.5739	0.6992	0.8265
CW&FD	0.2408	0.3315	0.4373	0.5583	0.6922	0.8308

Table 3.11: As table 3.9 but at the combined 78 & 141 & 203 MHz.

x co-ordinates / ± mm	15	14	13	12	11	10
CW	0.4116	0.5010	0.5967	0.6966	0.7968	0.8907
FD	0.1836	0.2727	0.3758	0.4922	0.6212	0.7582
CW&FD	0.1845	0.2716	0.3737	0.4916	0.6244	0.7667

For visual comparison, the minima values between the two PSF's at a separation of ± 15 mm at 141 MHz, 203 MHz and the combined 78 & 141 & 203 MHz can be seen in figure 3.22.

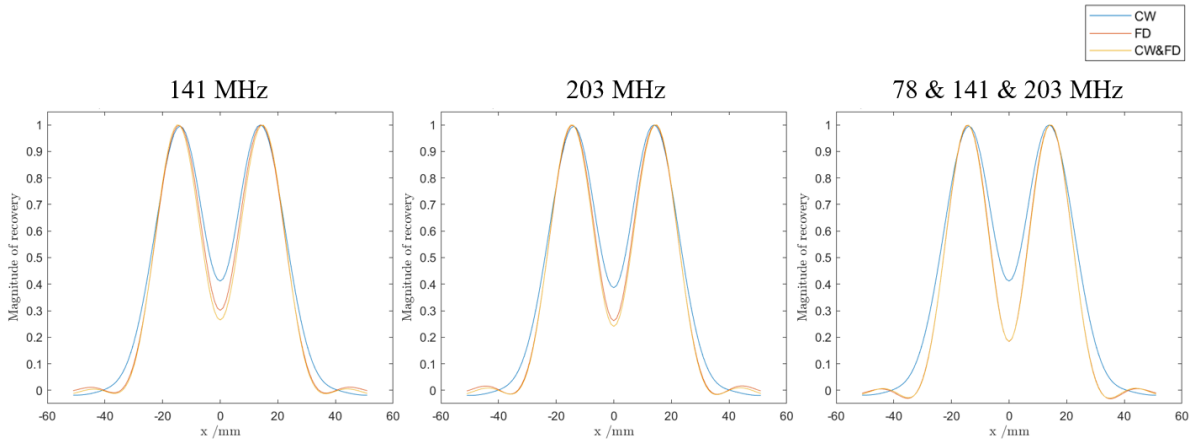

Figure 3.22: The minima values between the two PSF separations at 141 MHz, 203 MHz and the combined 78 & 141 & 203 MHz. The CW part of the data is at 141 MHz only. The two PSF's are at x = ± 15 mm y = 0 mm, z = -15 mm. The recoveries are normalized so that the maximum is unity across a given modulation frequency.

3.4 Discussions

This work shows that the combination of CW & FD data performs better than CW alone. This agrees with previous work done by Doulgerakis, Eggebrecht, and Dehghani, 2019, which demonstrated that the inclusion of FD data performs better than CW alone in HD-DOT. The data in figure 3.9 and table 3.3 show that for each performance metric, FD is between 5% to 12% better than CW alone. Building upon previous work, direct evaluation of a HD-DOT style grid is shown for the first time (figure 3.9) between CW, FD and CW&FD. Not only does CW&FD perform better than FD or CW alone in all metrics, but CW&FD provide more uniform recovery. This is demonstrated with lower standard deviations and visual artifacts around the edges of the FOV. As well as this CW&FD performs better as a function of depth in the cortex than CW or FD alone and has a better resolving power. This confirms that FD systems should utilise both CW and FD data for the best imaging performance.

The second focus of this study was looking at the effects of changing the modulation frequency of CW and FD measurements, which to date has not been evaluated for HD-DOT. The higher the modulation frequency, the better the imaging performance. This is demonstrated for all metrics for both CW and CW&FD data. The benefit of using higher modulation frequencies is smaller than combining CW and FD data. The biggest gain in performance is when using higher modulation frequencies and CW&FD data. This could be because a higher modulation frequency samples deeper into the model. Sensitivity matrices at 78 MHz, 141 MHz and 203 MHz show that there is increased sensitivity further away from the model surface at higher modulation frequencies, which is important for functional cerebral imaging, due to the thickness and effect of superficial tissue. This could also explain why there is an observed modulation frequency dependence on intensity data, which is contrary to the prior assumption that the intensity was independent of modulation frequency.

Another benefit of increased modulation frequency is that the change in measured phase for a given activation increases. For an activation at a depth of 15 mm, there is a 66% increase in the change of measured phase for NN1, between 78 MHz and 203 MHz. The same increase also occurs for 2^{nd} to 4^{th} Nearest Neighbour measurements (NN2-NN4). This is due to the deeper sensitivity of phase at higher modulation frequencies.

The biggest impact of this work is the effect of combining multiple modulation frequencies. For nearly all metrics, the best results came from combining FD measurements at different modulation frequencies (78 MHz, 141 MHz and 203 MHz) with a CW measurement at 141 MHz. It is expected that this is due to combining varying sensitivity profiles that different modulation frequencies have, which is the same reason why CW&FD performs better than CW or FD alone by providing additional sampling of tissue for a given source and detector pair. Due to the deeper sensitivity of phase data, combining measurements at different modulation frequencies essentially increases sensitivity away from the surface. Based upon this work, in vivo studies could take multiple phase measurements at different modulation frequencies and couple them with a CW measurement at a single (or multi) modulation frequency to perform HD-DOT with the highest accuracy.

For noise added data at 141 MHz, CW&FD outperforms FD and CW alone, table 3.3. However, the inclusion of noise causes the performance of FD data to decrease below that of CW alone. Combining the two data-types is a compromise between the two, where the better signal to noise ratio of CW data is complemented by the increased inherent contrast of FD data as shown in the noise free model. For the noise added data of the combined 78, 141 and 203 MHz respectively, the inclusion of three modulation frequencies increases the performance across the three metrics in table 3.5. The increased performance is due to the aforementioned reasons in noise free model. However, what is particularly important in the noise added data is the increased signal to noise ratio that three modulation frequencies can provide.

This study used four and three significant figures throughout the reporting of the mean and standard deviation values respectively for the performance metrics, which was chosen to to demonstrate the differences between data types and modulation frequencies. To address the appropriateness of these numbers of significant figures and the conclusions that can be drawn from the mean and standard deviations of the metrics (e.g table 3.3), violin plots were included. These plots allowed for the evaluation and comparison of the distribution of these metrics for different data types and modulation frequencies for sections 3.3.1, 3.3.2 and 3.3.3. In each section, it was discussed if there were statistically significant differences between the distributions of data types and modulation frequencies, by evaluating the non overlap of the 95% confidence intervals, as well as comparing the interquartile range of the metrics.

From evaluating the distributions of the LOCA, FWHM and ERES, it was consistently shown that the LOCA error had the smallest change in values across data types and modulation frequencies, which can be attributed to the fact that the LOCA is calculated from the euclidean distance between two data points in a 1 mm resolution FEM model, therefore differences in localisation accuracy are changing by the scale of the square root of integers on the order of ones. As well as this, whilst there were statistically significant differences when comparing data types and modulation frequencies, the distributions were shown to have overlap and similar shapes, combined with the smaller changes with the LOCA, which is why four significant figures had to be used across all the direct comparisons. The relative strengths and benefits reported in this study of FD and CW&FD compared to CW, or 141 MHz compared to the combined 78, 141 and 203 MHz are still valid, however they should be considered as another step towards higher accuracy tomographic imaging, rather than a generational leap forward such as the transition from sparse DOT to HD-DOT.

This study reports higher values for FWHM and ERES as compared to previous work such as White and Culver, 2010. For the HD grid, their CW data yields an average FWHM

of 12.10 mm and an ERES of 13.50 mm. At 141 MHz, this work has an average FWHM of 19.96 mm and an ERES of 21.64 mm. The reason why the FWHM and ERES are higher with this study is that metrics are formed at a deeper depth of -14 mm to -16 mm, whereas, in White and Culver 2010, their analysis is constrained to depths of -5 mm to -15 mm. Imaging performance becomes worse as a function of depth, as shown in Doulgerakis, Eggebrecht, and Dehghani, 2019. When the differences in depth are taken into account, the FWHM and ERES in this study become comparable to that in White and Culver 2010.

For imaging the cortex, the ERES for multi modulation frequency using CW&FD was 18.54 mm to 19.69 mm (-14 mm to -16 mm depth). This is still not as good as the resolution of fMRI, which is in the order of a few millimeters (Glover, 2011) to sub millimeter (Goense, Bohraus, and Logothetis, 2016). However, this work shows that the use of CW&FD measurements, along with combining multiple modulation frequencies can assist current fNIRS methods to gain maximum performance from the modality.

3.5 Conclusion

This work is consistent with previous studies showing that CW&FD data offers better imaging performance than CW alone as applied in fNIRS and HD-DOT. It has shown that CW&FD is better than FD alone, which in turn is better than CW alone. Using higher modulation frequencies for FD measurements cause an increase in performance. This also causes a higher SNR (Signal to Noise Ratio) for phase measurements at the expense of lower SNR for CW measurements. However, since phase data have a deeper sensitivity, this is preferable. Combining measurements at multiple modulation frequencies, mFD yields increased imaging performance, and from the simulated perturbations, this achieved the best image resolution and the best localization of point perturbations. The next step to realis-

ing the potential of FD and mFD measurements would be to use the combined CW&FD measurements with multiple modulation frequencies with real measurements, to see if the theoretical gain in performance translates to real life practice. In the context of functional brain imaging, sampling deeper in tissue is important so that changes in optical properties from the cortex are sampled more than those from superficial tissue. The next chapter in this thesis explores the history of mFD experiments and uses mFD measurements with HD-DOT on a phantom.

Chapter Four

Multi Frequency HD-DOT on the NeurOpt Phantom

During the first three chapters of this thesis, the theory and use of FD for brain imaging has been explained and discussed, alongside this the use of this field of imaging for assessing human brain health has been explored, particularly with a focus on traumatic brain injury. It has been established that there is opportunity for development of FD measurements, particularly in the use of phase data and combining modulation frequencies (mFD). The advantages of phase data have been studied by Doulgerakis, Eggebrecht, and Dehghani, 2019 where they established that phase samples deeper than intensity and is less sensitive to superficial tissue. It was then in the previous chapter, where the work of Perkins, Eggebrecht, and Dehghani, 2021 demonstrated that with simulations, that including phase data increased the resolution of HD-DOT and that by combining modulation frequencies during the image reconstruction led to the best performance in point perturbation localization and resolution of imaging. These simulated results are pertinent in the application of assessing brain health, because they lay out the starting point of a pathway that uses FD and mFD measurements to detect brain function, with higher spatial accuracy and more cortical influence than equivalent CW measurements.

This chapter builds upon the results from simulated data in the previous chapter that demonstrate the benefits of phase and mFD measurements and gives a comprehensive exploration into the field of mFD highlighting the need to perform HD-DOT with mFD measurements, which has not been done previously. The results and discussion from this chapter demonstrate and provide and platform for the importance and value of mFD measurements. As a note, for this chapter, the terms 'intensity' are used to describe the amplitude of the frequency domain signal, the 'phase' is the change in phase of the modulated light and correspond to the acronyms, CW, FD and mFD as denoted in table 4.1.

Table 4.1: The definitions of the acronyms CW, FD and mFD used in this chapter. For FD there is just one modulation frequency being used (ω_1), whereas for mFD there are three modulation frequencies being used together (ω_3). Here intensity is analogous to amplitude.

Chapter	**CW**	**FD**	**mFD**
4	Intensity	Intensity & Phase (ω_1)	Intensity & Phase (ω_3)

4.1 Multi modulation frequency studies

The current literature on the use of varying modulation frequencies can be categorised into three; simulation, data collected on a phantom and data collected in-vivo. Some studies have evaluated the use of a single modulation frequency at a time, whereas some combine and use multiple modulation frequencies simultaneously in image reconstruction, which will be referred to as multi-frequency FD (mFD). A summary of these studies can be found in Table 4.2 and will be outlined.

The use of different modulation frequencies in FD measurements was first reported by Patterson et al., 1991, they used single modulation frequencies across 10 MHz to 1000 MHz to spectroscopically recover the absorption and reduced scattering of a tissue mimicking phantom and building on this, similar work was done by Pham et al., 2000. Then Intes and Britton Chance, 2005 simulated the use of mFD-DOT (2D), using up to 13 simultaneous

modulation frequencies from 20 MHz to 500 MHz in 40 MHz increments. In their results, they found that using more than 7 frequencies yielded little additional benefit and modulation frequencies combined too close to each other would contain redundant information. The following year Burcin Unlu et al., 2006 performed mFD DOT on a cylindrical phantom using frequencies from 110 MHz to 280 MHz in 30 MHz increments. The higher number of combinations (total of 6) performed the best, followed by a combination of 3 frequencies (110 MHz + 200 MHz + 260 MHz), then 2 (110 MHz + 260 MHz) and then 200 MHz alone. Also in 2006, (Gulsen et al., 2006) used spectral (665 nm, 785 nm , 808 nm and 830 nm) mFD-DOT measurements on the same phantom to perform similar mFD-DOT analysis.

The first use of clinical mFD measurements was by (Hornung et al., 2011), where they used mFD measurements on 13 patients, imaging the uterine cervix during regular pregnancies to obtain physiological information (HbO, HbR and oxygen tissue saturation). To date, this appears to be the only use of mFD measurements in a clinical setting for imaging HbO and HbR, and no studies have used mFD for in-vivo human brain imaging. However, another use of mFD measurements were performed by Chung et al., 2012 for breast cancer imaging by using a range of frequencies between 50 MHz to 400 MHz to reconstruct for pure water content.

Since 2010, only one mFD study has included real data and the rest have been simulations. C. Chen et al., 2015 simulated the first use of HD-DOT on a 2D circular model, using frequencies between 100 MHz to 250 MHz in 50 MHz increments, as well as a new clustered sparsity reconstruction method to reconstruct absorption and reduced scattering coefficients simultaneously. They used 15 combinations of frequencies and found that the best imaging performance was from the combination of all four modulation frequencies. Then Mudeng, Nisa, and Sukmananda Suprapto, 2022 and Shifa, Sayem, and Islam, 2021 also simulated HD-DOT on a 2D circular model, using 3 frequencies, 100 MHz, 150 MHz and 200 MHz and found that mFD measurements of 100 MHz + 150 MHz and 100 MHz + 150 MHz + 200

MHz performed similarly to that of 200 MHz alone. Shifa, Sayem, and Islam, 2021 used frequencies between 100 MHz to 1000 MHz, however they only analysed up to 700 MHz. They found that the best tomographic reconstructions came from the combination of 100 MHz increments from 200 MHz to 700 MHz, however they assumed the same level of noise (20dB) for all modulation frequencies, which is a limitation of the study, as there is no penalty for the additional information content.

Perkins, Eggebrecht, and Dehghani, 2021 was the first study to simulate mFD-HD-DOT on a 3D model, using a cuboid 3 layered (skin/scalp, gray matter, white matter) and frequencies of 78 MHz, 141 MHz and 203 MHz, as available from a commercial system, the ISS Imagent. Focal activation were simulated and the use of intensity vs phase vs intensity & phase combined data, at the three modulation frequencies were compared. To evaluate the relative performances, the localization error of activations, full width half maximum error and effective resolution were used as metrics (White and Culver, 2010). The most accurate reconstructions of absorption coefficient came from when intensity data at 141 MHz was combined with phase data at 78 MHz + 141 MHz + 203 MHz, both in the case of no noise and noise-added data. Phase data performed better than intensity in the no noise case, but became worse than intensity in the presence of noise. However, the combination of intensity and phase with noise was better than intensity with noise alone.

The final two simulation studies also in 2021 were from deJong et al., 2021 and Fan, Dehghani, and Eggebrecht, 2021, where they both use 3D atlas models of the human adult head for HD-DOT, with Fan using 5 different head models. Fan uses 11 frequencies between 0 to 1000 MHz and found that without noise 700 MHz gave the most accurate localization of brain activations and 1000 MHz the lowest full width half maximum error in reconstruction of optical properties. The inclusion of noise and when including nearest neighbour 3 and 4 measurements respectively, 300 MHz performed the best. deJong et al., 2021 uses single value decomposition of the Jacobians (Sensitivity mapping function) of intensity and phase,

of single and combined frequencies between 100 MHz to 600 MHz in increments of 100 MHz to evaluate which combinations hold the most information content. Using this analysis and evaluating the localization of brain activation and the full width half maximum error, the combination of 500 MHz + 600 MHz performed the best. Finally towards the end of 2021, Stillwell et al., 2021 created a real time broadband mFD system that uses 6 wavelengths between 690 nm and 830 nm with modulation frequencies from 0 to 400 MHz in increments of 0.1 MHz. They performed system characterisation and calibration of the device using a block phantom with a simulated tumour inclusion 1 mm below the surface of 10 mm to 30 mm diameter. Then they took measurements on tissue to perform high speed quantification of hemodynamics by virtue of 2D spatial topographic mapping. They performed in-vivo arterial occlusion measurements by placing a blood pressure cuff on the upper arm of a healthy volunteer. This was the first demonstration of real time multi wavelength broadband mFD measurements and paves the way for further mFD studies in a research and clinical research setting.

Table 4.2: A table containing a summary of research within mFD measurements. The studies are ordered and categorized into simulations (Sim.), data collected on a phantom (Phant.) and then data collected in-vivo. Within the categories, studies are ordered by year from oldest to most recent. The geometry of the measurement is summarized, the range and number of wavelengths used (n/a means a single value of μ_a, μ_s' was used, $\lambda(N)$), as well as the range of modulation frequencies and number of frequencies (N) used in image reconstruction at a time. Then if the study reports absorption and/or scattering parameters and finally the type of output of the reconstructed data. Information about the exact modulation frequencies used and the full studies can be found with the corresponding references in table 4.3.

Ref.	**Data**	**Geometry**	λ **/nm (N)**	ω **/ MHz (N)**	$\Delta\mu_a/\mu_s'$	**Output**
1	Sim.	Slab	n/a	20-500 (7)	Both	2D DOT
2	Sim.	Circle	n/a	100-250 (4)	Both	HD-DOT
3	Sim.	Head	n/a	0-600 (2)	$\Delta\mu_a$	3D HD-DOT
4	Sim.	Head	690-850 (2)	0-1000 (1)	$\Delta\mu_a$	3D HD-DOT
5	Sim.	Circle	n/a	100-200 (3)	Both	2D HD-DOT
6	Sim.	Cuboid	n/a	78-203 (3)	$\Delta\mu_a$	3D HD-DOT
7	Sim.	Circle	n/a	100-1000 (5)	Both	2D HD-DOT
8	Phant.	Cylinder	755 (1)	10-1000 (1)	Both	2D NIRS
9	Phant.	Cylinder	674-956 (4)	0-1000 (1)	Both	2D NIRS
10	Phant.	Cylinder	665-830 (4)	110-280 (6)	Both	3D DOT
11	Phant.	Cylinder	665-830 (4)	110-280 (6)	Both	3D DOT
12	Phant.	Cylinder	690-980 (6)	50-300 (35)	Both	2D HD-DOT
12	In-Vivo	Arm	689-850 (2)	50-300 (35)	Both	2D NIRS
13	In-Vivo	Cervix	690-970 (7)	130-490 (36)	Both	2D NIRS

Table 4.3: The corresponding references from column 1 of table 4.2.

Ref.	**Reference**
1	Intes and Britton Chance, 2005
2	C. Chen et al., 2015
3	deJong et al., 2021
4	Fan, Dehghani, and Eggebrecht, 2021
5	Mudeng, Nisa, and Sukmananda Suprapto, 2022
6	Perkins, Eggebrecht, and Dehghani, 2021
7	Shifa, Sayem, and Islam, 2021
8	Patterson et al., 1991
9	Pham et al., 2000
10	Burcin Unlu et al., 2006
11	Gulsen et al., 2006
12	Stillwell et al., 2021
13	Hornung et al., 2011

Following from the studies described in Table 4.2, this study will be the first to use real mFD HD-DOT measurements to reconstruct parameters in 3D. Previous studies have either been single frequency 2D NIRS (Patterson et al., 1991 and Pham et al., 2000), or mFD-DOT (Burcin Unlu et al., 2006 and Gulsen et al., 2006) and not mFD-HD-DOT. The significant performance increase, and therefore importance of 'high density' DOT compared to non 'high density' measurements have been shown (White and Culver, 2010) and used in-vivo for mapping of distributed brain function (Eggebrecht et al., 2014). As well as this, Burcin Unlu et al., 2006 and Gulsen et al., 2006 perform their measurements on circular phantoms, having sources and detectors around the entire perimeter of the phantom. This study will use source and detectors on one surface of a cuboid block phantom, which represents a more realistic (in-vivo human brain imaging) use case.

Quantitative evaluations of how mFD-HD-DOT measurements perform have only been simulated Perkins, Eggebrecht, and Dehghani, 2021, deJong et al., 2021 and Fan, Dehghani, and Eggebrecht, 2021, so evaluating the performance of mFD on a phantom will eliminate factors which can effect the measurement outside of type of data itself, such as poor source-detector coupling and instrumental noise. As well as this, it allows for flexibility in the processing of data and methods for image reconstruction, due to the simple geometry and stable measurements on a phantom. Three modulation frequencies will be used of 78.125 (78) MHz, 140.625 (141) MHz and 203.125 (203) MHz, which are the same as the simulated mFD-HD-DOT evaluation as seen in Perkins, Eggebrecht, and Dehghani, 2021. The use of 3 frequencies is more than sufficient to observe the benefits of mFD and the difference between the 3 frequencies is such that there is a sufficient difference in data between the frequencies Intes and Britton Chance, 2005,Burcin Unlu et al., 2006, C. Chen et al., 2015 and Mudeng, Nisa, and Sukmananda Suprapto, 2022.

Whilst the most common approach for image reconstruction in HD-DOT/DOT is a single linear iteration in parameter recovery, this study will also investigate the use of an

iterative approach for image reconstruction, so that the relative performance of mFD v.s FD v.s CW can be assessed in both the single iteration and iterative reconstruction case.

4.2 Methods

4.2.1 Experimental Protocol

A mechanically switchable solid inhomogeneous phantom was used for data collection and detailed information about the phantom can be found elsewhere (Pifferi et al., 2015). The bulk properties of the phantom at 830 nm are $\mu_a = 0.01$ mm^{-1} and $\mu_s' = 0.7$ mm^{-1}. The phantom consists of a homogeneous 3D geometry, with a cylindrical hole running across it. The center of the hole is at 15 mm from the surface of the phantom and allows a rod to be inserted into it. The rod is inhomogenous as it contains a small cylindrical anomaly, made of black polyvinyl chloride (pvc), which causes it to act as a contrast as compared to the rest of the cylinder, which is made of the same material as the rest of the phantom. The rod can be moved across the phantom, and hence the position of the contrast anomaly can be changed. For reference, the optical properties of contrast anomaly are given in Table 4.4, these are for a μ_s' of approximately 1 mm^{-1}, which holds true around 700 nm.

Table 4.4: The dimensions of the contrast anomalys within each rod used (Pifferi et al., 2015). Rod N has a diameter of N mm and length N mm. The equivalent $\Delta\mu_a$ is for a μ_s' of approximately 1 mm^{-1}, which holds true around 700 nm and is derived using the equivalence relation (Martelli et al., 2013) and an inclusion of 10 mm^3.

Diameter / mm	**Length / mm**	**Volume / mm^3**	**Equivalent $\Delta\mu_a$ / mm $^{-1}$**
3	3	21	0.005
5	5	98	0.017
7	7	269	0.040

In order to take measurements on the phantom using the ISS Imagent (ISS, Champaign, IL, USA), a 3D printed cap was created for the phantom. The creation of the cap and the accompanying mounts can be seen in figure 4.1. Figure 4.1 A. shows the NeurOpt Phantom, and then a 3D scan is taken of the phantom using a 3D camera, called the Artec Leo (Artec3D, Luxembourg) and this scan is loaded onto Autodesk Meshmixer (Autodesk, CA, USA), figure 4.1 B. The 3D model of the phantom is then cropped such that the geometry of the model can sit on top of the phantom, and then holes of 11.1 mm diameter are created on top of the cap, figure 4.1 C. The arrangement of these holes, and hence source-detector locations are discussed in figure 4.2. Then cylindrical mounts were created in order to house and support the source and detector fibers, and these were printed separately to the phantom cap. The outer diameter of the cylinder was 11.09 mm as to fit in the holes on top of then phantom cap and the inner diameter was 9.98 mm in order to hold the source and detector fibers, and the height of the mounts was 30.0 mm, figure 4.2 D. Then, the cap was placed on the phantom with the mounts inserted into the holes, with the source and detector fibers pushed into the mounts so they were sat flush on top of the phantom. Plastic pipette tips were then used to keep the fibers taught within the mounts, to enable good fiber coupling to the surface of the phantom, figure 4.2 E.

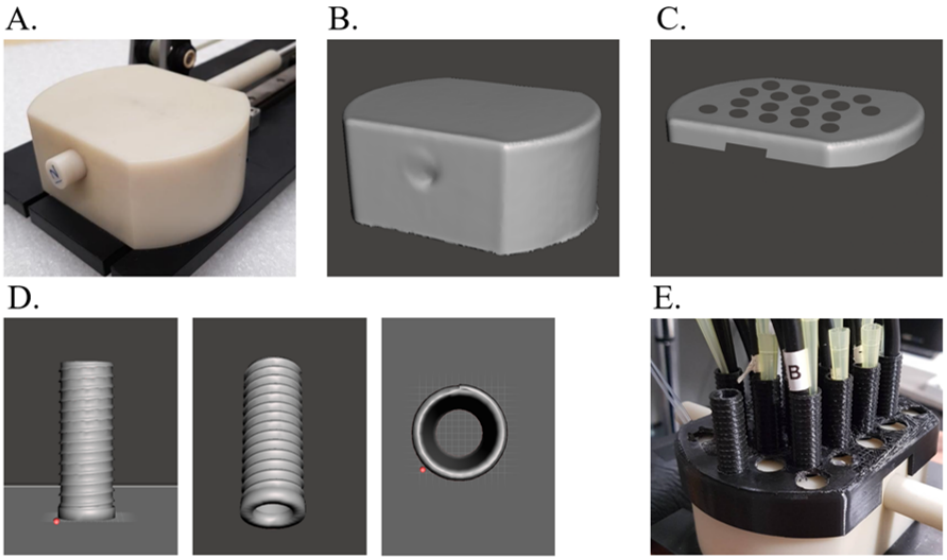

Figure 4.1: A. The NuerOpt Phantom. B. A 3D optical camera scan of the NuerOpt Phantom, loaded into Autodesk Meshmixer. C. The cropped scan forming the cap, with holes on top of the cap to allow source-detector mounts to go through. D. The creation of the source-detector mounts. E. The NuerOpt Phantom with the 3D printed cap, mounts and source-detector fibers on top.

Measurements were taken using the ISS Imagent (ISS, Champaign, IL, USA). Six sources and twelve detectors were placed in a high density array (Gibson et al., 2006; Zeff et al., 2007) on top of the phantom via a 3D printed cap. Each source emits light at 830 nm and 690 nm. The light emitted is sinusoidally modulated and measurements were taken at 78 MHz, 141 MHz and 203 MHz. Measurements were sampled at 39.73 Hz. The array of sources and detectors were centered about the middle of the phantom. This created five nearest neighbour (NN) measurements respectively of 13 mm (NN1), 29 mm (NN2), 39 mm (NN3), 46 mm (NN4) and 53.64 mm (NN5). Only measurements of NN1 (24 channels) and NN2 (28 channels) were used for image reconstruction, as measurements of NN3 to NN5 were deemed to have a too low signal to noise ratio. The source detector set up can be seen in Figure 4.2A and B. The array of detectors on the 3D printed cap can be seen in Figure 4.2C. Figure 4.2D shows for a given measurement, how the log intensity changes as a function of source-detector separation. Here there is a linear decrease in log intensity,

with discrete groups of log intensity corresponding to NN1-5. This measurement was made with the reference rod inserted into the phantom, i.e no contrast was present. It should be noted that the AC amplitude was used for the 'CW' data because the AC amplitude is less susceptible to external light contamination than the DC amplitude typically used in CW experiments. Whilst the AC and DC intensity behave similarly, they are not the exact same.

There is no exact definition of what classifies as a 'high density' arrangement of sources and detectors, although a study by Tian, Alexandrakis, and Liu, 2009 used various numbers of source-detector densities and found that image reconstruction quality in DOT did not improve after increasing the number of overlapping measurements for a given surface area past three, which this study uses. This study does not include measurements above NN2 (29 mm) separation, since data of NN3 and NN4 do not have sufficient signal to noise ratio, however this is in line with previous high density studies, for example White and Culver, 2010 evaluated 'high density' DOT using only up to NN2 (29 mm) measurements in their high density array.

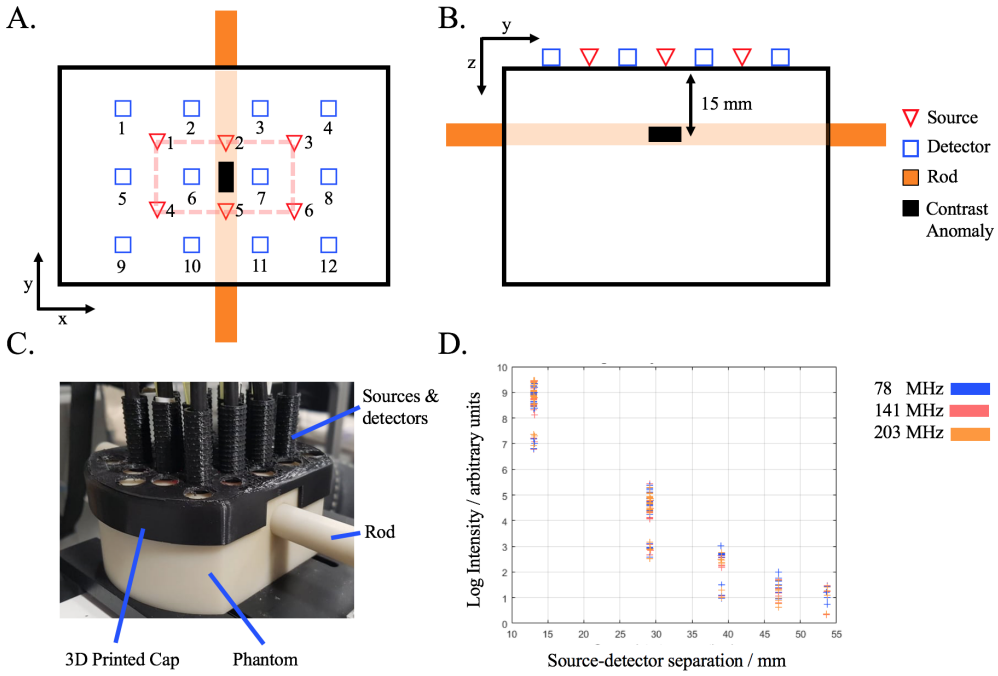

Figure 4.2: A. (z plane) and B. (x plane) A schematic diagram of the source-detector placement on top of the phantom, as well as the orientation of the movable rod which contains the contrast anomaly. For contrast anomaly measurements, the anomaly is centred at x = y = 0 mm and z = -15 mm. C. A photo of the phantom with the rod inserted. The sources and detectors are placed on the phantom using a 3d printed cap. D. A graph showing the log of the intensity as a function of source-detector separation at three modulation frequencies.

To obtain a measurement, a contrast rod was inserted into the phantom. The rod was positioned such that the contrast anomaly was positioned outside the phantom. Then, a minimum of 1000 frames (time points) were recorded, then the rod was moved such that the contrast was at the centre of the phantom (X = 0 mm, Y = 0 mm, Z = -15 mm) and a further minimum of a 1000 frames were recorded. Finally the rod was moved back to its original position to collect a minimum of another 1000 frames. This process was repeated for each contrast rod (rod 3, 5 and 7) and for each modulation frequency (78 MHz, 141 MHz, 203 MHz), so that there were nine measurements in total, each comprising of a minimum of 3000 frames of data (approximately 75 s).

In order to account for low frequency system drift, the medians of the reference mea-

surement before and after the contrast measurement were used as the baseline measurement. Then the median of the contrast measurement was used with the baseline measurement for image reconstruction. This was done so that the change in the signal due to the contrast anomaly would not be increased or decreased by a frequency filter. For example using a high pass filter effected the change in data due to the contrast anomaly.

4.2.2 Data analysis

In the following sets of equations, $\oslash$ denotes the Hadamard piecewise matrix division operator, and $\circ$ denotes the Hadamard piecewise matrix multiplication operator, otherwise standard matrix algebra applies. All variables represent matrices, unless explicitly defined as scalar values. To perform tomographic reconstructions of the spatial distribution of absorption coefficient, a mapping function, or Jacobian (J) (sometimes called the sensitivity or A matrix) is used to transform changes in measured data (∂Y) to changes in optical properties (∂X) of the medium, which is given in Eq. (4.1),

$$\partial Y = J\partial X \quad . \tag{4.1}$$

The explanation and background of Eq. (4.1) has been detailed previously (Perkins, Eggebrecht, and Dehghani, 2021 and Dehghani, Eames, et al., 2009). For this study, the measurements were calibrated (Dehghani, Pogue, et al., 2003) using modelled data from an finite element model (FEM) of the phantom. Model data was generated using the forward model of photon propagation in NIRFAST (Dehghani, Eames, et al., 2009). The experimental datum from the reference measurement is given by Y_{ref} and from the contrast anomaly $Y_{anomaly}$. The model data from NIRFAST is Y_{fem}, with the calibration factors being scaling factors for intensity (I) and offset for phase (ϕ), I_{SC} and ϕ_{OFF} respectively, and are given in

Eq. (4.2) and (4.3), where $\oslash$ is element wise division and $\circ$ is element wise multiplication,

$$I_{SC} = Y_{Ifem} \oslash Y_{Iref} \tag{4.2}$$

$$\phi_{OFF} = Y_{\phi fem} - Y_{\phi ref} \quad . \tag{4.3}$$

Using Eq. (4.2) and (4.3), the scaled changes in measured data, intensity (∂Y_I) and phase (∂Y_ϕ), due to the contrast anomaly are shown in Eq. (4.4) and (4.5),

$$\partial Y_I = log((Y_{Ianomaly} \circ I_{SC})/Y_{Ifem}) \tag{4.4}$$

$$\partial Y_\phi = (Y_{\phi anomaly} + \phi_{OFF}) - Y_{\phi fem} \quad . \tag{4.5}$$

From these changes in measured data ($\partial Y_{I,\phi}$) and using Eq. (4.1), the inverse of the Jacobian can be approximated (J_p) using the Moore-Penrose pseudoinverse (Penrose, 1955) ($J_p^\#$) and Tikhonov regularization to calculate the changes in optical properties of the phantom, ∂X. This is shown in Eq. (4.6),

$$\partial X = J_p^\# \partial Y_{I,\phi} \quad . \tag{4.6}$$

For CW data, the intensity data at 141 MHz is used, FD data, the intensity and phase at 141 MHz are stacked in the Y and J matrix, and for mFD data, intensity at 141 MHz is used with phase data at 78 MHz + 141 MHz + 203 MHz.

The reason why intensity data at multiple modulation frequencies was not in the mFD data type was that it has been shown that there is an appreciable increase in the sampling depth of phase data for increasing modulation frequencies, but that the change in sampling depth with intensity data is very small (Fan, Dehghani, and Eggebrecht, 2021), so it was decided that only additional phases would be used in the mFD data.

The structure of the data and the Jacobians for CW and FD can be seen in Eq. (4.7) and for mFD in Eq. (4.8),

$$Y_{CW} = \begin{bmatrix} I_{141} \end{bmatrix} \quad J_{CW} = \begin{bmatrix} J_{I141} \end{bmatrix} \quad Y_{FD} = \begin{bmatrix} I_{141} \\ \phi_{141} \end{bmatrix} \quad J_{FD} = \begin{bmatrix} J_{I141} \\ J_{\phi 141} \end{bmatrix} \tag{4.7}$$

$$Y_{mFD} = \begin{bmatrix} I_{141} \\ \phi_{78} \\ \phi_{141} \\ \phi_{203} \end{bmatrix} \quad J_{mFD} = \begin{bmatrix} J_{I141} \\ J_{\phi 78} \\ J_{\phi 141} \\ J_{\phi 203} \end{bmatrix} \quad . \tag{4.8}$$

Voxel and data normalization of the Jacobian are also applied prior to inversion, to allow scaling the depth sensitivity in the image reconstruction. The regularisation parameter is used to tune the balance between smoothing and over-fitting of a solution. A normalization parameter, β (scalar) and the regularization parameter, λ (scalar) are both set to 0.01. These values are chosen empirically and have been used in prior studies (White and Culver, 2010; Perkins, Eggebrecht, and Dehghani, 2021).

Voxel normalization of the Jacobian is applied to each column of J, denoted by

J(columns) by Eq. (4.9),

$$J(columns) = J_p \oslash \sqrt{L_V + \beta * max(L_V)} \tag{4.9}$$

where $L_V = \Sigma J^2_{voxel}$ (sum of columns in the Jacobian and each column represents a unique voxel), and data normalization is applied to each row of J, denoted by J(rows) by Eq. (4.10),

$$J(rows) = J_p \oslash M \tag{4.10}$$

where $M = \sqrt{L_D + \beta * max(L_D)}$ and $L_D = \Sigma J^2_{data}$ (sum of rows in the Jacobian and each row represents a unique source-detector channel). Then, Tikhonov regularisation is applied during the tomographic reconstruction which gives the change in optical properties of the phantom shown in Eq. (4.11),

$$\partial X = J^T \left(\frac{\partial Y_{I\phi} \oslash M}{(H + R)} \right) \oslash L_V^T \tag{4.11}$$

where the superscript ^{T} denotes the matrix is transposed, J is the normalized Jacobian of the phantom, H is the Hessian which is, $H = JJ^T$, R is the regularisation term, $R = \mathbb{1}\lambda * max(diag(H))$ (* is multiplication) and $\mathbb{1}$ is the identity matrix. For iterative image reconstruction, Eq. (5.8, 5.9 and 5.10) are applied for every iteration and λ has a starting value of $\lambda = 1000$ and decreases by a factor of $10^{0.2}$ at each iteration. In this work, only μ_a reconstructed images are shown.

To evaluate the performance of the image reconstructions, three evaluation metrics are calculated and used. These are the localisation error (LOCA), the full width half maximum

error (FWHM) and the effective resolution (ERES). The metrics were chosen from their use in previous related studies (White and Culver, 2010 and Perkins, Eggebrecht, and Dehghani, 2021) and are explained in chapter 3 and are visualized in figure 4.3.

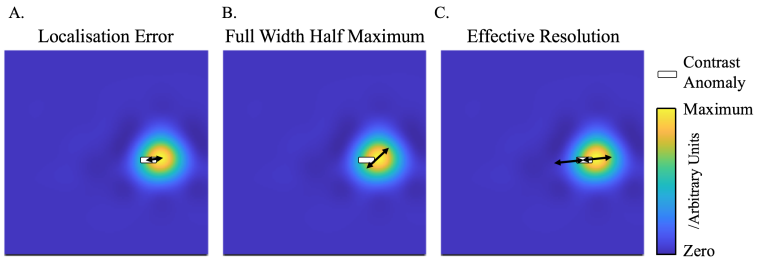

Figure 4.3: A diagram of how each performance metricWhite and Culver, 2010 Perkins, Eggebrecht, and Dehghani, 2021 is calculated. A. The LOCA is given by the distance between the centre of the contrast anomaly and the maximum recovery of absorption coefficient in the reconstructed image. B. The FWHM is given by the maximum distance between any two nodes that are more than or equal to 50% of the maximum of the reconstructed image. C. The ERES is twice the maximum distance between the centre of the contrast anomaly and any node that is more than or equal to 50% of the maximum of the reconstructed image.

To constrain the effect of artifacts in the reconstructed images, spatial constraints are applied to the four evaluation metrics. Only nodes within ± 13.8 mm in the x axis, ± 9.2 mm in the y axis and below -10 mm in the z axis in the phantom are considered for metric evaluation. The constraints in the x and y axis are half the field of view (FOV) of the source-detector placement and are outlined by solid black lines in the results.

4.3 Results

To contextualise the results of the tomographic reconstructions of absorption coefficient, typical measurements are shown in Figure 4.4. They display the reference measurement, followed by the contrast anomaly being moved into the middle of the phantom and then a reference measurement. This is evident by the decrease in intensity and phase respectively. The measurements are shown at the three modulation frequencies used at 830 nm and

are normalised by the mean of the reference measurement. Each modulation frequency had a separate measurement (Figure 4.4B) , which caused small variations in the length of measurement, however a minimum number of frames (1000) were always taken for the contrast anomaly and with the median values used for data analysis.

The statistics of the data formulated in Figure 4.4 are presented in Figure 4.5, which shows the standard deviation of the reference measurement and the contrast induced from the contrast anomaly. Box plots of these data are shown in Figure 4.6 for the intensity and Figure 4.7 for the phase. For NN1 measurements, as the modulation frequency increases, the standard deviation of data increases for log intensity and phase and for NN2 the standard deviation is minimum at 141 MHz. The contrast decreases for log intensity at NN1 and NN2 as the modulation frequency increases, and for phase the opposite is true.

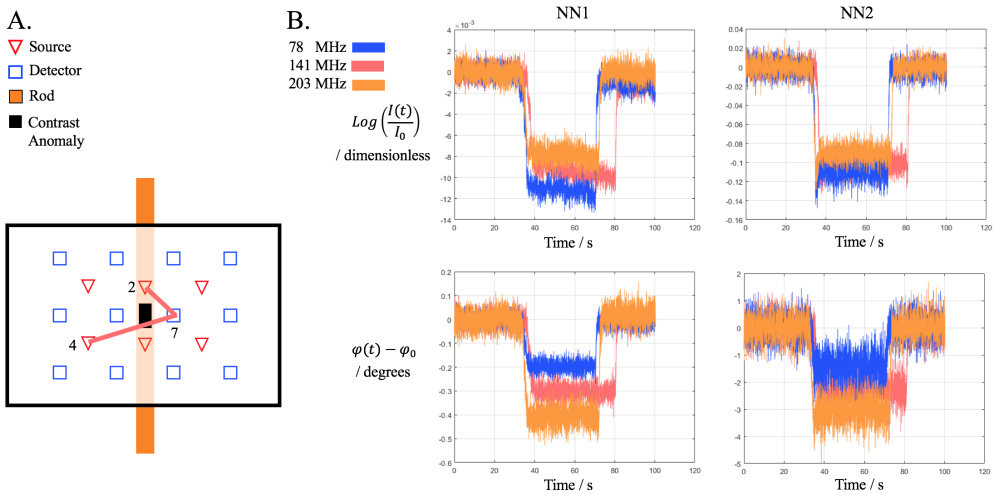

Figure 4.4: A. A schematic of which source-detector pairs are used for the data shown in Figure 4.4B. B. Log Intensity and Phase measurements of the reference rod volume and contrast anomaly of rod 7. NN1 measurement is between Source 2-Detector 7 of 13 mm separation and NN2 measurement is between Source 4-Detector 7 of 29 mm separation.

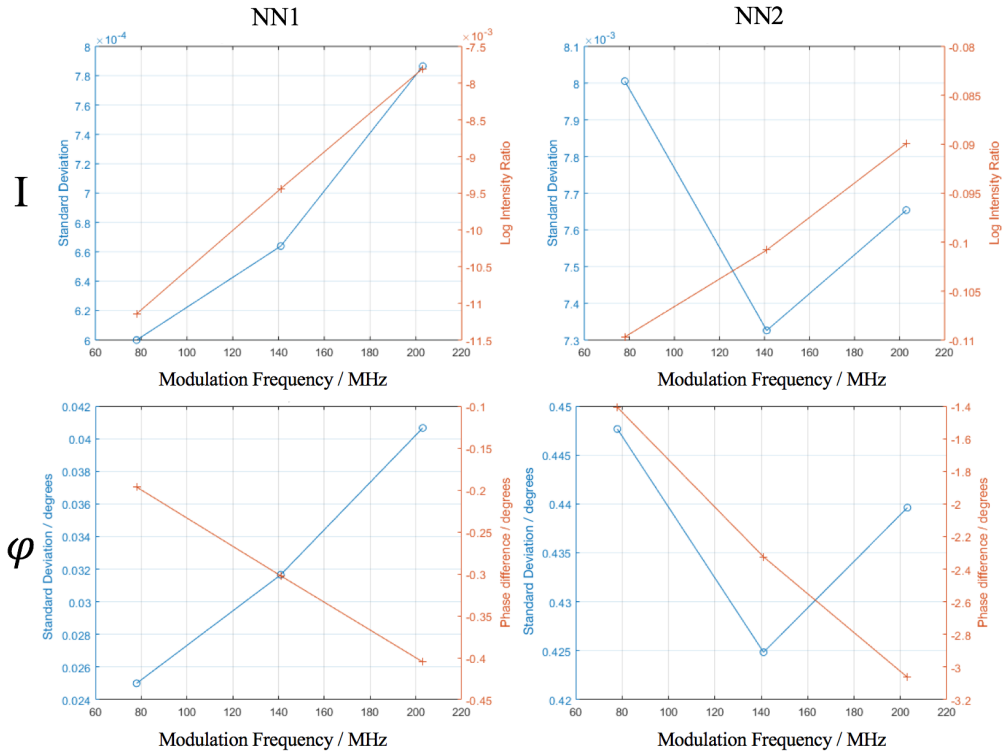

Figure 4.5: The standard deviation (left y-axis, circle ticks) and contrast (right y-axis, cross ticks) of the measurements shown in Figure 4.4. The standard deviation is that of the reference measurement. For intensity the contrast is the log ratio of the mean anomaly measurement to the mean reference measurement and is dimensionless. For phase, the contrast is the difference between the mean anomaly measurement and the mean reference measurement.

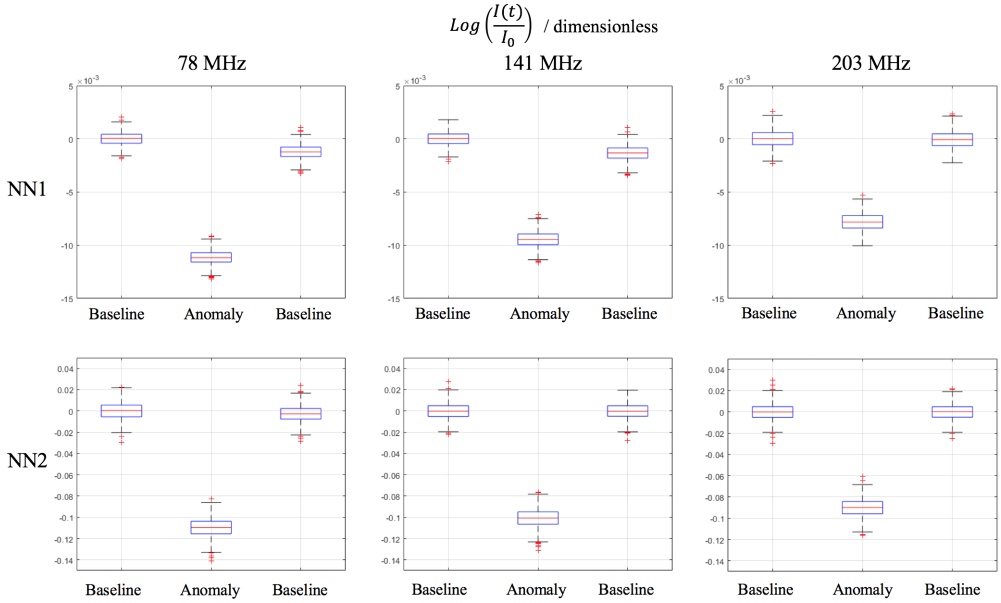

Figure 4.6: Box plots of the log ratio of intensity data of the reference rod (I_0) volume and contrast anomaly ($I(t)$) of rod 7. NN1 measurement is between Source 2-Detector 7 of 13 mm separation and NN2 measurement is between Source 4-Detector 7 of 29 mm separation. Measurements are shown at the three modulation frequencies, 78 MHz, 141 MHz and 203 MHz.

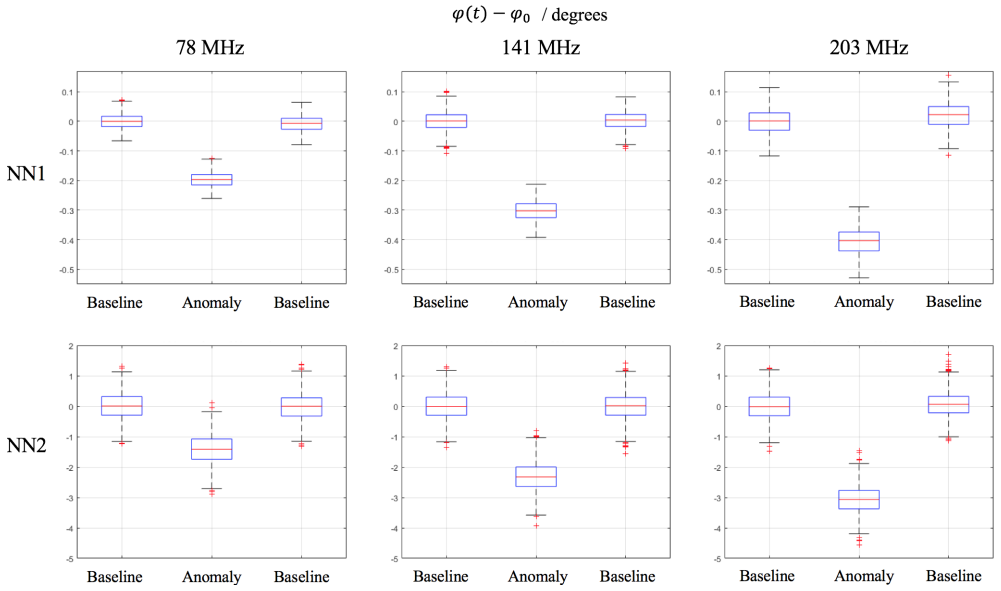

Figure 4.7: Box plots of the difference of phase data of the reference rod (ϕ_0) volume and contrast anomaly ($\phi(t)$) of rod 7. NN1 measurement is between Source 2-Detector 7 of 13 mm separation and NN2 measurement is between Source 4-Detector 7 of 29 mm separation. Measurements are shown at the three modulation frequencies, 78 MHz, 141 MHz and 203 MHz.

4.3.1 Single iteration reconstruction

The tomographic image reconstructions using a single iteration are shown in Figure 4.8, where each row shows contrast rod 3, 5 and 7 and each column shows the image reconstruction using CW data, FD data and mFD data. For each rod, a different colourbar scale was used but was the same for the different data types for a given rod. The first thing to note is that using NN1 and NN2 measurements, all data types reconstruct the contrast anomaly in approximately the correct location for all rods. Across all of the rods, the magnitude of the reconstructed absorption coefficient is higher using the FD and mFD data as compared to the CW data, which can be visibly seen. The maximum value of the reconstructed absorption coefficient also increases as the volume of the contrast anomaly increases, which can be seen in Table 4.5.

Table 4.5: A table showing the maximum values of the reconstructed absorption coefficient from the single iteration reconstructions seen in Figure 4.8.

Rod N	max μ_a (CW) /mm^{-1}	max μ_a (FD) /mm^{-1}	max μ_a (mFD) /mm^{-1}
3	0.078	0.227	0.254
5	0.098	0.294	0.331
7	0.227	0.653	0.689

There are artifacts present in all image reconstructions. Using the CW data, these artefacts appear to be prominent in the plane of the z axis, with a blurring in the reconstructed image seen from the surface down to the contrast anomaly. Whereas for the FD and mFD data, the artefacts in the Z direction are that of negative contrast and there is some small positive contrast blurring in the x and y directions.

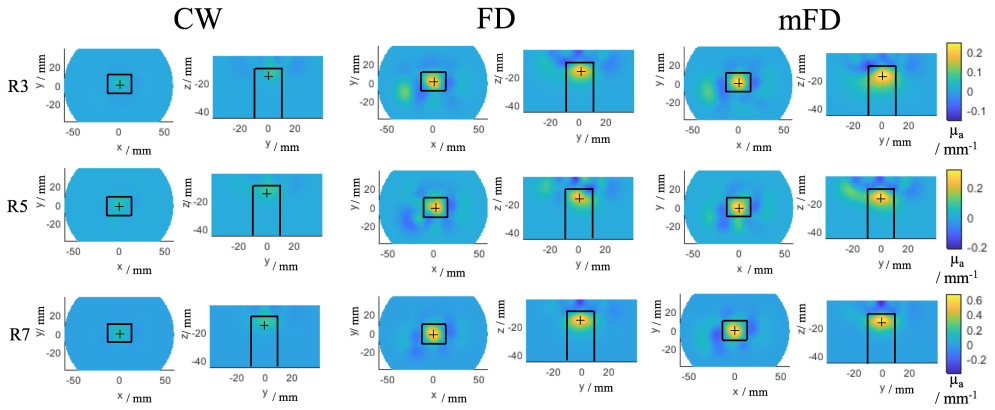

Figure 4.8: Single step tomographic reconstructions from rod 3, 5 and 7 (R3, 5 and 7 respectively) using CW, FD and mFD data respectively at 830 nm. For each reconstructed image, two views are shown, firstly the z plane at z = -15 mm and secondly the x plane at x = 0 mm. The colour bar scales are the same for each given rod. The solid black lines indicate the spatial constraints of the imaging metrics.

The image performance metrics are shown in Table 4.6, which correspond to the reconstructed images shown in Figure 4.8. Across all of the rods, the best LOCA is seen by using the mFD data and this general localisation performance can be observed when looking at the co-ordinates of the maximum value of absorption coefficient of the reconstructed image. Generally the maximum of the mFD and FD reconstructions are at z = - 14.5 or -15.5 mm, whereas the CW data is at z = - 11.5 mm or - 12.5 mm. The z axis error accounts for most of the differences in LOCA, however the mFD data also is more accurate in the x and y axis, with the average (x,y) co-ordinates being (0.33,1.00) mm , compared to (1.96,0.87) mm for FD and (1.30,1.89) mm for CW. The FWHM and ERES are more variable between the three data types. On average, CW data offers the best FWHM of 15.45 mm, whereas FD and mFD have an FWHM of 16.40 mm and 16.42 mm respectively. For the ERES, on average mFD (17.99 mm) performs better than FD (18.20 mm), which in turn is better than CW (19.83 mm).

Table 4.6: The evaluation metrics, the LOCA, FWHM and ERES shown for rod 3, 5 and 7 using CW, FD and mFD data respectively. These are from the reconstructed images shown in Figure 4.8, using a single iteration for image reconstruction.

Rod N	**Metric / mm**	**CW**	**FD**	**mFD**
3	LOCA	4.12	2.35	**2.20**
3	FWHM	**13.81**	15.58	16.60
3	ERES	20.31	**16.82**	18.53
5	LOCA	4.51	2.35	**0.81**
5	FWHM	16.36	17.46	**15.47**
5	ERES	19.59	20.16	**17.14**
7	LOCA	3.83	2.50	**0.81**
7	FWHM	16.19	**16.18**	17.19
7	ERES	19.59	**17.64**	18.30

4.3.2 Iterative reconstruction

The number of iterations were determined by a stopping condition, which was when each data type scored the lowest FWHM and ERES, which was the iteration before the lowest difference between the measured difference data and the forward model generated data. For CW data this was for eight iterations, for FD data this was for six iterations and for mFD data this was for four iterations. This means that the highest number of iterations and therefore the same amount of regularisation applied to each data type are four iterations, which are shown in Table 4.7 and Figure 4.9. The results from the highest number of iterations for each data type are shown in Table 4.8 and Figure 4.10.

For N = 4 iterative reconstructions of absorption coefficient the images are visually smoother as compared to single step reconstructions. Each reconstructed image shown is after four iterations and the colourbars are the same for each data type for a given rod. Similar to the single step iterations in Figure 4.8, the CW data shows positive artifacts in the z axis above the contrast anomaly, whereas the FD and mFD data shows negative contrast artifacts. The CW artifacts are more an extension of the anomaly itself, blurring in

the z direction, whereas the FD and mFD artifact is of negative contrast and just below the surface of phantom. The magnitude of the reconstructed absorption coefficient increases as the contrast increases, which was the case for the single step reconstruction. The magnitude of reconstructed absorption coefficient is largest for mFD data, as shown by rod 3, where mFD data is 0.0115 μ_a / mm^{-1}, compared to 0.0110 μ_a / mm^{-1} for FD data and 0.0103 μ_a / mm^{-1} for CW data.

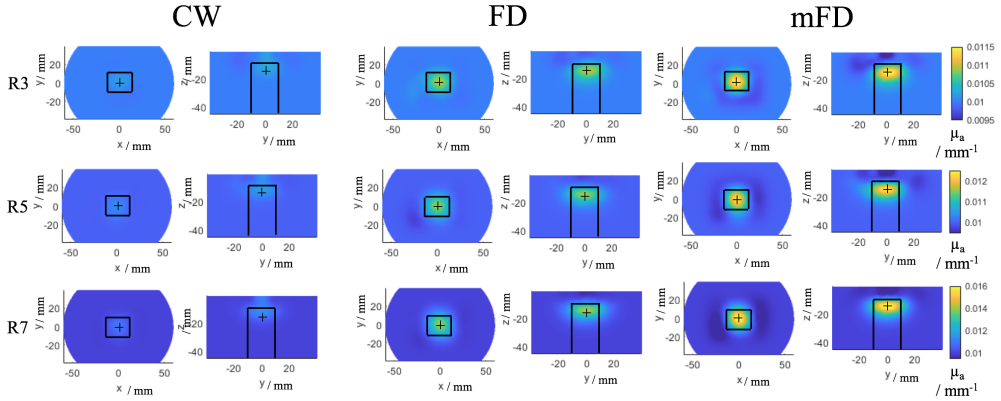

Figure 4.9: Iterative (4 iterations) tomographic reconstructions from rod 3, 5 and 7 (R3, 5 and 7 respectively) using CW, FD and mFD data respectively at 830 nm. For each reconstructed image, two views are shown, firstly the z plane at z = -15 mm and secondly the x plane at x = 0 mm. The colour bar scales are the same for each given rod. The solid black lines indicate the spatial constraints of the imaging metrics.

The imaging metrics are shown in Table 4.7, the LOCA is the best for FD and mFD data, where it is 0.81 mm for rod 5 and 7 respectively. mFD data has the best FWHM and ERES across all rods, with an average FWHM of 13.46 mm, compared to 20.32 mm for FD and 17.34 mm for CW data, and for the ERES, mFD data is 14.87 mm, compared to 21.29 mm for FD and 30.48 mm for CW data.

Table 4.7: The evaluation metrics, the LOCA, FWHM and ERES shown for rod 3, 5 and 7 using CW, FD and mFD data respectively. These are from the reconstructed images shown in Figure 4.9. This is using four iterations for each data type.

Rod N	Metric / mm	CW	FD	mFD
3	LOCA	3.83	2.33	**2.20**
3	FWHM	17.72	19.75	**13.23**
3	ERES	30.67	21.61	**15.66**
5	LOCA	3.83	**0.81**	**0.81**
5	FWHM	17.42	20.35	**12.24**
5	ERES	30.39	20.91	**13.31**
7	LOCA	3.83	**0.81**	**0.81**
7	FWHM	16.89	20.88	**14.92**
7	ERES	30.39	21.36	**15.66**

For a higher number of iterations, the magnitude of absorption coefficient in the reconstructed image increases, which is why the reconstructed image from CW data appears brighter and tighter relative to the FD and mFD data compared to figures 4.8 and 4.9. This increases the performance of the CW data, as it causes the artifact in the z axis to have less influence on the imaging metrics. The use of more iterations also helps the FD data, as the reconstruction of the contrast anomaly also appears brighter and is less spread out compared to the lower number of iterations shown in figures 4.8 and 4.9.

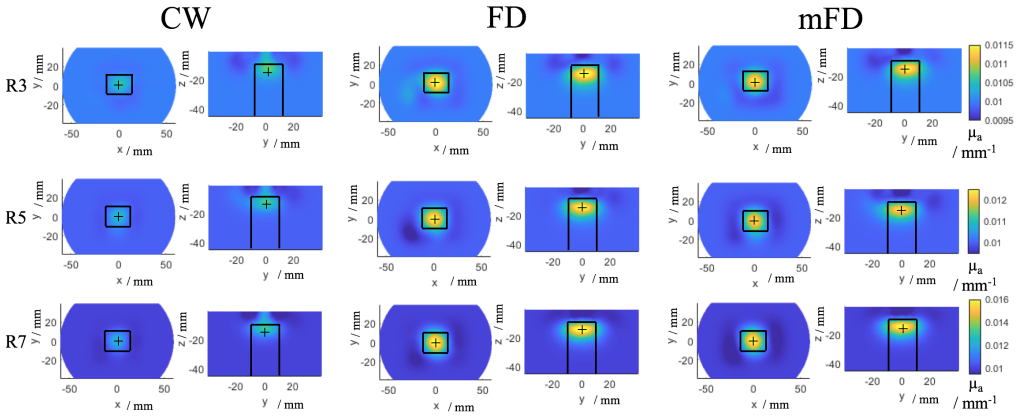

Figure 4.10: Iterative tomographic reconstructions from rod 3, 5 and 7 (R3, 5 and 7 respectively) using CW (8 iterations), FD (6 iterations) and mFD (4 iterations) data respectively at 830 nm. For each reconstructed image, two views are shown, firstly the z plane at z = -15 mm and secondly the x plane at x = 0 mm. The colour bar scales are the same for each given rod. The solid black lines indicate the spatial constraints of the imaging metrics.

Table 4.8 shows the imaging metrics corresponding to the reconstructed images shown in Figure 4.10. The LOCA remains virtually identical to that of the four iterations shown in Table 4.7, with the only differences being for CW and FD data for rod 3 and 7. The increased number of iterations of CW and FD data causes the average FWHM and ERES to reduce compared to four iterations, with the reductions being more significant for the CW case. For the FWHM these reductions are 17.34 mm to 11.85 mm for CW, and 20.32 mm to 17.22 mm for FD, and for the ERES the changes are 30.48 mm to 16.35 mm for CW and 21.29 mm to 18.30 mm for FD data. Overall CW data has a lower FWHM, whereas mFD data has the lowest ERES, and in both cases FD performs worse than either CW or mFD data.

Table 4.8: The evaluation metrics, the LOCA, FWHM and ERES shown for rod 3, 5 and 7 using CW, FD and mFD data respectively. These are from the reconstructed images shown in Figure 4.10. This is using a eight iterations for CW data, six iterations for FD data and four iterations for mFD data.

Rod N	**Metric / mm**	**CW**	**FD**	**mFD**
3	LOCA	4.12	2.32	**2.20**
3	FWHM	**13.08**	16.86	13.23
3	ERES	18.75	18.38	**15.66**
5	LOCA	3.83	**0.81**	**0.81**
5	FWHM	**11.25**	17.20	12.24
5	ERES	15.27	17.78	**13.31**
7	LOCA	3.82	**0.81**	**0.81**
7	FWHM	**11.24**	17.60	14.92
7	ERES	**15.04**	18.76	15.66

4.4 Discussion

This study assesses the performance of real mFD-HD-DOT measurements on a phantom, which means the relative merits and disadvantages of mFD data are evaluated. One of the main criticisms of using phase data is how it is inherently noisier than intensity data for a given modulation frequency and that the contrast to noise ratio of phase data should

increase with source-detector separation and modulation frequency (Fantini and Sassaroli, 2020). This leads to questions about the inclusion of phase data, such as is the contrast in phase data in functional brain imaging sufficient to perform accurate DOT despite the noise. The experimental data shown in Figure 4.4 attempts to answer the aforementioned questions, by showing intensity and phase data at three modulation frequencies (78 MHz, 141 MHz and 203 MHz) at two different source-detector separations (NN1 = 13 mm and NN2 = 29 mm). From the statistics in Figure 4.5, the contrast to noise ratio is smaller in the phase measurements than intensity, and for both intensity and phase increases as the source-detector separation increases, which is already well established. There appears to be a trade off when choosing a modulation frequency and what data types to include between the noise of the signal, and the quality of information content (contrast and depth sensitivity) that can be obtained. This is demonstrated by the approximately linear and inverse relationship that the intensity and phase data have with each other with respect to their signal to noise ratio, such that the lower frequency for intensity and the higher frequency phase offer the best signal to noise ratio. The limitation of this analysis is that only NN1 and NN2 are investigated. In some 'high density' arrangements, NN3 (39 mm) and NN4 (46 mm) can be used (Eggebrecht et al., 2014), however were excluded from use in reconstruction in this study because the signal was too low (Figure 4.2D.). This is due to the intensity of light being too strong from NN1 measurements, which causes the voltage bias of detectors to be low, and this means there is lower signal from higher NN measurements.

For the single iteration case, mFD performed better than FD or CW data (Table 4.6). For the LOCA, mFD was the smallest error each time, followed by FD and then CW was the largest LOCA. For the FWHM and ERES metrics, the performance was variable across the three data types, however only in one instance was the smallest FWHM or ERES from CW data (rod 3), for rod 5 and 7, the smallest FWHM or ERES was from FD or mFD data. This is due to the increased magnitude of maximum reconstructed absorption coefficient

from the FD and mFD data, as a more concentrated, less broader reconstruction will yield lower metrics. The ERES is closely coupled to the LOCA, with a larger LOCA effectively scaling the ERES, which is why CW data never had the best LOCA or ERES. The FWHM is independent of these two metrics and is influenced by the tomographic reconstruction itself and is not influenced by the true location of the contrast anomaly. Due to the lower inherent noise of CW data, which should lead to a 'cleaner' reconstructed image the FWHM for CW was comparable (rod 5 and 7) if not better (rod 3) than for FD or mFD. However, the main disadvantage of the CW data is that the sensitivity is shallower compared to FD data (Doulgerakis, Eggebrecht, and Dehghani, 2019), which can be seen by the reconstructed images in Figure 4.8 for all three rods and the fact that CW had a tendency to localize the anomaly a 2-3 mm higher compared to FD or mFD. There is an upward tail to the reconstruction of the contrast anomaly which extends to the surface of the phantom from the CW case, which is not observed for the FD or mFD case. As is previously established, phase data samples deeper than intensity data (Doulgerakis, Eggebrecht, and Dehghani, 2019 and Fan, Dehghani, and Eggebrecht, 2021), which are evident in the FD and mFD reconstruction of absorption coefficient. However, the FD and mFD reconstructions suffer from some positive and negative contrast artifacts, which are seen above the contrast anomaly instead of the positive tail in the CW case. The spatial constraints on metrics will dampen the effect of these artifacts for all three data types, mainly the FWHM for CW and ERES for FD and mFD.

For the iterative reconstructions of absorption coefficient of the same number of iterations (4, Table 4.7), mFD by far performs the best having the lowest metrics for all rods and jointly lowest for the LOCA on rod 5 and 7 with FD data. The regularisation after four iterations for mFD data causes the optimum balance between over-fitting noisy data and under-fitting data and excluding features in the signal. Just like for the single iteration case, mFD data has the highest magnitude of reconstructed absorption coefficient at four itera-

tions, which is visible in Figure 4.9, which will favour the LOCA and ERES metrics. Unlike the single iteration case where for rod 3 and 7 CW had a lower FWHM than mFD, mFD has smaller FWHM's, which could be due to under-fitting of CW data, since CW data has it's best solution at N = 8 iterations. Generally the artifacts present for the single iteration case appear smoothed out for the multi iteration case, particularly in the x-y direction for FD and mFD data, however the shallow tail still appears for CW and a negative contrast artifact is still present for mFD.

For the case of the best number of iterations (8-CW, 6-FD, 4-mFD, Table 4.8), CW performs better compared to N = 4 number of iterations. mFD and FD still perform the best for the LOCA, and the ERES is lowest from mFD for rod 3 and 5. CW data can go to a higher number of iterations compared to FD or mFD as it is less susceptible to noise, which helps refine the reconstructed image, as demonstrated by the lowest FWHM metrics for all three rods. However, this does not eliminate the inherent sampling profile of CW data, as the localisation is still the worst compared to FD or mFD. For the case of rod 7, even though the FWHM is 28.1% lower in CW compared to mFD, the poor LOCA means that the ERES is only 4.03% lower.

The reconstructed values of the absorption coefficient in the single iteration case are higher than that of the reported equivalent absorption coefficients (Table 4.4), which could be because an non optimal regularisation parameter for imaging the phantom was used, however the regularisation parameter chosen to be consistent with previous studies (White and Culver, 2010 and Perkins, Eggebrecht, and Dehghani, 2021). For the N = 4 iterative case, the values of reconstructed absorption coefficient are smaller than the reported values in Table 4.4, which could be due to the higher regularisation parameter used and the use of multiple iterations. The absorption coefficients were quoted in this study to see the relative difference of them between the data types. Further study is warranted to compare these to the given values of the phantom, which could include using a higher resolution FEM of the

phantom and optimising the regularisation parameter to obtain the absorption coefficients in the nodes where the contrast anomaly are.

There are four limitations of this study. Firstly, only measurements up to NN1 (13 mm) and NN2 (29.02 mm) were used, which excludes NN3 (39 mm) and NN4 (46 mm). Some HD-DOT experiments, channels above 30 mm source-detector separation are included (Eggebrecht et al., 2014), however due to the high intensity of light from NN1 channels, the voltage bias of detectors had to be lowered in order to not saturate the measurement, which meant the dynamic range was shifted away from the higher source-detector separations. However due to the nature of the study and the depth of the contrast anomaly (-15 mm), NN1 and NN2 measurements were completely sufficient to perform HD-DOT. Secondly, for measurements at different modulation frequencies, the contrast anomaly was manually moved to the centre position (x = y = 0 mm), which means there may have been small differences between the true location of the contrast anomaly. However, these differences would be on order of 0 mm to 2 mm, which for HD-DOT reconstructing a contrast anomaly at 15 mm depth, is a lot smaller than the imaging resolution. Finally, spatial constraints were applied to the evaluation metrics after image reconstruction to dampen the effects of artifacts away from the contrast anomaly, as to measure the performance of the three data types with the benefit of prior information. These spatial constraints were chosen to be within the FOV of the source-detector probes on top of the phantom.

Finally, some of the increase in imaging performance of FD and mFD data compared to CW data could be attributed to the longer integration time of measurement (more samples used), since FD data contains CW data and mFD data contains FD data, which would increase the SNR of FD and mFD data. However, if the additional data was redundant (i.e the phase at one frequency for FD and the phase at multiple frequencies for mFD), then it would not provide a significant advantage, since the CW data is already using 2000 samples for the reference and 1000 samples for the perturbation measurements respectively.

In addition, the use of FD and mFD data in this study represents realistic use cases of FD and mFD systems in real practice (Stillwell et al., 2021) as FD systems collect intensity and phase data simultaneously, so there would be no reason not to use all of the phase and multi-frequency data in analysis. The ISS Imagent system is the worst case scenario for mFD data, since it can only measure at one modulation frequency at a time, whereas new systems are being developed to measure multiple modulation frequencies simultaneously (Stillwell et al., 2021), meaning no extra time or repeated measurements are required to collect mFD data.

For future studies and experiments using FD systems and considering what modulation frequency to use and if modulation frequencies should be combined, there exists a trade-off. Figure 4.5 shows that for NN1 and NN2 measurements, the higher modulation frequencies used, there will be increased phase contrast, but lower intensity contrast and that these relationships are linear. For NN1 measurements, the noise of intensity and phase data increases linearly as the modulation frequency increases, however for NN2, the noise behaves like a quadratic curve, with the minima being at 141 MHz. The quadratic nature of the standard deviation could be due to the characteristics of the instrumentation, rather than something fundamental about the modulation frequency. Too high a modulation frequency may lead to an immeasurable signal, as experimentally when using the ISS Imagent, increasing the modulation frequency meant the voltage bias of detectors had to be increased, otherwise there would not be a signal, and for frequencies above 300 MHz the AC and DC signal was very weak. For the combination of modulation frequencies systems like the ISS Imagent can only measure one frequency at a time, so for N frequencies, N repeated measurements have to be taken. On a phantom this factor is easy to overcome, however for in-vivo imaging practical problems may arise, such as source-detector probes moving position between measurements and the increased time by factor N of data acquisition. For those reasons and not wanting to use redundant data as suggested by Intes and Britton Chance, 2005, the three modulation frequencies used in this study represent a feasible number of fre-

quencies to use, as these had an interval of ≈ 70 Hz and using more modulation frequencies would decrease the interval between these frequencies. Finally higher modulation frequencies have a deeper distribution of sensitivity compared to lower modulation frequencies (Fan, Dehghani, and Eggebrecht, 2021), which means what modulation frequency and the number of frequencies to use depends strongly on the geometry of what is being imaged, the depth sampling required, source-detector separation and any unique experimental factors, such as if repeat measurements are possible and if the system can acquire multiple frequencies simultaneously.

4.5 Conclusion

This study assesses the use of multiple modulation frequency data in frequency domain high-density diffuse optical tomography. Three data types were compared, CW (intensity at 141 MHz), FD (intensity and phase at 141 MHz) and mFD (intensity at 141 MHz and phase at 78 MHz + 141 MHz + 203 MHz), and overall mFD performed better than FD and CW data across single and iterative reconstruction of absorption coefficient. This is shown by the fact for single iteration reconstruction (Table 4.6), mFD scored the best metric in five out of nine cases, and for the N = 4 iterative reconstruction case (Table 4.7), where the same regularisation was applied to each data type, mFD scored the best metric seven out of nine times and joint best with FD in the other two cases.

Generally, FD performed better than CW data, particularly in the localisation of the contrast anomaly, however as demonstrated in the iterative reconstructions, FD reconstructed images were broader and so CW demonstrated lower FWHM. This is where the using multiple modulation frequencies was most effective, as mFD data in iterative reconstruction considerably increased the accuracy and resolution of tomography. The use of three

frequencies could be considered a practical limit for typical in-vivo applications, as to use more frequencies would require more acquisitions of data being taken, as the system used was not capable of simultaneous modulation frequencies. Future studies using FD data should consider if it feasible to collect data at multiple modulation frequencies simultaneously, and for systems capable of simultaneous frequency acquisition, then mFD data is essential to unlock the best performance from FD imaging.

Chapter Five

Frequency domain measurements on healthy subjects

5.1 Introduction

This chapter is about creating and evaluating a workflow to use frequency domain measurements for fNIRS and DOT for functional brain imaging on healthy subjects. The motivations of this are built upon the work and results found in the previous two chapters. Firstly, chapter 3, where simulations of HD-DOT found that phase data offered increased accuracy for image reconstruction of a point perturbation, as well as the combination of intensity and phase data at multiple modulation frequencies yielded the best performance. Secondly chapter 4, where phase data and multi-modulation frequency data were collected on a phantom that had a contrast anomaly within it, supported the results from the simulation study. As it was shown with the phantom measurements that the most accurate localization of the contrast anomaly and the highest resolution of the tomographic reconstruction of the contrast anomaly came from the use of intensity and phase data at multiple modulation frequencies. This was consistent with the simulation study of chapter 3. From investigating simulated

data, to then data collected on a phantom, it then follows that subject in-vivo is the next progression to test and evaluate the previously mentioned results.

This chapter will use frequency domain measurements, by collecting intensity and phase data on three healthy subjects, as well as describing a workflow which includes subject specific registration using a 3D optical camera, as well as the creation of a data collection cap with a specifically designed source-detector array. Finally, spectroscopic and tomographic results are presented and evaluated. The use of mFD measurements are not included in the results of this chapter, because in the experimental trials, sufficient SNR could not be achieved at higher modulation frequencies than the reference 141 MHz used throughout this thesis, and whilst chapter 4 could achieve these measurements on a phantom, the added complexities of a subject measurements coupled with signal reduction from hair and source-detector coupling meant that sufficient repeatable mFD measurements couldn't be made with the hardware available.

5.2 Methods

As explained in chapter 1.4, data collection for fNIRS and DOT experiments relies on the implementation of coupling source and detector probes to a subject's scalp, measurements being made for a duration of an experiment (ranging from 10 minutes up to over an hour) and then the data undergoing a series of preprocessing steps to remove motion artifacts and regress out the influence of superficial tissue changes (provided short separation measurements are made) and then parameter recovery and image reconstruction is calculated. This requires a well designed implementation of a probe cap, that carefully considers the needs of the experiment and data processing steps. As seen in figure 1.8 in chapter 1.4, the hardware used in this thesis for data collection is the ISS Imagent which deploys separate

source-detector fibers from modules which need to be coupled to the subject's scalp. Since this system doesn't have a manufacturer made cap, the coupling has to be designed from the ground up.

5.2.1 Helmet creation

The helmet used for data collection was a 'Zone 3 Neoprene Swimcap - Size Medium' (Zone 3, United Kingdom). This was chosen due to its flexibility to conform to different head shapes sizes as well as being able to cut holes in the cap to attach source-detector fibres. The helmet was placed on the subject and then the M3 and M4 landmark positions were found by standard anatomical measures (Tyagi et al., 2020). Other anatomical landmarks were found, including the inion, nasion, vertex and the left and right preauricular points respectively. From these landmarks, the source-detector array, figure 5.4 were positioned over the M3 and M4 landmark points, such that they were centered in the bottom right quadrant of the array on the left hemisphere, and bottom left quadrant on the right hemisphere.

An array of 3D printed mounts were used to support the source-detector fibres. These mounts were printed using an Ultimaker S5 3D printer, with Ultimaker Black PLA (Ultimaker, United States). Holes were cut into the cap and the mounts were pressed through from underneath the cap through to the surface of the cap, figures 5.3 A-D. The 3D printed mounts for the sources and detectors had different dimensions which are shown in figure 5.1 and were designed using Fusion 360 (Autodesk, United States). The height of the detector mount was 17.50 mm, with an inner diameter of 6.5 mm and an outer diameter of 9.00 mm, whilst the same dimensions of the source mount were 14.50 mm, 3.4 mm and 5.5 mm respectively.

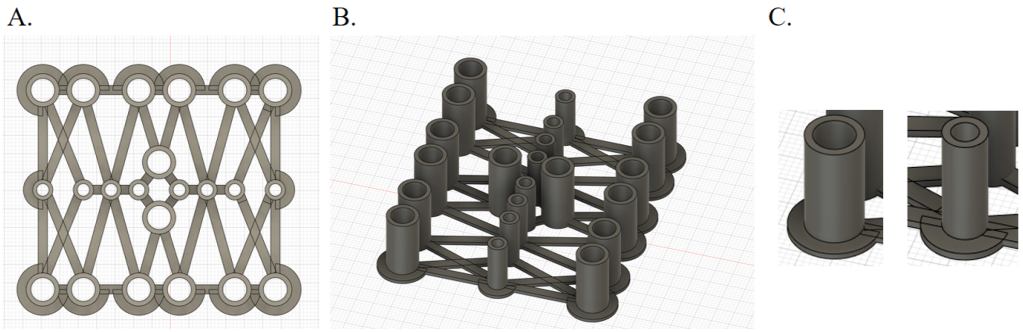

Figure 5.1: The 3D design of the source-detector mounts. A. A view of the entire source-detector array from above. B. The source-detector array showing the difference in height of the source and detector mounts. C. The individual detector and source mount respectively.

The dimensions of the source and detector mounts were chosen such that the normal contact friction between the fibres and the inside of the mounts would be sufficient to hold the fibres in place, so that they could be pushed onto the subjects scalp and then would stay in place and keep contact with the scalp.

These were on top of a base, of 1 mm thickness made from Ultimaker TPU 85-A. The base was chosen to be made out of TPU, since it is more flexible than PLA. However PLA was used for the mounts holding the source-detector probes as they require rigidity to support the weight of the fibers. This is to reduce the chance that motion artifacts will occur in the data, due to sudden or slow movement of the fibers relative to the subject's scalp and that the flat surface of the fibers can sit parallel to the subject's scalp.

The mounts were designed on the computer aided design software Fusion 360 (Autodesk, United States) to create an .stl file, and then this .stl file was exported into Cura (Ultimaker, United States). Cura is software that accompanies the Ultimaker S5 3D printer and is used to convert 3D models into the 'g-code' that instructs the 3D printer how to print a given 3D geometry. Two pads were printed, each consisting of 14 detector mounts and 8 source mounts respectively, figure 5.4, and these took approximately 3 hours to print a single pad using the default printer settings.

5.2.2 Data collection protocol

A motor cortex activation task was designed and was chosen because motor cortex activation is easy to invoke and shows a response which is well understood, and can be separated between the left and right hemispheres, due to co-lateral activation from the left-right motor activity respectively. Previous studies have used motor cortex activation as a way to study TBI, such as Urban et al., 2015, during which they compared the functional activation between 12 mTBI and 8 non TBI patients performing a finger tapping task. So far the development and evaluation of FD measurements have been conducted with simulations (chapter 3) and on a phantom (chapter 4), testing in-vivo on the motor cortex would make these developments relevant for TBI assessment.

In this experiment, the subject undertook a hand gripping task, where they gripped their hand at approximately 1Hz for 16 seconds followed by a random rest period of 16 to 32 seconds. A pseudo-random combination of left and right hand grips were performed by the subject, totaling 16 hand gripping periods, 8 for the left hand and 8 for the right hand, figure 5.2. The stimulus length of 16 s was chosen based upon previous fNIRS studies looking at motor cortex activation (D. G. Wyser et al., 2022). The rest period was chosen to be a random length between 16 to 32 seconds to minimise the chance that the stimulus-rest periods would coincide with resting physiological changes in scalp or brain haemodynamics.

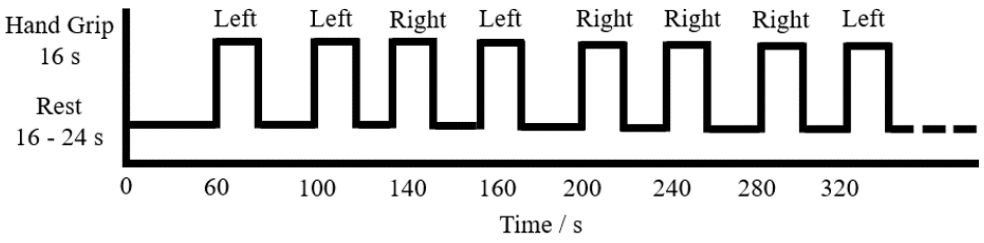

Figure 5.2: The design of the experimental paradigm. A pseudo random left-right hand grip order is used. Each stimulus period lasts 16 s and each rest period lasts a random amount of time between 16 to 24 s in order to minimise the chance of the stimulus-rest periods synchronising with physiological noise.

The subject was sat in a chair approximately a meter away from a screen displaying the experiment instructions and the lights in the room were turned off to minimise ambient light contamination, figure 5.3 A. Views of the subject wearing the cap can be observed in figures 5.3 B. C. and D.

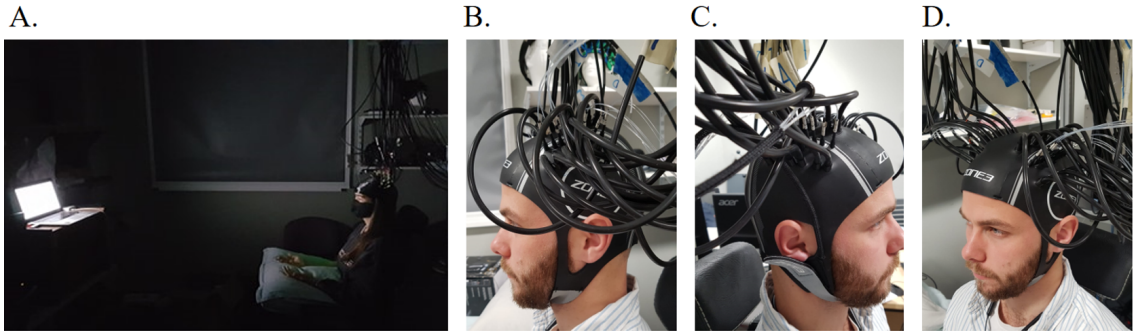

Figure 5.3: A. The subject observed in the conditions of the experiment. A screen displaying instructions of rest, left grip, or right grip is visible to the subject. B. C. D. The subject wearing the data collection helmet from three different perspectives.

Information about the subjects can be seen in table 5.1.

Table 5.1: Subject information for the experiment.

Subject N	**Sex**	**Age**	**Handedness**
1	M	28	Right
2	M	25	Right
3	M	30	Right

The source-detector array can be seen in figure 5.4, where 14 detectors and 8 sources are used. The design of the source-detector array was chosen to achieve four goals: Firstly, the detectors use photomultiplier tubes, which means the dynamic range of the signal is limited. For example, a detector which is 10 mm away from a source will have to have a lower voltage bias across the photomultiplier tube so that the signal is not saturated. This means the maximum measured signal from sources further away are reduced and thus reduces the maximum measurable source-detector separation, where the SNR is greater than the noise floor of the detectors. With this in mind, detectors 1 to 12 were made to have

channels at a minimum of 27 mm, so that realistic measurements could be made from 27 to 37 mm. These are the long separation channels. The minimum of 27 mm was chosen such that the diagonal channels would be on order of 30 mm separation, since this offers a good balance between depth sampling in tissue and sufficient SNR (Brigadoi and Cooper, 2015). The second goal was to enable short signal regression in the data analysis, the importance of this has been highlighted fNIRS literature (Brigadoi and Cooper, 2015 and Yücel et al., 2021). To achieve this, detectors 13 and 14 were placed about sources 4 and 5 respectively, such that they measure a combined four channels of 9 mm. Two of these channels are in the top half of the array and two of these channels are in the bottom half of the array.

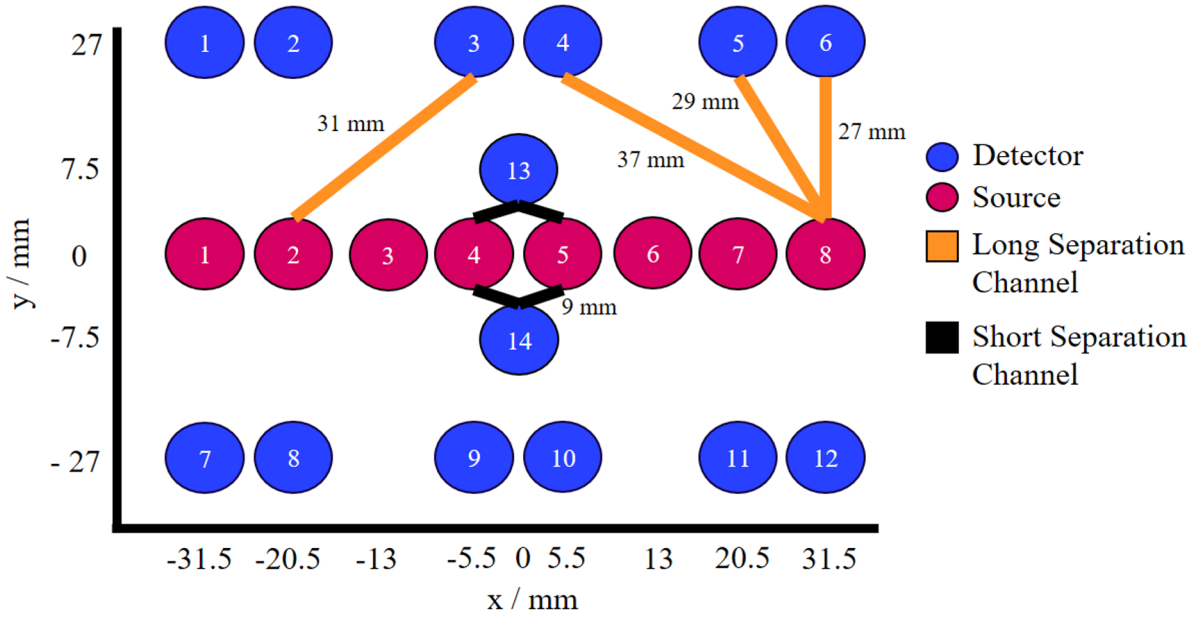

Figure 5.4: The source-detector array in 2D. There are 8 detectors and 14 sources used. Each source consists of two wavelengths, 830 nm and 690 nm. This gives up to 112 channels on each hemisphere, with four channels between sources 4 and 5 and detectors 13 and 14 being used exclusively for short signal regression.

The third goal of the array was to have spatially overlapping channels so that regions of the brain could be sampled by multiple channels in order to see correlation in spectro-

scopic reconstruction of the HRF's (Hemodynamic Response Function) as well as to facilitate tomographic reconstructions. This is achieved by having detectors positioned next to each other (e.g Detectors 1 & 2, 3 & 4, 5 & 6 etc.) in a row, adjacent to a row of sources, so that there are multiple diagonal channels (e.g The 29, 31 and 37 mm channels). The fourth goal of the array was to allow the potential to perform dual slope (Blaney, Sassaroli, et al., 2020). This technique offers a novel way to perform spectroscopic reconstructions of the HRF's, offering different advantages compared to standard single channel spectroscopic reconstructions. These are that dual slope measurements are self calibrating, as they mathematically remove changes in measured data from changes in source-detector coupling and they have a 'nut' shaped sensitivity profile, which for phase data has a deeper sensitivity profile, as opposed to the classic 'banana' shaped profile. From the source-detector array, there exists four distinct quadrants, which are marked by detectors 1 to 3, 4 to 6, 7 to 9 and 10 to 12.

5.2.3 3D optical registration

To minimise the error in the estimation of the source-detector positions on the head 3D optical registration can be applied. The goal of registration is to register the atlas model space to the subject space, i.e the 3D real life space that the subject inhabits wearing the cap. Other methods exist such as using the Polhemus digitiser (Polhemus, United States), which uses disturbances in electromagnetic fields to mark the location of probe positions, however metal can distort these measurements, and are therefore not suitable for use in certain environments. The method of optical registration works by using a 3D scanner, in this study the Artec Leo (Artec3D, Luxembourg) camera is used. Figure 5.5 A. and B. show the Artec Leo in use. In these figures the cap is just representative of the cap used for this motor cortex activation study. The subject is scanned wearing the cap and then from this, the scan is processed on Artec Studio 14 (Artec3D, Luxembourg and exported as an .ply file

(Polygon file format) and .stl (Standard Tessellation Language format). A visualisation of the .ply of the subject can be seen in figure 5.5 C.

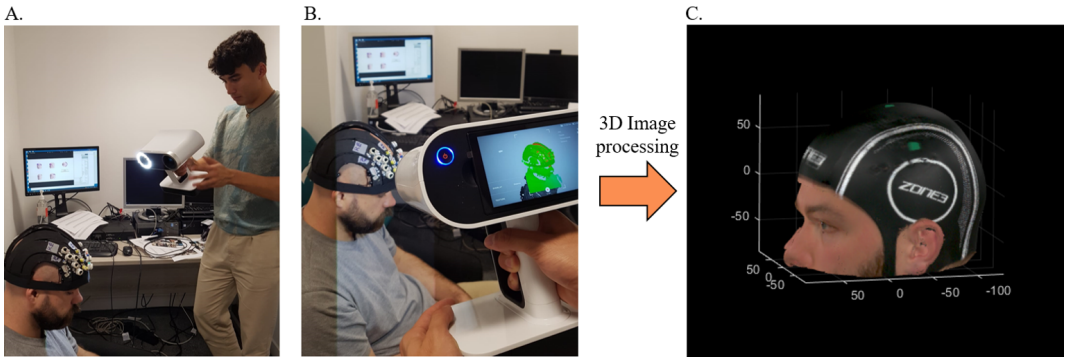

Figure 5.5: A. and B. A representation of scanning a subject with the artec leo. C. The 3D model output from the Artec Leo scan.

The surface model of the subject is shown in figure 5.6 with five different views shown between A. (Left), B. (Right), C. (Infront), D. (Top), E. (Behind), all showing the .stl file format. This was the 3D model of the subject that was used in the registration between the subject and the atlas model.

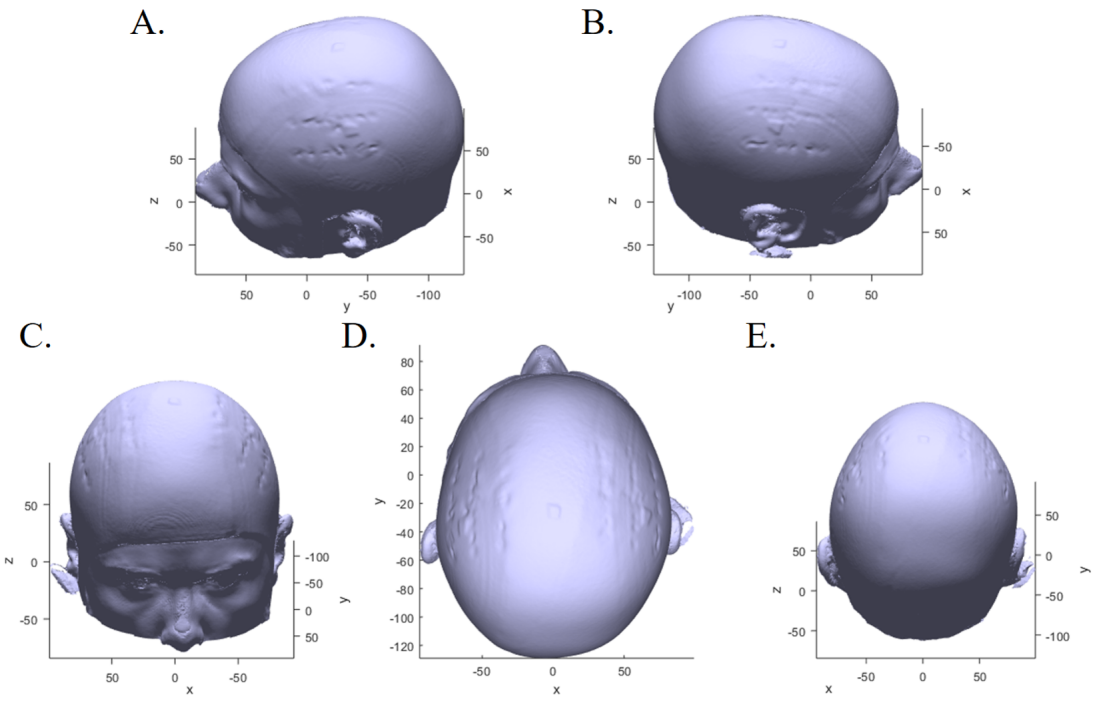

Figure 5.6: A. to E. Five different perspectives of the scanned subject wearing the swim cap.

The atlas model used is a 3D FEM taken from the Colin27 model (Strangman, Q. Zhang, and Z. Li, 2014). The Colin-27 model is a 3D model created from the average of 27 T1-MRI scans. In this model there are 5 tissue types. The scalp, the skulls, cerebral spinal fluid, gray matter and white matter. This can be seen in figure 5.7 from the same points of view as the subject .stl, where the right hemipshere of the head model shows the scalp surface, and the left hemisphere shows only the gray and white matter of the brain. Figure 5.7 B. shows a 2D slice along the sagittal plane of the atlas model. The FEM atlas contains 413674x 3 nodes, comprised of 2469811 elements.

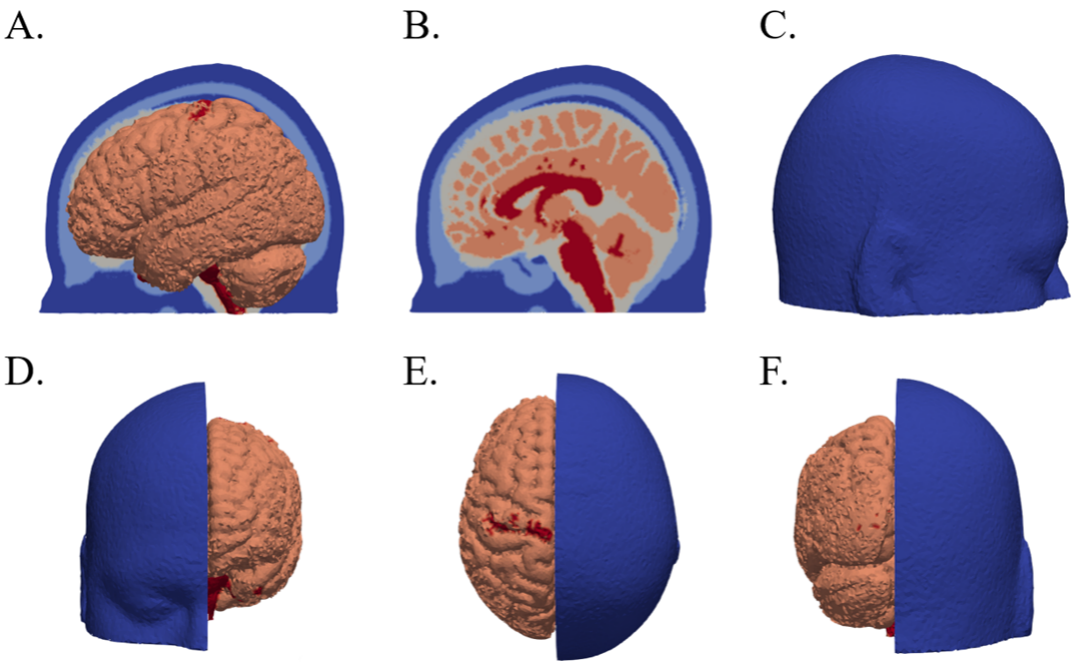

Figure 5.7: A. to F. Six different perspectives of the atlas mesh model. For these images, the left hemisphere of the head model is hidden, and the entire cortex remains visible.

The subject model and atlas model were loaded into the same euclidean space, figure 5.8 A. Before co-registration between the atlas and the subject models can take place, the subject model was manually rotated and translated so that it is aligned with the atlas model, such that their centre of masses are within 40 mm of each other. This can be seen between figures 5.8 A. B. and C. Finally, the subject model was cropped so that just the portion of the head above and including the nose remained, figure 5.8 D. This was done so that an equivalent centre of mass between the subject and the atlas model could be found, since the atlas model only has the portion of the head above the nose as well.

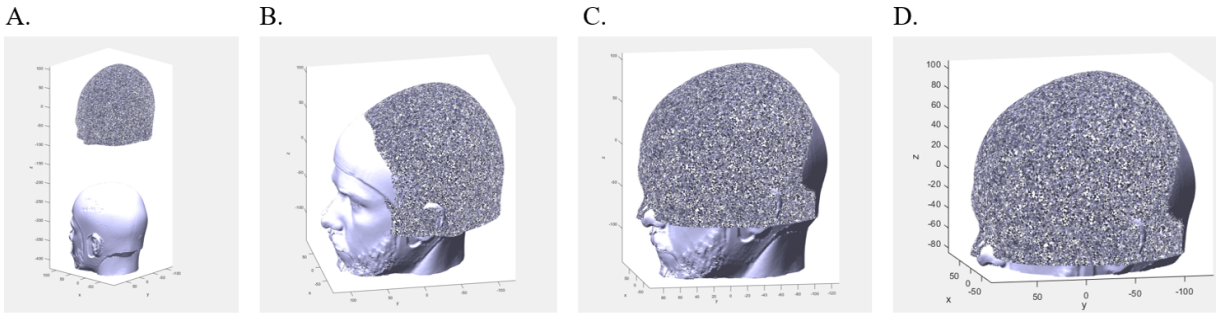

Figure 5.8: A. The atlas model (above) and the subject scan (below) loaded together in the same 3D space. B. and C. The atlas was then manually approximately rotated and translated to align with the subject. D. The bottom of the subject's head was cropped so that the atlas and the subject model had a similar proportion of the head.

Once the subject and atlas models are aligned within 40 mm of each other, landmark points can be taken from the atlas and subject spaces. There are five landmark points, the nasion (1) (between the eyes and on top of the nose), the inion (2) (The part of the skull that feels like a lump in the area of the visual cortex at the back of the head), the left (3) and right (4) preauricular points respectively (positioned just inside the ear next to the tragus) and the vertex (5) (The intersection of the paths along the surface of the head between the left and right preauricular points and the nasion and inion). These landmark points are obtained for the atlas and subject and can be seen in figures 5.9 A. and B. respectively.

For the atlas FEM, all five landmark points were found manually by visual inspection, whereas for the subject model, the nasion and left and right preauricular points were found by inspection, but the inion and vertex were located by marking green spots of tape on the subject's cap. An affine transformation matrix is then obtained which defines the transformation between the landmark points in the atlas space into the subject space. The transformation finds a vector which describes a linear translation, rotation and scale that can be applied to all five landmark points which minimises the euclidean distance (L2 Norm) between the landmarks in the registered atlas space to the subject space. This can be seen in figure 5.9 C, where the registered atlas landmarks are closer to the subject landmarks

than the pre registered atlas landmarks.

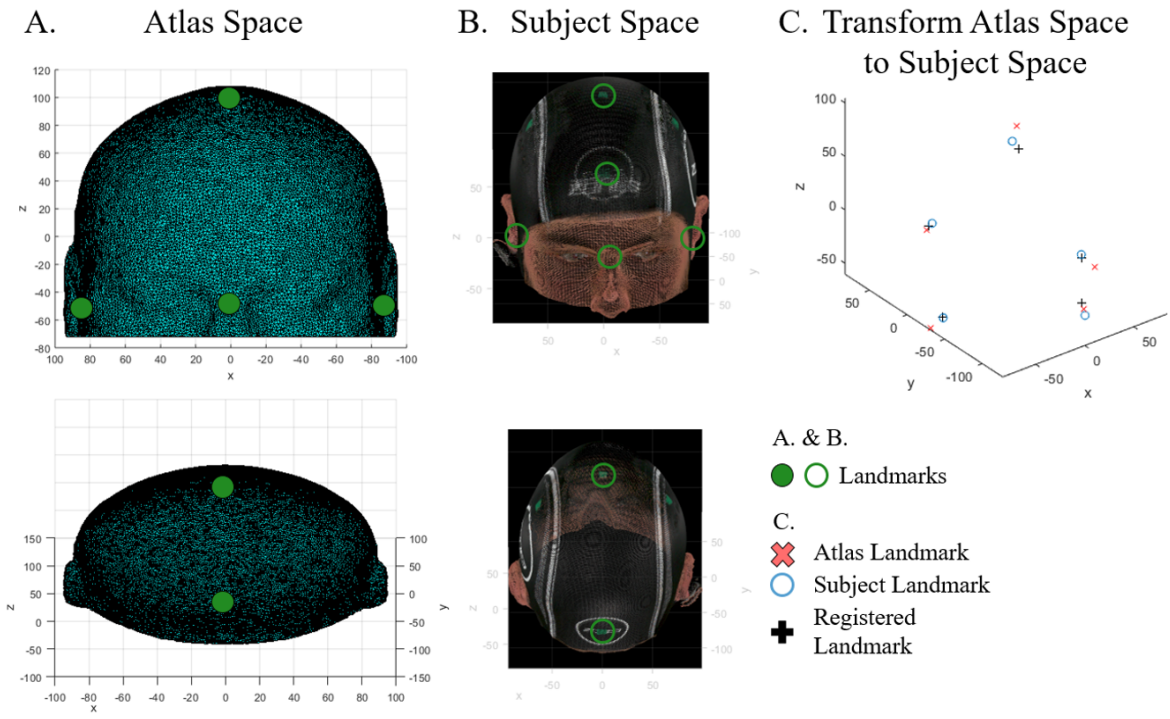

Figure 5.9: A. and B. Obtaining the 5 landmark points from the atlas and subject respectively. C. Then generating a transformation (affine) matrix to register the atlas into subject space. The matrix is found by minimising the L2 norm between the atlas and subject landmark points respectively.

Once the transformation matrix has been calculated that transforms the atlas space into the subject space, the locations of the source-detector positions on the subject need to be found. This was done by looking at the polygon format (.ply) of the subject scan. In order to locate the centre of the source-detector probe positions closest to the subject's scalp, the scan used was one without the physical probes in place. The positions of where the source-detector probes are can be found where there are changes in the topography of the surface of the 3D scan. The locations of the sources (red circles) and detectors (blue circles) are presented in figure 5.10.

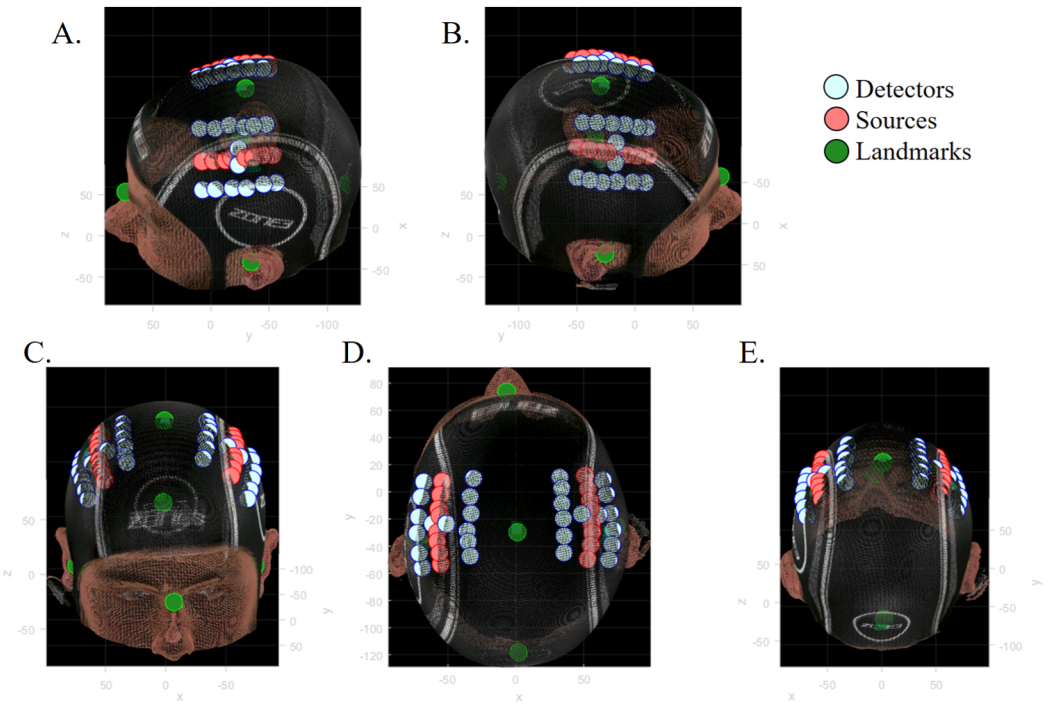

Figure 5.10: A. to E. The source and detector points being shown in the subject space.

From the arrangement of the sources and detectors, as presented in figures 5.4 and 5.10, there are four distinct regions of interest, figure 5.11, which are located about the M3 (left hemisphere) and M4 (right hemisphere) landmark points. These regions of interest will be used to average the HRF's from the motor cortex stimuli.

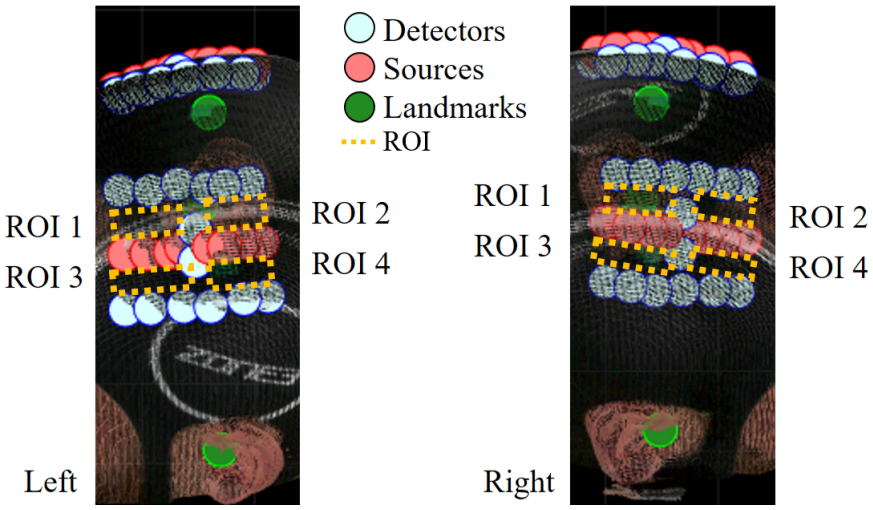

Figure 5.11: The four ROI's (Region of Interest) of the source-detector array.

The final part of the registration method is to obtain the locations of the source-detector probes on the registered atlas model. To recap, a transformation matrix was found to register the atlas into the subject space. In the subject space the source-detector probe locations were found from the subject scan. These source-detector locations in the subject space were then projected to the nearest node on the surface of the registered atlas to yield the source-detector locations on the atlas registered into subject space. This process can be visualised within figure 5.12.

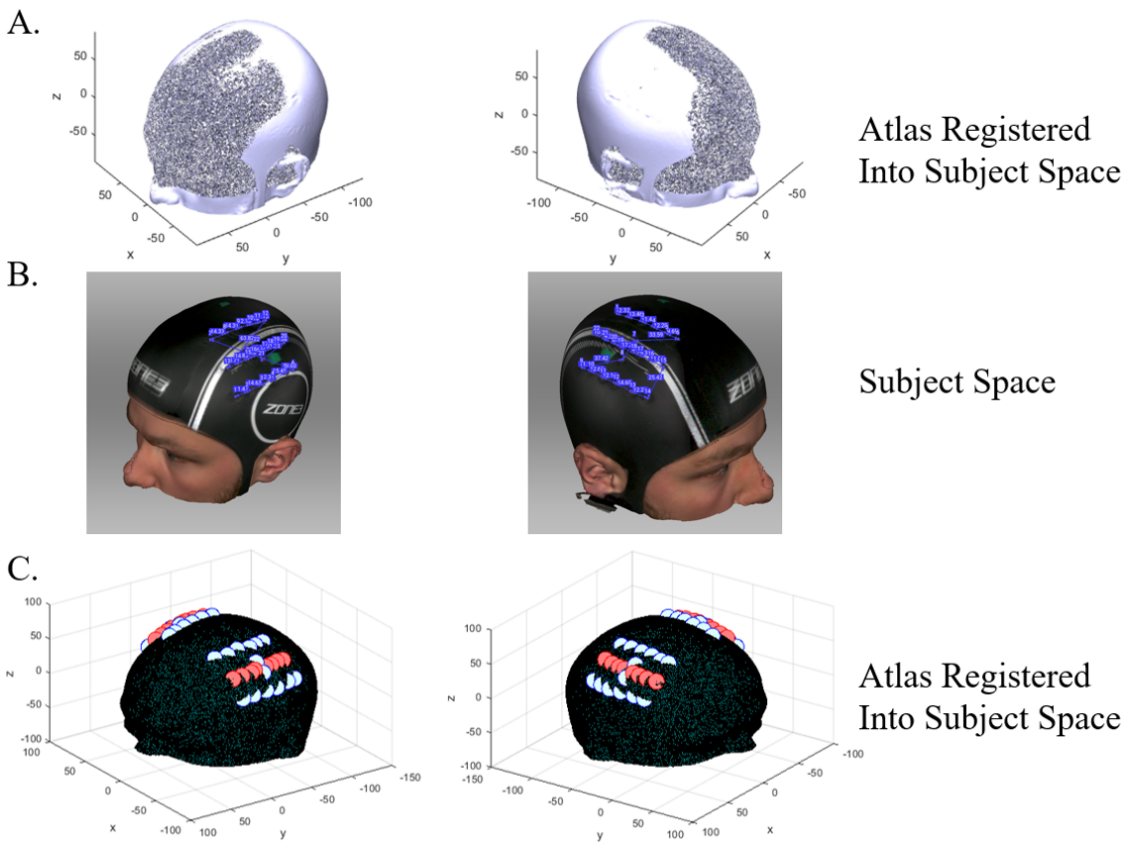

Figure 5.12: A. Registering the atlas into subject space. B. Locating the source-detector co-ordinates in subject space. C. Moving the source-detector co-ordinates to the closest surface node in the registered atlas in subject space.

5.2.4 Data analysis

The ISS Imagent collects three types of raw data, AC and DC intensity data respectively and phase data at 830 nm and 690 mn. The AC and DC intensities are arbitrary units ranging from zero to 16,384 (14 bit integer) and the phase data has units of degrees and typically ranges from 0 to 360 degrees, however the phase can have values above 360 degrees and below 0 degrees. The first part of this section will show AC intensity and phase data for a single channel, and will go through every operation used in the analysis pipeline. The channel used is for source 5-detector 5 (31 mm separation) on the left hemisphere of the subject and is between 131 s (stimulus minus 5 s) to 172 s (stimulus plus 36 s), which contains a right hand

grip period (Co-lateral stimulus) and a rest period, that can be seen in figure 5.13.

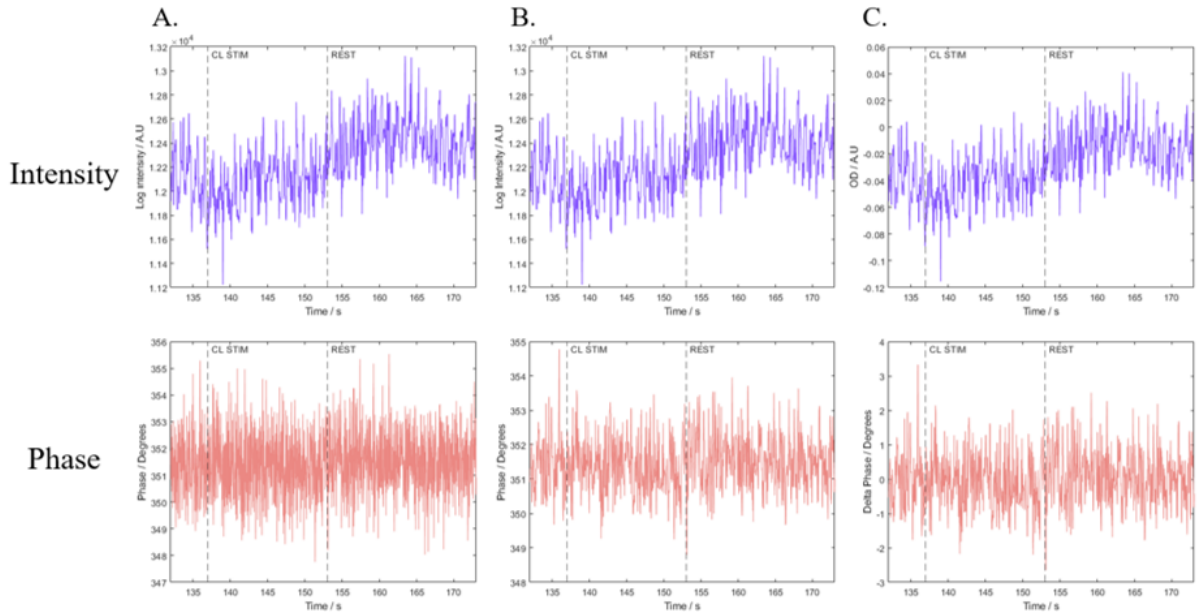

Figure 5.13: Sample of data from Source 5 Detector 5 at 830 nm. A. Raw Data. B. Median Filter. C. Delta optical density (intensity) and change in phase mean (phase).

Figure 5.13 A. shows the raw data for intensity and phase respectively and it can be observed that visually the contrast to noise ratio for the intensity data is higher than that of the phase data for the stimulus period. The first operation was to apply a median filter (third-order one-dimensional median filter), figure 5.13 B., which aims to smooth the data and reduce spikes in the data and then the optical density for intensity (OD) and delta phase (ϕ) were calculated, figure 5.13 C., given by equations 5.1 and 5.2 respectively,

$$OD = log(\frac{I(t)}{I_0}) \tag{5.1}$$

$$\Delta\phi = \phi(t) - \phi_0 \tag{5.2}$$

where $I(t)$ and $\phi(t)$ are the timeseries data for intensity and phase and I_0 and ϕ_0 are

the mean values of intensity and phase respectively. The next operation in the pipeline is to apply a bandpass filter, which is common practice in fNIRS data analysis (Yücel et al., 2021) and can be seen in figure 5.14 A. The bandpass is a 5th order butterworth filter of highpass 0.01 Hz and lowpass 0.09 Hz. The aim of the highpass filter is to remove slow signal changes from system drift, which can come from changes in the intensity of the source due to heating effects, and the aim of the lowpass filter is to remove changes in the signal from physiology, such as the cardiac cycle (1Hz), respiration (0.3 Hz) and alpha oscillations in the brain (0.1 Hz). The bandpass filter does not exclude the stimulus frequencies from the experiment which are between 0.025 Hz to 0.031 Hz, which are the inverse of the period for the shortest stimulus:rest length (16 s + 16 s) and longest stimulus:rest length (16 s + 24 s). The next operation is to apply wavelet motion correction (T. J. Huppert et al., 2009), which works by applying a discrete wavelet transform (DWT) that decomposes a time series signal into a number of sets defined by a coefficients in the wavelet domain (Molavi and Dumont, 2012), so that motion artifacts appear as isolated large coefficients in the discrete wavelet domain. The threshold for determining motion artifacts are wavelet coefficients larger than 1 times the interquartile range of wavelet coefficients, these are then removed from the signal, which is shown in figure 5.14 B.

The data was then downsampled to 1Hz from the original sampling frequency of 39.7Hz, so that the SNR is increased, figure 5.14 C. The next operation was to apply short signal regression, figure 5.14 D., which is common practice in fNIRS analysis and the aim of short signal regression (SSR) is to use short separation channels, typically 5 to 13 mm, and regress the changes in optical density/delta phase out of longer separation channels. The premise behind this operation are that shorter channel separation sample shallower and therefore are influenced more by changes in heamodyamics of superficial tissue, whereas longer channel separation will sample deeper into tissue and be influenced by changes in hemodynamics of superficial tissue and the outer cortex. By performing short channel re-

gression on longer channels, the resulting signal will have minimum influence from non cortex tissue. This technique is described by Wyser in 2020 (D. Wyser et al., 2020) and demonstrated between equations 5.3 to 5.6, where X is the design matrix containing $\overline{Y}_{ss}$, which is the mean of the data (Optical density and mean phase changes) from the short channels,

$$X = \begin{bmatrix} 1 & \overline{Y}_{ss} \end{bmatrix} \tag{5.3}$$

The regressor term, β is defined solving equation 5.4 for β as expressed in equation 5.5,

$$Y_{ls} = \beta X \tag{5.4}$$

$$\beta = Y_{ls} X^{-1} \tag{5.5}$$

and then the short channel regression is calculated in equation 5.6, where ϵ is the regressed data,

$$\epsilon = Y_{ls} - (\beta \cdot 1) - (\beta \cdot \overline{Y}_{ss}) \tag{5.6}$$

Equations 5.3 to 5.6 are performed for each measurement channel of the intensity and phase data. Only intensity data is used for the design matrix, i.e $\overline{Y}_{ss}$ is from intensity data only, as it has been shown that due to the deeper sampling of phase data compared to intensity (Veesa and Dehghani, 2021), some cortex signal content can be lost by regressing phase data with phase data. Only channels of separation below 13 mm were used to calculate

$\overline{Y}_{ss}$, and all channels with longer separation than 13 mm were classed as Y_{ls}, which were typically between 27 mm to 35 mm.

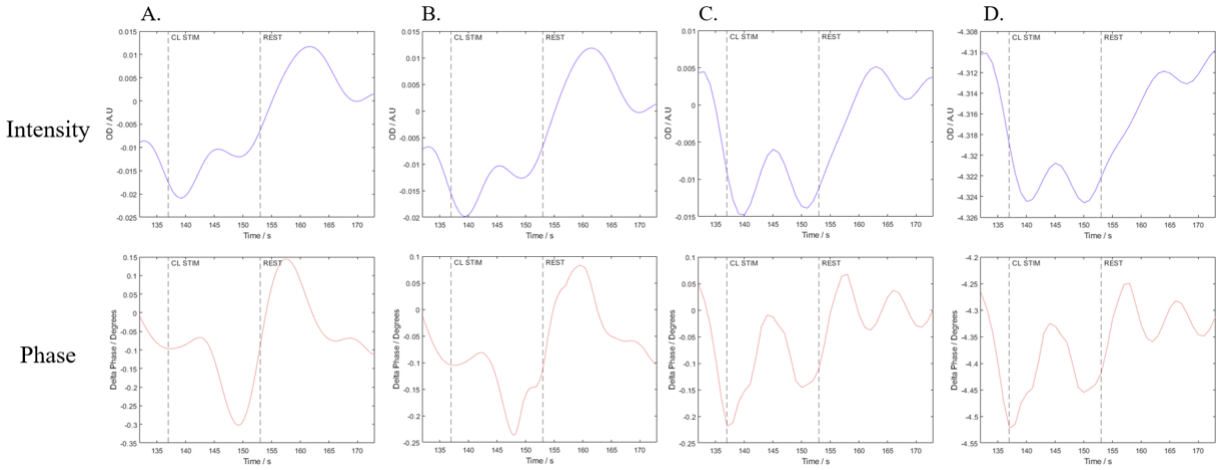

Figure 5.14: A. Bandpass filter (0.01-0.09 Hz). B. Wavelet motion correction. C. Downsample to 1 Hz. D. Short Signal Regression.

After the short signal regression was applied, the data was then block averaged, in order to increase the SNR of the response to the stimulus, as explained in section 1.4. During the experiment, markers were placed in the data to denote the start of a stimulus period and the start of a rest period. The data from all eight co-lateral (CL) stimuli and all eight uni-lateral (UL) stimuli was averaged from 2 s before the start of the stimulus up until 16 s after the end of the stimulus, i.e from -2 s to +32 s, which can be seen in figure 5.15 A. Block averaging shows the average change in optical density and delta phase across the stimulus:rest period, however for this data to be useful for relative difference imaging, a baseline needs to be subtracted so changes in data are relative to the rest period. The baseline used for the stimulus:rest period were the mean of the 2 s before the start of the stimulus, and this baseline is subtracted from the stimulus:rest period, figure 5.15 B. So far, only data at 830 nm has been shown, but in figure 5.15 B. the dashed line shows the corresponding change in data at 690 nm, which behaves in an inverse manor to the data at 830 nm. From the changes in data, of optical density and delta phase, changes in the absorption coefficient can

be calculated and then changes in HbO, Hb and HbT, which is described in the next section.

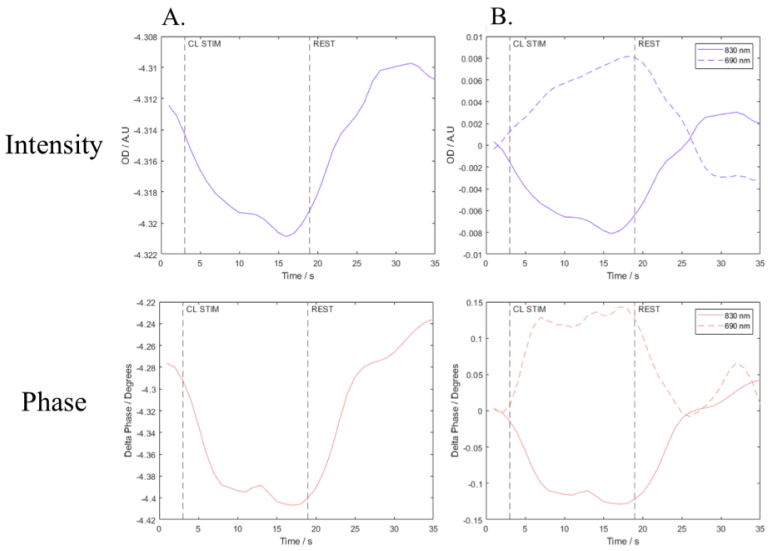

Figure 5.15: A. Block averaging of the time series data. B. Subtracting the baseline period, of 2 s before the stimulus.

5.2.5 Spectroscopic and tomographic reconstruction

The method for spectroscopic and tomographic reconstruction follow the same procedure as outlined in section 4.2.2 since the data types are the same. Section 4.2.2 were handling data on a phantom, whereas this section is handling data in-vivo. For the ease of reading and consistency of notation, the changes in optical density and delta phase can be denoted by Y_x, where x is the type of data, given in equation 5.7,

$$Y_I = \begin{bmatrix} OD \end{bmatrix} \quad Y_\phi = \begin{bmatrix} \Delta\phi \end{bmatrix} \quad Y_{I\phi} = \begin{bmatrix} OD \\ \Delta\phi \end{bmatrix} \quad . \tag{5.7}$$

For spectrscopic reconstruction, the diffusion approximation is used with the software NIRFAST (Dehghani, Eames, et al., 2009), using a semi infinite single voxel Jacobian , where each measurement has it's own Jacobian based upon the source detector separation (SDS), with number of rows equal to the number of measurements and a single column. For tomographic reconstruction, the Jacobian is generated from the subject registered atlas model, as described in figure 5.12 and contains 413,674 voxels, such that the number of rows are equal to the number of measurements and the number of columns equal to the number of voxels. For both spectroscopy and tomography, the Jacobian can be referred to as J and the structure of J for the three data types are the same as the data types in equation 5.7.

The workflow allows for voxel and data normalization of the Jacobian to be applied prior to inversion, to allow scaling the depth sensitivity in the image reconstruction. The regularisation parameter is used to tune the balance between smoothing and over-fitting of a solution. An example of normalization parameter, β (scalar) and the regularization parameter, λ (scalar) are both 0.01. These values are chosen empirically and have been used in prior studies (White and Culver, 2010; Perkins, Eggebrecht, and Dehghani, 2021).

Voxel normalization (only applicable for tomography) of the Jacobian is applied to each column of J, denoted by J(columns) by Eq. (5.8), where $\oslash$ is element piecewise division,

$$J(columns) = J_p \oslash \sqrt{L_V + \beta * max(L_V)} \tag{5.8}$$

where $L_V = \Sigma J^2_{voxel}$ (sum of columns in the Jacobian and each column represents a unique voxel), and data normalization is applied to each row of J, denoted by J(rows) by Eq. (5.9),

$$J(rows) = J_p \oslash M \tag{5.9}$$

where $M = \sqrt{L_D + \beta * max(L_D)}$ and $L_D = \Sigma J_{data}^2$ (sum of rows in the Jacobian and each row represents a unique source-detector channel). Then, Tikhonov regularisation is applied during the tomographic reconstruction which gives the change in optical properties of the biological tissue shown in Eq. (5.10),

$$\partial\mu_a = J^T \left(\frac{\partial Y_{I\phi} \oslash M}{(H + R)} \right) \oslash L_V^T \tag{5.10}$$

where the superscript ^{T} denotes the matrix is transposed, J is the normalized Jacobian of the phantom, H is the Hessian which is, $H = JJ^T$, R is the regularisation term, $R = \nVdash\lambda * max(diag(H))$ and $\nVdash$ is the identity matrix. For spectroscopy, a normalisation parameter of 0.01 was used, and for tomography, no normalisation or regularisation was calculated, i.e $L_v = L_D = 1$.

Changes in μ_a were found for data at 830 nm ($\mu_{a\lambda_1}$) and 690 nm ($\mu_{a\lambda_2}$), and an example of this for spectroscopy can be seen in figure 5.16.

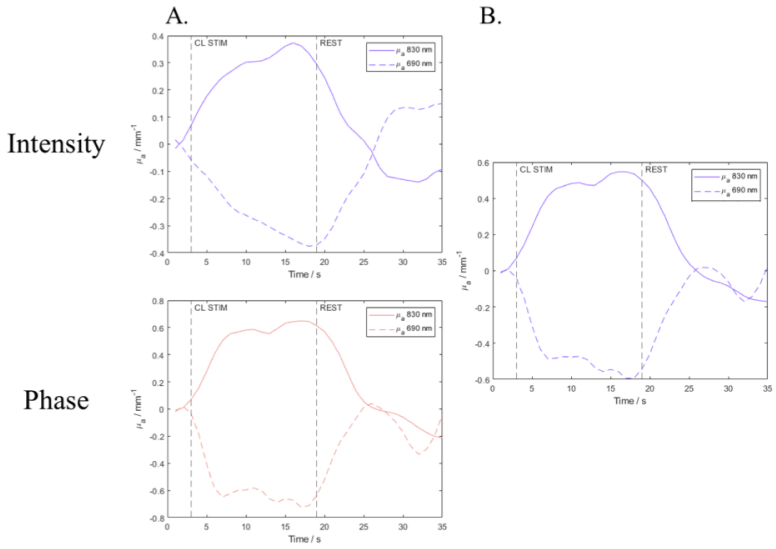

Figure 5.16: A. Calculate changes in μ_a. B. Changes in μ_a using intensity and phase simultaneously.

Following from calculating changes in μ_a, changes in HbO and Hb can be calculated using equation 5.11 where ϵ is the extinction coefficient of the chromophore, denoted in the subscript and is wavelength dependent, where λ_1 is 830 nm and λ_2 is 690 nm,

$$\begin{bmatrix} \Delta HbO \\ \Delta Hb \end{bmatrix} = \begin{bmatrix} \epsilon_{\lambda_1 HbO} & \epsilon_{\lambda_1 Hb} \\ \epsilon_{\lambda_2 HbO} & \epsilon_{\lambda_2 Hb} \end{bmatrix}^{-1} \begin{bmatrix} \Delta\mu_{a\lambda_1} \\ \Delta\mu_{a\lambda_2} \end{bmatrix}. \tag{5.11}$$

Changes in total hemoglobin concentration, ΔHbT, are given by $\Delta HbO + \Delta Hb$. The values of ϵ ($\mathrm{mM}^{-1}\ \mathrm{mm}^{-1}$) used in equation 5.11 are taken from Cope M. 1991 (Cope, 1991) and are shown in equation 5.12,

$$\begin{bmatrix} \epsilon_{\lambda_1 HbO} & \epsilon_{\lambda_1 Hb} \\ \epsilon_{\lambda_2 HbO} & \epsilon_{\lambda_2 Hb} \end{bmatrix} = \begin{bmatrix} 0.10507 & 0.07804 \\ 0.03123 & 0.21382 \end{bmatrix} \tag{5.12}$$

and then using equation 5.11 with the values of ϵ in equation 5.12 yields changes in HbO and Hb shown in figure 5.17.

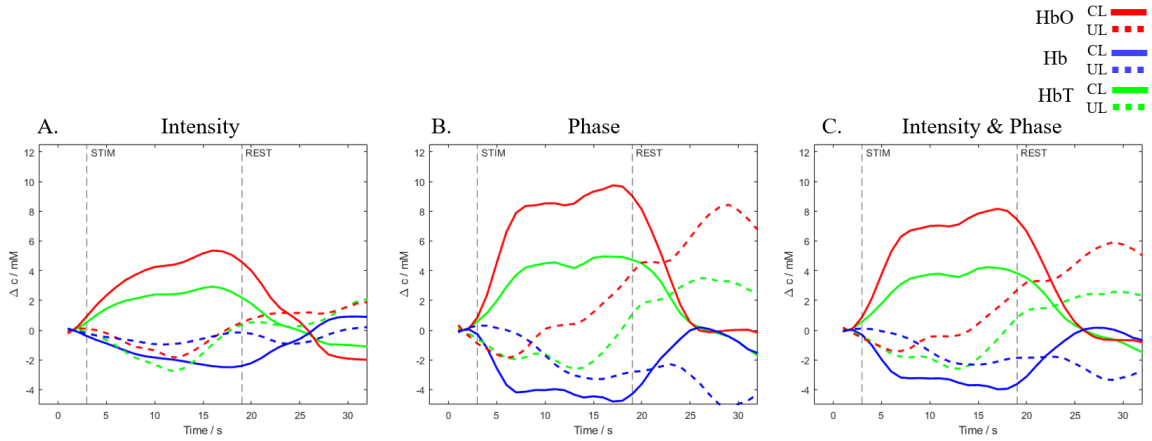

Figure 5.17: Changes in HbO, Hb and HbT calculated from A. Intensity. B. Phase. C. Intensity and phase simultaneously. Solid line are the co-lateral stimuli, dashed line is the uni-lateral stimuli.

5.2.6 Dual Slopes Reconstruction

As mentioned in chapter 5.2.1, one of the aims of the source-detector design was to accommodate the use of other methods of image reconstruction. One method is the use of dual slopes, which uses the average of the slopes between sources and detectors following a particular geometrical constraint. The method is described by Blaney in 2019 (Blaney, Sassaroli, et al., 2020) and the dual slopes are shown in figure 5.18.

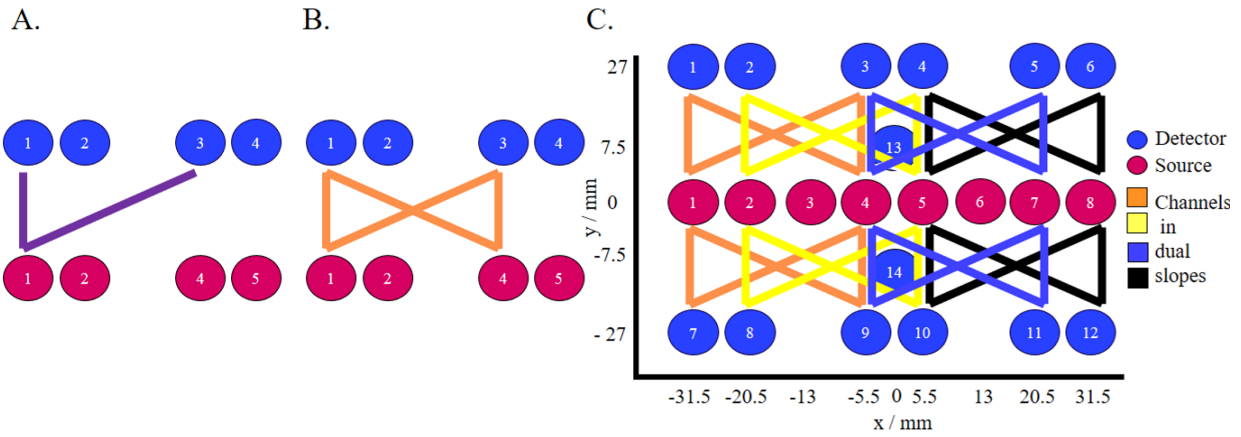

Figure 5.18: A. A single slope between a set of sources and detectors. The single slope is the difference in measurement between source 1 to detector 3 and source 1 to detector 1. B. A dual slope measurement. This is the average of the two single slopes between sources 1 and 4, and detectors 1 and 3. C. The dual slopes for the source-detector array for each hemisphere. There are 8 dual slopes on each hemisphere.

Using figure 5.18 as a reference, the construction of a dual slope is demonstrated in the following equations. Equation 5.13 shows that a single slope, SS_1, is formed by taking the difference in data between source 1-detector 2, Y_{12} and source 1 detector 1, Y_{11} and dividing this by the difference in the source detector separation between these measurement channels, SDS_{12} and SDS_{11} respectively.

$$SS_1 = \frac{Y_{12} - Y_{11}}{SDS_{12} - SDS_{11}} \quad SS_2 = \frac{Y_{31} - Y_{33}}{SDS_{31} - SDS_{33}} \quad . \tag{5.13}$$

It then follows that the dual slope, DS_1 is made up of the average of the single slopes, as described in equation 5.14,

$$DS_1 = \frac{SS_1 + SS_2}{2} \tag{5.14}$$

and the associated jacobian, JSS_{NM}, of the single slopes follow the same organisation

as the data, with the same notation where N and M are the source and detector number respectively and is shown in equation 5.15,

$$JSS_1 = J_{12} - J_{11} \quad JSS_2 = J_{31} - J_{33} \quad . \tag{5.15}$$

Then the jacobian for the dual slope, JDS_1, is the average of the two jacobian's for the single slopes, JSS_1 and JSS_1, and is shown in equation 5.16,

$$JDS_1 = \frac{JSS_1 + JSS_2}{2} \quad . \tag{5.16}$$

5.3 Results

Using the workflow outlined in section 5.2, spectroscopic and tomographic reconstruction of HbO, Hb and HbT was performed on three subjects. In each instance, three cases were considered, a. Using intensity data only, b. using phase data only, c. using intensity and phase data simultaneously. For the spectroscopic reconstruction, the changes of chromophore in each ROI (defined by figure 5.11) given by each measurement channel are averaged to give a HRF per ROI. Only channels satisfying all the data quality criteria are used. The criteria are measurements that have a SDS of 50 mm or less, have an average AC intensity at 830nm and 690 nm of more than or equal to 50 units and have a standard deviation less than or equal to 0.1 for the log mean intensity at 830 and 690 nm. For a channels phase component to be considered, the intensity component must fulfil the aforementioned criteria and the maximum change in μ_a at 830 nm and 690 nm must be less than or equal to 0.2 mm^{-1}.

The four ROI on each hemisphere occupy different spatial areas on the surface of the head. For each subject, the cap may be placed on with different alignments with respect to

the C3 (left) and C4 (right) scalp landmark positions, which are the motor cortex areas in the EEG 10-20 system and can be found along the line from the vertex to the pre-auriciular points. It is expected that the HRF from motor cortex activation will be seen over the C3 and C4 points, so only the ROI's along the line from the vertex to the pre-auriciular points are shown. For subject's 1 and 3 these are ROI 2 and 4 on the left hemisphere (LHS) and ROI 1 and 3 on the right hemisphere (RHS). For subject 2 this is ROI 2 and 4 on the LHS and ROI 2 and 4 on the RHS.

5.3.1 Standard HRF Subject 1

From spectroscopy on subject 1 using intensity data, figure 5.19, there are HRF's from motor cortex activation in LHS ROI 2 and RHS ROI 1 in the co-lateral (CL) response, both showing increases in HbO during the stimulus period, followed by a decrease in HbO during the rest period. The opposite is observed for Hb, whereby Hb decreases during the stimulus period and increases during the rest period. For the uni-lateral (UL) response there are no physiological meaningful changes in either HbO or Hb during the stimulus rest period. LHS ROI 4 and RHS ROI 3 show changes in HbO/Hb/HbT which are characteristic of systematic hemodynamic changes in superficial tissue for both the CL and UL responses.

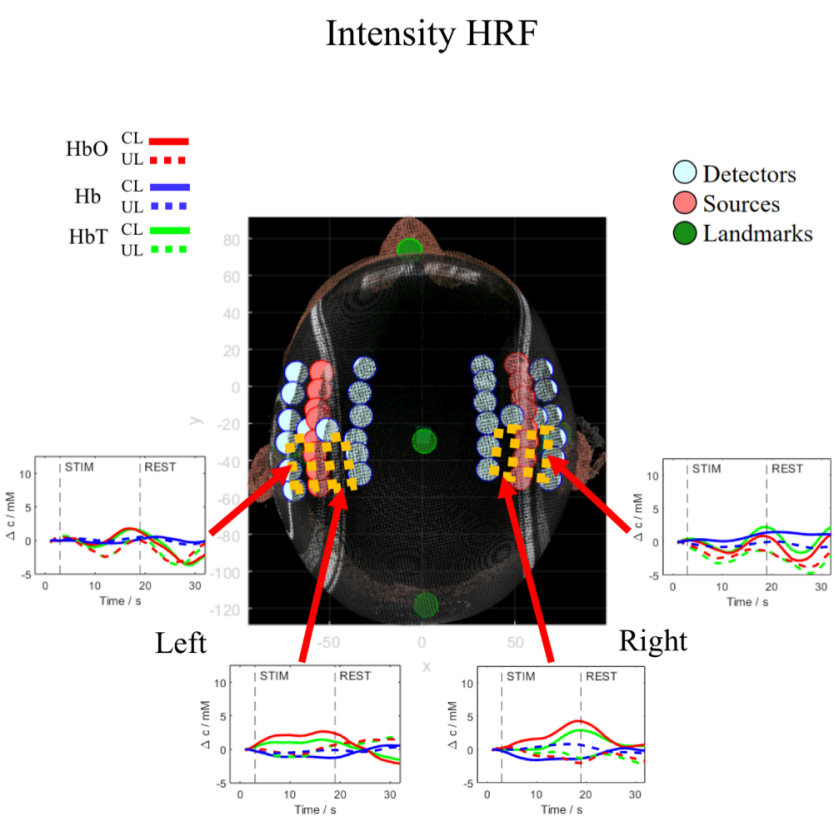

Figure 5.19: Changes in HbO, Hb and HbT calculated from Intensity

Figure 5.20 shows the HRF's for subject 1 using phase data, and as with the intensity case, LHS ROI 2 and RHS ROI 1 show the response due to motor cortex activation respectively. The judgment of if an haemodynamic response is due to motor cortex activity comes from visual assessment of what is happening to the changes in HbO and Hb respectively. Whilst there may be co-founding factors that contribute to a HRF which are not from motor cortex activity such as systemic changes in HbO and Hb in superficial tissue, it is known from literature that there are key features in the HRF from functional brain activation. These are an increase in HbO within seconds of the subject responding to the stimulus, coupled with an smaller decrease in Hb (D. G. Wyser et al., 2022). In addition, it has been shown that changes in Hb are more robust against systemic physiology compared to changes in HbO, therefore a decrease in Hb in response to the stimulus is a more reliable indicator of a 'true' functional haemodynamic response (Kirilina et al., 2013).

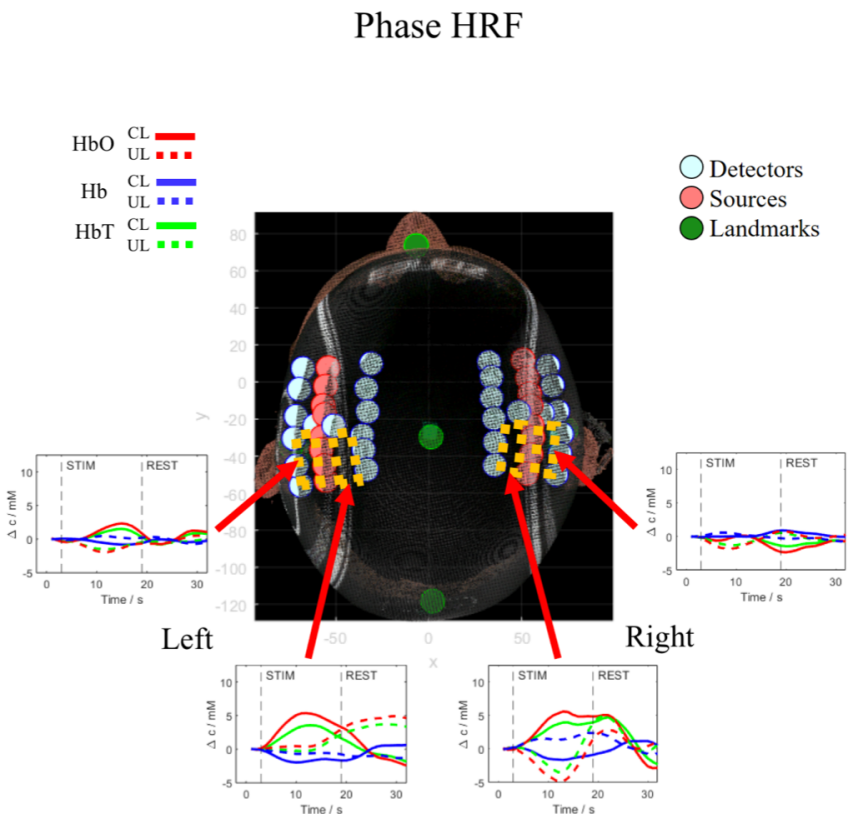

Figure 5.20: Changes in HbO, Hb and HbT calculated from Phase.

Then the combined intensity and phase case is shown in figure 5.21, with the same ROI's on the LHS and RHS showing the motor cortex HRF as seen with the separate intensity (figure 5.19) and phase (figure 5.20) cases.

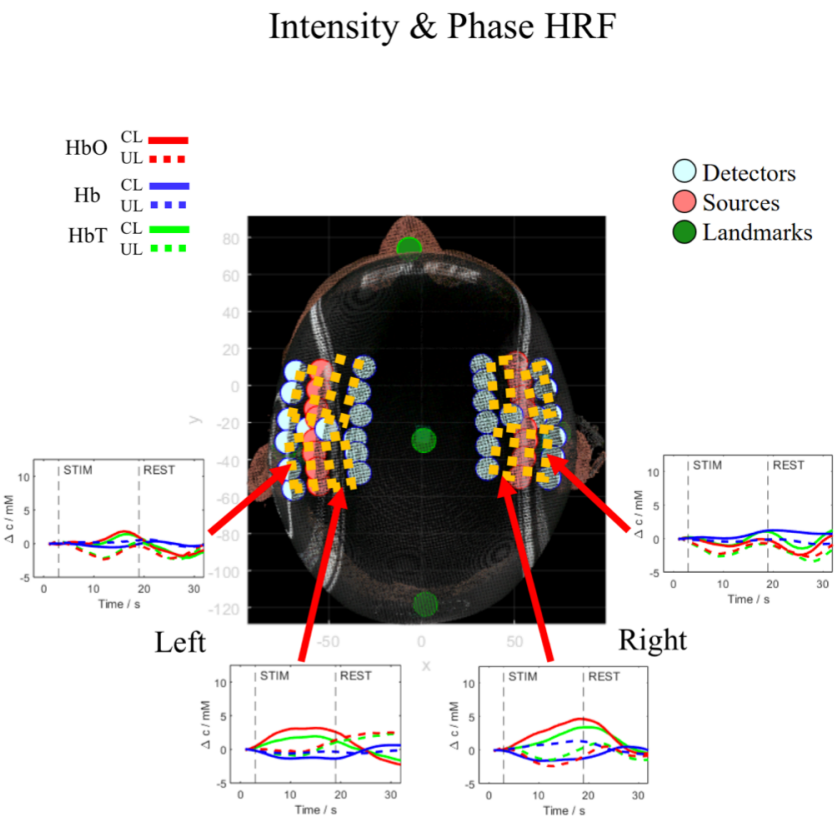

Figure 5.21: Changes in HbO, Hb and HbT calculated from Intensity and Phase combined

Figure 5.22 shows a direct comparison of the HRF using intensity, phase and the combined intensity & phase data for the ROI on each hemisphere corresponding directly to the motor cortex activation. For both the LHS and RHS, phase data shows a greater increase in HbO and a greater decrease in Hb than intensity data alone. For phase, HbO on the LHS increases to 5 mM, whereas for intensity the increase is to 3 mM. For the RHS, the peak change for HbO from phase is 5 mM whereas from intensity this is 4.5 mM. For Hb from phase data on the LHS, the peak change is -2 mM whereas from intensity this is -1 mM and on the RHS, the peak change from phase and from intensity are -2 mM. The shape of the HRF on the RHS from phase is broader than intensity, and for the LHS the shape of the HRF is similar between intensity and phase.

The advantages of using phase data is that there is a higher contrast in the HRF

compared to intensity data, however, the UL HRF of phase data for both the LHS and RHS shows more change than the UL HRF of intensity data. Ideally, the UL response would show minimal changes in response to the stimulus-rest period. When the data types are combined, the HRF for both the LHS and RHS attain attributes from the intensity and phase data. Combined intensity and phase show more contrast in CL HbO/Hb change compared to intensity alone, as well as showing smaller changes in the UL HRF compared to phase alone. Subject 1 shows that it is by combining intensity and phase that the positive aspects of phase data are retained, but that the negative aspects of phase data are reduced by the influence of the intensity data.

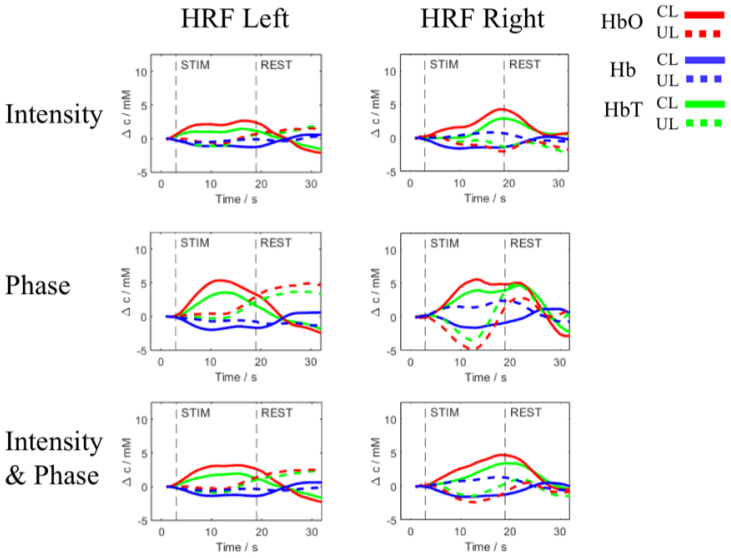

Figure 5.22: Comparing changes in HbO, Hb and HbT calculated from intensity, phase and intensity and phase combined from LHS ROI 2 and RHS ROI 1 in subject 1.

5.3.2 Standard HRF Subject 2

For subject 2, the placement of the cap was not symmetrically aligned on the subject, as can be observed with the source-detector locations in figure 5.23. This means that the ROI's on the LHS and RHS of the subject are not symmetric and the areas of expected motor cortex activation are ROI 2 and 4 on the LHS (as was subject 1), but they are ROI 2 and 4 on

the RHS. For intensity, a HRF from the motor cortex activation can be observed on the LHS between ROI 2 and 4, with an increase in HbO and a decrease in Hb seen in the CL response, whereas the UL responses do not show characteristics of cortical activation. On the RHS, intensity data doesn't show a clear CL HRF, as there is no discernible difference between the CL and UL changes in HbO and Hb.

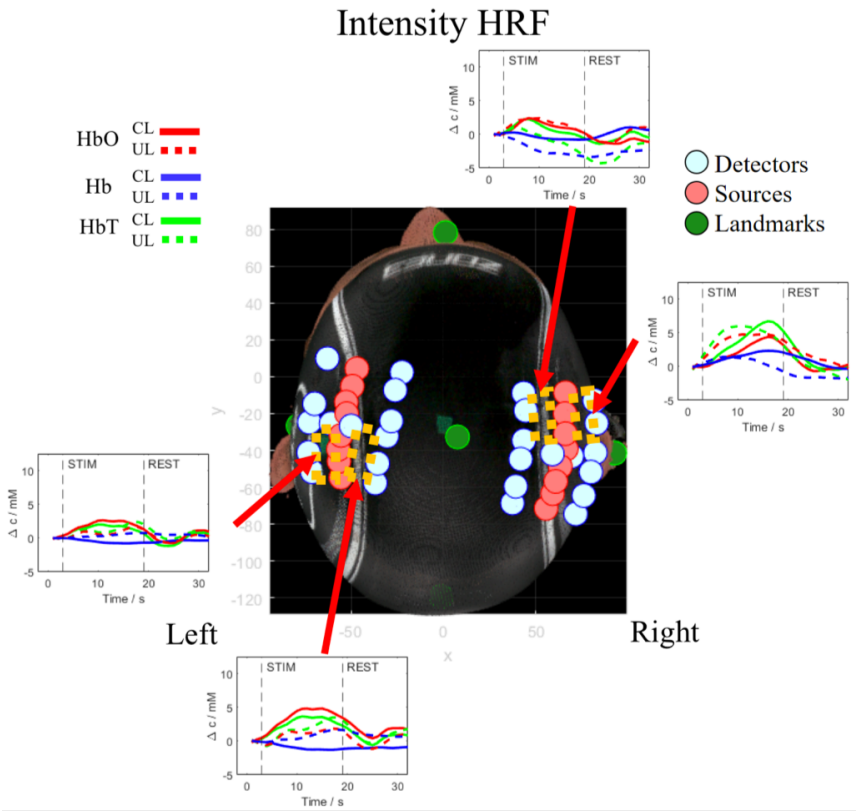

Figure 5.23: Changes in HbO, Hb and HbT calculated from Intensity

Figure 5.24 shows the HRF from phase data. On the LHS there are increases in HbO and decreases in Hb for the CL response in ROI 2 and 4. However the decrease in HbO after the stimulus period ends is observed to be slower than expected, as typically HbO will show negative changes after a stimulus period and recover back to a baseline of zero change. This is true for both ROI 2 and 4 on the LHS. This could be due to the positioning of the source-detector probes, as the M3 motor cortex area of the brain is on the edge of the LHS

ROI 2 and 4, so that the HRF's shown may have contributions from the motor cortex area, as well as non motor cortex surface of the brain. This may explain why the recovery of HbO to the baseline happens slower than expected.

The RHS shows a clearer HRF to motor cortex activation, as observed in ROI 2. HbO increases during the stimulus period, peaks at 8 s and then decreases back to zero during the rest period. During this time period in ROI 2, Hb decreases reaching a minima at 10 s and then increasing to zero during the rest period. On the RHS in ROI 4, there is no significant difference between the CL and UL response, therefore the hemodynamics observed here are likely to not be from motor cortex activation.

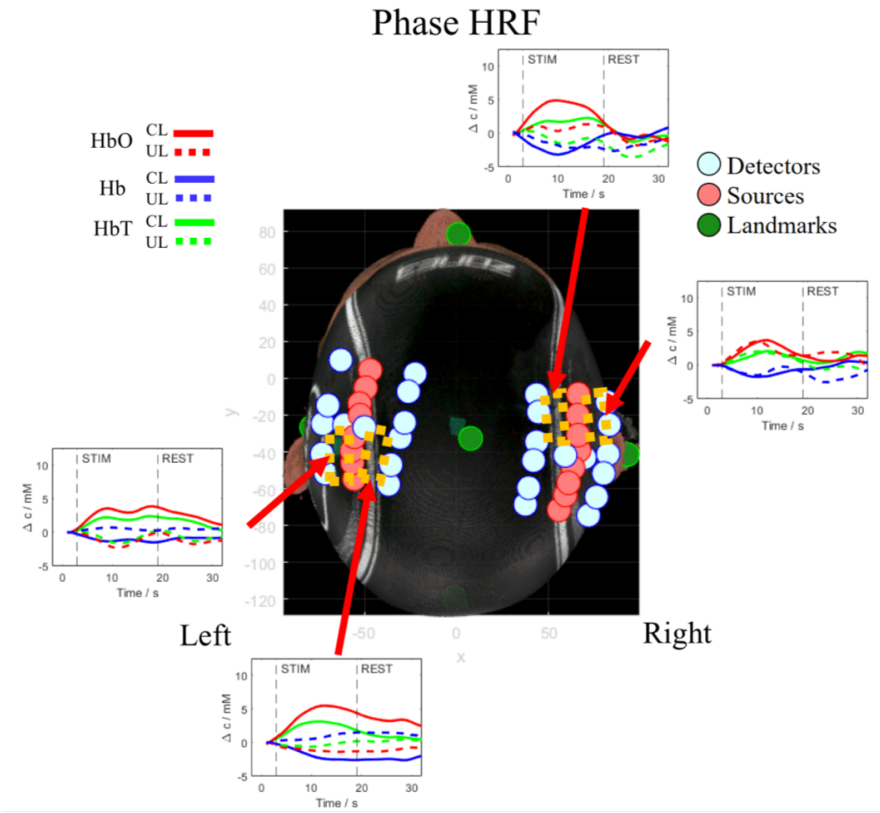

Figure 5.24: Changes in HbO, Hb and HbT calculated from Phase.

Figure 5.25 shows the HRF from the combined intensity and phase case for subject 2. In the combined case, motor cortex activation is observed in on the LHS across ROI 2 and

4, just as with the separate intensity and phase case. However on the RHS in ROI 2 and 4, combining intensity and phase data together means that a distinction between the CL and UL changes of HbO/Hb are not observed.

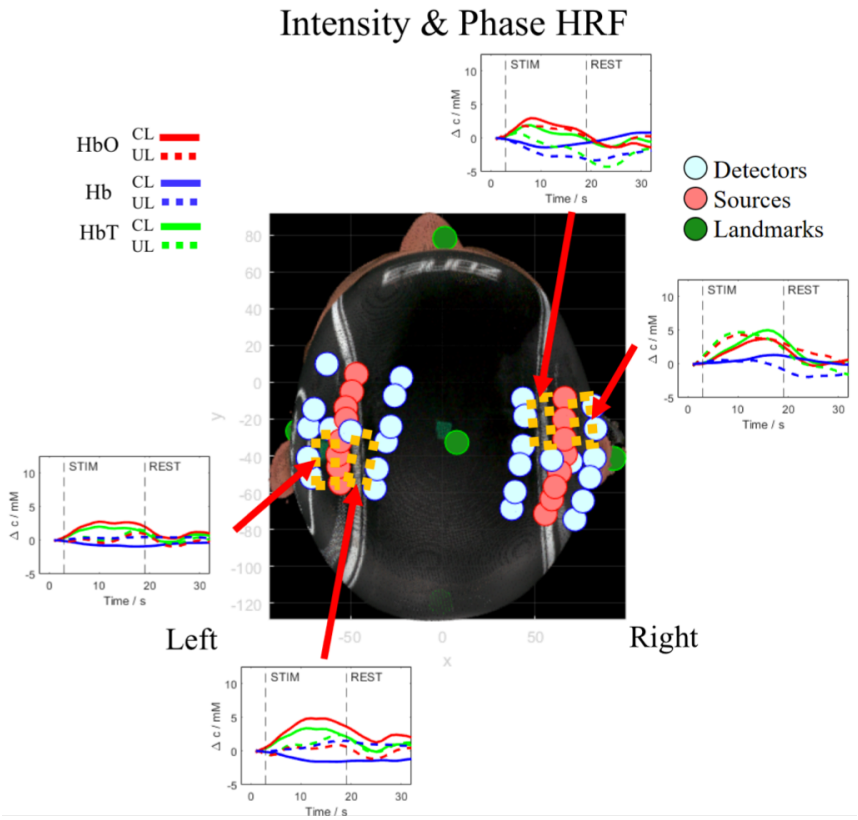

Figure 5.25: Changes in HbO, Hb and HbT calculated from Intensity and Phase combined

A direct comparison of the HRF's from each data type for subject 2 is given in figure 5.26. Firstly the most significant result from this is that for the RHS, phase data can detect motor cortex activation whereas for the same sources and detectors, intensity data can't. Secondly, as observed in subject 1, phase data increases the contrast of the HRF. The peak increase in HbO on the LHS is 5 mM from intensity data whereas this is shown to be 6 mM for phase data. Similarly the maximum decrease in Hb is 1 mM from intensity data and -2.5 mM from phase data.

The combined intensity and phase data behaves similarly to that of subject 1, where

the attributes of both data types are shared. This means that on the LHS, the shape of the HRF for HbO decreases closer to the zero baseline during the rest period than in the phase case alone, whilst retaining the contrast from phase data. On the RHS however, there becomes a smaller difference between the CL and UL HRF, particularly in the changes of HbO. This means that based upon the combined intensity and phase case alone, it is hard to suggest the HRF is attributed from motor cortex activation, whereas for the phase case alone, the HRF behaves as expected from cortical activation. So subject 2 tells us that whilst phase data can again show increased contrast, careful thought should be employed as to when to include intensity data.

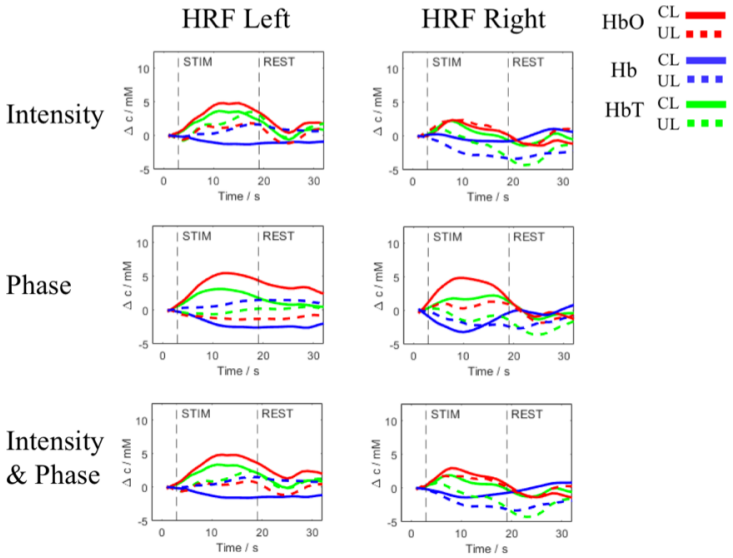

Figure 5.26: Comparing changes in HbO, Hb and HbT calculated from intensity, phase and intensity and phase combined from LHS ROI 2 and RHS ROI 2 in subject 2.

5.3.3 Standard HRF Subject 3

Subject 3 has a similar source-detector probe alignment to subject 1, where the location of the M3/M4 points align with ROI 2 and 4 on the LHS and ROI 1 and 3 on the RHS, which can be seen in the intensity case in figure 5.27. For the intensity case, it appears that the LHS may contain changes in HbO/Hb which appear to come from superficial tissue, despite

the use of SSR. This is demonstrated by the double peak nature of the change in HbO for the CL response, as well as the large change in HbO for the UL. This could be due to the the fact the channels used for SSR are in the center of the S-D array, and therefore do not sample superficial tissue across the entire S-D array. For the RHS, ROI 1 shows a small HRF from motor cortex activation with an increase in HbO during the stimulus period and a decrease during the rest period, additionally there is an expected decrease in Hb during the stimulus period and a recovery to baseline in the rest period. Similar behaviour of the HRF is observed for the CL response of ROI 3 on the RHS, however there are also considerable changes in the HRF for the UL response in this area.

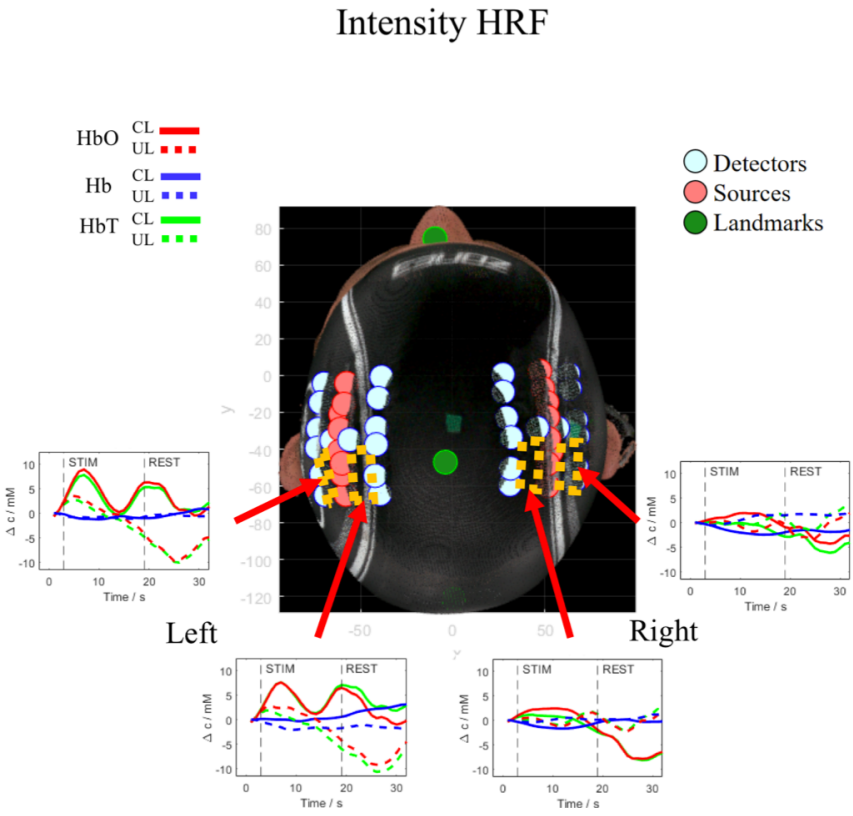

Figure 5.27: Changes in HbO, Hb and HbT calculated from Intensity

Figure 5.28 shows the phase case of the HRF for subject 3. On the LHS in ROI 2 and 4 are HRF's which have characteristics of cortical activation, particularly ROI 4 with a sustained broad increase of CL HbO and a decrease in CL Hb during the stimulus period,

followed by a relaxation of both chromophores to the baseline during the rest period. On the RHS, ROI 3 clearly shows the HRF from motor cortex activity. The CL response in ROI 1 is characteristic of functional activation, but the UL response contains a lot of noise.

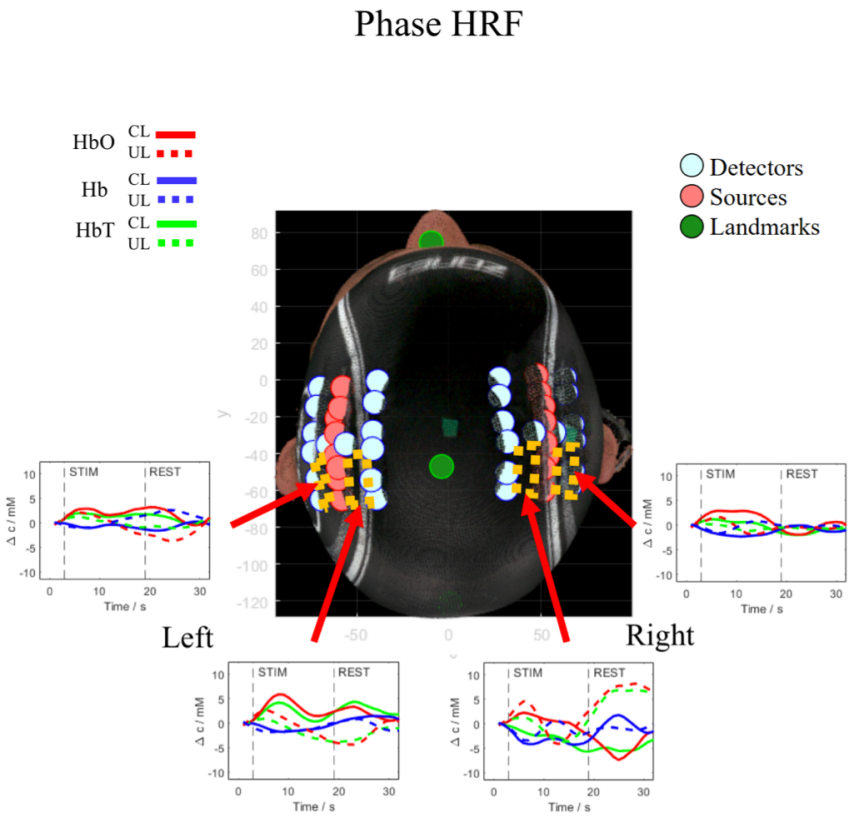

Figure 5.28: Changes in HbO, Hb and HbT calculated from Phase.

Figure 5.29 shows the combined intensity and phase case for subject 3.

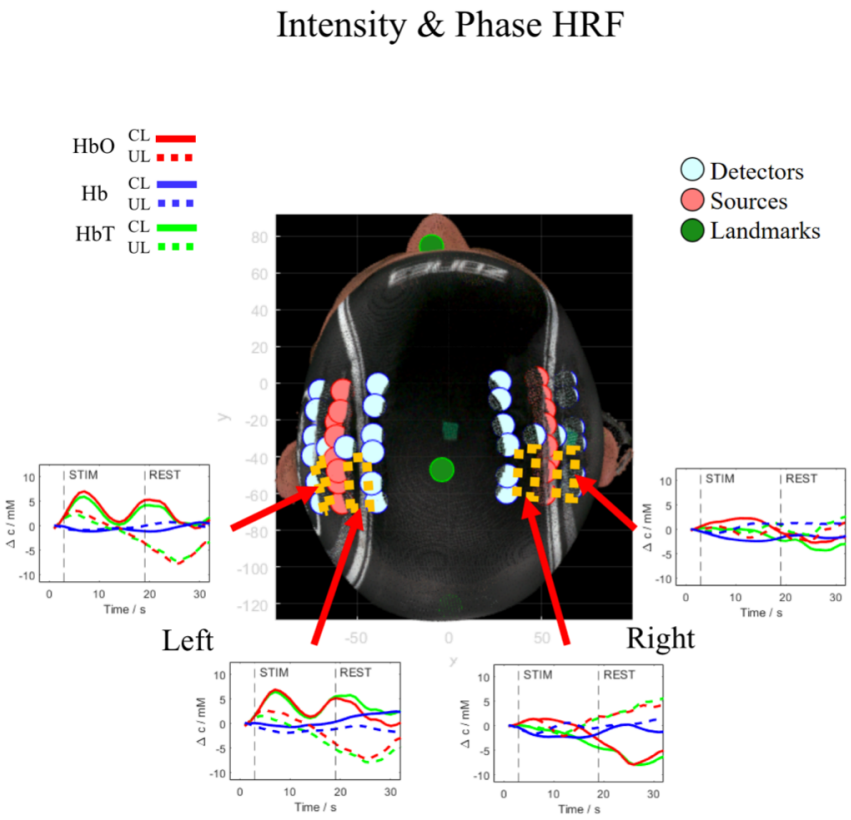

Figure 5.29: Changes in HbO, Hb and HbT calculated from Intensity and Phase combined.

Finally, figure 5.30 shows the direct comparison between the different data types for subject 3. By looking at the LHS, it can be observed that the intensity signal had significant influence from superficial tissue hemodynamics, as characterised from the double peak in the change of CL HbO. The phase derived HRF on the LHS shows significantly less influence of superficial tissue, and reveals the cortical activity from the motor cortex, due to it's broad shape and increases in CL HbO and decreases in CL Hb during the stimulus period. There is still a slight double peak shape within the phase CL HRF, but this is suppressed compared to the intensity derived CL HRF. This is consistent with what is known about phase data being less sensitive to superficial tissue compared to intensity data and that phase samples slightly deeper in tissue than intensity data (Doulgerakis, Eggebrecht, and Dehghani, 2019).

As well as being able to detect brain activation over the motor cortex region, the UL

response from phase data is more stable compared to the UL response in intensity on the LHS, which again suggests that whilst phase data is inherently nosier than intensity data, it has less influence from superficial tissue than intensity data.

The LHS HRF derived from the combined intensity and phase data for subject 3 is a good visualisation about how the characteristics of the two data types combine. In the combined data type case, there is the double peak change in CL HbO, which is smaller and less pronounced than seen in the intensity only case, however the CL HbO HRF doesn't reach the broadness as observed in the phase only case.

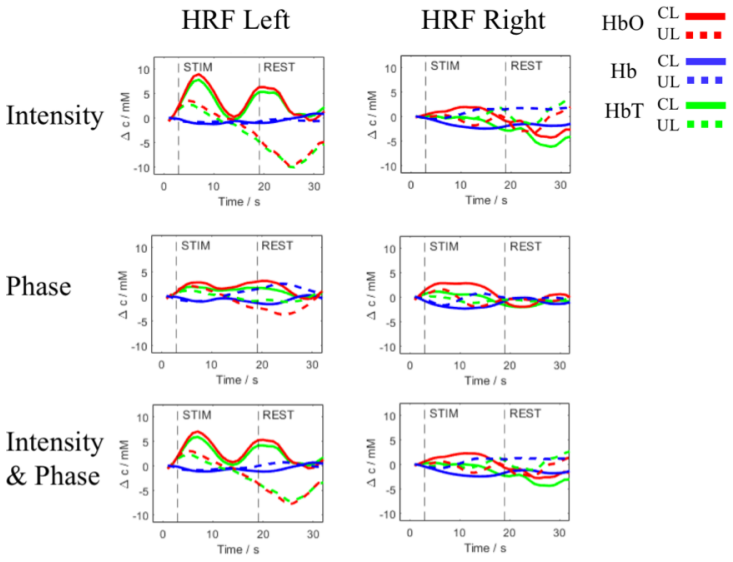

Figure 5.30: Comparing changes in HbO, Hb and HbT calculated from intensity, phase and intensity and phase combined from LHS ROI 4 and RHS ROI 3 in subject 3.

For the HRF on the RHS, all three data types show the HRF to motor cortex activity, however it is most distinguishable for the phase only case. This is due to the fact that the largest and broadest increases in CL HbO during the stimulus period for the phase case, where the peak increase of HbO is 3.5 mM, whereas for intensity it is 2.5 mM. There is also a larger and broader decrease in CL Hb for the phase case compared to the intensity case, of -2.5 mM to -2 mM respectively.

Both HbO and Hb recover back to the baseline during the start of the rest period and are more stable in the phase derived HRF's compared to the intensity derived HRF's. As well as this, the HbO/Hb UL changes in the intensity case are less stable than the phase case, which is similar to what was observed on the LHS for subject 3. When intensity and phase are combined, as with subject 1 and 2, subject 3 shows that the characteristics of both data types are shared, which means a clearer and cleaner HRF can be seen when compared to intensity alone.

5.3.4 Tomography Subject 1

Changes in HbO, Hb and HbT were calculated using tomographic reconstruction as outlined in section 5.2, using the jacobian of the registered subject atlas FEM for each subject. The channels in the active ROI shown in the spectroscopic reconstructions for each subject respectively, i.e LHS ROI 2 & 4 for subject 1, 2 and 3, RHS ROI 1 & 3 for subject 1 and 3, RHS ROI 2 & 4 for subject 3, were used for the tomographic reconstruction. The figures shown have been normalized with respect to each data type, such that meaningful comparisons can be made between intensity, phase and the combined intensity and phase. The normalization scales from the maximum increase (+ 1) to the maximum decrease (- 1).

For all subjects, changes in HbO are shown, whereas the changes in Hb and HbT are only given for subject 1. This is because the changes in Hb and HbT from subject 1 are representative for subjects 2 and 3. The tomographic reconstruction for subject 1 can be seen in figure 5.31, where changes in HbO can seen from using intensity, phase and combined intensity and phase data. All three data types show a response in both the left and right hemisphere around the expected C3 and C4 landmark points respectively. The maximum increase in the normalized change of HbO is from the phase data on the left hemisphere (1.00) and from the combined intensity and phase on the right hemisphere (0.86), which can

be noted in table 5.2. Both the left and right hemispheres activation's are clearly seen for the phase (1.00 LHS and 0.85 RHS) and combined intensity and phase case (0.99 LHS and 0.86 RHS), whereas for intensity alone, the maximum change in HbO is much smaller (0.58 LHS and 0.37 RHS). This demonstrates that phase data can show brain activation that intensity is not able to reveal and that combining both intensity and phase together, the features of both data types are combined.

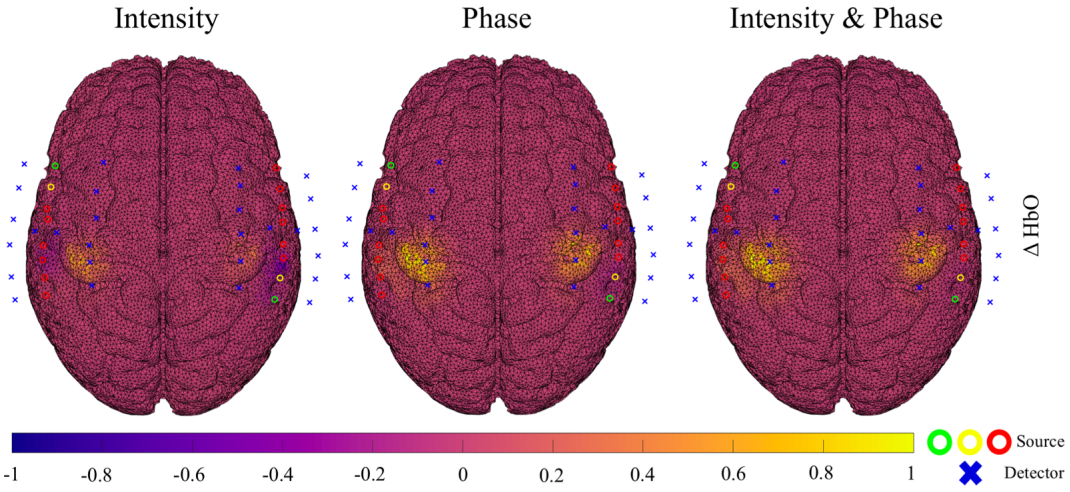

Figure 5.31: Tomographic reconstruction of HbO at t = 8 s for subject 1, using intensity, phase and combined intensity and phase data.

Table 5.2: The maximum (top row) and minimum (bottom row) values from the normalized changes in HbO of subject 1 from figure 5.31.

LHS			RHS		
I	ϕ	I ϕ	I	ϕ	I ϕ
0.58	1.00	0.99	0.37	0.85	0.86
-0.24	-0.03	0.00	-0.63	-0.19	-0.13

Changes in Hb from the tomographic reconstruction of subject 1 are shown in figure 5.32 and the maximum changes are seen in table 5.3. The decreases in Hb are seen in the same ROI as the increase of HbO, which are ROI 2 on the LHS and ROI 1 on the RHS. The accompanying maximum and minimum changes in Hb are seen in table 5.3. For all three data types, there is a broad decrease in Hb, of -0.290 to -0.398 and a minimal increase

in Hb, of 3.01x10^{-12} to 0.197. This aligns with the expected HRF for Hb for functional activation, which shows that Hb decreases in the region of the cortex responsible for the stimulus response and is consistent with the spectroscopic results shown in figure 5.22.

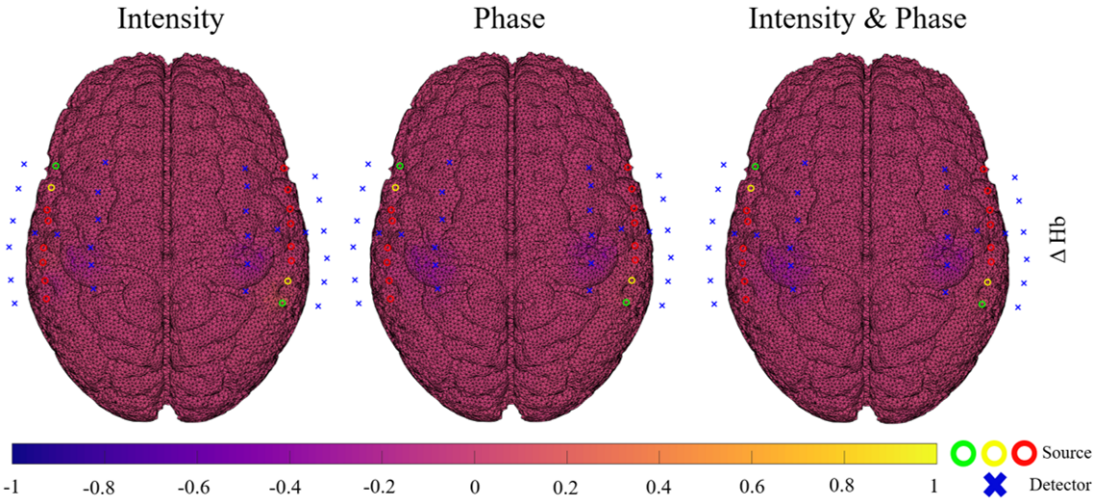

Figure 5.32: Tomographic reconstruction of Hb at t = 8 s for subject 1, using intensity, phase and combined intensity and phase data.

The inclusion of phase data increase the contrast in changes in Hb, in both phase data alone, and the combination of intensity and phase. This is demonstrated as on the LHS, the maximum decrease of Hb is given by phase, -0.343 and intensity and phase, -0.348, whereas from intensity data, there is a smaller decrease of -0.290. On the RHS, the difference in contrast is smaller compared to the LHS, but phase and intensity and phase (-0.398 and -0.393) show a bigger decrease in Hb compared to intensity (-0.339). As well as a larger decrease in Hb, phase and intensity and phase show a smaller increase in Hb compared to intensity. For the LHS, Hb increases by 0.053 compared to 0.0015 for phase and 3.01x10^{-12} for intensity and phase, and similarly, Hb increases the most with intensity, 0.197, and less with phase, 0.063 and intensity and phase, 0.052. This shows that the inclusion of phase increases Hb contrast and suppresses artifacts of increases in Hb in response to functional activation.

Table 5.3: The maximum (top row) and minimum (bottom row) values from the normalized changes in Hb of subject 1 from figure 5.32.

LHS			RHS		
I	ϕ	I ϕ	I	ϕ	I ϕ
0.053	0.0015	$3.01\text{x}10^{-12}$	0.197	0.063	0.052
-0.290	-0.343	-0.348	-0.339	-0.398	-0.393

Changes in HbT from the tomographic reconstruction for subject 1 are shown in figure 5.33 and the maximum changes are seen in table 5.4. The behaviour of HbT is directly linked to both changes in HbO and Hb, since HbT is directly derived from the changes in HbO and Hb. On both the LHS and RHS, the inclusion of phase increases the contrast in the change of HbT. This is most significant on the RHS, where intensity yields a maximum change of 0.033, whereas for phase this is 0.450 and for intensity and phase this is 0.464. Intensity data also shows an maximum decrease in HbT on the LHS of -0.250, whereas for phase this is 0.657 and 0.650 for intensity and phase. This is the net result of smaller increases from intensity derived HbO changes and this is not consistent with spectroscopic results seen in 5.22. This suggests part of the tomography derived cortex changes in HbT are influenced by changes absorption superficial tissue. The maximum decrease in HbT is smaller with phase and intensity and phase, for both the LHS and RHS, which is consistent with the spectroscopic changes in HbT, which suggests these data types are more accurately reflecting the true changes in HbT on the surface of the cortex.

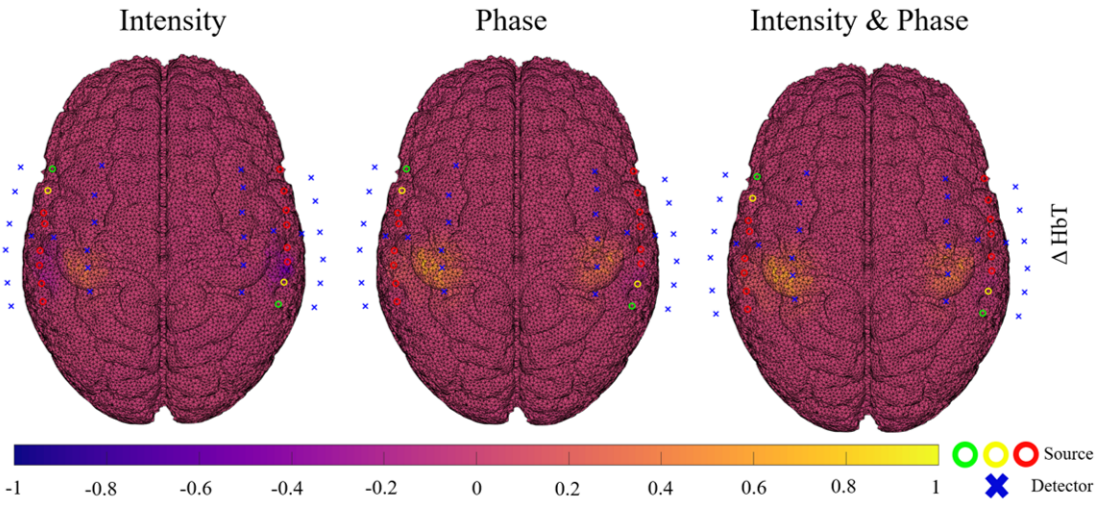

Figure 5.33: Tomographic reconstruction of HbT at t = 8 s for subject 1, using intensity, phase and combined intensity and phase data.

Table 5.4: The maximum (top row) and minimum (bottom row) values from the normalized changes in HbT of subject 1 from figure 5.33.

LHS			RHS		
I	ϕ	I ϕ	I	ϕ	I ϕ
0.329	0.657	0.650	0.033	0.450	0.464
-0.250	-0.036	-2.232x10^{-4}	-0.637	-0.153	-0.102

The Z score was calculated from the tomographic reconstruction for subject 1 using equation 5.17 (Ichikawa et al., 2019) , where $\overline{C_s}$ is the mean concentration change during the stimulus period, $\overline{Y_b}$ is the mean concentration change during the baseline period and $\sigma(C_r)$ is the standard deviation of the data during the baseline period.

$$Z = \frac{\overline{C_s} - \overline{C_r}}{\sigma(C_r)} \tag{5.17}$$

The Z score was calculated for each node on the surface of the cortex and for each data type (Intensity, phase and Intensity and phase) for both the LHS and RHS separately. The Z scores then presented are from the node on the cortex that had the highest change in

chromophore concentration at t = 8 s during tomography. For subject 1, this can be seen in figure 5.34. HbO and HbT show positive Z scores, whereas Hb shows a negative Z score, which is expected due to the increase in HbO and HbT during the stimulus period and the decrease in Hb during the stimulus period. For the LHS, phase and the combined intensity and phase show higher Z scores than intensity for both HbO and HbT, suggesting a more significant change due to the stimulus period. However for the RHS, the opposite is true. For Hb, for both the LHS and RHS, phase and intensity and phase record a larger negative Z score. For example for Hb on the LHS the Z score are -1.62 to -2.63 to -2.49 for intensity, phase and intensity and phase respectively. This suggests that phase data for subject 1, was more sensitive to showing significant changes in Hb with respect to functional activation from tomography compared to intensity data. Whereas for HbO and HbT, intensity and phase performed variably depending on the hemisphere of the cortex (LHS or RHS).

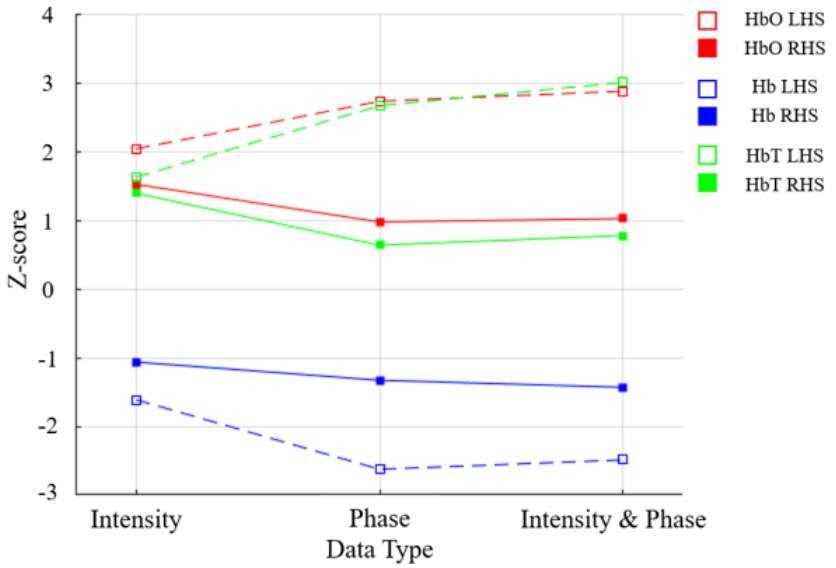

Figure 5.34: The Z score for subject 1 each data type of HbO, Hb and HbT. Z scores given are taken from the node on the cortex that has the highest change in concentration at t = 8 s. for each chromophore respectively (figure 5.33).

5.3.5 Tomography Subject 2

The tomographic reconstruction for subject 2 can be seen in figure 5.35. For intensity data, the maximum change in HbO is much larger in the LHS (0.87) compared to the RHS (0.47). Whereas, for phase (0.86 LHS and 0.98 RHS) and the combined intensity and phase (0.89 LHS and 0.98 RHS), changes in HbO are clearly seen on both the LHS and RHS. The change in HbO from intensity on the RHS is half of that compared to the RHS changes in HbO from phase and intensity and phase. This can be seen in table 5.5. There is an asymmetry of the HbO response between the LHS and RHS for the phase data and combined intensity and phase data. This is caused by the fact that the ROI's used on the LHS and RHS are not perfectly symmetrical, i.e the cap was tilted about the sagittal axis on the subject's head. Despite this, there is still a symmetry in the partial overlap of the changes in HbO between the LHS and RHS.

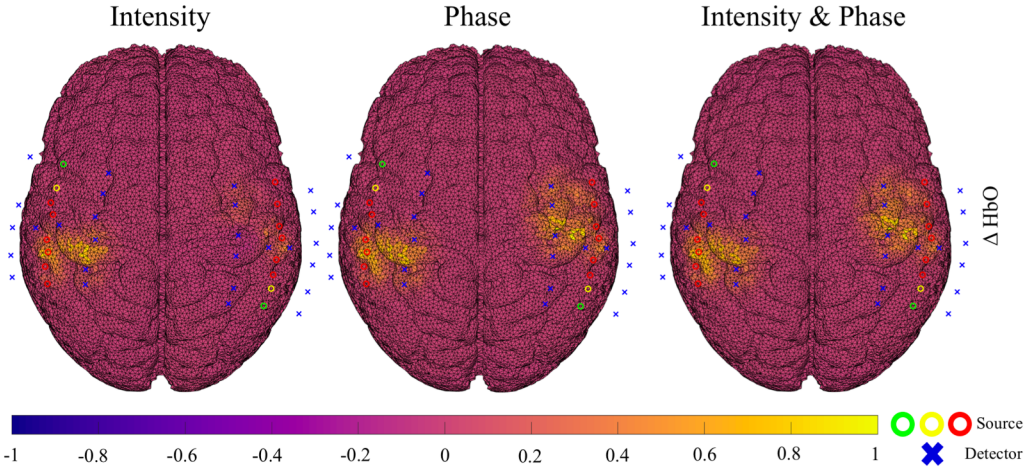

Figure 5.35: Tomographic reconstruction of HbO at t = 8 s for subject 2, using intensity, phase and combined intensity and phase data.

Table 5.5: The maximum (top row) and minimum (bottom row) values from the normalized changes in HbO of subject 2 from figure 5.35.

LHS			RHS		
I	ϕ	I ϕ	I	ϕ	I ϕ
0.87	0.86	0.89	0.47	0.98	0.98
0.00	0.00	0.00	-0.06	0.00	0.00

The Z scores for subject 2 are shown in figure 5.36. For the LHS, both HbO and HbT had the highest Z score for intensity (3.42, HbO) compared to phase (1.08, HbO) and intensity and phase (1.17, HbO), however for the RHS, phase (10.40, HbO) and intensity and phase (9.78, HbO) recorded a higher Z score than intensity (2.70, HbO). These values for phase and intensity and phase are significantly higher than intensity alone, however the magnitude of these Z scores are unrealistically high, as they imply that HbO changed by 10 standard deviations of the baseline data. Such a large Z score could be due to the fact that these are Z scores calculated from the tomographic reconstruction of chromophores. Since the Z score of only one node was considered (the node with the highest change in chromophore concentration) for each data type and chromophore, it is possible that there exists local variations in Z score between nearby nodes, and that the single node chosen could exhibit behaviour which deviates from nodes around it.

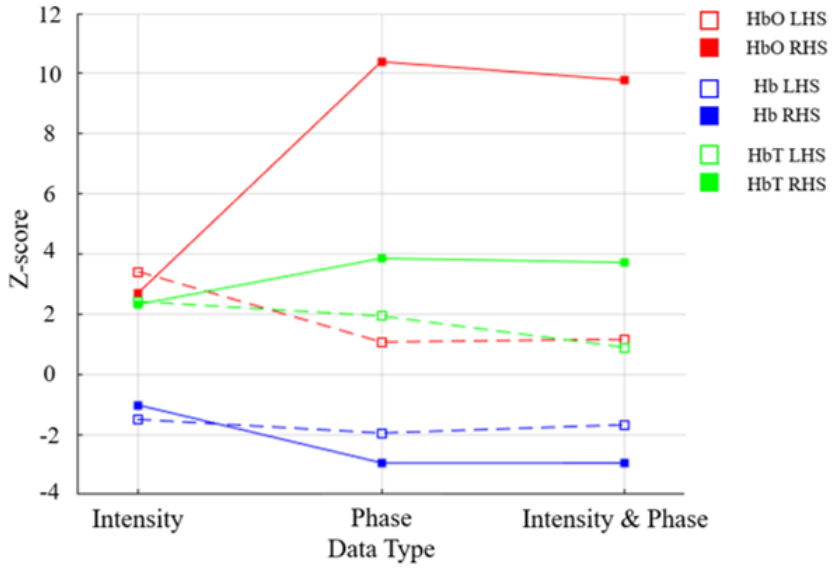

Figure 5.36: The Z score for subject 2 each data type of HbO, Hb and HbT. Z scores given are taken from the node on the cortex that has the highest change in concentration at t = 8 s. for each chromophore respectively (figure 5.35).

Similar to subject 1, for Hb on both the LHS and RHS, phase and the combined intensity and phase show a larger decrease in Z score compared to intensity. For the LHS

that is -1.95 for phase, -1.68 for intensity and phase and -1.50 for intensity, whereas for the RHS, the differences are larger, -2.94 for phase, -2.95 for intensity and phase, compared to -1.02 for intensity. This suggests, as with subject 1, the inclusion of phase data shows more significant changes in Hb as compared to intensity data alone.

5.3.6 Tomography Subject 3

The tomographic reconstruction for subject 3 can be seen in figure 5.37, and as with subject 1 and 2, the response in HbO is observed around the M3 and M4 landmark locations. For intensity, the change in HbO (0.44 LHS and 0.40 RHS) is smaller than that of phase (0.73 LHS and 1.00 RHS) and the combined intensity and phase (0.77 LHS and 1.00 RHS) and the intensity derived response is less visible on both the LHS and RHS. This can be seen in table 5.6.

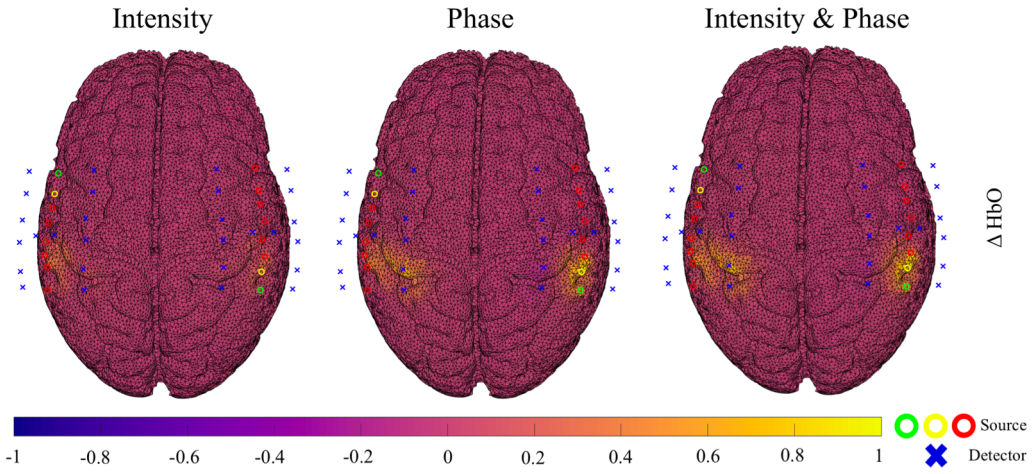

Figure 5.37: Tomographic reconstruction of HbO at t = 8 s for subject 3, using intensity, phase and combined intensity and phase data.

Table 5.6: The maximum (top row) and minimum (bottom row) values from the normalized changes in HbO of subject 3 from figure 5.37.

LHS			RHS		
I	ϕ	I ϕ	I	ϕ	I ϕ
0.44	0.73	0.77	0.40	1.00	1.00
0.00	0.00	0.00	0.00	-0.13	-0.08

The Z score for subject 3 can be seen in figure 5.38. For HbO on the LHS, phase has the highest Z score of 1.72 compared to 1.34 for intensity and 1.50 for intensity and phase. HbO for the RHS shows that the intensity, 2.16 and phase, 2.06 have similar Z scores, whereas the combined intensity and phase has the highest Z score of 2.53 and that the HbT on the RHS follows this pattern. For HbT on the LHS, both the intensity and the phase exhibit typical behaviour, with phase having a slightly higher Z score of 1.75 compared to 1.37 of intensity. However, for HbT on the LHS, the Z score is actually negative, suggesting that HbT does not increase during the stimulus period. As seen with subject 2's LHS HbO (figure 5.36 ,it is possible that the single node selection has yielded an anomaly. Finally, as seen in subject 1 and subject 2, the inclusion of phase causes a bigger decrease of Z score when compared to intensity alone. For the RHS, HbO has a small positive score of 0.36 from intensity and for the LHS the Z score is -0.39, which suggests that intensity is not as sensitive to changes in Hb, when compared to phase. This is demonstrated as phase shows a score of -2.33 and -1.14 for the LHS and RHS respectively.

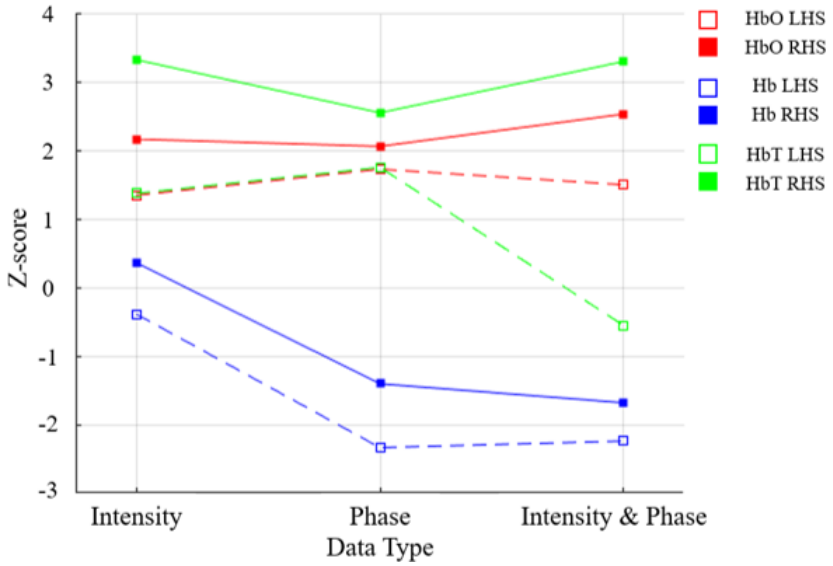

Figure 5.38: The Z score for subject 3 each data type of HbO, Hb and HbT. Z scores given are taken from the node on the cortex that has the highest change in concentration at t = 8 s. for each chromophore respectively (figure 5.37).

5.3.7 Dual slopes Subject 1

A demonstration of dual slopes reconstruction is shown for subject 1, using intensity and phase data separately, which can be seen in figures 5.39 and 5.40 respectively. For each ROI on each hemisphere, there are 2 dual slopes, so for ROI 2 and ROI 4 on the LHS there are a total of 4 dual slopes, and for ROI 1 and ROI 3 on the RHS there are a toal of 4 dual slopes, as demonstrated in figure 5.18. Figure 5.39 shows that the expected HRF can be seen in ROI 2 on the LHS and in ROI 1 on the RHS, which is the same as the standard spectroscopic result in figure 5.19. The HRF functions in ROI 4 on the LHS and ROI 3 on the RHS do not appear to show activation from the stimulus. Only a single dual slope reconstruction is shown in ROI 2 on the LHS and ROI 1 on the RHS respectively, this is because the dual slope requires four specific measurement channels to be available, i.e meet the criteria for SNR, and this was not met in all the channels required for full dual slopes reconstruction.

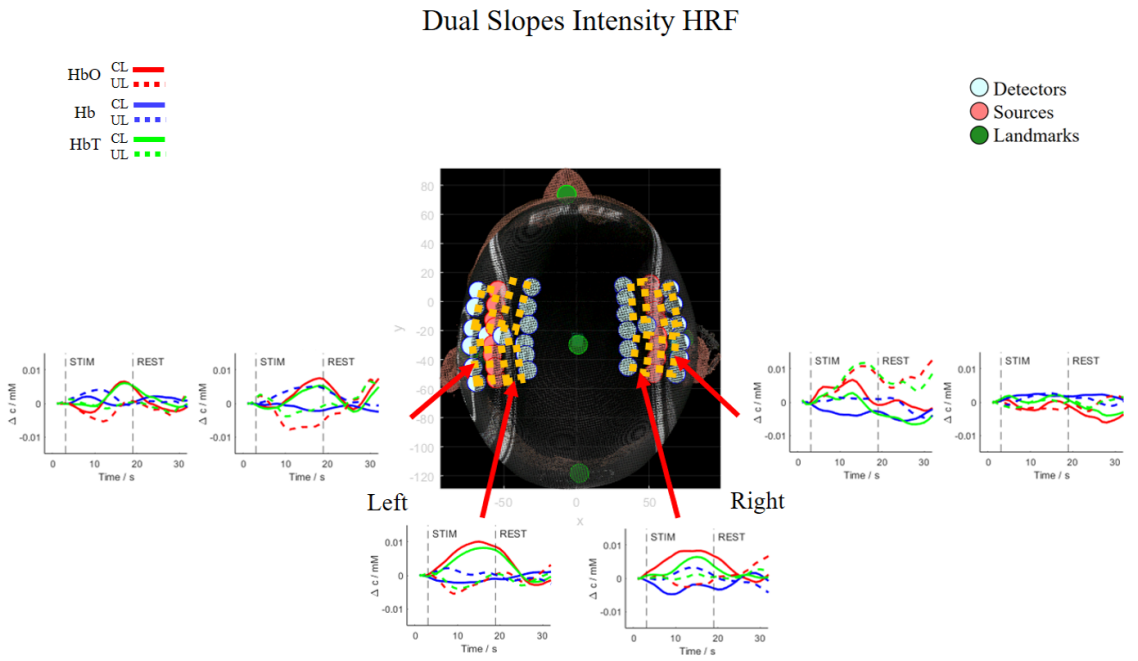

Figure 5.39: Changes in HbO, Hb and HbT calculated from intensity data using dual slopes.

For phase data, the dual slope reconstruction was not as effective as the intensity reconstruction, as the HRF was only observed in ROI 2 on the LHS. No dual slopes reconstruction was possible in ROI 1 on the RHS, because the required channels for dual slope reconstruction were not available. These results demonstrate that the design of the source detector array can reconstruct dual slopes, however, the sensitivity of the phase data with respect to the noise of the data, means it is susceptible to loose channels required to create the dual slopes. For this demonstration of dual slopes, the combined intensity and phase case is not shown,

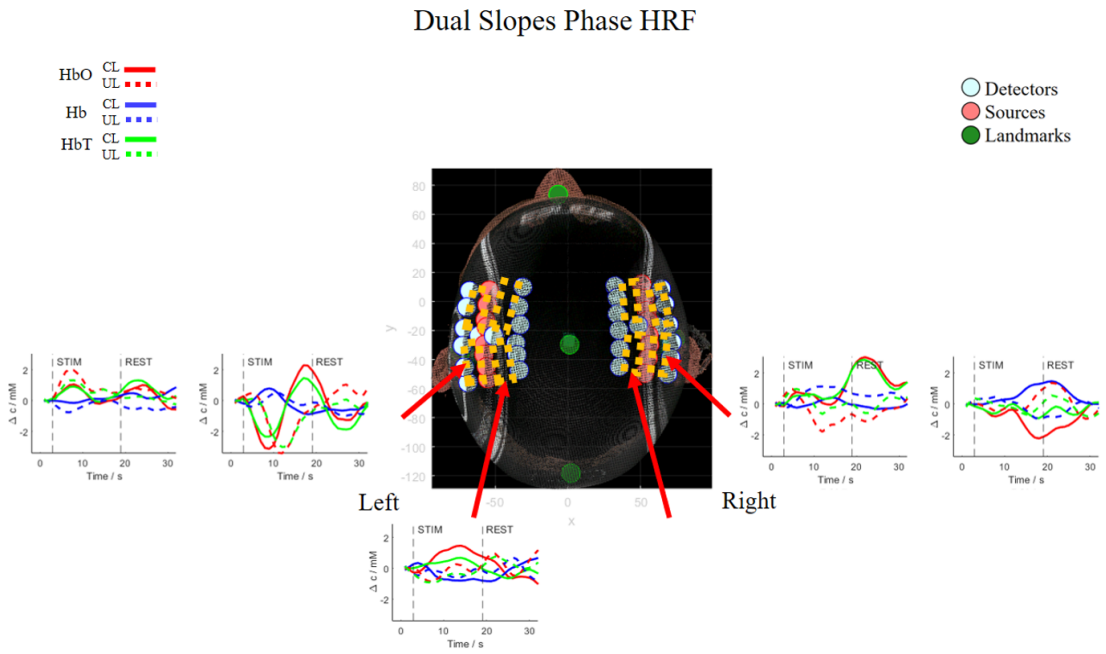

Figure 5.40: Changes in HbO, Hb and HbT calculated from phase data using dual slopes.

5.4 Discussion

In this chapter, the use of Frequency domain data has been evaluated for functional brain imaging on three healthy subjects. The workflow demonstrated has shown the use of 3D printed source-detector mounts (figure 5.3), a design of a source-detector array for standard and dual slope reconstruction paradigms, including the use of short signal regression (figure 5.4), the use of a subject specific 3D camera registration method (figure 5.5) and the use of intensity and phase data for both spectroscopic (figures 5.19 to 5.30) and tomographic reconstruction (figures 5.31 to 5.37).

The use of the neoprene cap and 3D printed mounts allowed for data collection using the ISS Imagent Frequency Domain system. The ISS Imagent allows the end user to be fully flexible with their data collection approach, because the system provides no manufacturer made source-detector cap or source-detector geometry. The advantage of this, is the

experimental flexibility, however the disadvantage is that it can be challenging to solve the engineering problem of enabling adequate and reliable source-detector coupling to a subject's head. The neoprene cap could accommodate for varying head shapes and sizes, as well as different hairstyles, however the cap has a preference for smaller heads, as when the material is stretched too much, it was prone to sliding and moving on the head. The 3D printed mounts held the source-detector fibers in place, however the success rate of the mounts to keep the fibers in contact with the scalp was very sensitive to the mount diameter and it was challenging to adjust fibers once they had all been put on the subject (figure 5.3 B. to D.). So whilst this set up allowed for data collection, there were challenges present and optimisations could have been made.

The source-detector arrangement (figure 5.4) was designed to allow standard and dual slope paradigm reconstruction. That was achieved, since both spectroscopy and tomography was performed, with short channel regression, however because of the number of sources and detectors available, only a maximum of 8 dual slopes were available on each hemisphere. Of these 8, only a limited number could be used for each subject, due to the fact dual slopes requires very specific channels to be available. Because of some of the experimental challenges described above, this caused some sources and detectors to not have sufficient scalp coupling, thus rendering some of the dual slopes unusable.

A key difference between the source-detector design presented in this work and that in dual slopes literature (Blaney, Fernandez, et al., 2023), 15 sources and 10 detectors were used on the scalp on the area visual cortex, which is one more source than used in this study, and importantly the probes in this study were split between the left and right hemisphere, whereas in Blaney, Fernandez, et al., 2023, they were not split. This meant less potential dual slopes were available, as in this study 8 were available on each hemisphere, for a total of 16, but in Blaney, Fernandez, et al., 2023, a total of 30 dual slope sets were available. Overall the engineering solutions to data collection presented in chapters 5.2.1 and 5.2.2 allowed for

reasonable data collection to be performed, however these still presented some challenges, so more tailored engineering solutions from the manufacturer would lead to easier and more reliable data collection.

The 3D optical registration method presented in chapter 5.2.3 demonstrated a workflow that could register a general atlas (Colin-27) to the anatomical surface features of a subject's head and allow for the source-detector placement on the registered atlas, depending on where the sources and detectors were on the subject during the data collection. In previous literature other methods of registration include using 3D digitiser devices such as the Polhemus Digitizer (Polhemus, United States) have been reported for fNIRS subject registration (Tsuzuki and Dan, 2014) or using MRI markers on the scalp, to then obtain source-detector positions from subject MRI scans (M. Chen et al., 2017).

The main difference between the approach presented here, and those cited, is that the 3D camera can be used in many different environments. For example, the Polhemus Digitizer relies on electromagnetic fields, so is sensitive to metal, which causes artifacts in the registration. This means the device may not be suitable for some lab or clinical settings. A similar study using an optical registration method (Uchitel et al., 2022) has been previously reported, but instead of using the Artec Leo 3D camera, they used a high end smartphone. However like the previously mentioned studies, they also require the subject specific MRI scan in their workflow, whereas this workflow doesn't require subject specific MRI scans.

Overall the 3D camera registration worked as intended, and the biggest advantage of the method was being able to locate source-detector locations in 3D on the subjects head, and then register these onto the scalp surface of the registered atlas model, instead of guessing or approximating these source-detector locations. A criticism of the method presented, is that currently no quantitative evaluation of the registration was performed or evaluated. This is because of the absence of MRI and fMRI measurements meant that a. the

subject's true anatomy could not be obtained for comparison to the registered atlas and b. the functional activation from the tomographic reconstruction using this registration, can't be compared to the functional activation that would be seen from fMRI. So future studies that aim to quantify the accuracy and benefit of this technique should incorporate MRI and simultaneous fNIRS-fMRI measurements, in order to evaluate the registration. Another aspect of the method that could be evaluated was the use of the anatomical landmarks in the registration, v.s using a cloud point based registration on all of the nodes present on the face and surface of the scalp. This was not evaluated because the use of five landmark points was simple to implement, in both the registration algorithms and reliably obtaining the 5 landmark points.

For the spectroscopic reconstruction, phase data has a HRF that is more sensitive to cortical tissue than the HRF from intensity data, and that phase data is less influenced by superficial tissue compared to intensity data and this is demonstrated on subject's 1, 2 and 3. For subject 1, the contrast in the HRF's from phase data are larger than that of intensity, for both HbO and Hb, on both the LHS and RHS, which is seen in figure 5.22. For subject 2, phase also shows an increase contrast between the increase of HbO and the decrease of Hb when compared to intensity, and in particular there is better separation from the CL and UL response in phase. Phase data shows a broad curve typical of a HRF from functional activation, as seen in figure 5.26 (Phase, HRF Right). In particular, intensity struggles to show decreases in Hb, with the response showing minimal decrease on the LHS, as well not showing a separation between the CL and UL response on the RHS. Whereas phase shows a meaningful decrease in Hb on both the LHS and RHS, since the UL response is shallow, and the CL response follows the expected HRF shape. This suggests intensity is less sensitive to optical property changes from the cortex and more sensitive to superficial tisse changes than phase. The HRF's from subject 3 (figure 5.26) affirm this, since the intensity HRF shows a double peak (LHS) characteristic of superficial tissue changes, whereas phase shows an HRF

that is broad and characteristic of functional activity.

These results support previous studies (Doulgerakis, Eggebrecht, and Dehghani, 2019, Perkins, Eggebrecht, and Dehghani, 2021, Perkins, Eggebrecht, and Dehghani, 2022 and Blaney, Fernandez, et al., 2023) that showed that phase data showed a deeper distribution of sensitivity to changes in optical properties, in simulated data using tomography (Doulgerakis, Eggebrecht, and Dehghani, 2019), phantom data using tomography (Perkins, Eggebrecht, and Dehghani, 2022) and in subject data using spectroscopy (Blaney, Fernandez, et al., 2023). What these results offer which is different to the subject data study is the use of combining intensity and phase together. This has already been demonstrated by simulation (Perkins, Eggebrecht, and Dehghani, 2021) and on phantom data (Perkins, Eggebrecht, and Dehghani, 2022), but not on subject data. The benefits of combining intensity and phase can be understood by considering the characteristics of the two data types. As aforementioned, phase data offers more contrast for HbO and Hb than intensity. However, phase data is inherently noisier, i.e the signal contains more noise and is effected more by poor source-detector scalp coupling. The greater noise in phase data compared to intensity data was shown by Perkins, Eggebrecht, and Dehghani, 2021 and when using various thresholds for channel selection, as described in chapter 5.3, intensity data retains more channels than phase data. Due to the advantages and disadvantages of both data types, the strengths of intensity and phase can be aggregated, as well as the weaknesses of the data types minimised. I.e the combined intensity and phase shows more contrast than intensity alone, whilst being able to utilise more measurement channels than phase alone.

From the combination of intensity and phase, the spectroscopic results show the combination of the strengths and an alleviation of the weaknesses of both data types. Subject 1 (figure 5.22), shows that combining the data types, increases the contrast of the HRF compared to intensity alone, and reduces the artifacts seen in the UL response when compared to phase alone. Subject 3 (figure 5.30) shows that the combination of the data types can

reduce the influence of superficial tissue, as the double peak HRF from intensity is reduced and broadened with intensity and phase combined. Finally subject 2 (figure 5.26) shows that it may not be desirable to combine the data types in every case, for example, the HRF for the RHS shows separation between the UL and CL response for phase, but this separation is not present for the combined intensity and phase.

The tomographic results presented in chapters 5.3.4 to 5.3.6 show consistent results with the spectroscopy, in that phase offers greater contrast than intensity due to its inherently larger cortical sensitivity. This is demonstrated not only by the normalized increases in HbO and decreases in Hb being larger from phase tomography than intensity, but also by evaluating the ability to see changes in HbO and Hb on both hemispheres. The most succinct evaluation of this comes from looking at the changes in HbO across figures 5.31, 5.35 and 5.37 and the Z score graphs, shown in figures 5.34, 5.36 and 5.38. The Z score graphs show that for HbO and HbT, there is no clear pattern between either intensity or phase having a higher Z score, as for each subject, intensity or phase will have a higher Z score depending on the hemisphere being considered. The consistent feature between all three subjects for both hemispheres, is that phase is able to show more significant decreases in Hb compared to intensity alone. A better Hb sensitivity was shown with spectroscopy as well, which suggests that phase data is more sensitive for Hb than intensity.

5.5 Conclusion

In conclusion, this chapter has demonstrated a workflow which has utilised and evaluated frequency domain measurements on healthy human subjects, as well as demonstrating advancements that will be beneficial and relevant for assessing human brain health, namely traumatic brain injury. This is because the inclusion of phase data can show more contrast

of the HRF from functional brain activity, which could aid studies comparing functional responses with TBI and non TBI populations. The workflow includes subject specific registration, using a 3D camera that doesn't require any subject MRI scans and is compatible within a typical clinical environment since a common alternative is to use a 3D digitiser device, which is prone to interference from nearby metal objects. With the guiding aim of developing fNIRS for assessing TBI, a workflow that is compatible within a clinical environment is important.

The source-detector design allows for spectroscopy and tomography using short channel regression and the potential use of other imaging paradigms, such as dual slopes reconstruction. Davies, Clancy, et al., 2019 stated during a TBI assessment study, that superficial tissue contamination was a key limitation in using diffuse optics for TBI assessment. The use of short channel regression reduces the influence of superficial tissue, which was not available in the aforementioned study, and the potential use of phase data in dual slopes achieves deeper sensitivity.

It has been demonstrated that phase data offers better contrast in obtaining the HRF for HbO, Hb and HbT, by evaluating the functional response using a motor cortex stimulus experiment. In particular, across the spectroscopy and tomography, using the magnitudes of the changes in chromophore and the Z score in tomography, phase data showed a better ability to evaluated changes in Hb in every case. Detecting a higher contrast HRF may be crucial in differentiating responses from healthy brains to brains subjected to TBI, as studied in the motor cortex by Urban et al., 2015. However they only used intensity data from CW measurements, so the use of phase data as demonstrated in this chapter could have provided richer information for their analysis.

This FD workflow could also be applied directly to the study from Forcione, Antonio Maria Chiarelli, et al., 2020, where they detected the functional response in the prefrontal

cortex in two sports concussion patients using FD DOT, but did not include phase data in their analysis. Their study was proof of concept, but with the workflow in this chapter could be applied such that multiple concussion and non concussion subject's could be measured with full intensity and phase FD-DOT.

Future directions for this FD workflow would be to develop the source-detector array to use high density measurements, which may require modifications to the hardware in order to avoid the problems of detector saturation from nearby sources. The FD HD-DOT measurements could be processed as demonstrated in section 4, which would increase image resolution and yield to more accurate localization of functional activity due to more overlapping measurements. In order to unlock the full potential of frequency domain measurements, multiple modulation frequencies could be used. With the current hardware of the ISS Imagent, this may not be possible to do simultaneously within the same measurement. However, with hardware modification or use of other devices, such as the mFD NearWave (Stillwell et al., 2021), simultaneous mFD measurements could be used in order to perform the most accurate and highest resolution tomography, which can be vital in TBI assessment.

The next chapter of this thesis takes aspects of the developments shown in this section and presents the use of FD measurements in the ICU for the investigation of S-TBI patients.

Chapter Six

Demonstration of frequency domain measurements on acute Severe Traumatic Brain Injury Patients

6.1 Introduction

The final working chapter of this thesis builds upon the review of the use of NIRS for investigating human brain health, in particular for TBI as shown in chapter 2 and leverages on the use and development of FD measurements, as demonstrated across chapters 3, 4 and 5. The aim of this chapter is to demonstrate the use of FD measurements for the assessment of S-TBI in the ICU. S-TBI patients were chosen as they would likely exhibit the largest deviation of measurable physiology when compared to a healthy brain. In addition, as reviewed by (Forcione, Antonio M Chiarelli, et al., 2020), it may be possible to use diffuse optics to investigate BBB damage using the injection of ICG as a contrast agent. To recap, this method relies on the principles shown in figure 6.1.

Figure 6.1 A. shows four states in time, 1-4 of a healthy brain. The colour and size

of the arrows going into and out of the brain denote the relative volume of the flow of oxygenated (red) and de-oxygenated (blue) blood respectively and in figure 6.1 A.1, these are denoted as operating healthily. Figure 6.1 A.2 shows that upon the injection of ICG, represented by the colour green, the concentration of ICG increases uniformly firstly in the intracranial tissue (ICT) and then in the extracranial tissue (ECT), figure 6.1 A.3. Figure 6.1 A.3 also shows that as time passes, the concentration of ICG in the ICT decreases due to the normal circulation of blood, whilst it is increasing in the ECT, due to the slower blood transit time in the ECT compared to the ICT. By the last time step in figure 6.1 A.4, the concentration of ICG in the ICT and ECT will steadily decay to pre injection levels as the ICG is flushed out, but the concentration of ICG will remain higher in the ECT than in the ICT.

Figure 6.1 B demonstrates the injection of ICG on a brain that has suffered a TBI, such that there is spatially localised BBB damage. In figure 6.1 B.1 we observe a normal physiological state and then in figure 6.1 B.2 the ICG is injected. At first, the concentration of ICG doesn't increase in the ICT before the ECT, due to the reduction of brain perfusion due to the TBI and then in figure 6.1 B.3 the ICG reaches the ICT and ECT at a similar time. Finally in figure 6.1 B.4, the concentration of ICG decreases due to dilution and circulation in the ICT and ECT, but due to the BBB damage, there is leakage of ICG across the BBB, which is shown in the figure as dark green spots across the brain.

From this model of ICG kinetic, it is proposed that for brains which have suffered a S-TBI, there will be a contrast in the measured signal between areas of the brain with BBB damage and without BBB damage, since areas with BBB damage will have higher relative concentrations of ICG compared to those without. As well as this, there should be a difference in the measured kinetic of ICG between S-TBI and healthy non S-TBI brains.

It is plausible that NIRS can provide information to detect these differences. This chapter will demonstrate the implementation of this method, as well as looking at some sample measurements and then providing recommendations for future studies using diffuse optics for S-TBI.

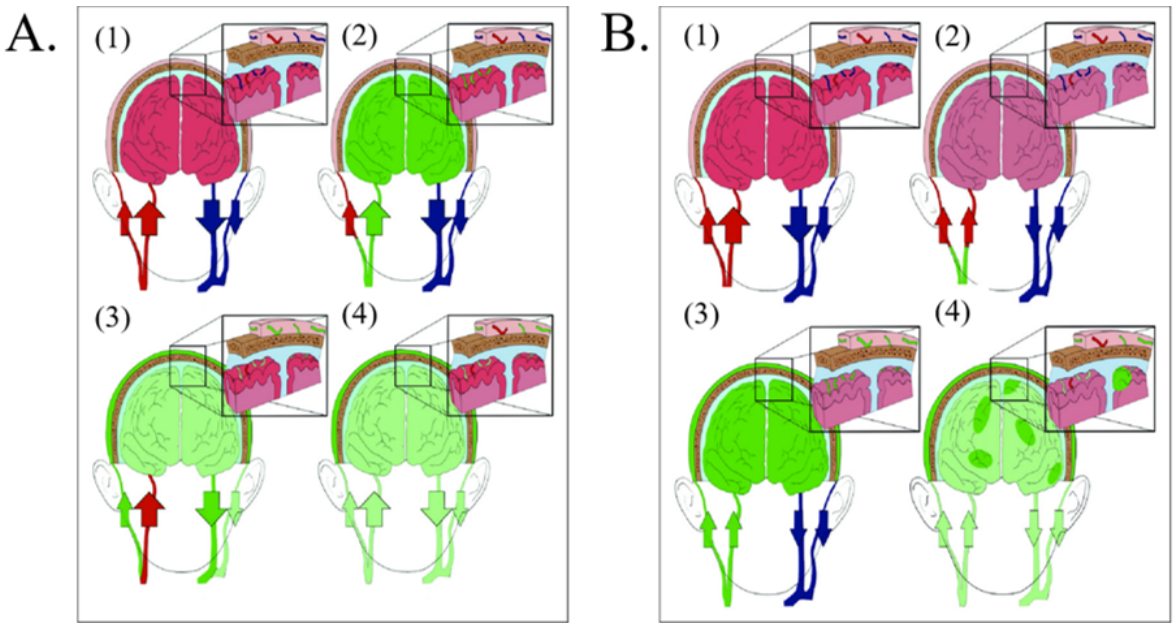

Figure 6.1: Demonstration of the perfusion of ICG contrast in a healthy brain (A) and brain with S-TBI (B). Figure reproduced with permission from Forcione, Antonio M Chiarelli, et al., 2020.

6.2 Methods

This experiment was conducted within the framework of the Red Diamond study (Near Infra RED Cerebral Spectroscopy in the DIrection And early MONitoring of therapy in patients with traumatic brain injury) and was approved by the East of England-Cambridge Central Research Ethics Board (Ref REC: 14/EE/0165; IRAS ID: 144979). Awake patients took part in this study after providing informed written consent. For those in an incapacitated state, a written consent form was received from the next of kin or from a person designated to give consent. The study conforms to the Declaration of Helsinki (as revised in 2013) and

was devised from the proposals in Forcione, Yakoub, et al., 2020 and Forcione, Antonio M Chiarelli, et al., 2020.

Firstly, a bespoke data collection helmet was designed to meet the needs and requirements of S-TBI patients in the ICU, shown in figure 6.2 . These are that the helmet must cause minimal physical interference with the patient, i.e be soft and flexible, and be placeable over open wounds, since patients that have had a S-TBI are likely to have cuts and wounds on their head. The helmet must also be compatible with the likely placement of an ICP probe, which is why there is a gap along the central area of the head. The helmet had source-detector probe holders designed to be used with the ISS-Imagent, by the number of source-detector holders and the diameter of these holders. The ISS Imagent was the same device used for data collection in chapter's 4 and 5. The location of the source-detector probes were designed so that the number of measurement channels maximised by using spatial separation of sources and detectors across the left and right hemisphere of the head, such that if two sources of light were on at the same time, only light from one of these sources would be measured by a given detector. Finally, small white painted dots were added across the surface of the cap in order to facilitate the use of optical registration, similar to the method of registration demonstrated in chapter 5.

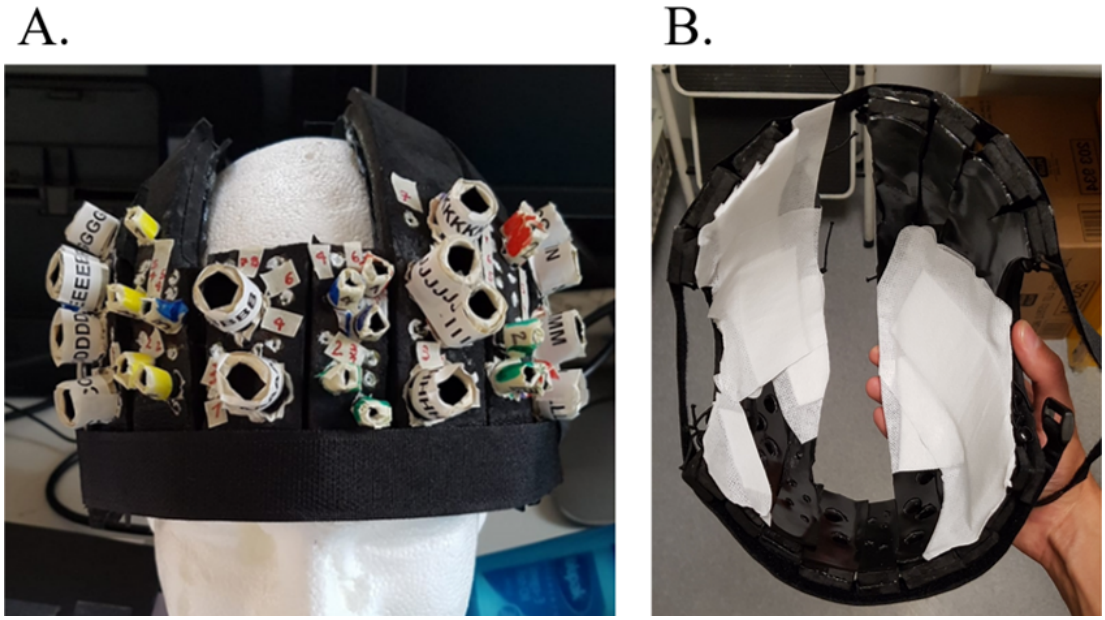

Figure 6.2: A. The outside of the helmet used for data collection in the ICU, showing the source and detector probe holders. B. The underside of the helmet, with white bandaging to accommodate for placement on top of patient head wounds.

From the creation of the helmet, there are 16 source and 15 detector probe slots used for measurements, which are distributed across the left and right hemispheres of the frontal part of the head, seen in figure 6.3. This created a maximum of 240 measurement channels (120 channels at 830 nm and 690 nm respectively), with 130 measurement channels below a SDS of 40 mm (65 channels at 830 nm and 690 nm respectively), over a SDS range of 9.6 mm to 39.9 mm.

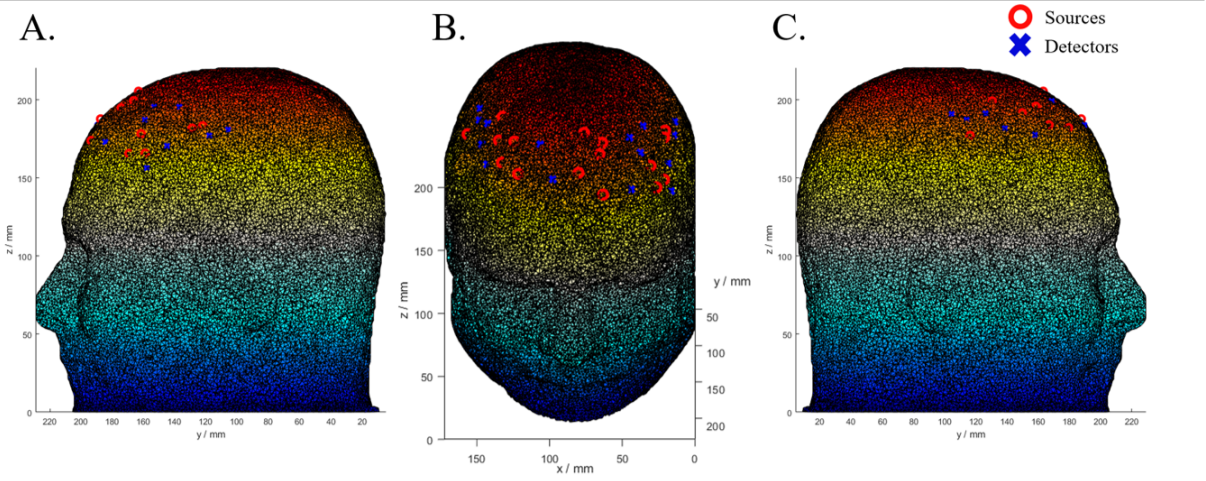

Figure 6.3: A 3D mesh model used for the experiment, with source and detector probe locations shown, across three views in A. B. and C.

In order to use the ISS Imagent device in the hospital and in the ICU, a wheelable rack was created to move the device. This construction is shown in figure 6.4, where the top of the rack, figure 6.4A. holds the PC monitor, mouse and keyboard on top, followed by the source module on the top shelf. Figure 6.4B. shows that the detector module is placed on the shelf below the source module and the bottom shelf is used to hold the PC as well as any other items, such as notebooks, pipette tips or cleaning wipes. The entire ensemble can be seen in figure 6.4C. and this rack was able to be moved around the hospital and due to the slim vertical design and physical dimensions, it fit behind and next to the bed units in the ICU.

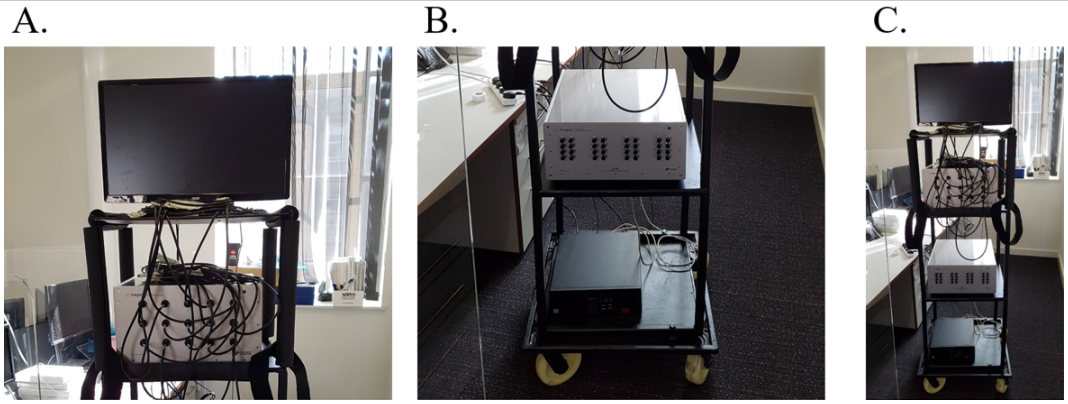

Figure 6.4: The wheelable rack used to move the ISS Imagent, PC and monitor around the hospital. A. The PC monitor and detector module of the ISS Imagent. B. The source module of the ISS Imagent and PC. C. The entire rack.

Finally, before describing the data collection protocol, the helmet can be seen worn on a patient without probes, figure 6.5A. and with probes, figures 6.5B. and C. In order to put the helmet on a patient, one person must slowly lift the patient's head, and another person slowly brings the helmet onto the patient's head, taking care to minimise pressure on any wounds and allowing the helmet to rest in equilibrium such that the helmet doesn't move during data collection, and there is good contact between the surface of the scalp and area of the helmet where the source-detector probes are. As well as this, the ears of the patient are made to be visible, such that they can be used in the optical registration process.

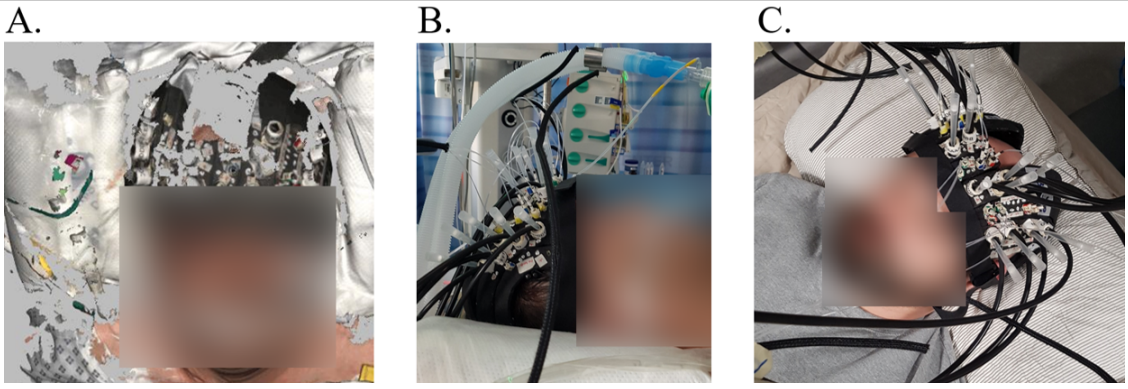

Figure 6.5: Three perspectives of the custom made helmet being used. A. From a 3D scan of an S-TBI patient showing the front of the helmet. B. From a photo of an S-TBI patient showing the side of the helmet. C. On a healthy volunteer showing sources and detectors in the helmet from above.

For this experiment, data was collected from acute S-TBI patients in the ICU and trauma non-TBI patients, such that measurements could be compared between S-TBI and non-TBI patients with differences due to other variables minimized. Table 6.1 describes the cohorts of each population of patients recruited.

Table 6.1: Patient information, where male is detonated by the letter M and female by the letter F. The mean days since admission are from when the patient was admitted to the hospital and when the data acquisition occurred. The standard deviation of mean values are given by σ.

Statistic	**TBI**	**Non TBI**
N patients	10	8
Sex (M or F)	7M 3F	6M 2F
Mean Age (Years)	52 ($\sigma = 8$)	54 ($\sigma = 13$)
Mean days since admission	3 ($\sigma = 1.7$)	8 ($\sigma = 3.9$)

For each patient, the imaging rack (figure 6.4) was taken to the beside and the ISS Imagent was turned on and given at least 10 minutes to warm up. As previously described, the helmet was carefully put onto the subject. Then the subject was scanned using the Artec Leo to obtain 3D co-ordinates of the white landmark points on the helmet, as well as the anatomical landmarks of the patients head (The nasion and the left and right preauricular

points respectively), which can be seen in figure 6.6. Figures 6.6 A. and B. demonstrate the scan of the patient taking place and figure 6.6 C. is an example of the 3D output from the optical scan.

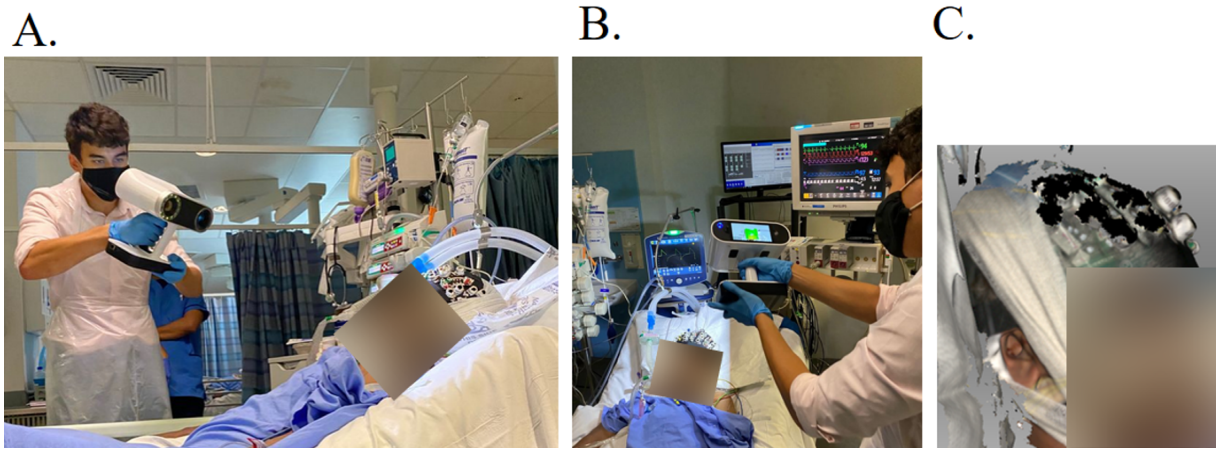

Figure 6.6: Using the Artec Leo camera, A. and B. Taking a 3D optical scan of the patient to be used for registration. C. An example output of the 3D scan.

After the Artec Leo scan is completed, the source and detector probes were inserted into the holders on the helmet. Pipette tips were used in order to keep the sources-detector probes in place during data collection, and for all subjects apart from two, all source-detector probes could be inserted. For the two subjects where not all source-detector probes could be used, this was due to sensitive wounds being present on the surface of the patients head. The voltage gains of each detector was manually adjusted to achieve the maximum signal from nearby sources without saturating the detectors. Finally, before data acquisition starts, the resting state experimental setup is shown in figure 6.7.

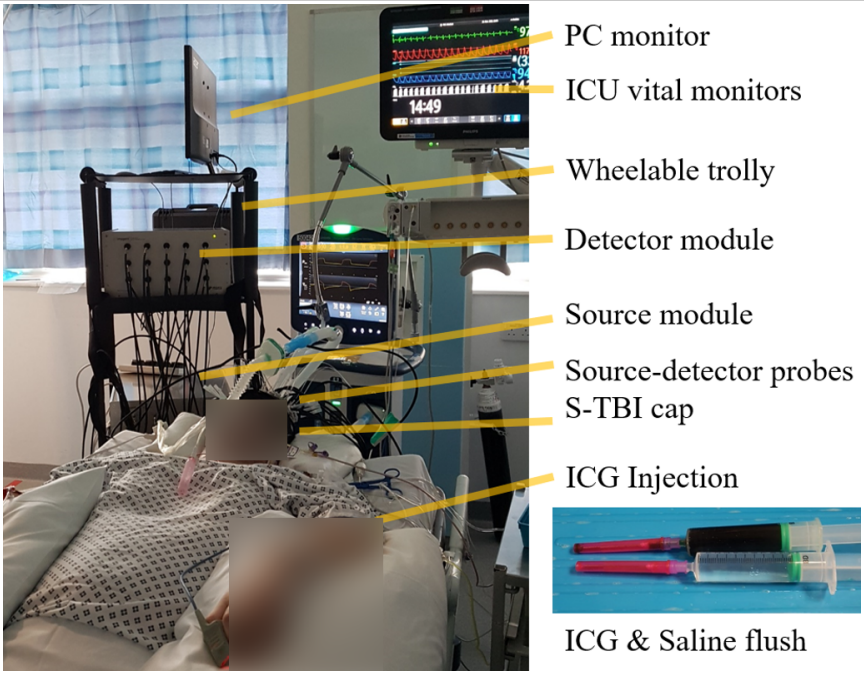

Figure 6.7: The final experimental setup used for data collection, showing the imaging trolley holding the PC and ISS Imagent, the standard ICU measurement devices behind the bed, and the helmet on the patient.

For each patient, two sets of data are collected, which are composed of a minimum of 2 minutes of resting state data, then the ICG bolus is injected into the central cannula, or the peripheral cannula if the central line is not available, immediately followed by a saline solution flush. The start and end of each injection is marked in the data. Measurements are taken continuously for 10 minutes, by which time the concentration of the ICG contrast should be negligible in the ICT and ECT. This procedure is then repeated again, such that there are two sets of data for each patient. Procedures during the data collection protocol can be seen in figure 6.8.

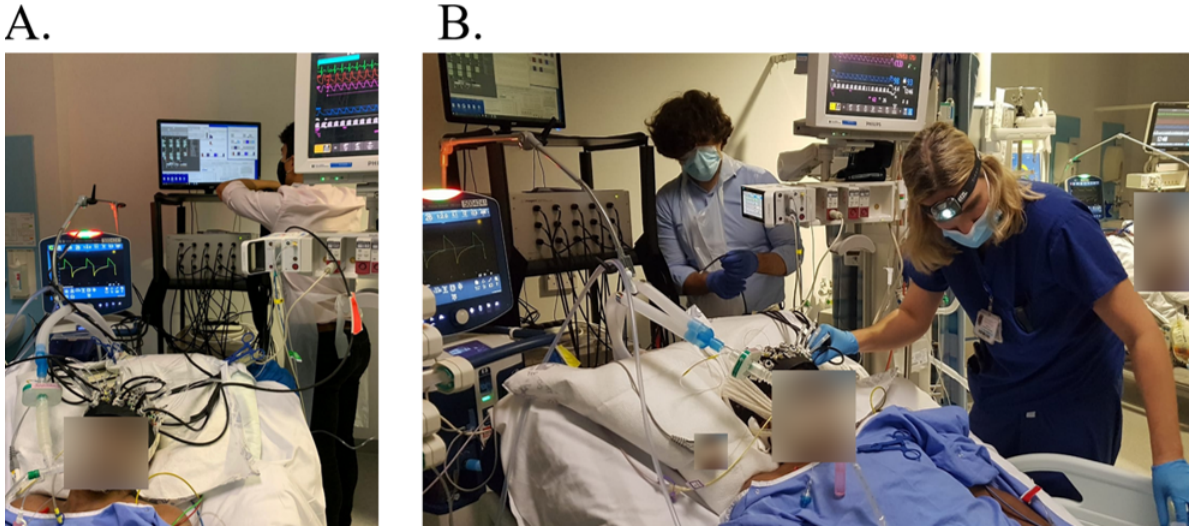

Figure 6.8: A. The ISS Imagent being set up using the BOXY software on the PC. B. Clinicians inserting the source-detector probes in the paitent helmet.

Pre-processing

From the measurements using the ISS Imagent, the intensity data was taken from the AC amplitude and the phase data was just the phase shift of the modulated intensity. Data was processed by firstly correcting phase wrapping on the phase data. Then a signal quality check for each channel was conducted such that each channel had to meet the following criteria from the intensity measurement: 1. The mean intensity had to be more than 50 units, 2. The SNR of the log-mean in the 1000 frames before the ICG injection had to be greater than 0.1 and 3. the intensity of the signal had to decrease from the start of the ICG injection to 100 seconds after the end of the ICG injection. These three criteria meant that only channels were selected that would be from source-detector probes making good contact with the patient's scalp and an example of the distribution of channels that meet these criteria can be seen in figure 6.9.

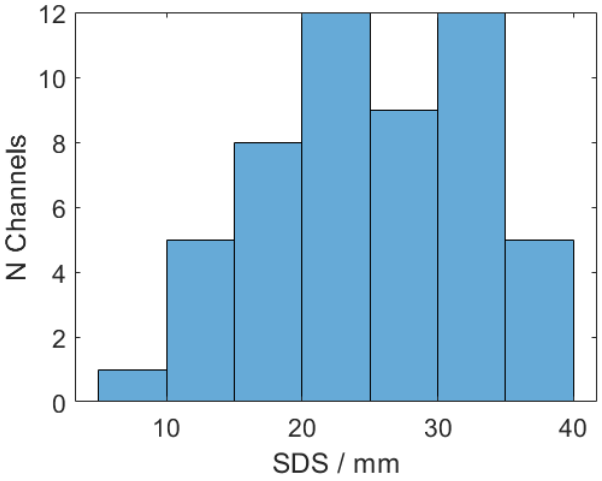

Figure 6.9: A histogram of the number of channels that meet 'good' channel selection criteria. A contribution of a channel to N channels is given when a channel has good measurements at both 830 nm and 690 nm. For this example, there are 52 good channels.

Channels were then categorised by their hemisphere, left or right and then if the channel was of short, medium or long source-detector separation length. This was done in order to perform simple preliminary analysis on the intensity and phase signals. Short separation was defined as < 16 mm, medium separation as ≥ 16 mm to ≤ 30 mm and long separation as > 30 mm separation. Left hemisphere source-detector probes are those with an x co-ordinate < 90 cm and the right hemisphere was defined as $x > 90$ cm, as shown in figure 6.3.

From the measurements described in the previous paragraphs, some preliminary analysis was performed, however for this thesis, due to constraints which are explained in the discussion, full analysis of the data was not conducted. Therefore these results represent a demonstration of the method. To contextualise the analysis, figure 6.10 shows an example of how a measured signal responds to the ICG injection. Each green line on figure 6.10 represents an injection marker, the first and second lines are the start and end of the ICG injection respectively. The third and fourth green line are the start and end of the saline flush respectively. The preliminary analysis of the measurements focused on the features of

the ICG-curve as described in figure 6.10.

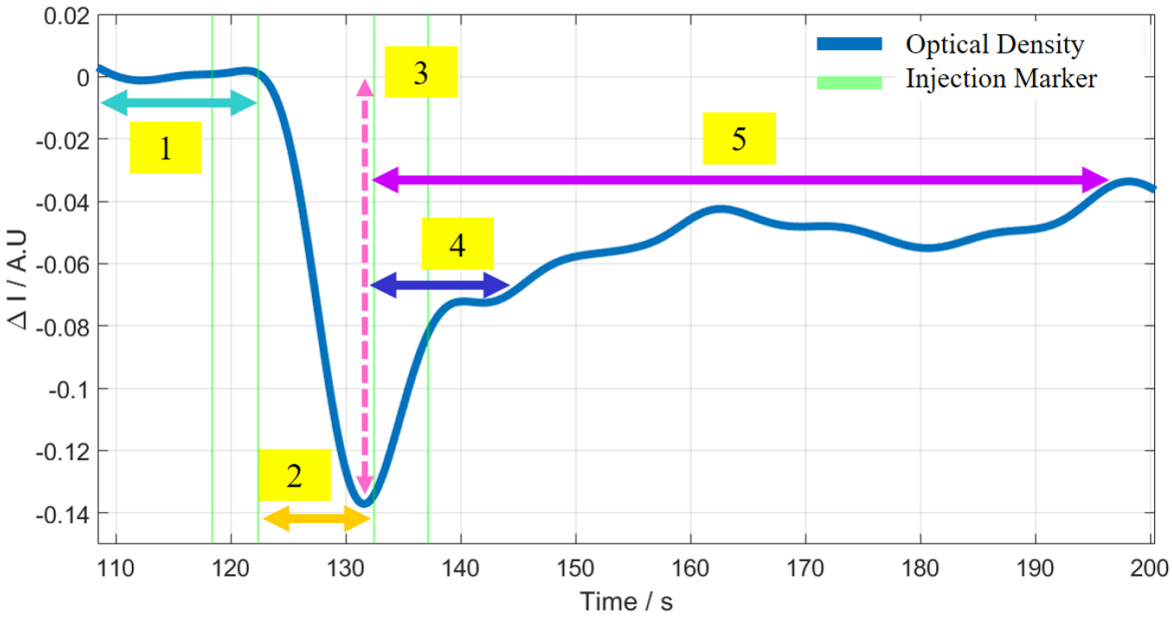

Figure 6.10: The response of optical density to ICG injection, taken from measured data from a S-TBI subject. Feature 1 is the baseline measurement prior to ICG injection. Feature 2 is the time taken from the end of the injection of ICG to the minimum of optical density. This is due to the decrease in signal due to the increased attenuation of light from the injection of ICG. Feature 3 is the magnitude of the decrease in optical density across the time of feature 2. Feature 4 is the time taken for the optical density to recover to 50% from the minima to the baseline and feature 5 is the time taken to recover to 25% of the the minima to the baseline.

6.3 Example measurements

Measurements of intensity and phase were taken simultaneously and an example of the optical density changes from the intensity measurements are shown in figure 6.11 , and changes in 'delta phase' are shown in figure 6.12.

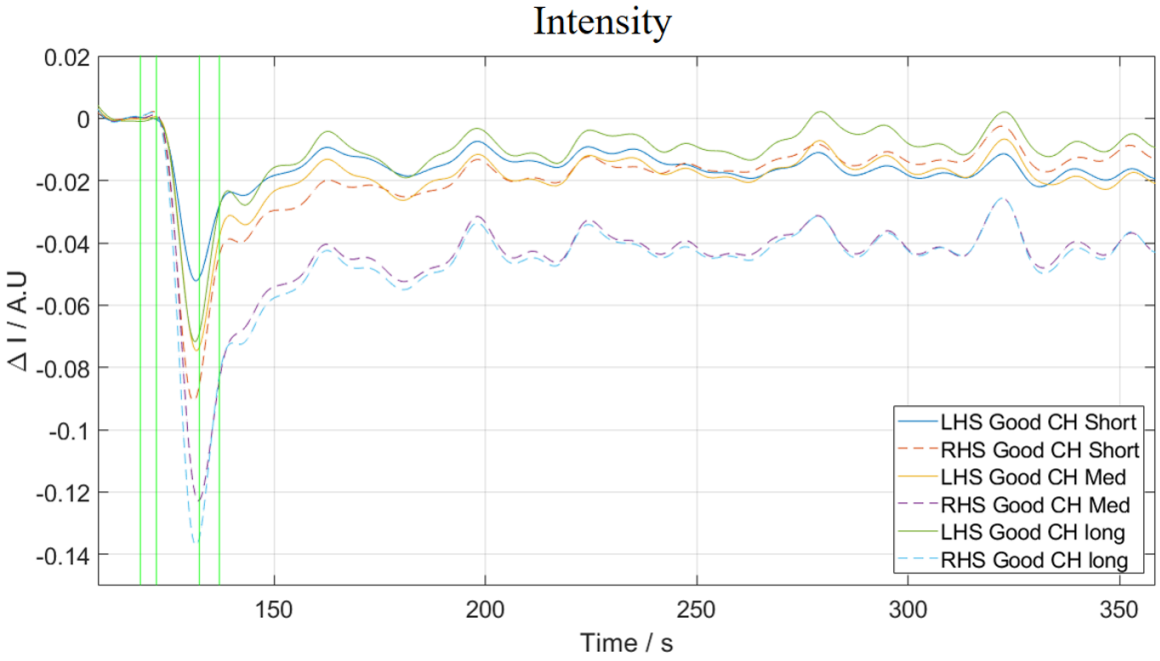

Figure 6.11: A. The ISS Imagent being set up using the BOXY software on the PC. B. Clinicians inserting the source-detector probes in the paitent helmet.

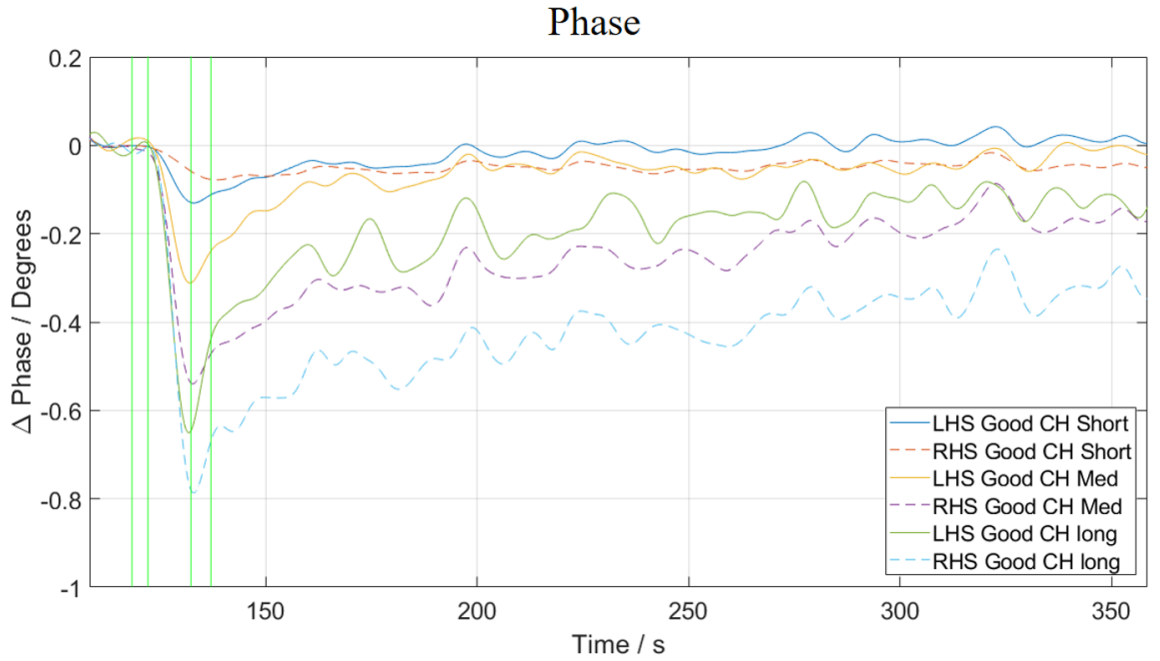

Figure 6.12: A. The ISS Imagent being set up using the BOXY software on the PC. B. Clinicians inserting the source-detector probes in the paitent helmet.

Using the intensity curve as an example, it can be seen that post ICG injection, there is a rapid decrease in intensity followed by a slow recovery period of the intensity towards the initial baseline values. The curves shown in figure 6.11 from an intensity measurement and 6.12 for a phase measurement are separated between the left and right hemisphere, as well as if they were from short, medium and long channels as described in chapter 6.2. For the intensity data, the long channel from the RHS shows the largest decrease in intensity, followed by the medium and then the short channels respectively from the RHS. This is to be expected, since longer separation channels should have deeper sampling distributions and it is hypothesized that the inflow of ICG will reach the deeper ICT first, before the shallower ECT (Forcione, Antonio M Chiarelli, et al., 2020). For the LHS, the medium and long channels decrease by a similar proportion to each other, whilst the short channels exhibit the smallest decrease. Whilst it would be expected that the long channel would have a larger decrease in signal, there could be small discrepancies in the designed SDS and the actual physical SDS due to source-detector probes making angled contacts with the patients scalp, which could change the SDS by mm's.

For the sample phase data in figure 6.12, the signal response is similar to that of the intensity data. However, for the phase data, the decrease in signal as a function of SDS is consistent with the known theory that larger SDS's have deeper depth sampling, and that the ICG reaches vessels in the ICT before the ECT. Since for the phase signal, the largest decrease in mean phase is shown by the long channel on both hemispheres, followed by the medium channels and then the short channels show the smallest decrease in signal. The response from the phase data to ICG injection provides evidence that phase data samples deeper in tissue compared to intensity data, due to the larger decreases of phase signal as SDS increases on both hemispheres.

6.4 Discussion

Although these data are just an example of the FD-ICG experiment on S-TBI patients and no clinical conclusions are being made, it demonstrates a viable method to investigate S-TBI in the ICU using NIRS. The hypothesis of this method are that the features of the curves can tell us information about the injury state of the brain. For example, if there were differences in brain injury between the left and right hemisphere of the brain, such as swollen tissue, hemorrhages or haematomas, the kinetic of ICG would change based upon this (Forcione, Antonio M Chiarelli, et al., 2020) and these changes would be reflected in the intensity and phase responses to ICG injection. In particular the detection of leakage of ICG into the interstitial tissue (between the intra and extra-cranial tissues) in the areas with BBB damage, as shown in figure 6.1.

The strengths of these demonstrated measurements are that it shows that a lab based FD NIRS device can be adapted to be brought into the ICU, overcoming challenges in portability via the wheel-able rack and ergonomic challenges of measurements on S-TBI patients by the creation of a custom soft antiseptic helmet. As well as this, it was shown that intensity and phase signals could be measured using FD hardware (ISS Imagent, USA) to detect the ICG kinetic (figure 6.11 for intensity and figure 6.12 for phase). The full implementation of this demonstrated experiment should incorporate a complete cohort of S-TBI patients, with complimentary medical imaging data such as x-ray CT's of the patients to compare the assessments made from the ICG-NIRS data to the x-ray CT's.

The difficulties and limitations of the demonstrated experiment are three fold. Firstly, there are challenges in achieving optimal probe contact across the helmet due to the variability in head sizes of patients which means the helmet may fit tightly for some subjects and loose for others. Since the patients are lying down, when a loose fitting helmet is applied there may be a gap between the helmet and the surface of the front of the patient's

scalp. This can make it harder to properly make the source-detector probes achieve good contact with the scalp. As well as this, patient's may have cuts or lacerations on their scalp, which means certain areas of the scalp can't have source-detector probes pressed on them. In order to address these challenges, multiple helmets could be created in order to account for multiple head sizes and S-TBI patient selection criteria could be modified to minimize S-TBI patients with major lacerations on their scalp.

Secondly, to date, good quality measurements were only obtained on S-TBI patients. There was considerable difficulty achieving good quality measurements on the non TBI patients. This is because the trauma non TBI patients were awake, and in many cases found it difficult to minimize their head motion during the measurements. This caused many motion artifacts in the signal and given the signature of the ICG kinetic in the signal, motion artifact correction methods had adverse effects on the intensity and phase signals. To minimize this problem, there could be a stricter experimental protocol in place with the trauma non TBI subjects in order to minimize motion artifacts.

Thirdly, due to a combination of the two aforementioned challenges, it may be more difficult to obtain good quality phase signal from these measurements, since they are less robust than the intensity signal. Incorporating the phase data into the analysis would be important in order to use the advantageous that come from phase data, namely the deeper depth sampling and lower sensitivity of superficial tissue which could give more accurate detection of the passage of ICG at the depth of the BBB.

6.5 Conclusion

Overall this chapter demonstrated a method which could allow FD NIRS measurements to be used in the ICU to assess S-TBI, by showing a method of using ICG to act as a dynamic

contrast agent and measuring the kinetic of the ICG across the ICT and ECT with the aim of localizing the brain injury. A demonstration of the method was shown with example data evaluated from intensity and phase data (figures 6.11 and 6.12). Full analysis of the measurements were not completed due to the challenges and limitations of data collection which meant good signal quality from control patients couldn't be obtained and the data from S-TBI patients couldn't be compared to non TBI controls. To move the study forward, these limitations should be addressed, with particular aim to collect good quality data on trauma non S-TBI patients. However the main aspect of the experimental protocol was successful, which was to bring lab designed FD hardware into to the ICU and collect data on S-TBI patients using an experimental protocol with the potential to assess the brain injury.

Chapter Seven

Conclusion

This thesis has developed frequency domain functional near infrared spectroscopy and diffuse optical tomography towards the application of assessing human brain health by exploring the use of phase data and modulation frequency for functional brain imaging. The first two chapters of this thesis introduces diffuse optics, in particular fNIRS and DOT and outlines the advancements in this field, as well as introducing where diffuse optics can be used within human brain health. In particular, how fNIRS and DOT can be used for assessing traumatic brain injury, which is a significant pathology in human brain health and why the specific features of the aforementioned techniques can be exploited in this field. From the basis of these first two chapters, the use of frequency domain was evaluated and developed through chapters 3 to 5 by developing novel methods on how phase data and modulation frequency could be used for functional brain imaging with the overarching aim of applying these methods for assessment of traumatic brain injury. Finally chapter 6 demonstrated a method for the use of FD measurements on S-TBI patients in the ICU.

7.1 Diffuse Optics

The first chapter introduced diffuse optics and the main paradigms within this domain of imaging, namely continuous wave, frequency domain and time domain, and outlined the uses and differences between these. Each of these paradigms have distinct features, such that currently CW is the most robust and offers the best value, due to relatively simple instrumentation, portability and use. TD offers absolute imaging of absorption and scattering coefficients respectively and the ability to tune depth sensitivity, whilst generally being the most expensive. FD offers the use of modulated phase and intensity data, which offers advantages against CW in that phase data samples deeper than intensity data and is less sensitive to superficial tissue, and is generally less expensive than TD devices. Then the development of fNIRS and diffuse optics was reviewed, starting from the initial functional spectroscopy measurements on the human brain, to topographic and tomographic imaging and each advancement had the aim in providing richer and more accurate information about brain function. It is with these aims in mind that influenced the developments within FD and in data pre-processing techniques, such as using dual slopes imaging in FD in order to provide a deeper sensitivity or using short signal regression in data pre-processing to reduce the influence of hemodynamic superficial tissue changes.

From this review of the literature, the current state of the art for functional brain imaging using diffuse optics comes in the form of high density diffuse optical tomography, which offers the best resolution of tomographic imaging of the surface of the brain (White and Culver, 2010), as well as facilitating a comprehensive use of data pre-processing techniques (Yücel et al., 2021). The state of the art within the use of FD measurements were that it had been shown that simulations on a head model demonstrated phase data could sample deeper than intensity, which are analogous to CW measurements and that they are less influenced by superficial tissue (Doulgerakis, Eggebrecht, and Dehghani, 2019). This was demonstrated

by using the dual slopes reconstruction technique on measurements looking at visual cortex activation (Blaney, Fernandez, et al., 2023), however from reviewing the literature on the use of FD, there were no evaluations of using FD-HD-DOT or using phase data directly in fNIRS, nor was there the evaluation of varying the modulation frequency in HD-DOT. These omissions in the literature, provided the motivation of the aims of the development in FD fNIRS and DOT, however the specific aims for this thesis would require an investigation in how diffuse optics could be used for assessing human brain health.

7.2 Diffuse Optics For Brain Health

The second chapter of this thesis considered the use of diffuse optics for human brain health. Diffuse optics are non invasive, non ionising and can be used at the bedside, which makes it an attractive imaging technique for brain imaging. It was found that brain health encompasses multiple factors, paradigms and pathologies within this and that the highest incident of all neurological disorder is traumatic brain injury (Maas et al., 2022). It was from this starting point that traumatic brain injury was further studied with the consideration of how diffuse optics, in particular FD methods, could be used for traumatic brain injury assessment.

The investigation into TBI found that there are three categorisations of severity from the injury, mild, moderate and severe, each existing on a spectrum and currently being assessed subjectively using the Glasgow Coma Scale (Jain and Iverson, 2023). The GCS grades the TBI by assessing visual, verbal and motor response of a patient and then depending on the grading, the patient will undergo suitable treatment and therapies. It is within this assessment that presents an opportunity for diffuse optics to image the brain to provide additional information about the condition of the brain in order to better asses the injury severity. There are two methodologies that optical measurements can be conducted

in, functional and resting state. The latter in the context of TBI can be used to assess physiological parameters (Roldán and Kyriacou, 2021) such as inter cranial pressure, tissue oxygenation, in both cerebral tissue and superficial tissue and cerebral blood flow. These parameters can in turn be used to investigate hematoma detection, brain oxygenation, cerebral perfusion, cerebral autoregulation, cerebral metabolism and neurorehabilitation, which are all relevant clinical measures in monitoring TBI. These measures are more suited to S-TBI, since these patients may be unconscious or unresponsive, meaning that they would not be able to complete voluntary functional tasks, as well as the fact that these clinical parameters are expected to deviate more from a healthy baseline in more severe TBI cases, meaning they could be easier to detect. As found in the literature, assessing these resting state parameters can be challenging, in part due to concerns of signal contamination by superficial artefacts (Davies, Clancy, et al., 2019) and the fact that these parameters require a form of absolute imaging. This in itself is difficult because absolute imaging is less robust than difference data imaging, and is more sensitive to poor source-detector coupling, which is reflected in the fact that NIRS devices are not used in the mainstream clinical practice. Therefore, the attention of the use of diffuse optics for TBI assessment turned to functional imaging.

Functional imaging, as established in the first section of this thesis works on the premise of detecting localised hemodynamic responses that occur due to brain function, usually in response to a stimulus, such as motor control in the motor cortex, a response to a visual stimulus in the visual cortex or mental processing in the pre-frontal cortex. Therefore, the use of diffuse optics for functional imaging is most suitable for mTBI and M-TBI patients, since they will be able to respond and engage with stimuli required to induce a functional response. It is detecting functional activation using FD fNIRS and DOT that this thesis targeted for it's aims, since this could be used to perform functional brain imaging on mTBI and M-TBI patients, but in order to better define the aims, the needs within functional studies of TBI patients had to be assessed. Forcione, Antonio Maria Chiarelli,

et al., 2020 used mTBI and non TBI subject groups in order to compare the differences in functional brain activity in response to given stimuli, which include language tasks targeting the pre-frontal cortex and Urban et al., 2015 for the same premise used finger tapping task to target the motor cortex. This evaluation demonstrated that sampling the cortex, accurate imaging and broad spatial coverage across the brain are all vital components in being able to distinguish differences between m/M-TBI and non TBI subjected brains. Therefore, these needs guided the aims of this thesis, along with the research opportunities presented in chapter 1, which culminated in developing FD fNIRS and DOT, in order to perform the most accurate functional brain imaging.

More specifically, chapter 1 showed that FD should be developed because FD can harness phase data, which samples deeper in tissue than intensity data and is less sensitive to changes in hemodynamics in superficial tissue, as well as that, evaluating and exploring the use of different modulation frequencies is an area of FD development that has not fully been harnessed. Both of these features of FD could attribute to better image resolution and localisation in tomography and HRF's less influenced by superficial tissue in fNIRS. As seen in chapter 2 and as discussed in the previous paragraph, the focus of the assessment of human brain health through diffuse optics comes in the form of functional brain imaging in the pathology of TBI. Coupling the research opportunities of chapter 1 with the clinical needs of chapter 2 together, meant that the overall aims of the thesis were to develop FD fNIRS and DOT, in order to detect functional brain activation, for the most accurate spectroscopic and tomographic imaging, in order to be directly applicable for assessing TBI.

7.3 Multi Frequency HD-DOT simulations

The third chapter started the investigation into how the inclusion of phase data and combination of modulation frequency effects the performance of FD measurements in HD-DOT, using simulated measurements on a 3D model. The motivation for this study came from the opportunities and needs presented in the first two chapters, namely the need for more accurate imaging and the unexplored avenues in FD imaging. Firstly, the behavior of FD data was investigated by measuring how intensity and phase changes at different source-detector separations as a function absorption and scattering properties and modulation frequencies using simulations with a 2D circular FEM. This revealed that changes in intensity increased as changes in both absorption and scattering increased and that changes in phase increased as changes in scattering increased, but changes in phase decreased as absorption decreased. This revealed that it may be possible to detect changes in scattering use phase data, however due to changes in phase being attributed to changes in absorption, cross talk between these two parameters may be prevalent. It is within the changes of intensity and phase as a function of modulation frequency that form the starting point of this study, in that as modulation frequency increases from 50 MHz to 200 MHz, there is little to negligible changes in intensity, whereas there are significant changes in phase data. This suggested that by changing the modulation frequency, there is significant contrast in phase data, which means that phase data at multiple modulation frequencies contains additional information that can be used in image reconstruction.

For the study, a 3D FEM model was used with three layers with tissue mimicking optical properties and thicknesses and on top of the model, a HD grid of 24 sources and 28 detectors were placed. Point perturbations of a small change in the absorption coefficient was made at each node within the FEM across a 100 mm by 60 mm field of view in the x and y axis respectively for depths of 14 mm, 15 mm and 16 mm. From each point perturbation,

image reconstruction was conducted using changes in intensity and phase data and then three performance metrics were calculated for each reconstruction. These were a localization error, which is the distance between the point perturbation and the reconstructed maxima of the perturbation, the FWHM of the reconstructed image and the ERES of the reconstructed image. For each set of reconstructions, three data types were used (CW, FD, CW&FD), which are intensity only data at the reference 141 MHz, intensity and phase data combined at the reference 141 MHz and then intensity data at 141 MHz combined with phase data at 78 MHz, 141 MHz and 203 MHz.

The results of the study (Perkins, Eggebrecht, and Dehghani, 2021) showed that the combination of intensity and phase data, CW&FD performed better than CW alone, which agreed with the previous study of Doulgerakis, Eggebrecht, and Dehghani, 2019, as well as that phase data alone performed better than intensity data for HD-DOT. This was demonstrated by the results that on average, phase data caused better localisation, smaller FWHM and smaller ERES compared to intensity data in the single modulation frequency case. As well as this, the image performance across the FOV was more uniform for the phase data case compared to the intensity data case, which is a desirable characteristic when sampling the surface of the cortex. This was a promising result, because it showed that at typical cortical depths of between 14 mm to 16 mm, phase data offered better performance, which supports the idea that phase samples deeper than intensity. However, these results were for the noise free considerations and when noise models were included for intensity and phase data respectively, then the performance of intensity and phase in the same simulations and metrics became worse. Intensity data performed better than phase data in the noises added models at a single modulation frequency. This posed the question about the merit of phase data when realistic noise was added and the solution to this was found in two different forms, firstly by combining intensity and phase data, and secondly by use of changing and combining different modulation frequencies.

The first of these two questions was studied using the combined CW&FD data case. In the noise free models, CW&FD data performed better than both FD and CW alone respectively in each imaging metric and most significantly had a more uniform performance metric across the FOV. In the noise added case, for localisation and the FWHM, CW&FD performed better than CW and FD, and for the ERES, the CW&FD performed to within 0.01 mm to CW alone. This showed that combining intensity and phase together within image reconstruction could be a powerful way to employ phase data, and as discussed in chapter 3, it is hypothesised that this is due to combining the features of both types of data. Phase data contains more noise than intensity data, which is why when realistic noise was added to both data types, phase data suffered more and saw a larger performance decrease compared to phase. However, as previously mentioned, phase data samples deeper than intensity and is less sensitivity to changes in optical properties in superficial tissue, i.e it has more sensitivity distributed away from shallow depths. It is these two properties that when intensity and phase are combined, the advantageous features from both are combined and there is an increase in the SNR. Combining intensity and phase is just one part of FD measurements, because the other part depends on the modulation frequency, which holds the most potential in FD measurements.

The second question to be answered about the merit of phase data is the use of different modulation frequencies and combining them together. When the modulation frequency was changed between 78 MHz to 141 MHz and 203 MHz, as it increased, the performance of all data types increased, with the largest performance gains being for the combined CW&FD case. This was the expected result, since the contrast in phase data increases significantly as the modulation frequency increase, and it suggests that the contrast in intensity data increases by a smaller rate than phase data for increases in modulation frequency. Another point of significance from these results are that for each modulation frequency, for the combined CW&FD case each performance metric scored differently, which showed that

different modulation frequencies have different information content, which is in differences of the distribution of sensitivity, i.e higher modulation frequencies sample deeper.

The biggest potential for phase data lies within the combination of phase data at different modulation frequencies, since nearly all metrics, the best results came from combining intensity data at the reference 141 MHz with phase data at 78 MHz, 141 MHz and 203 MHz. The combined case yielded the most uniform FOV for each metric, which provides a desirable trait applicable for imaging the surface of the cortex. This performance is due to the fact that more information is being used in image reconstruction, more specifically for phase data, three different jacobians are being combined, and these jacobians contain different information since phase changes as a function of modulation frequency. In addition to this, by coupling these multi-frequency phase data with a single frequency intensity data, the advantages of intensity data are included, in the robustness and increased SNR of intensity. Another strength of multi-frequency data is that the combination of modulation frequencies minimises the negative effects of noise in phase data. This is most pertinently demonstrated by comparing the noise added results of the CW&FD case, for the combined modulation frequency case, each imaging metric is better compared to the single modulation frequency case.

To further enhance the analysis of the results, violin plots were created to contextualize the differences in the distribution of the performance metrics for the different data types. Whilst there were statistically significant differences when comparing data types and modulation frequencies, the distributions were shown to have overlap and similar shapes, combined with the smaller changes with the LOCA, which is why four significant figures had to be used across all the direct comparisons. The relative strengths and benefits reported in this study of FD and CW&FD compared to CW, or 141 MHz compared to the combined 78, 141 and 203 MHz are still valid, however they should be considered as another step towards higher accuracy tomographic imaging, rather than a generational leap forward such as the

transition from sparse DOT to HD-DOT.

The results in this simulation study showed that the biggest potential of FD measurements could come in the form of the use of multi-frequency phase data. This is because the study showed that although when single frequency intensity and phase data were compared in the noise added case, intensity data performed better, when multi-frequency intensity & phase data was used, it outperformed the single frequency intensity and phase.

The study presented in this chapter contributes towards diffuse optics literature by presenting an evaluation of HD-DOT using FD measurements, which built upon the seminal paper of White and Culver, 2010 where they evaluated CW HD-DOT, and from that paper they showed that HD-DOT was the strongest use of CW DOT. Analogous to those findings, the results and conclusion from this study show that the multi-frequency FD measurements are the strongest use of FD-DOT. As well as this, this study provided the first step of the answer to the one of aims of this thesis, which was that phase data should be utilised in FD data for the tomographic reconstruction of point perturbations, which mimic functional activation in the brain, and that multi-frequency FD measurements offer the benefits of phase data, whilst minimising the drawback of being inherently nosier than intensity data and thus the best use case of FD measurements. The next step naturally was to investigate these findings using real measurements, instead of simulated measurements, because one of the key limitations of this study are that it negates any challenges presented by instrumentation or experimental technique. This limitation is addressed with the study of the next chapter, which used real data to perform multi-frequency FD HD-DOT.

7.4 Multi Frequency HD-DOT the NeurOpt Phantom

Chapter 4 of this thesis builds upon the work presented in chapter 3 and evaluates FD measurements using HD-DOT on an inhomogeneous phantom using intensity, phase and multi-frequency data. Firstly, an extensive literature review was conducted into the use of multi-frequency FD measurements, since the strength of multi-frequency was the most significant finding from the previous chapter. In total, 14 studies on mFD were found, ranging from the first being conducted in 1991 (Patterson et al., 1991) until the most recent in 2022 (Mudeng, Nisa, and Sukmananda Suprapto, 2022), and of these 14, 7 were simulation based, 5 were phantom based and 2 were in-vivo measurements. Analysing these studies revealed that within the domain of simulated measurements, multiple geometries and combinations of several modulation frequencies had been studied for standard DOT and HD-DOT. From these simulation based studies, it was found that combining modulation frequencies yielded the best performance (Burcin Unlu et al., 2006) and that although higher frequencies performed better (700 MHz Fan, Dehghani, and Eggebrecht, 2021), when noise was considered there existed an optimal modulation frequency that was lower at 300 MHz, due to comprise between increased noise and deeper sampling. As well as this, it was found that using over 7 frequencies combined yielded small additional benefit and that modulation frequencies too close to each other contained redundant information (Intes and Britton Chance, 2005).

From the phantom studies that had been conducted using real measurements, combining more modulation frequencies performed better, in Burcin Unlu et al., 2006, 6 frequencies combined between 110 MHz to 280 MHz, was better than using 3, 2 or a single frequency. As well as this, each phantom study was found to have been conducted on a cylindrical phantom, whereas the study in chapter 4 proposed to use rectangular cuboid phantom, with an array of sources and detectors on the surface, which represented a more realistic (in-vivo human brain imaging) use case. In addition, none of the previous phantom studies used HD-DOT

in 3D, which means that there was space in the literature to perform mFD measurements using HD-DOT in 3D as this had not been done before. Both of the in-vivo studies used mFD measurements to obtain spectroscopic reconstruction of optical properties, but neither of this were for functional brain imaging. This presented motivation to use the NeurOpt inhomogeneous phantom, which mimics functional brain activation by having a small moveable cylindrical anomaly inside it at a depth of 15 mm, which is representative of the depth of the surface of the cortex in an adult.

The experiment used six sources and twelve detectors on the surface of the NuerOpt phantom (Pifferi et al., 2015) arranged in a high-density array. The phantom itself was homogenous, however it contained a moveable rod with a small cylindrical anomaly at a depth of 15 mm. There were three different sizes of contrast anomaly, with volumes of 21 (rod 3), 98 (rod 5) and 269 mm (rod 7) cubed respectively. FD measurements were taken using the ISS Imagent at 78 MHz, 141 MHz and 203 MHz for when the contrast anomaly was present in the middle of the phantom and for when the anomaly was removed. From these measurements, tomographic reconstructions of the anomaly were conducted and then imaging performance metrics were calculated, using the same metrics at the mFD simulation study. The general aims of this study were to evaluate the performance of mFD measurements using HD-DOT with real data to compare if the findings of the simulated mFD experiment to mFD on a phantom, in particular the effectiveness and strengths of phase compared to intensity and the strengths of multi-frequency.

The study showed that for using the ISS Imagent for these FD measurements, as modulation frequency increased the contrast in the signal when detecting the anomaly increased for phase data and decreased for intensity data, with a linear trend for both data types, for both short and long separation measurement. For both data types at short separation measurements, as modulation frequency increased, the standard deviation of the baseline signal increased. Whereas, for both data types at long separation measurements, the stan-

dard deviation is the smallest at 141 MHz. This supports the idea that higher modulation frequencies sample deeper because, deeper sampling will mean more photons are absorbed by the contrast anomaly at a 15 mm depth, which causes the contrast between the baseline and the anomaly measurement to increase.

The study used two different methods of image reconstruction which were a single iteration approach, which is most commonly used for image reconstruction, and an iterative based reconstruction approach. For the single iteration case, mFD measurements performed the best, showing the best localisation for all three contrast rods and between FD and mFD measurements, they displayed the best score for 8/9 metrics for the three rods. In particular, a common observation was that when phase data was included, the centre of the contrast anomaly was reconstructed at a more accurate depth between z = -14.5 mm and Z = -15.5 mm for FD and mFD, whereas for the CW case, the reconstructed depth was between z = -11.5 mm to -12.5 mm. This observation reiterated the idea that phase samples deeper than intensity data and the deeper sampling not alone led to better depth localisation, but improved localisation in the x-y plane, with the average (x,y) co-ordinates being (0.33,1.00) mm for mFD compared to (1.96, 0.87) mm for FD and (1.30, 1.89) mm for CW.

Using the iterative reconstruction method saw that mFD performed the best in all metrics, with FD joint best in 2/9 metrics with mFD for the case where the number of iterations was the same (N =4) between the different data types. For when the number of iterations for each data type was allowed to run until the stopping condition for each data type was met (N=8 for CW, N=6 for FD and N=4 for mFD), the performance between CW, FD and mFD was variable. CW had the best FWHM error for all three rods, and FD and mFD had the best localisations for each rod. The inherent strengths of the phase data allowed for better localisation, with a lower number of iterations before reaching the stopping condition, whereas for intensity data, a higher number of iterations meant that a smaller anomaly was reconstructed with a more focused central maxima, which led to lower

FWHM scores.

The limitations of the study were that only measurements in the NN1 and NN2 regime were used, which highlights a limiting factor for the hardware present, in that due to sensitivity of the detectors (photomultiplier tube based), whilst good SNR can be achieved for NN1 and NN2 measurements, this comes at the expense that longer channel based measurements don't have sufficient SNR. The implications for this are that HD-DOT studies presented in literature make use of longer separation channels (Eggebrecht et al., 2014), and longer channels have inherently greater depth sensitivity, which means that the benefits of both intensity and phase measurements made at longer separations may not be fully utilised and compared to each other. As well as this, the measurements at different modulation frequencies were performed separately, which means that for N modulation frequencies sampled, N measurements had to be made. In some in-vivo conditions this may not be a feasible method of data collection, particularly in clinical environments where time with a patient is limited. So this currently implementation of mFD on phantoms may be difficult to achieve in-vivo. Finally, the results from the study were evaluated using a constrained FOV, which mitigated some artefacts in the tomographic reconstruction on the phantom for all data types, and this prior spatial assumption of where changes in optical properties will occur may not always be available for in-vivo measurements. However, during the study, the FOV was consistent for all analysis, so each data type was compared using the same methods and metrics.

Overall this study contributed to the HD-DOT and the FD field, because it showed that phase data, in particular using multi-frequency measurements lead to a better localisation and effective resolution for detecting changes in optical properties, in this case the absorption coefficient when using HD-DOT. The reasons for this, as explained in the chapter and in this conclusion are primarily that phase data samples deeper than intensity data and because the sensitivity of phase data changes as a function of modulation frequency, combining phase data at different modulation frequencies gives the richest information content

and sampling. FD and mFD HD-DOT had not been evaluated previously for full 3D tomographic reconstructions using measured data, either in-vivo or on a phantom, nor had their previously been a literature review into the development and use of mFD measurements, which the introduction of this chapter provided.

The significance of this study is that it should give future researchers confidence and assurance that using phase data offers benefits compared to intensity data, which builds upon Doulgerakis, Eggebrecht, and Dehghani, 2019, and that multi-frequency data offers the best performance in the FD. The future direction from this work, should be that FD and mFD should be used and evaluated for in-vivo functional brain imaging, using simultaneous multi-frequency measurements to perform FD and mFD-HD-DOT. Simultaneous multi-frequency has been shown to be possible, recently by Stillwell et al., 2021 and the ultimate test for FD and mFD would be to evaluate how it compares to CW-HD-DOT in detecting functional brain activation. Based upon this work and previous simulation of mFD-HD-DOT, mFD has the highest potential in performance, which could be crucial in the field of diffuse optics, for any studies relying on localisation accuracy and higher resolutions for tomographic brain imaging.

7.5 Frequency domain measurements on healthy subjects

The penultimate experimental chapter in this thesis aimed to use the motivations discussed in chapters 1 and 2, and then build upon the progress in chapters 3 and 4 by developing and implementing an FD workflow for fNIRS and DOT as applied to human brain imaging. The motivations in chapter 1 and 2 were to develop FD imaging for functional brain imaging, as such advances would be relevant and could be applied to human brain health assessment in the form of TBI. By using FD measurements, phase data could be utilised, which offers

the benefits of deeper sampling and less sensitivity from superficial tissue compared to the conventionally used intensity data. In the application of assessing brain health by measuring functional activation, deeper sensitivity and less superficial tissue influence can be vital for accurately measuring functional responses in the brain. The progress made in chapters 3 and 4 were that the use of phase data and multi frequency phase data offered better image reconstruction for simulated point perturbations and a functional activation mimicking phantom when used in HD-DOT. In the studies presented in those chapters showed that the combination of intensity and phase data, performed better than the use of intensity data alone and that the strongest use of FD measurements came in the form of multi-frequency measurements. Chapter 5 of this thesis aimed to apply these principles and develop a comprehensive workflow for functional brain imaging.

The study used a motor task paradigm to invoke a response in the motor cortex, using a series of pseudo random separate left and right hand gripping period, with an 16 s stimulus and an rest of random duration between 16 s and 24 s. These choices ensured that the impact of physiological noise were minimised. As discussed in chapter 1.4.1, a key challenge in data collection is having optimal source-detector coupling on the scalp. To address this problem, a custom designed source-detector probe holder was 3D printed, alongside the use of a neoprene cap in order to hold the source-detector probes. The use of a flexible cap is similar to that of commercially available fNIRS and HD-DOT imaging systems, particularly for recent portable devices (Vidal-Rosas et al., 2021).

Key features of the cap and probe design for the study were that the cap allowed for 3D anatomical subject specific registration, since it was tight fitting to the head and markers could easily be placed on the cap to obtain landmark points. The purpose of this was that subject specific registration could be performed using these subject landmark points and corresponding landmark points on an anatomical model, using scans from a 3D camera. This feature was developed because co-registering the subject to anatomical models can lead

to more accurate localisations of functional activation, which is important for the clinical application of this thesis. Other registration methods are used, such as using a digitiser (Tsuzuki and Dan, 2014), but these may not be clinically compatible due to sensitivity from metal interference.

Another feature of the cap was the probe layout, which used 14 detectors and 8 sources per hemisphere, with long channel measurements between 27 mm to 37 mm for sampling the surface of the cortex and four specific channels for short channel separation at 9 mm length, to reduce the influence of superficial tissue by performing short signal regression. The spatial arrangement was designed to maximise the number of overlapping channels in order to facilitate DOT, as well as to ensure that none of the long channel detectors succumb to detector saturation, which is why the shortest long channel was set to be 27 mm. Finally, the array was designed to be compatible with other methods of parameter recovery, which for this array was the dual slopes method of reconstruction. There were 8 dual slope arrangements per hemisphere, split equally into the 4 quadrants of the imaging array. The benefits of the probe array are that standard fNIRS, DOT and Dual Slopes reconstruction can be performed, with a workflow that incorporates the collection of intensity and phase data all simultaneously with subject specific registration. The significance of this, is that it allowed the use of phase data for functional brain imaging to be investigated, alongside the current best experimental practices for fNIRS/DOT data collection (Yücel et al., 2021).

The FD measurements were performed on 3 healthy subjects and their HRF was obtained using fNIRS, using intensity only data, phase only data and a combined intensity and phase. Tomographic reconstructions using DOT of the HRF were obtained for the same three conditions of data. For the HRF's using fNIRS, the HRF's using phase data showed evidence that they were more sensitive to cortical tissue than the HRF's using intensity data and that the contributions using phase data were less influenced by superficial tissue. This was demonstrated on each subject, where in most cases HRF's using phase data showed

a canonical HRF expected from functional activation from motor cortex activity. HRF's derived from intensity only data showed HRF's expected from functional activation as well, however displayed visible changes in HbO and Hb akin to hemodynamic changes in the superficial tissue.

Another observed advantage of phase data was that the contrast in changes of HbO and Hb were larger than using intensity data. For each subject, the HRF from phase, showed larger changes of HbO and Hb during the co-lateral stimuli, in which HbO increased and Hb decreased. The increased contrast was found due to higher cortex sampling and lower superficial tissue sampling, in particular this was observed with subject 3, in which for the LHS, the intensity data showed a HRF of two consecutive double peaks. Whereas for the HRF derived from phase data on the LHS exhibits a broader shape, in which HbO increases and Hb decreases during the stimulus period and they recover to zero during the rest period. As well as greater contrast, phase data also separates more effectively from the co-lateral and uni-lateral stimuli compared to intensity data, which is observed particularly in subject 2 and 3. On the RHS for subject 2, for intensity data, the HRF for the co-lateral and uni-lateral hand grip shows two HRFs which are indistinguishable from eachother. However, for the two HRFs using phase data, there is a clear separation between the left and right hand grip, with the uni-lateral HRF showing the expected smaller response and the co-lateral HRF showing a larger, contrasting increase of HbO and decrease of Hb.

Despite the evidence of the benefits of phase data, there were still signs of some limitations of phase data, particularly in the quality of the signal. For example, less channels could be utilised to obtain the average HRF due to lower signal to the noise of the resting state signal compared to intensity data, which could be a problem for source-detector arrays with a limited number of channels and this suggested phase data is more sensitive to source-detector coupling on the scalp. In addition, phase data had to be treated for 'phase wrapping', which is an extra pre-processing step to ensure that the phase measurement didn't contain any

discontinuities as the phase measurement goes from 0 degrees to 360 degrees. Since the phase data was more sensitive to poor probe coupling or changes in coupling during the experiment, it was observed in some of the uni-lateral responses that artefacts in the HRF were present, which was seen for subject 1. Despite these limitations, there was still an overall benefit in using phase data, and each limitation could be minimised by making careful decisions with the design of data collection and data analysis. Finally, due to these limitations of phase data, the dual slopes reconstruction was limited in that the HRF derived from intensity data showed the functional activation on both hemispheres, whereas the HRF derived from phase data could only show the HRF on the LHS. This is because DS reconstruction requires a specific selection of channels to be used in the parameter recovery and if one channel is missing from the four required, then the DS reconstruction can't be applied for that DS.

The most effective methods of mitigation of the limitations of phase data were to combine the intensity and phase data together in parameter recovery and to design the probe array to maximise the stable contact between the probes and the scalp. The probe array was 3D printed and designed such that the source and detector fibers holders had a sub 0.5 mm tolerance to the source-detector fibers themselves, such that the contact friction between the holder and the fiber would keep the fiber from moving and the fiber could be pushed against the scalp. For data processing, as was done in the FD simulation study of chapter 3 and the FD phantom study of chapter 4, intensity and phase data were combined together and in doing so combined the benefits of phase and intensity data, whilst minimising the limitations of both data types. The additional channels of intensity could be used, where the same phase channels didn't meet the required quality checks. Where intensity and phase were used together, the contrast of the HRF was larger than when intensity was used alone and the artefacts in the uni-lateral HRF's were reduced compared to when phase was used alone.

The use of multi-frequency measurements was not evaluated because these measure-

ments were too difficult to measure in-vivo with the current hardware that was available for use. This is because measurements at higher modulation frequencies (203 MHz) had a weak SNR for both intensity and phase measurements and could not be reliably measured in the data collection protocol. As well as this, these measurements would have required multiple repeated measurements for each separate modulation frequency. This highlights a limitation of the current use of mFD, in that the hardware used for the mFD phantom study in chapter 4 was not robust enough for measurements in-vivo on a human head and demonstrates the need that simultaneous mFD measurements are required for practical in-vivo use of mFD, as shown by devices such as the mFD Nearwave (Stillwell et al., 2021).

The findings from the tomographic reconstructions, follow that from the spectroscopic reconstructions in that there is higher contrast in functional activation from phase data compared to intensity data, which is visibly seen in the tomographic reconstructions displayed on the surface of the cortex. Most pertinently for all subjects, the hemodynamic response from intensity data on the right hemisphere is less than half the magnitude compared to the equivalent response from phase data for HbO. Another consistent feature of the phase data derived images, were that they showed more significant decreases in Hb compared to intensity alone, which was also observed in spectroscopy. These observations repeatedly supported the hypothesis that the inclusion of phase data leads to more sampling of cortical tissue compared to intensity data and that phase data is less influenced by superficial tissue. Overall this work developed a successful FD workflow for detecting functional brain activation, as demonstrated using fNIRS and DOT, with both intensity and phase data.

The findings from the final experimental chapter are significant because they demonstrate that phase data are more sensitive to cortical tissue than intensity data, as well as being less sensitive to superficial tissue. This supports the findings of Doulgerakis, Eggebrecht, and Dehghani, 2019, Perkins, Eggebrecht, and Dehghani, 2021, Perkins, Eggebrecht, and Dehghani, 2022, Blaney, Fernandez, et al., 2023 and is the first study to demonstrate

this using fNIRS and DOT for in-vivo detection of functional activation. This is important for several applications within the field of fNIRS and DOT research, in particular where detecting functional activation is important, such as the original aims of this entire thesis, where the detection of functional activation was targeted as one method of assessing TBI, under the overarching aim of using FD diffuse optics to assess human brain health. Although chapter 5 only considered FD measurements at a single modulation frequency, chapter 3 and 4 covered the use of mFD and the significance of these chapters showed that mFD measurements are the most powerful use of FD measurements, due to their enhanced SNR of phase data and the variable depth sampling of phase data, which when coupled with intensity data, yielded the highest performance for HD-DOT.

From this thesis, the main contributions for the field of fNIRS and DOT are that FD measurements offer higher sensitivity to cortical activations by virtue of enhanced depth sampling compared to conventional intensity data, as used with CW measurements and that they are less sensitive to superficial tissue changes. Which means that given the choice, FD measurements are more powerful than CW measurements for detecting functional brain activation due to the use of phase data and the advantages that phase offers. Simultaneously, the limitations of phase data can be mitigated by coupling phase with intensity data in the FD to offer superior imaging with fNIRS and DOT than intensity data alone. If the specific hardware and experimental condition allows, than the use of multi-frequency measurements are encouraged, because it was demonstrated that mFD measurements offer the best imaging performance compared to single frequency FW measurements.

7.6 Demonstration of frequency domain measurements on acute Severe Traumatic Brain Injury Patients

The final experimental chapter of this thesis aimed to demonstrate that FD measurements could be made in the ICU with the aim to assess the brain injury of S-TBI patients. The experiment was built upon the hypothesis that NIRS could detect changes in the kinetic of an injected contrast dye ICG across the BBB, due to brain injuries causing changes in the perfusion of ICG. This hypothesis was formulated in the review paper of Forcione, Antonio M Chiarelli, et al., 2020 and preliminary results were obtained in Forcione, Yakoub, et al., 2020, where they showed that there was a significantly larger FWHM in the Z score of attention change in the TBI patients compared to the non TBI control group. The main limitation of that study is that they only used 4 measurement channels across a relatively small area of the patient's scalp, which means there was limited spatial specificity on where BBB damage may be, and areas with BBB damage may not be sampled.

To build upon that study, the proposed experiment used the ISS Imagent (ISS, USA), which along with a newly made helmet, allowed for coverage of the prefrontal cortex across the left and right hemispheres, with up to 120 measurement channels. As well as this, only intensity data was used in the experiment of Forcione, Yakoub, et al., 2020, whereas this study aimed to collect and use both intensity and phase data respectively, which could use the benefits of phase data such as deeper tissue sampling. This could allow more accurate detection of ICG across the BBB.

Data was collected on 10 S-TBI patients in the ICU and 8 trauma non-TBI patients and the experimental method was outlined in section 6. Example intensity and phase signals were shown in response to the injection of ICG, which show the rapid decrease in signal due to the absorption of light by the ICG, followed by a slow recovery of signal back to the

baseline (figure 6.11 for intensity and figure 6.12 for phase). However a full analysis of results could not be completed due to challenges in data collection on trauma non TBI control patients, as well as some limitations on the S-TBI patients. These are related to motion artifacts with the control patients, as well as difficulties in source-detector probe coupling on patient's scalps due to differing head sizes, which meant there could be gaps between the patient's scalp and the helmet. The next phase in this experiment would be to address the limitations by creating helmets of differing sizes and employing a stricter experimental protocol for the non TBI patients to minimize motion artifacts in the data. Then the ICG kinetic could be properly compared between S-TBI and non TBI patients across the left and right hemisphere of the prefrontal cortex to demonstrate of NIRS could localize where BBB damage had occurred.

7.7 Future Work

For future research from this thesis there are two natural areas that should be explored. Firstly, is the use of mFD measurements in-vivo for imaging functional brain activity. To date, no study has been presented that uses mFD for brain imagining, however there are proposed current applications for breast tissue imaging using mFD measurements (Stillwell et al., 2021). These are done using simultaneous mFD measurements, which should be the aspiration of the first mFD brain imaging study, since sampling multiple modulation frequencies offers the most realistic use case of mFD. Such a study could use a specific set of modulation frequencies that fulfill the criteria of having a sufficient baseline SNR, and each different frequency could be found by performing a sweep of frequencies from 0 MHz to several hundred MHz. Based upon previous studies (Intes and Britton Chance, 2005), 3 to 7 different modulation frequencies could be chosen, covering the range of frequencies and all offering different sampling distributions of tissue. Then these could be combined for a

subject-subject basis, incorporating the best intensity and phase signals for each subject, to perform imaging for fNIRS and DOT. Then the results of these in-vivo mFD measurements could be compared to single frequency FD and intensity only reconstructions to quantify and evaluate the potential strengths and weaknesses of mFD for brain imaging.

The second focus of future research from this thesis should be in the application of the developed FD and mFD measurements and workflow to measure brain activity in TBI patients. As has been demonstrated from previous studies looking at mTBI Forcione, Antonio Maria Chiarelli, et al., 2020 and Urban et al., 2015, functional activation could be detected on concussion patients. However, this time these measurements would be done in the FD for both fNIRS and DOT. The purpose of performing similar studies using FD data would be that the aforementioned studies only used intensity data, so that the use of phase data may reveal new information and provide enhanced results, namely in the enhanced contrast of the HRF to functional activation in both fNIRS and DOT. Therefore, a suitably proposed study would be to conduct FD fNIRS and DOT on a population of mTBI and non TBI subjects using an experimental protocol that induces functional response in the brain. Then, an evaluation of the different responses between the two groups could be made in order to advance understanding in the differences that these injuries have on the brain and to find any parameter that may predict if a brain has been subject to TBI.

Combining the two questions of further research, as previously explained, would entail using mFD measurements for the assessment of human brain health, more specifically in the imaging of functional activation of TBI patients, as described in the previous paragraph. This would provide an opportunity to answer the questions of the effectiveness of mFD for brain imaging compared to FD and conventional CW measurements, as well as answering questions in the domain of human brain health within mTBI.

References

Akila, V. and Anita Christaline Johnvictor (Apr. 2023). "Functional near infrared spectroscopy for brain functional connectivity analysis: A graph theoretic approach". In: *Heliyon* 9.4, e15002. ISSN: 2405-8440. DOI: 10.1016/j.heliyon.2023.e15002. URL: https://www.sciencedirect.com/science/article/pii/S2405844023022090 (visited on 08/31/2023).

Ban, Han Y. et al. (Jan. 2022). "Kernel Flow: a high channel count scalable time-domain functional near-infrared spectroscopy system". In: *Journal of Biomedical Optics* 27.07. ISSN: 1083-3668. DOI: 10.1117/1.JBO.27.7.074710. URL: https://www.spiedigitallibrary.org/journals/journal-of-biomedical-optics/volume-27/issue-07/074710/Kernel-Flow--a-high-channel-count-scalable-time-domain/10.1117/1.JBO.27.7.074710.full (visited on 06/05/2023).

Bevilacqua, Frédéric et al. (Aug. 1999). "In vivo local determination of tissue optical properties: applications to human brain". en. In: *Applied Optics* 38.22, p. 4939. ISSN: 0003-6935, 1539-4522. DOI: 10.1364/AO.38.004939. URL: https://opg.optica.org/abstract.cfm?URI=ao-38-22-4939 (visited on 06/06/2023).

Bigio, Irving J. and Sergio Fantini (Jan. 2016). *Quantitative Biomedical Optics: Theory, methods, and applications*. 1st ed. Cambridge University Press. ISBN: 978-0-521-87656-8 978-1-139-02979-7. DOI: 10.1017/CBO9781139029797. URL: https://www.cambridge.

org/highereducation/books/quantitative-biomedical-optics/5CAD764FCF30B1B%20B9EEA3DA7B60B7A4F#contents (visited on 06/05/2023).

Blaney, Giles, Cristianne Fernandez, et al. (Jan. 2023). "Dual-slope imaging of cerebral hemodynamics with frequency-domain near-infrared spectroscopy". In: *Neurophotonics* 10.01. ISSN: 2329-423X. DOI: 10.1117/1.NPh.10.1.013508. URL: https://www.spiedigitallibrary.org/journals/neurophotonics/volume-10/issue-01/013508/Dual-slope-imaging-of-cerebral-hemodynamics-with-frequency-domain-near/10.1117/1.NPh.10.1.013508.full (visited on 06/05/2023).

Blaney, Giles, Angelo Sassaroli, et al. (Jan. 2020). "Phase dual-slopes in frequency-domain near-infrared spectroscopy for enhanced sensitivity to brain tissue: First applications to human subjects". en. In: *Journal of Biophotonics* 13.1. ISSN: 1864-063X, 1864-0648. DOI: 10.1002/jbio.201960018. URL: https://onlinelibrary.wiley.com/doi/10.1002/jbio.201960018 (visited on 06/05/2023).

Brigadoi, Sabrina, Lisa Ceccherini, et al. (Jan. 2014). "Motion artifacts in functional near-infrared spectroscopy: a comparison of motion correction techniques applied to real cognitive data". eng. In: *NeuroImage* 85 Pt 1.0 1, pp. 181–191. ISSN: 1095-9572. DOI: 10.1016/j.neuroimage.2013.04.082.

Brigadoi, Sabrina and Robert J. Cooper (May 2015). "How short is short? Optimum source–detector distance for short-separation channels in functional near-infrared spectroscopy". en. In: *Neurophotonics* 2.2, p. 025005. ISSN: 2329-423X. DOI: 10.1117/1.NPh.2.2.025005. URL: http://neurophotonics.spiedigitallibrary.org/article.aspx?doi=10.1117/1.NPh.2.2.025005 (visited on 06/07/2023).

Burcin Unlu, Mehmet et al. (2006). "Diffuse optical tomographic reconstruction using multifrequency data". en. In: *Journal of Biomedical Optics* 11.5, p. 054008. ISSN: 10833668. DOI: 10.1117/1.2363370. URL: http://biomedicaloptics.spiedigitallibrary.org/article.aspx?doi=10.1117/1.2363370 (visited on 06/06/2023).

Chance, B et al. (Apr. 1993). "Cognition-activated low-frequency modulation of light absorption in human brain." In: *Proceedings of the National Academy of Sciences of the United States of America* 90.8, pp. 3770–3774. ISSN: 0027-8424. URL: https://www.ncbi.nlm.nih.gov/pmc/articles/PMC46383/ (visited on 08/28/2023).

Chen, Chen et al. (Apr. 2015). "Multi-frequency diffuse optical tomography for cancer detection". In: *2015 IEEE 12th International Symposium on Biomedical Imaging (ISBI)*. Brooklyn, NY, USA: IEEE, pp. 67–70. ISBN: 978-1-4799-2374-8. DOI: 10.1109/ISBI.2015.7163818. URL: http://ieeexplore.ieee.org/document/7163818/ (visited on 06/06/2023).

Chen, Michelle et al. (Sept. 2017). "Spatial Coregistration of Functional Near-Infrared Spectroscopy to Brain MRI: Spatial Coregistration of NIRS to MRI". en. In: *Journal of Neuroimaging* 27.5, pp. 453–460. ISSN: 10512284. DOI: 10.1111/jon.12432. URL: https://onlinelibrary.wiley.com/doi/10.1111/jon.12432 (visited on 06/07/2023).

Chen, Yaohua et al. (2022). "Defining brain health: A concept analysis". en. In: *International Journal of Geriatric Psychiatry* 37.1. ISSN: 1099-1166. DOI: 10.1002/gps.5564. URL: https://onlinelibrary.wiley.com/doi/abs/10.1002/gps.5564 (visited on 09/11/2023).

Chung, So Hyun et al. (June 2012). "Molecular imaging of water binding state and diffusion in breast cancer using diffuse optical spectroscopy and diffusion weighted MRI". en. In: *Journal of Biomedical Optics* 17.7, p. 071304. ISSN: 1083-3668. DOI: 10.1117/1.JBO.17.7.071304. URL: http://biomedicaloptics.spiedigitallibrary.org/article.aspx?doi=10.1117/1.JBO.17.7.071304 (visited on 10/31/2024).

Cope, M. (1991). "The development of a near infrared spectroscopy system and its application for non invasive monitoring of cerebral blood and tissue oxygenation in the newborn infants". eng. Publication Title: Doctoral thesis, University of London. Doctoral. University of London. URL: https://discovery.ucl.ac.uk/id/eprint/1317956/ (visited on 06/07/2023).

Davies, David J. (July 2017). "Cerebral near infra-red spectroscopy in traumatic brain injury as a potential independent monitoring modality and alternative to invasive tissue oxygen tension sensors". English. d_ph. University of Birmingham. URL: https://etheses.bham.ac.uk/id/eprint/7325/ (visited on 06/06/2023).

Davies, David J., Michael Clancy, et al. (Apr. 2019). "Cerebral Oxygenation in Traumatic Brain Injury: Can a Non-Invasive Frequency Domain Near-Infrared Spectroscopy Device Detect Changes in Brain Tissue Oxygen Tension as Well as the Established Invasive Monitor?" en. In: *Journal of Neurotrauma* 36.7, pp. 1175–1183. ISSN: 0897-7151, 1557-9042. DOI: 10.1089/neu.2018.5667. URL: https://www.liebertpub.com/doi/10.1089/neu.2018.5667 (visited on 06/06/2023).

Davies, David J., Zhangjie Su, et al. (July 2015). "Near-Infrared Spectroscopy in the Monitoring of Adult Traumatic Brain Injury: A Review". en. In: *Journal of Neurotrauma* 32.13, pp. 933–941. ISSN: 0897-7151, 1557-9042. DOI: 10.1089/neu.2014.3748. URL: http://www.liebertpub.com/doi/10.1089/neu.2014.3748 (visited on 06/06/2023).

Dehghani, Hamid, Matthew E. Eames, et al. (June 2009). "Near infrared optical tomography using NIRFAST: Algorithm for numerical model and image reconstruction". en. In: *Communications in Numerical Methods in Engineering* 25.6, pp. 711–732. ISSN: 10698299, 10990887. DOI: 10.1002/cnm.1162. URL: https://onlinelibrary.wiley.com/doi/10.1002/cnm.1162 (visited on 06/05/2023).

Dehghani, Hamid, Brian W. Pogue, et al. (Jan. 2003). "Multiwavelength three-dimensional near-infrared tomography of the breast: initial simulation, phantom, and clinical results". en. In: *Applied Optics* 42.1, p. 135. ISSN: 0003-6935, 1539-4522. DOI: 10.1364/AO.42.000135. URL: https://opg.optica.org/abstract.cfm?URI=ao-42-1-135 (visited on 06/07/2023).

deJong, Max et al. (2021). "Multifrequency Frequency Domain Diffuse Optical Tomography". en. In: *European Conferences on Biomedical Optics 2021 (ECBO)*. Munich: Optica Publishing Group, EM1A.28. ISBN: 978-1-943580-95-8. DOI: 10.1364/ECBO.2021.

EM1A.28. URL: https://opg.optica.org/abstract.cfm?URI=ECBO-2021-EM1A.28 (visited on 06/06/2023).

Delpy, D T et al. (Dec. 1988). "Estimation of optical pathlength through tissue from direct time of flight measurement". In: *Physics in Medicine and Biology* 33.12, pp. 1433–1442. ISSN: 0031-9155, 1361-6560. DOI: 10.1088/0031-9155/33/12/008. URL: https://iopscience.iop.org/article/10.1088/0031-9155/33/12/008 (visited on 06/05/2023).

Diamond, Solomon Gilbert et al. (Mar. 2006). "Dynamic physiological modeling for functional diffuse optical tomography". en. In: *NeuroImage* 30.1, pp. 88–101. ISSN: 10538119. DOI: 10.1016/j.neuroimage.2005.09.016. URL: https://linkinghub.elsevier.com/retrieve/pii/S1053811905007196 (visited on 10/31/2024).

Doulgerakis, Matthaios, Adam T. Eggebrecht, and Hamid Dehghani (Aug. 2019). "High-density functional diffuse optical tomography based on frequency-domain measurements improves image quality and spatial resolution". In: *Neurophotonics* 6.03, p. 1. ISSN: 2329-423X. DOI: 10.1117/1.NPh.6.3.035007. URL: https://www.spiedigitallibrary.org/journals/neurophotonics/volume-6/issue-03/035007/High-density-functional-diffuse-optical-tomography-based-on-frequency-domain/10.1117/1.NPh.6.3.035007.full (visited on 06/05/2023).

Eggebrecht, Adam T. et al. (June 2014). "Mapping distributed brain function and networks with diffuse optical tomography". en. In: *Nature Photonics* 8.6, pp. 448–454. ISSN: 1749-4885, 1749-4893. DOI: 10.1038/nphoton.2014.107. URL: https://www.nature.com/articles/nphoton.2014.107 (visited on 06/06/2023).

Fan, Weihao, Hamid Dehghani, and Adam T. Eggebrecht (Nov. 2021). "Investigation of effect of modulation frequency on high-density diffuse optical tomography image quality". In: *Neurophotonics* 8.04. ISSN: 2329-423X. DOI: 10.1117/1.NPh.8.4.045002. URL: https://www.spiedigitallibrary.org/journals/neurophotonics/volume-8/issue-04/045002/Investigation-of-effect-of-modulation-frequency-on-high-density-diffuse/10.1117/1.NPh.8.4.045002.full (visited on 06/06/2023).

Fang, Qianqian and David A. Boas (Oct. 2009). "Monte Carlo Simulation of Photon Migration in 3D Turbid Media Accelerated by Graphics Processing Units". EN. In: *Optics Express* 17.22. Publisher: Optica Publishing Group, pp. 20178–20190. ISSN: 1094-4087. DOI: 10.1364/OE.17.020178. URL: https://opg.optica.org/oe/abstract.cfm?uri=oe-17-22-20178 (visited on 09/04/2023).

Fantini, Sergio and Angelo Sassaroli (2016). "Frequency-Domain Techniques for Tissue Spectroscopy and Imaging". en. In: *Handbook of Optical Biomedical Diagnostics, Second Edition, Volume 1: Light-Tissue Interaction*. SPIE PRESS. ISBN: 978-1-62841-909-2. DOI: 10.1117/3.2219603.ch7. URL: http://ebooks.spiedigitallibrary.org/content.aspx?bookid=2021&sectionid=149199428 (visited on 06/06/2023).

— (Apr. 2020). "Frequency-Domain Techniques for Cerebral and Functional Near-Infrared Spectroscopy". In: *Frontiers in Neuroscience* 14, p. 300. ISSN: 1662-453X. DOI: 10.3389/fnins.2020.00300. URL: https://www.frontiersin.org/article/10.3389/fnins.2020.00300/full (visited on 06/05/2023).

Fischl, Bruce and Anders M. Dale (Sept. 2000). "Measuring the thickness of the human cerebral cortex from magnetic resonance images". en. In: *Proceedings of the National Academy of Sciences* 97.20, pp. 11050–11055. ISSN: 0027-8424, 1091-6490. DOI: 10.1073/pnas.200033797. URL: https://pnas.org/doi/full/10.1073/pnas.200033797 (visited on 06/06/2023).

Forcione, Mario, Antonio M Chiarelli, et al. (Aug. 2020). "Cerebral perfusion and blood–brain barrier assessment in brain trauma using contrast-enhanced near-infrared spectroscopy with indocyanine green: A review". en. In: *Journal of Cerebral Blood Flow & Metabolism* 40.8, pp. 1586–1598. ISSN: 0271-678X, 1559-7016. DOI: 10.1177/0271678X20921973. URL: http://journals.sagepub.com/doi/10.1177/0271678X20921973 (visited on 06/06/2023).

Forcione, Mario, Antonio Maria Chiarelli, et al. (Aug. 2020). "Tomographic Task-Related Functional Near-Infrared Spectroscopy in Acute Sport-Related Concussion: An Ob-

servational Case Study". en. In: *International Journal of Molecular Sciences* 21.17, p. 6273. ISSN: 1422-0067. DOI: 10.3390/ijms21176273. URL: https://www.mdpi.com/1422-0067/21/17/6273 (visited on 06/06/2023).

Forcione, Mario, Kamal Makram Yakoub, et al. (Nov. 2020). "Dynamic contrast-enhanced near-infrared spectroscopy using indocyanine green on moderate and severe traumatic brain injury: a prospective observational study". In: *Quantitative Imaging in Medicine and Surgery* 10.11, pp. 2085–2097. ISSN: 22234292, 22234306. DOI: 10.21037/qims-20-742. URL: http://qims.amegroups.com/article/view/49126/html (visited on 06/06/2023).

Franceschini, Maria Angela et al. (July 2003). "Hemodynamic evoked response of the sensorimotor cortex measured noninvasively with near-infrared optical imaging". en. In: *Psychophysiology* 40.4, pp. 548–560. ISSN: 0048-5772, 1469-8986. DOI: 10.1111/1469-8986.00057. URL: https://onlinelibrary.wiley.com/doi/10.1111/1469-8986.00057 (visited on 06/05/2023).

Fujimoto, James G. et al. (Jan. 2000). "Optical Coherence Tomography: An Emerging Technology for Biomedical Imaging and Optical Biopsy". en. In: *Neoplasia* 2.1-2, pp. 9–25. ISSN: 14765586. DOI: 10.1038/sj.neo.7900071. URL: https://linkinghub.elsevier.com/retrieve/pii/S1476558600800172 (visited on 06/05/2023).

Gibson, A.P. et al. (Apr. 2006). "Three-dimensional whole-head optical tomography of passive motor evoked responses in the neonate". en. In: *NeuroImage* 30.2, pp. 521–528. ISSN: 10538119. DOI: 10.1016/j.neuroimage.2005.08.059. URL: https://linkinghub.elsevier.com/retrieve/pii/S1053811905007330 (visited on 06/05/2023).

Gioux, Sylvain, Amaan Mazhar, and David J. Cuccia (June 2019). "Spatial frequency domain imaging in 2019: principles, applications, and perspectives". In: *Journal of Biomedical Optics* 24.07, p. 1. ISSN: 1083-3668. DOI: 10.1117/1.JBO.24.7.071613. URL: https://www.spiedigitallibrary.org/journals/journal-of-biomedical-optics/volume-24/

issue-07/071613/Spatial-frequency-domain-imaging-in-2019--principles-applications-and/10.1117/1.JBO.24.7.071613.full (visited on 06/05/2023).

Glover, Gary H. (Apr. 2011). "Overview of Functional Magnetic Resonance Imaging". en. In: *Neurosurgery Clinics of North America* 22.2, pp. 133–139. ISSN: 10423680. DOI: 10.1016/j.nec.2010.11.001. URL: https://linkinghub.elsevier.com/retrieve/pii/S1042368010001129 (visited on 06/06/2023).

Goense, Jozien, Yvette Bohraus, and Nikos K. Logothetis (June 2016). "fMRI at High Spatial Resolution: Implications for BOLD-Models". In: *Frontiers in Computational Neuroscience* 10. ISSN: 1662-5188. DOI: 10.3389/fncom.2016.00066. URL: http://journal.frontiersin.org/Article/10.3389/fncom.2016.00066/abstract (visited on 06/06/2023).

Gratton, Gabriele, Paul M. Corballis, et al. (1995). "Shades of gray matter: Noninvasive optical images of human brain reponses during visual stimulation". en. In: *Psychophysiology* 32.5, pp. 505–509. ISSN: 1469-8986. DOI: 10.1111/j.1469-8986.1995.tb02102.x. URL: https://onlinelibrary.wiley.com/doi/abs/10.1111/j.1469-8986.1995.tb02102.x (visited on 08/30/2023).

Gratton, Gabriele and Monica Fabiani (2010). "Fast optical imaging of human brain function". In: *Frontiers in Human Neuroscience* 4. ISSN: 1662-5161. URL: https://www.frontiersin.org/articles/10.3389/fnhum.2010.00052 (visited on 08/30/2023).

Gulsen, Gultekin et al. (2006). "Design and implementation of a multifrequency near-infrared diffuse optical tomography system". en. In: *Journal of Biomedical Optics* 11.1, p. 014020. ISSN: 10833668. DOI: 10.1117/1.2161199. URL: http://biomedicaloptics.spiedigitallibrary.org/article.aspx?doi=10.1117/1.2161199 (visited on 06/06/2023).

Hale, George M. and Marvin R. Querry (Mar. 1973). "Optical Constants of Water in the 200-nm to 200-um Wavelength Region". en. In: *Applied Optics* 12.3, p. 555. ISSN: 0003-6935, 1539-4522. DOI: 10.1364/AO.12.000555. URL: https://opg.optica.org/abstract.cfm?URI=ao-12-3-555 (visited on 09/23/2023).

Han, Weimin, Wenxiang Cong, and Ge Wang (2006). "Mathematical Study and Numerical Simulation of Multispectral Bioluminescence Tomography". en. In: *International Journal of Biomedical Imaging* 2006, pp. 1–10. ISSN: 1687-4188, 1687-4196. DOI: 10.1155/IJBI/2006/54390. URL: http://www.hindawi.com/journals/ijbi/2006/054390/abs/ (visited on 06/05/2023).

Hernandez, Samuel Montero and Luca Pollonini (Apr. 2020). "NIRSplot: A Tool for Quality Assessment of fNIRS Scans". EN. In: *Biophotonics Congress: Biomedical Optics 2020 (Translational, Microscopy, OCT, OTS, BRAIN) (2020), paper BM2C.5*. Optica Publishing Group, BM2C.5. DOI: 10.1364/BRAIN.2020.BM2C.5. URL: https://opg.optica.org/abstract.cfm?uri=BRAIN-2020-BM2C.5 (visited on 08/31/2023).

Herold, Fabian et al. (Nov. 2018). "Applications of Functional Near-Infrared Spectroscopy (fNIRS) Neuroimaging in Exercise–Cognition Science: A Systematic, Methodology-Focused Review". en. In: *Journal of Clinical Medicine* 7.12, p. 466. ISSN: 2077-0383. DOI: 10.3390/jcm7120466. URL: https://www.mdpi.com/2077-0383/7/12/466 (visited on 06/05/2023).

Hornung, René et al. (Mar. 2011). "Frequency-domain near-infrared spectroscopy of the uterine cervix during regular pregnancies". en. In: *Lasers in Medical Science* 26.2, pp. 205–212. ISSN: 0268-8921, 1435-604X. DOI: 10.1007/s10103-010-0832-7. URL: http://link.springer.com/10.1007/s10103-010-0832-7 (visited on 06/06/2023).

Hoshi, Yoko and Mamoru Tamura (Feb. 1993). "Detection of dynamic changes in cerebral oxygenation coupled to neuronal function during mental work in man". en. In: *Neuroscience Letters* 150.1, pp. 5–8. ISSN: 03043940. DOI: 10.1016/0304-3940(93)90094-2. URL: https://linkinghub.elsevier.com/retrieve/pii/0304394093900942 (visited on 08/28/2023).

Huang, Ruisen et al. (2022). "Motion artifacts removal and evaluation techniques for functional near-infrared spectroscopy signals: A review". In: *Frontiers in Neuroscience* 16.

ISSN: 1662-453X. URL: https://www.frontiersin.org/articles/10.3389/fnins.2022.878750 (visited on 08/31/2023).

Huppert, T.J. et al. (Jan. 2006). "A temporal comparison of BOLD, ASL, and NIRS hemodynamic responses to motor stimuli in adult humans". en. In: *NeuroImage* 29.2, pp. 368–382. ISSN: 10538119. DOI: 10.1016/j.neuroimage.2005.08.065. URL: https://linkinghub.elsevier.com/retrieve/pii/S1053811905005823 (visited on 06/05/2023).

Huppert, Theodore J. et al. (Apr. 2009). "HomER: a review of time-series analysis methods for near-infrared spectroscopy of the brain". en. In: *Applied Optics* 48.10, p. D280. ISSN: 0003-6935, 1539-4522. DOI: 10.1364/AO.48.00D280. URL: https://opg.optica.org/abstract.cfm?URI=ao-48-10-D280 (visited on 06/07/2023).

Ichikawa, Hiroko et al. (Feb. 2019). "A longitudinal study of infant view-invariant face processing during the first 3–8 months of life". en. In: *NeuroImage* 186, pp. 817–824. ISSN: 10538119. DOI: 10.1016/j.neuroimage.2018.11.031. URL: https://linkinghub.elsevier.com/retrieve/pii/S1053811918321098 (visited on 06/07/2023).

Intes, Xavier and Britton Chance (Oct. 2005). "Multi-frequency diffuse optical tomography". en. In: *Journal of Modern Optics* 52.15, pp. 2139–2159. ISSN: 0950-0340, 1362-3044. DOI: 10.1080/09500340500217290. URL: http://www.tandfonline.com/doi/abs/10.1080/09500340500217290 (visited on 06/06/2023).

Jain, Shobhit and Lindsay M. Iverson (2023). "Glasgow Coma Scale". eng. In: *StatPearls*. Treasure Island (FL): StatPearls Publishing. URL: http://www.ncbi.nlm.nih.gov/books/NBK513298/ (visited on 06/06/2023).

Jöbsis, Frans F. (Dec. 1977). "Noninvasive, Infrared Monitoring of Cerebral and Myocardial Oxygen Sufficiency and Circulatory Parameters". en. In: *Science* 198.4323, pp. 1264–1267. ISSN: 0036-8075, 1095-9203. DOI: 10.1126/science.929199. URL: https://www.science.org/doi/10.1126/science.929199 (visited on 08/19/2023).

Kanazawa, So and Ippeita Dan (Oct. 2018). "Editorial: fNIRS in Psychological Research: Functional Neuroimaging Beyond Conventional Fields: Editorial". en. In: *Japanese*

Psychological Research 60.4, pp. 191–195. ISSN: 00215368. DOI: 10.1111/jpr.12230. URL: https://onlinelibrary.wiley.com/doi/10.1111/jpr.12230 (visited on 06/05/2023).

Kassab, Amal et al. (Jan. 2015). "Functional near-infrared spectroscopy caps for brain activity monitoring: a review". EN. In: *Applied Optics* 54.3. Publisher: Optica Publishing Group, pp. 576–586. ISSN: 2155-3165. DOI: 10.1364/AO.54.000576. URL: https://opg.optica.org/ao/abstract.cfm?uri=ao-54-3-576 (visited on 09/07/2023).

Kato, T. et al. (May 1993). "Human visual cortical function during photic stimulation monitoring by means of near-infrared spectroscopy". eng. In: *Journal of Cerebral Blood Flow and Metabolism: Official Journal of the International Society of Cerebral Blood Flow and Metabolism* 13.3, pp. 516–520. ISSN: 0271-678X. DOI: 10.1038/jcbfm.1993.66.

Kirilina, Evgeniya et al. (2013). "Identifying and quantifying main components of physiological noise in functional near infrared spectroscopy on the prefrontal cortex". In: *Frontiers in Human Neuroscience* 7. ISSN: 1662-5161. URL: https://www.frontiersin.org/articles/10.3389/fnhum.2013.00864 (visited on 08/31/2023).

Koizumi, Hideaki et al. (Oct. 1999). "Higher-order brain function analysis by trans-cranial dynamic near-infrared spectroscopy imaging". In: *Journal of Biomedical Optics* 4.4. Publisher: SPIE, pp. 403–413. ISSN: 1083-3668, 1560-2281. DOI: 10.1117/1.429959. URL: https://www.spiedigitallibrary.org/journals/journal-of-biomedical-optics/volume-4/issue-4/0000/Higher-order-brain-function-analysis-by-trans-cranial-dynamic-near/10.1117/1.429959.full (visited on 08/29/2023).

Lacerenza, Michele et al. (Oct. 2020). "Wearable and wireless time-domain near-infrared spectroscopy system for brain and muscle hemodynamic monitoring". en. In: *Biomedical Optics Express* 11.10, p. 5934. ISSN: 2156-7085, 2156-7085. DOI: 10.1364/BOE.403327. URL: https://opg.optica.org/abstract.cfm?URI=boe-11-10-5934 (visited on 06/05/2023).

Lane, Lucas A, Ruiyang Xue, and Shuming Nie (Aug. 2018). "Emergence of two near-infrared windows for in vivo and intraoperative SERS". en. In: *Current Opinion in Chemical*

Biology 45, pp. 95–103. ISSN: 13675931. DOI: 10.1016/j.cbpa.2018.03.015. URL: https://linkinghub.elsevier.com/retrieve/pii/S1367593118300188 (visited on 08/14/2023).

Lawrence, T et al. (Nov. 2016). "Traumatic brain injury in England and Wales: prospective audit of epidemiology, complications and standardised mortality". en. In: *BMJ Open* 6.11, e012197. ISSN: 2044-6055, 2044-6055. DOI: 10.1136/bmjopen-2016-012197. URL: https://bmjopen.bmj.com/lookup/doi/10.1136/bmjopen-2016-012197 (visited on 06/06/2023).

Lee, Hwan et al. (Oct. 2021). "Use of Magnetic Resonance Imaging in Acute Traumatic Brain Injury Patients is Associated with Lower Inpatient Mortality". en. In: *Journal of Clinical Imaging Science* 11, p. 53. ISSN: 2156-5597, 2156-7514. DOI: 10.25259/JCIS_148_2021. URL: https://clinicalimagingscience.org/use-of-magnetic-resonance-imaging-in-acute-traumatic-brain-injury-patients-is-associated-with-lower-inpatient-mortality/ (visited on 06/06/2023).

Maas, Andrew I. R. et al. (Nov. 2022). "Traumatic brain injury: progress and challenges in prevention, clinical care, and research". eng. In: *The Lancet. Neurology* 21.11, pp. 1004–1060. ISSN: 1474-4465. DOI: 10.1016/S1474-4422(22)00309-X.

Maki, Atsushi et al. (1995). "Spatial and temporal analysis of human motor activity using noninvasive NIR topography". en. In: *Medical Physics* 22.12, pp. 1997–2005. ISSN: 2473-4209. DOI: 10.1118/1.597496. URL: https://onlinelibrary.wiley.com/doi/abs/10.1118/1.597496 (visited on 08/29/2023).

Martelli, Fabrizio et al. (June 2013). "Phantoms for diffuse optical imaging based on totally absorbing objects, part 1: basic concepts". en. In: *Journal of Biomedical Optics* 18.6, p. 066014. ISSN: 1083-3668. DOI: 10.1117/1.JBO.18.6.066014. URL: http://biomedicaloptics.spiedigitallibrary.org/article.aspx?doi=10.1117/1.JBO.18.6.066014 (visited on 06/07/2023).

Molavi, Behnam and Guy A Dumont (Feb. 2012). "Wavelet-based motion artifact removal for functional near-infrared spectroscopy". In: *Physiological Measurement* 33.2, pp. 259–

270. ISSN: 0967-3334, 1361-6579. DOI: 10.1088/0967-3334/33/2/259. URL: https://iopscience.iop.org/article/10.1088/0967-3334/33/2/259 (visited on 06/07/2023).

Mudeng, Vicky, Wahdiyatun Nisa, and Sena Sukmananda Suprapto (June 2022). "Computational image reconstruction for multi-frequency diffuse optical tomography". en. In: *Journal of King Saud University - Computer and Information Sciences* 34.6, pp. 3527–3538. ISSN: 13191578. DOI: 10.1016/j.jksuci.2020.12.015. URL: https://linkinghub.elsevier.com/retrieve/pii/S1319157820306236 (visited on 06/06/2023).

Nakamura, Shunsuke (2011). "Monitoring of jugular venous oxygen saturation". In: *Japanese journal of clinical medicine* 69.4, pp. 704–7.

Nolte's The Human Brain (2023). *Nolte's The Human Brain: An Introduction to its Functional Anatomy - Todd W. Vanderah - Douglas J. Gould - Libro in lingua inglese - Elsevier - Health Sciences Division - | IBS*. it. URL: https://www.ibs.it/nolte-s-human-brain-introduction-libro-inglese-todd-w-vanderah-douglas-j-gould/e/9780323653985 (visited on 06/06/2023).

Okada, Eiji et al. (Jan. 1997). "Theoretical and experimental investigation of near-infrared light propagation in a model of the adult head". en. In: *Applied Optics* 36.1, p. 21. ISSN: 0003-6935, 1539-4522. DOI: 10.1364/AO.36.000021. URL: https://opg.optica.org/abstract.cfm?URI=ao-36-1-21 (visited on 06/06/2023).

Ortega-Martinez, Antonio et al. (Oct. 2022). "How much do time-domain functional near-infrared spectroscopy (fNIRS) moments improve estimation of brain activity over traditional fNIRS?" In: *Neurophotonics* 10.01. ISSN: 2329-423X. DOI: 10.1117/1.NPh.10.1.013504. URL: https://www.spiedigitallibrary.org/journals/neurophotonics/volume-10/issue-01/013504/How-much-do-time-domain-functional-near-infrared-spectroscopy-fNIRS/10.1117/1.NPh.10.1.013504.full (visited on 08/16/2023).

Overview | Head injury (May 2023). *Overview | Head injury: assessment and early management | Guidance | NICE*. eng. Publisher: NICE. URL: https://www.nice.org.uk/guidance/ng232 (visited on 06/06/2023).

Patterson, Michael S. et al. (Nov. 1991). "Frequency-domain reflectance for the determination of the scattering and absorption properties of tissue". en. In: *Applied Optics* 30.31, p. 4474. ISSN: 0003-6935, 1539-4522. DOI: 10.1364/AO.30.004474. URL: https://opg.optica.org/abstract.cfm?URI=ao-30-31-4474 (visited on 06/06/2023).

Penrose, R. (July 1955). "A generalized inverse for matrices". en. In: *Mathematical Proceedings of the Cambridge Philosophical Society* 51.3, pp. 406–413. ISSN: 0305-0041, 1469-8064. DOI: 10.1017/S0305004100030401. URL: https://www.cambridge.org/core/product/identifier/S0305004100030401/type/journal_article (visited on 06/06/2023).

Perkins, Guy A., Adam T. Eggebrecht, and Hamid Dehghani (May 2021). "Quantitative evaluation of frequency domain measurements in high density diffuse optical tomography". In: *Journal of Biomedical Optics* 26.05. ISSN: 1083-3668. DOI: 10.1117/1.JBO.26.5.056001. URL: https://www.spiedigitallibrary.org/journals/journal-of-biomedical-optics/volume-26/issue-05/056001/Quantitative-evaluation-of-frequency-domain-measurements-in-high-density-diffuse/10.1117/1.JBO.26.5.056001.full (visited on 06/05/2023).

— (Oct. 2022). "Multi-modulated frequency domain high density diffuse optical tomography". en. In: *Biomedical Optics Express* 13.10, p. 5275. ISSN: 2156-7085, 2156-7085. DOI: 10.1364/BOE.467614. URL: https://opg.optica.org/abstract.cfm?URI=boe-13-10-5275 (visited on 06/07/2023).

Pham, Tuan H. et al. (June 2000). "Broad bandwidth frequency domain instrument for quantitative tissue optical spectroscopy". en. In: *Review of Scientific Instruments* 71.6, pp. 2500–2513. ISSN: 0034-6748, 1089-7623. DOI: 10.1063/1.1150665. URL: https://pubs.aip.org/aip/rsi/article/71/6/2500-2513/351227 (visited on 06/06/2023).

Pifferi, Antonio et al. (July 2015). "Mechanically switchable solid inhomogeneous phantom for performance tests in diffuse imaging and spectroscopy". en. In: *Journal of Biomedical Optics* 20.12, p. 121304. ISSN: 1083-3668. DOI: 10.1117/1.JBO.20.12.121304. URL:

http://biomedicaloptics.spiedigitallibrary.org/article.aspx?doi=10.1117/1.JBO.20.12.121304 (visited on 06/07/2023).

Plichta, M.M. et al. (Nov. 2006). "Event-related functional near-infrared spectroscopy (fNIRS) based on craniocerebral correlations: Reproducibility of activation?" In: *Human Brain Mapping* 28.8, pp. 733–741. ISSN: 1065-9471. DOI: 10.1002/hbm.20303. URL: https://www.ncbi.nlm.nih.gov/pmc/articles/PMC6871457/ (visited on 08/31/2023).

Quaresima, Valentina and Marco Ferrari (Sept. 2019). "A Mini-Review on Functional Near-Infrared Spectroscopy (fNIRS): Where Do We Stand, and Where Should We Go?" en. In: *Photonics* 6.3. Number: 3 Publisher: Multidisciplinary Digital Publishing Institute, p. 87. ISSN: 2304-6732. DOI: 10.3390/photonics6030087. URL: https://www.mdpi.com/2304-6732/6/3/87 (visited on 09/23/2023).

Roldán, María and Panayiotis A. Kyriacou (Feb. 2021). "Near-Infrared Spectroscopy (NIRS) in Traumatic Brain Injury (TBI)". en. In: *Sensors* 21.5, p. 1586. ISSN: 1424-8220. DOI: 10.3390/s21051586. URL: https://www.mdpi.com/1424-8220/21/5/1586 (visited on 06/06/2023).

Scholkmann, F. et al. (May 2010). "How to detect and reduce movement artifacts in near-infrared imaging using moving standard deviation and spline interpolation". eng. In: *Physiological Measurement* 31.5, pp. 649–662. ISSN: 1361-6579. DOI: 10.1088/0967-3334/31/5/004.

Scholkmann, Felix, Ilias Tachtsidis, et al. (July 2022). "Systemic physiology augmented functional near-infrared spectroscopy: a powerful approach to study the embodied human brain". In: *Neurophotonics* 9.3, p. 030801. ISSN: 2329-423X. DOI: 10.1117/1.NPh.9.3.030801. URL: https://www.ncbi.nlm.nih.gov/pmc/articles/PMC9272976/ (visited on 08/31/2023).

Scholkmann, Felix and Martin Wolf (Oct. 2013). "General equation for the differential pathlength factor of the frontal human head depending on wavelength and age". In: *Journal of Biomedical Optics* 18.10. Publisher: SPIE, p. 105004. ISSN: 1083-3668, 1560-2281.

DOI: 10.1117/1.JBO.18.10.105004. URL: https://www.spiedigitallibrary.org/journals/journal-of-biomedical-optics/volume-18/issue-10/105004/General-equation-for-the-differential-pathlength-factor-of-the-frontal/10.1117/1.JBO.18.10.105004.full (visited on 09/04/2023).

Schweiger, Martin and Simon R. Arridge (Apr. 2014). "The Toast++ software suite for forward and inverse modeling in optical tomography". In: *Journal of Biomedical Optics* 19.4. Publisher: SPIE, p. 040801. ISSN: 1083-3668, 1560-2281. DOI: 10.1117/1.JBO.19.4.040801. URL: https://www.spiedigitallibrary.org/journals/journal-of-biomedical-optics/volume-19/issue-4/040801/The-Toast-software-suite-for-forward-and-inverse-modeling-in/10.1117/1.JBO.19.4.040801.full (visited on 09/04/2023).

Sherafati, Arefeh et al. (Mar. 2020). *Global Motion Detection and Censoring in High-Density Diffuse Optical Tomography*. en. Pages: 2020.02.22.961219 Section: New Results. DOI: 10.1101/2020.02.22.961219. URL: https://www.biorxiv.org/content/10.1101/2020.02.22.961219v2 (visited on 08/31/2023).

Shifa, Nafhatul Zinan, Md. Mahmudur Rahman Sayem, and Md. Asiful Islam (Feb. 2021). "Improved Image Reconstruction Using Multi frequency Data for Diffuse Optical Tomography". In: *2021 International Conference on Information and Communication Technology for Sustainable Development (ICICT4SD)*. Dhaka, Bangladesh: IEEE, pp. 264–268. ISBN: 978-1-66541-460-9. DOI: 10.1109/ICICT4SD50815.2021.9396993. URL: https://ieeexplore.ieee.org/document/9396993/ (visited on 06/06/2023).

Stillwell, Roy A. et al. (Nov. 2021). "A scalable, multi-wavelength, broad bandwidth frequency-domain near-infrared spectroscopy platform for real-time quantitative tissue optical imaging". en. In: *Biomedical Optics Express* 12.11, p. 7261. ISSN: 2156-7085, 2156-7085. DOI: 10.1364/BOE.435913. URL: https://opg.optica.org/abstract.cfm?URI=boe-12-11-7261 (visited on 06/06/2023).

Stocker, Reto A. (Feb. 2019). "Intensive Care in Traumatic Brain Injury Including Multi-Modal Monitoring and Neuroprotection". en. In: *Medical Sciences* 7.3, p. 37. ISSN:

2076-3271. DOI: 10.3390/medsci7030037. URL: http://www.mdpi.com/2076-3271/7/3/37 (visited on 06/06/2023).

Strangman, Gary E., Zhi Li, and Quan Zhang (Aug. 2013). "Depth Sensitivity and Source-Detector Separations for Near Infrared Spectroscopy Based on the Colin27 Brain Template". In: *PLoS ONE* 8.8, e66319. ISSN: 1932-6203. DOI: 10.1371/journal.pone.0066319. URL: https://www.ncbi.nlm.nih.gov/pmc/articles/PMC3731322/ (visited on 08/29/2023).

Strangman, Gary E., Quan Zhang, and Zhi Li (Jan. 2014). "Scalp and skull influence on near infrared photon propagation in the Colin27 brain template". en. In: *NeuroImage* 85, pp. 136–149. ISSN: 10538119. DOI: 10.1016/j.neuroimage.2013.04.090. URL: https://linkinghub.elsevier.com/retrieve/pii/S1053811913004497 (visited on 06/06/2023).

Sun, Binghai et al. (Nov. 2021). "Cooperation with partners of differing social experience: An fNIRS-based hyperscanning study". en. In: *Brain and Cognition* 154, p. 105803. ISSN: 02782626. DOI: 10.1016/j.bandc.2021.105803. URL: https://linkinghub.elsevier.com/retrieve/pii/S0278262621001238 (visited on 06/05/2023).

Tachtsidis, Ilias et al. (2009). "False Positives In Functional Nearinfrared Topography". en. In: *Oxygen Transport to Tissue XXX*. Ed. by Per Liss et al. Advances in Experimental Medicine and Biology. Boston, MA: Springer US, pp. 307–314. ISBN: 978-0-387-85998-9. DOI: 10.1007/978-0-387-85998-9_46.

Takeuchi, Mikinobu et al. (Nov. 2009). "Brain Cortical Mapping by Simultaneous Recording of Functional Near Infrared Spectroscopy and Electroencephalograms from the Whole Brain During Right Median Nerve Stimulation". In: *Brain Topography* 22.3, pp. 197–214. ISSN: 0896-0267. DOI: 10.1007/s10548-009-0109-2. URL: https://www.ncbi.nlm.nih.gov/pmc/articles/PMC2749167/ (visited on 08/28/2023).

Tian, Fenghua, George Alexandrakis, and Hanli Liu (May 2009). "Optimization of probe geometry for diffuse optical brain imaging based on measurement density and distribution". en. In: *Applied Optics* 48.13, p. 2496. ISSN: 0003-6935, 1539-4522. DOI:

10.1364/AO.48.002496. URL: https://opg.optica.org/abstract.cfm?URI=ao-48-13-2496 (visited on 06/07/2023).

Tong, Yunjie and Blaise deB. Frederick (Nov. 2010). "Time lag dependent multimodal processing of concurrent fMRI and near-infrared spectroscopy (NIRS) data suggests a global circulatory origin for low-frequency oscillation signals in human brain". In: *NeuroImage* 53.2, pp. 553–564. ISSN: 1053-8119. DOI: 10.1016/j.neuroimage.2010.06.049. URL: https://www.sciencedirect.com/science/article/pii/S1053811910009079 (visited on 08/31/2023).

Torricelli, Alessandro et al. (Aug. 2001). "*In vivo* optical characterization of human tissues from 610 to 1010 nm by time-resolved reflectance spectroscopy". In: *Physics in Medicine and Biology* 46.8, pp. 2227–2237. ISSN: 0031-9155, 1361-6560. DOI: 10.1088/0031-9155/46/8/313. URL: https://iopscience.iop.org/article/10.1088/0031-9155/46/8/313 (visited on 06/06/2023).

Tremblay, Julie et al. (June 2018). "Comparison of source localization techniques in diffuse optical tomography for fNIRS application using a realistic head model". In: *Biomedical Optics Express* 9.7, pp. 2994–3016. ISSN: 2156-7085. DOI: 10.1364/BOE.9.002994. URL: https://www.ncbi.nlm.nih.gov/pmc/articles/PMC6033567/ (visited on 09/04/2023).

Tsuzuki, Daisuke and Ippeita Dan (Jan. 2014). "Spatial registration for functional near-infrared spectroscopy: From channel position on the scalp to cortical location in individual and group analyses". en. In: *NeuroImage* 85, pp. 92–103. ISSN: 10538119. DOI: 10.1016/j.neuroimage.2013.07.025. URL: https://linkinghub.elsevier.com/retrieve/pii/S1053811913007805 (visited on 06/07/2023).

Tuchin, Valery V. (2015). *Tissue Optics: Light Scattering Methods and Instruments for Medical Diagnosis*. en. Society of Photo-Optical Instrumentation Engineers (SPIE). ISBN: 978-1-62841-516-2. DOI: 10.1117/3.1003040. URL: http://ebooks.spiedigitallibrary.org/book.aspx?doi=10.1117/3.1003040 (visited on 06/05/2023).

Tyagi, Oshin et al. (Nov. 2020). "Neural Signatures of Handgrip Fatigue in Type 1 Diabetic Men and Women". In: *Frontiers in Human Neuroscience* 14, p. 564969. ISSN: 1662-5161. DOI: 10.3389/fnhum.2020.564969. URL: https://www.frontiersin.org/articles/10.3389/fnhum.2020.564969/full (visited on 06/07/2023).

Uchitel, Julie et al. (Nov. 2022). "Reliability and similarity of resting state functional connectivity networks imaged using wearable, high-density diffuse optical tomography in the home setting". en. In: *NeuroImage* 263, p. 119663. ISSN: 10538119. DOI: 10.1016/j.neuroimage.2022.119663. URL: https://linkinghub.elsevier.com/retrieve/pii/S1053811922007844 (visited on 06/07/2023).

Urban, Karolina J. et al. (June 2015). "Functional Near-Infrared Spectroscopy Reveals Reduced Interhemispheric Cortical Communication after Pediatric Concussion". en. In: *Journal of Neurotrauma* 32.11, pp. 833–840. ISSN: 0897-7151, 1557-9042. DOI: 10.1089/neu.2014.3577. URL: http://www.liebertpub.com/doi/10.1089/neu.2014.3577 (visited on 06/06/2023).

Veesa, Joshua D. and Hamid Dehghani (Mar. 2021). "Signal regression in frequency-domain diffuse optical tomography to remove superficial signal contamination". In: *Neurophotonics* 8.01. ISSN: 2329-423X. DOI: 10.1117/1.NPh.8.1.015013. URL: https://www.spiedigitallibrary.org/journals/neurophotonics/volume-8/issue-01/015013/Signal-regression-in-frequency-domain-diffuse-optical-tomography-to-remove/10.1117/1.NPh.8.1.015013.full (visited on 06/07/2023).

Vidal-Rosas, Ernesto E. et al. (Apr. 2021). "Evaluating a new generation of wearable high-density diffuse optical tomography technology via retinotopic mapping of the adult visual cortex". In: *Neurophotonics* 8.02. ISSN: 2329-423X. DOI: 10.1117/1.NPh.8.2.025002. URL: https://www.spiedigitallibrary.org/journals/neurophotonics/volume-8/issue-02/025002/Evaluating-a-new-generation-of-wearable-high-density-diffuse-optical/10.1117/1.NPh.8.2.025002.full (visited on 06/05/2023).

Vilkė, Alina et al. (2014). "Predictive value of early near-infrared spectroscopy monitoring of patients with traumatic brain injury". en. In: *Medicina* 50.5, pp. 263–268. ISSN: 1010660X. DOI: 10.1016/j.medici.2014.10.001. URL: http://linkinghub.elsevier.com/retrieve/pii/S1010660X14000871 (visited on 06/06/2023).

Villringer, A. et al. (May 1993). "Near infrared spectroscopy (NIRS): a new tool to study hemodynamic changes during activation of brain function in human adults". eng. In: *Neuroscience Letters* 154.1-2, pp. 101–104. ISSN: 0304-3940. DOI: 10.1016/0304-3940(93)90181-j.

Wabnitz, Heidrun et al. (Aug. 2020). "Depth-selective data analysis for time-domain fNIRS: moments vs. time windows". en. In: *Biomedical Optics Express* 11.8, p. 4224. ISSN: 2156-7085, 2156-7085. DOI: 10.1364/BOE.396585. URL: https://opg.optica.org/abstract.cfm?URI=boe-11-8-4224 (visited on 08/16/2023).

Wang, Yongjun, Yuesong Pan, and Hao Li (Oct. 2020). "What is brain health and why is it important?" In: *The BMJ* 371, p. m3683. ISSN: 0959-8138. DOI: 10.1136/bmj.m3683. URL: https://www.ncbi.nlm.nih.gov/pmc/articles/PMC7555053/ (visited on 09/11/2023).

Weigl, Wojciech et al. (Nov. 2016). "Application of optical methods in the monitoring of traumatic brain injury: A review". en. In: *Journal of Cerebral Blood Flow & Metabolism* 36.11, pp. 1825–1843. ISSN: 0271-678X, 1559-7016. DOI: 10.1177/0271678X16667953. URL: http://journals.sagepub.com/doi/10.1177/0271678X16667953 (visited on 06/06/2023).

White, Brian R. and Joseph P. Culver (Mar. 2010). "Quantitative evaluation of high-density diffuse optical tomography: in vivo resolution and mapping performance". In: *Journal of Biomedical Optics* 15.02, p. 1. ISSN: 1083-3668. DOI: 10.1117/1.3368999. URL: https://www.spiedigitallibrary.org/journals/journal-of-biomedical-optics/volume-15/issue-02/026006/Quantitative-evaluation-of-high-density-diffuse-optical-tomography--in/10.1117/1.3368999.full (visited on 06/05/2023).

WHO (2023). *Brain health*. en. URL: https://www.who.int/health-topics/brain-health (visited on 09/08/2023).

Wojtkiewicz, Stanislaw, Karolina Bejm, and Adam Liebert (Apr. 2022). "Lock-in functional near-infrared spectroscopy for measurement of the haemodynamic brain response". en. In: *Biomedical Optics Express* 13.4, p. 1869. ISSN: 2156-7085, 2156-7085. DOI: 10.1364/BOE.448038. URL: https://opg.optica.org/abstract.cfm?URI=boe-13-4-1869 (visited on 06/07/2023).

Wray, Susan et al. (Mar. 1988). "Characterization of the near infrared absorption spectra of cytochrome aa3 and haemoglobin for the non-invasive monitoring of cerebral oxygenation". en. In: *Biochimica et Biophysica Acta (BBA) - Bioenergetics* 933.1, pp. 184–192. ISSN: 00052728. DOI: 10.1016/0005-2728(88)90069-2. URL: https://linkinghub.elsevier.com/retrieve/pii/0005272888900692 (visited on 09/23/2023).

Wyser, Dominik et al. (Sept. 2020). "Short-channel regression in functional near-infrared spectroscopy is more effective when considering heterogeneous scalp hemodynamics". In: *Neurophotonics* 7.03. ISSN: 2329-423X. DOI: 10.1117/1.NPh.7.3.035011. URL: https://www.spiedigitallibrary.org/journals/neurophotonics/volume-7/issue-03/035011/Short-channel-regression-in-functional-near-infrared-spectroscopy-is-more/10.1117/1.NPh.7.3.035011.full (visited on 06/07/2023).

Wyser, Dominik G. et al. (Mar. 2022). "Characterizing reproducibility of cerebral hemodynamic responses when applying short-channel regression in functional near-infrared spectroscopy". In: *Neurophotonics* 9.01. ISSN: 2329-423X. DOI: 10.1117/1.NPh.9.1.015004. URL: https://www.spiedigitallibrary.org/journals/neurophotonics/volume-9/issue-01/015004/Characterizing-reproducibility-of-cerebral-hemodynamic-responses-when-applying-short-channel/10.1117/1.NPh.9.1.015004.full (visited on 06/07/2023).

Yücel, Meryem A. et al. (Jan. 2021). "Best practices for fNIRS publications". In: *Neurophotonics* 8.1. Publisher: SPIE, p. 012101. ISSN: 2329-423X, 2329-4248. DOI: 10.1117/1.NPh.8.1.012101. URL: https://www.spiedigitallibrary.org/journals/neurophotonics/

volume-8/issue-1/012101/Best-practices-for-fNIRS-publications/10.1117/1.NPh.8.1.012101.full (visited on 06/05/2023).

Zeff, Benjamin W. et al. (July 2007). "Retinotopic mapping of adult human visual cortex with high-density diffuse optical tomography". en. In: *Proceedings of the National Academy of Sciences* 104.29, pp. 12169–12174. ISSN: 0027-8424, 1091-6490. DOI: 10.1073/pnas.0611266104. URL: https://pnas.org/doi/full/10.1073/pnas.0611266104 (visited on 06/05/2023).

Zhan, Yuxuan (Dec. 2013). "Model-based high-density functional diffuse optical tomography of human brain". English. d_ph. University of Birmingham. URL: https://etheses.bham.ac.uk/id/eprint/4450/ (visited on 06/06/2023).

Zhang, Yiheng et al. (2005). "Eigenvector-based spatial filtering for reduction of physiological interference in diffuse optical imaging". eng. In: *Journal of Biomedical Optics* 10.1, p. 11014. ISSN: 1083-3668. DOI: 10.1117/1.1852552.